



Ingenierie des Nanomatériaux pour Application Energétique

Par

Rania Afia Nuamah

Sous la supervision du Prof. Dilip Sarkar

**Thèse présentée à l'Université du Québec à Chicoutimi en vue de l'obtention du grade
de doctorat en ingénierie**

Québec, Canada

© Rania Afia Nuamah, 2022



Engineered Nanomaterials for Energy Application

By

Rania Afia Nuamah

Under supervision of Prof. Dilip Sarkar

Thesis presented to the University of Quebec at Chicoutimi in Partial Fulfillment of the Requirements for the Degree of Doctor of Philosophy Ph.D.

Defended on 08 December 2022

BOARD OF EXAMINERS:

Professor Dilip Sarkar, Department of Applied Sciences at UQAC, Internal Member of examiners

Dr. Zhan Zhang, Department of Applied Sciences at UQAC, President of the board of examiners

Professor David Dodoo-Arhin, Department of Materials Science and Engineering at the University of Ghana, Legon, External Member of examiners

Dr. Saleema Noormohammed, Trans Al, Internal Member of examiners

Professor Duygu Kocafee, Department of Applied Sciences at UQAC, Internal Member of examiners

Québec, Canada

© Rania Afia Nuamah, 2022

RÉSUMÉ

Le remplacement des combustibles fossiles classiques par des sources d'énergie renouvelables et respectueuses de l'environnement, en raison de l'empreinte carbone élevée de ces dernières, a entraîné une demande accrue de dispositifs de stockages d'énergie présentant des propriétés de puissance et de densité énergétique élevées. Comme de nombreux pays, le Québec (Canada) interdira les voitures à essence d'ici 2035 pour laisser la place aux voitures électriques. La recherche de dispositifs de stockage d'énergie performants est donc plus que jamais d'actualité. Ces derniers temps, les supercondensateurs sont apparus comme une technologie de stockage d'énergie propice pour combler le fossé de la densité d'énergie et de puissance des dispositifs de stockage d'énergie traditionnels tels que les condensateurs diélectriques et les batteries. Néanmoins, si la densité d'énergie des supercondensateurs est supérieure à celle des condensateurs classiques, elle est considérablement inférieure à celle des batteries et des piles à combustible. Pour répondre aux exigences pratiques des dispositifs de stockage d'énergie, il est souhaitable de fabriquer des supercondensateurs avec des matériaux d'électrode nanostructurés à haute capacité, présentant une surface spécifique élevée, une densité d'énergie élevée, une longue stabilité de cycle et un coût réduit. Comme de nombreux pays, le Canada (Québec) interdira les voitures à essence d'ici 2035 pour laisser la place aux voitures électriques. La recherche de dispositifs de stockage d'énergie performants est donc plus que jamais d'actualité. Ces derniers temps, les supercondensateurs sont apparus comme une technologie de stockage d'énergie propice pour combler le fossé entre la densité d'énergie et la de puissance des dispositifs de stockage d'énergie traditionnels tels que les condensateurs diélectriques et les batteries. Néanmoins, si la densité d'énergie des supercondensateurs est supérieure à celle des condensateurs classiques, elle est considérablement inférieure à celle des batteries et des piles à combustible. Pour répondre aux exigences pratiques des dispositifs de stockage d'énergie, il est souhaitable de fabriquer des supercondensateurs avec des matériaux d'électrode nanostructurés à haute capacité présentant une surface spécifique élevée, une densité d'énergie élevée, une longue stabilité de cycle et un coût réduit.

Dans cette recherche, des matériaux d'électrode de supercondensateur nanostructurés ont été conçus et synthétisés à l'aide de procédés hydrothermiques et d'électrodéposition et leurs propriétés électrochimiques ont été évaluées. Une comparaison des résultats a montré que la voie électrochimique est la plus efficace pour synthétiser des matériaux nanostructurés avec une capacité élevée proche des valeurs théoriques. Par conséquent, cette thèse est principalement axée sur les matériaux d'électrodes de supercondensateur nanostructurés fabriqués par le biais du processus électrochimique.

La première stratégie consiste à fabriquer des matériaux d'électrode de NiO et de Co₃O₄ par une voie de synthèse par précipitation chimique simple et rentable. Les électrodes fabriquées ont fourni une capacité spécifique maximale de 40 F/g et 28 F/g à un courant spécifique de 1 A/g pour les électrodes NiO et Co₃O₄ respectivement. Cependant, les valeurs de capacité spécifique obtenues étaient bien en dessous de la capacité théorique attendue de NiO (2573 F/g) et de Co₃O₄ (3560 F/g).

La deuxième stratégie consiste à optimiser le processus électrochimique pour la fabrication de films minces nanocomposites Ni-NiO, Co-Co₃O₄ et Ag/Co-Co₃O₄ en utilisant une nouvelle technique qui combine la voltamétrie cyclique et les techniques d'électrodéposition inverse pulsée. Il a été constaté que la cristallinité et les caractéristiques morphologiques des films déposés, entraînées par la concentration d'électrolyte avec des variations molaires et les modes d'électrodéposition, influencent les performances de capacité spécifiques. Les électrodes à couches minces nanocomposites Ni-NiO, Co-Co₃O₄ et Ag/Co-Co₃O₄ fabriquées ont obtenu des valeurs de capacité spécifiques élevées de 2000 F/g, 2580 F/g et 2800 F/g à un courant spécifique de 1 A/g respectivement. Les électrodes fabriquées ont également montré une stabilité à long terme après environ 1000 cycles de charge-décharge répétés, montrant des valeurs de rétention de capacité de 98,6 %, 78,2 % et 82,6 % pour les électrodes Ni-NiO, Co-Co₃O₄ et Ag/Co-Co₃O₄, respectivement à 20 A/g.

Dans la stratégie finale, l'utilisation de l'aluminium comme substrat a été valorisée en modifiant la maille d'alliage d'aluminium AA6061 en utilisant un revêtement de nickel. De plus, le revêtement de polypyrrole comme matériau actif sur la maille d'aluminium modifiée a été réalisé en utilisant une technique simple et économique d'électrodéposition potentiostatique. L'aluminium modifié au nickel revêtu de polypyrrole, comparé à une maille en acier inoxydable revêtu de polypyrrole, a montré des performances supérieures en fournissant une capacité spécifique de ~100 F/g à un courant spécifique appliqué de 1 A/g avec une excellente conductivité révélée par une petite résistance série d'équivalence de 0,18 $\Omega \cdot \text{cm}^2$. Les résultats obtenus et les observations ont montré que la morphologie pilotée par le type de substrat influence les performances des supercondensateurs des électrodes à base de polypyrrole.

Les résultats obtenus dans cette thèse ont démontré que la nouvelle technique combinée de voltampérométrie cyclique et d'électrodéposition inverse pulsée présente une méthode efficace et rentable pour développer des matériaux d'électrode nanostructurés performants pour des applications pratiques dans les dispositifs de stockage d'énergie à supercondensateur.

ABSTRACT

The switch from conventional fossil-based fuel to renewable and environmentally friendly energy sources due to the former's high carbon footprint has resulted in an increased demand for energy storage devices with high power and energy density properties. Like many countries, Quebec, Canada will ban the gasoline-powered automobile by the year 2035 to make way for electric cars. Thus, the search for high-performance energy storage devices has become pertinent now more than ever. In recent times, supercapacitors have surfaced as propitious energy storage technology to bridge the energy and power density gap of traditional energy storage devices such as dielectric capacitors and batteries. Nevertheless, while the energy density of supercapacitors is higher than conventional capacitors, it is considerably lower than that of batteries and fuel cells. To meet the practical requirements of energy storage devices, it is desirable to fabricate supercapacitors with high capacitance nanostructured electrode materials, having high specific surface area, high energy density, long cycle stability, and lower cost.

In this research, nanostructured supercapacitor electrode materials have been designed and synthesized using chemical precipitation and electrodeposition processes, and their electrochemical properties were evaluated. A comparison of the results has shown the electrochemical route to be efficient in synthesizing nanostructured materials with high capacitance close to theoretical values. Hence, this thesis is predominantly focused on nanostructured supercapacitor electrode materials fabricated through electrochemical process.

The first strategy is the fabrication of NiO and Co₃O₄ electrode materials by a simple, cost-effective chemical precipitation synthesis route. The fabricated electrodes delivered a maximum specific capacitance of 40 F/g and 28 F/g at a specific current of 1 A/g for the NiO and Co₃O₄ electrodes respectively. However, the obtained specific capacitance values were far below the expected theoretical capacitance of NiO (2573 F/g) and Co₃O₄ (3560 F/g).

The second strategy involves optimizing the electrochemical process for the fabrication of Ni-NiO, Co-Co₃O₄, and Ag/Co-Co₃O₄ nanocomposite thin films using a novel technique that combines cyclic voltammetry and pulse reverse electrodeposition techniques. Crystallinity and morphological features of the deposited films, driven by the electrolyte concentration with molar variations and the electrodeposition modes have been found to influence specific capacitance performance. The fabricated Ni-NiO, Co-Co₃O₄, and Ag/Co-Co₃O₄ nanocomposite thin film electrodes obtained high specific capacitance values of 2000 F/g, 2580 F/g, and 2800 F/g at a specific current of 1 A/g respectively. The fabricated electrodes also exhibited long-term stability after ~1000 repeated charge-discharge cycles, showing capacitance retention values of 98.6 %, 78.2 %, and 82.6 % for Ni-NiO, Co-Co₃O₄, and Ag/Co-Co₃O₄ electrodes, respectively at 20 A/g.

In the final strategy, the use of aluminum as a substrate has been valorized by modifying AA6061 aluminum alloy mesh using a coating of nickel. Furthermore,

polypyrrole coating as active material on the modified aluminum mesh was performed using a simple cost-effective potentiostatic electrodeposition technique. The polypyrrole-coated nickel-modified aluminum compared to a polypyrrole-coated stainless-steel mesh has shown superior performance by providing a specific capacitance of $\sim 100 \text{ Fg}^{-1}$ at an applied specific current of 1 Ag^{-1} with an excellent conductivity revealed by a small equivalence series resistance of $0.18 \text{ } \Omega \cdot \text{cm}^2$. The obtained results and observations have shown that the morphology driven by the type of substrate influences the supercapacitor performance of polypyrrole-based electrodes.

The results obtained in this thesis have demonstrated that the novel combined cyclic voltammetry and pulse reverse electrodeposition technique presents an efficient and cost-effective method for developing high-performing nanostructured electrode materials for practical applications in supercapacitor energy storage devices.

TABLE OF CONTENTS

RÉSUMÉ	IV
ABSTRACT.....	VI
TABLE OF CONTENTS.....	VIII
LIST OF TABLES.....	XII
LIST OF FIGURES	XIII
LIST OF SYMBOLS AND ABBREVIATIONS.....	XIX
DEDICATION.....	XXII
ACKNOWLEDGEMENTS	XXIII
CHAPTER 1: INTRODUCTION	1
1.1 Introduction.....	1
1.2 Problem statement.....	3
1.3 Originality Statement.....	4
1.4 Objectives.....	5
1.5 Methodology	6
1.6 References.....	9
CHAPTER 2: LITERATURE REVIEW	10
2.1 Introduction to supercapacitors.....	10
2.2 Types of supercapacitors.....	11
2.2.1 Electrochemical double-layer capacitors (EDLCs).....	11
2.2.2 Pseudocapacitors (PCs).....	14
2.2.3 Hybrid supercapacitors.....	15
2.3 Supercapacitor electrode materials	16
2.3.1 Carbon materials	16
2.3.2 Pseudocapacitive electrode materials.....	22
2.3.3 Composite materials.....	35
2.4 Electrolytes.....	36
2.5 Current collector/Substrates	36
2.6 Parameters and electrochemical techniques for supercapacitor electrode material evaluation.....	37
2.6.1 Cyclic voltammetry.....	37
2.6.2 Galvanostatic charge-discharge (GCD)	38
2.6.3 Electrochemical Impedance Spectroscopy (EIS)	40
2.7 Synthesis of supercapacitor electrode materials.....	41

2.7.1 Electrodeposition.....	42
2.7.2 Sol-gel	45
2.7.3 Hydrothermal	46
2.7.4 Chemical precipitation.	47
2.8 Applications of supercapacitors	49
2.9 References.....	49
CHAPTER 3: EXPERIMENTAL PROCEDURE	55
3.1 Materials synthesis.....	55
3.1.1 Chemicals and Materials.....	55
3.1.2 Substrate preparation.....	57
3.1.3 Chemical precipitation synthesis.....	58
3.1.4 Electrodeposition synthesis.....	60
3.2 Materials Analysis.....	68
3.2.1 Microstructural analysis by scanning electron microscopy	68
3.2.2 Fourier transform infrared spectroscopy	69
3.2.3 X-ray diffractometry	71
3.2.4 Electrochemical Characterization	72
3.3 References.....	77
CHAPTER 4: CHEMICAL PRECIPITATION SYNTHESIS OF NiO AND Co ₃ O ₄ SUPERCAPACITOR ELECTRODE MATERIALS.....	78
4.1 Abstract.....	78
4.2 Introduction.....	78
4.3 Experimental procedure	80
4.4 Results and discussion	81
4.4.1 Structural, morphological, and chemical analysis.....	81
4.3.2 Electrochemical analysis.....	84
4.4 Conclusions.....	87
4.5 References.....	88
CHAPTER 5: PULSED REVERSE POTENTIAL ELECTRODEPOSITION OF CARBON-FREE Ni-NiO NANOCOMPOSITE THIN FILM ELECTRODE FOR ENERGY STORAGE SUPERCAPACITOR ELECTRODES	91
5.1 Abstract.....	91
5.2 Introduction.....	92
5.3 Experimental Section	93
5.4 Results and discussion	94

5.4.1 Structural, morphological, and chemical analysis.....	94
5.4.2 Electrochemical measurements	96
5.5 Conclusions.....	99
5.6 References.....	99
5.7 Supporting Information.....	100
CHAPTER 6: EFFECT OF MOLAR RATIO MODULATION OF COBALT PRECURSORS ON SUPERCAPACITOR BEHAVIOR OF ENGINEERED Co-Co₃O₄ NANOCOMPOSITE ELECTRODES	
106	
6.1 Abstract.....	106
6.2 Introduction.....	107
6.3 Experimental section.....	110
6.4 Results and discussion	113
6.4.1 Structural, morphological, and chemical analysis.....	113
6.4.2 Electrochemical measurements	122
6.5 Conclusions.....	130
6.6 References.....	131
6.7 Supplementary information.....	134
CHAPTER 7: SPECIFIC CAPACITANCE BEHAVIOR OF Co-Co₃O₄ NANOCOMPOSITE THIN FILMS SYNTHESIZED VIA DIFFERENT ELECTRODEPOSITION MODES	
139	
7.1 Abstract.....	139
7.2 Introduction.....	140
7.3 Experimental Section	142
7.4 Results and discussion	145
7.4.1 Electrodeposition of Co-Co ₃ O ₄	145
7.4.2 Structural, morphological, and chemical analysis.....	147
7.4.3 Electrochemical measurements	153
7.5 Conclusion	161
7.6 References.....	162
7.7 Supporting information.....	164
CHAPTER 8: SUPERCAPACITOR PERFORMANCE EVALUATION OF NANOSTRUCTURED Ag-DECORATED Co-Co₃O₄ COMPOSITE THIN FILM ELECTRODE MATERIAL	
170	
8.1 Abstract.....	170
8.2 Introduction.....	171
8.3 Experimental details.....	175
8.4 Results and discussion	177

8.4.1 Structural, morphological, and chemical analysis.....	177
8.5.2 Electrochemical measurements	183
8.5 Conclusions.....	193
8.6 References.....	194
8.7 Supporting information.....	198
CHAPTER 9: CAPACITIVE BEHAVIOR OF ELECTROCHEMICALLY SYNTHESIZED POLYPYRROLE COATINGS ON NICKEL-MODIFIED ALUMINUM MESH AND STEEL MESH SUBSTRATES	203
9.1 Abstract.....	203
9.2 Introduction.....	204
9.3 Experimental details.....	205
9.4 Results and discussion	206
9.4.1 Structural, morphological, and chemical analysis.....	206
9.4.2 Electrochemical measurements.....	209
9.5 Conclusions.....	211
9.6 References.....	212
9.7 Supporting information.....	212
CHAPTER 10: GENERAL CONCLUSIONS AND FUTURE RECOMMENDATIONS	216
10.1 Conclusions.....	216
10.2 Future recommendations.....	220
LIST OF PUBLICATIONS	222
Journal articles	222
Conferences Attended (Oral and Poster presentations).....	223

LIST OF TABLES

Table 2.1 : Summary of specific capacitance of NiO electrodes	29
Table 2.2 : Summary of specific capacitance of Cobalt oxide electrodes	33
Table 3.1 : List of chemicals and materials used	55
Table 6.1: Summary of electrodeposition electrolyte solutions consisting of different molar ratios of cobalt acetate $\text{Co}(\text{CH}_3\text{COO})_2$ and cobalt chloride (CoCl_2).....	112
Table 7.1 : Summary of the different modes of electrodeposition	144
Table S7.1. : Crystallite size of the Co (102) and Co_3O_4 (400) planes estimated from the XRD data and thickness of the various types of Co- Co_3O_4 nanocomposite thin films	168

LIST OF FIGURES

Figure 2.1 Ragone plot for different energy storage systems: capacitors, supercapacitors, batteries, and fuel cells (Specific power against specific energy). Reproduced with permission from reference [3]. Copyright © 2019 Springer Nature.	11
Figure 2.2 Schematic presentation of an Electrochemical double-layer capacitor (EDLC). Reproduced with the permission of reference [12]. Copyright © 2019 MDPI	13
Figure 2.3 Schematic diagram of the charge storage mechanism of a Pseudocapacitor. Reproduced with the permission of reference [13]. Copyright © 2019 John Wiley and Sons.....	15
Figure 2.4. Schematic representation of the pore size network of activated carbon grain. Adapted from the reference [19] with permission. Copyright © 2008 The Electrochemical Society.	18
Figure 2.5. Schematic diagram of (A) single-walled carbon nanotube (SWCNT) and (B) multi-walled carbon nanotube. Adapted from reference [21] with permission. Copyright © 2013 SAGE Publications.....	19
Figure 2.6 (a) SEM micrograph (b) cyclic voltammetry curves at different scan rates (CV), (c) galvanostatic charge-discharge profiles at different specific currents of 3DG/CNT composite material. Adapted from reference [25] with permission. Copyright © 2020 Elsevier.	20
Figure 2.7. (a) SEM image (b) cyclic voltammetry curves at different scan rates (c) Galvanostatic charge-discharge curves of graphene paper. Adapted from reference [29] with permission. Copyright © 2017 Elsevier.	22
Figure 2.8 (a) SEM image (b) cyclic voltammetry curves at different scan rates (c) Galvanostatic charge-discharge curves of graphene paper (d) cycle performance of RuO ₂ nanoparticles anchored on graphene nanosheets. Adapted from reference [33] with permission. Copyright © 2018 Elsevier.....	24
Figure 2.9 (a) SEM micrograph of β-MnO ₂ nanoneedles (b) electrochemical performance of β-MnO ₂ nanoneedles (NNs) presented by CV at different scan rates. Adapted from reference [40] with permission. Copyright © 2018, American Chemical Society.	26
Figure 2.10 (a) SEM of NiO hierarchical microspheres, (b) cyclic voltammetry (CV) at different scan rates (c) galvanostatic charge-discharge (GCD) curves at different specific currents, (d) specific capacitance estimated from the GCD curves, and (e) cyclic performance at 10 Ag ⁻¹ of the NiO hierarchical microspheres on nickel foam electrode. Adapted from reference [44] with permission. Copyright © 2018, Elsevier.	28
Figure 2.11 Cubic crystal structure of Co ₃ O ₄ exhibiting Co ²⁺ and Co ³⁺ cations tetrahedrally and octahedrally coordinated to oxygen anions respectively. Adapted from [55] with permission. Copyright © 2018, Elsevier	31
Figure 2.12 (a) SEM image of thin-wall Co ₃ O ₄ spheres (b) cyclic voltammograms (c) galvanostatic charge-discharge profiles (c) specific capacitance values calculated from charge-discharge curves at different current densities of the thin-wall Co ₃ O ₄ spheres. Adapted from [58] with permission. Copyright © 2018, MDPI.	32
Figure 2.13 Schematic diagram of the p-and n-doping-dedoping process of PTH. Adapted from reference [65] with permission. Copyright © 2001, Elsevier.	34
Figure 2.14. Typical cyclic voltammetry signatures for EDLC (red curve), pseudocapacitor (violet curve), and battery-like (green curve) electrode materials. Adapted from reference [38] with permission. Copyright © 2020, Springer Nature.	38
Figure 2.15. Typical galvanostatic charge-discharge (GCD) profiles for EDLC (red curve), pseudocapacitor (violet curve), and battery-like (green curve) electrode materials. Adapted from reference [38] with permission. Copyright © 2020, Springer Nature.	39
Figure 2.16 Nyquist plot of electrode material for supercapacitors. Adapted from reference [38] with permission. Copyright © 2020, Springer Nature.	41

Figure 2.17 Schematic representation of (a) two-electrode (b) three-electrode electrodeposition cell configurations.....	44
Figure 2.19 Schematic illustration of hydrothermal synthesis of (a) NiO nanorods, (b) Ni(OH) ₂ nanowall, (c) Co ₃ O ₄ nanosheet, and (d) Co ₃ O ₄ nanowire. Adapted from [81] with permission. Copyright © 2013, Elsevier.	47
Figure 3.1. Schematic diagram of the hydrothermal synthesis and electrode fabrication process of Co ₃ O ₄ electrode material.....	60
Figure 3.2 Three-electrode system setup for the electrodeposition synthesis of Co-Co ₃ O ₄ nanocomposite electrode material.....	63
Figure 3.3 Electropolymerization process of pyrrole. Adapted from [3] with permission.	67
Figure 3.4. Scanning electron microscope (model SEM JEOL JSM 6480LV), CURAL, UQAC....	69
Figure 3.5. ATR-FTIR spectroscopy apparatus (Agilent Technologies Cary 360), CURAL, UQAC.	70
Figure 3.6 X-ray diffractometer, Bruker D8 Discover system, CURAL, UQAC.	72
Figure 3.7. Three-electrode setup with the Solartron SI1287 electrochemical interface and the Solartron 1254A frequency analyzer.....	73
Figure 4.1. FTIR spectra of (a) NiO and (b) Co ₃ O ₄ electrode materials on titanium (Ti) substrates	82
Figure 4.2. SEM micrographs and EDX images (a, c) NiO, (b, d) Co ₃ O ₄ electrode materials on titanium substrates.....	83
Figure 4.3 (a,c) Cyclic voltammetry (CV) curves of NiO and Co ₃ O ₄ on titanium (Ti) substrate electrodes at different scan rates respectively (b,d) Galvanostatic charge-discharge (GCD) curves of NiO and Co ₃ O ₄ on Ti substrate electrodes at different specific currents respectively.	85
Figure 5.1. (a) XRD spectrum of the carbon-free Ni-NiO nanocomposite thin film on Ti-substrate. Table 200. C-fitted peak of Ni (111), D-smoothed data, (b, c) SEM images of Ti-substrate and carbon-free Ni-NiO nanocomposite thin film (d) EDX spectrum corresponding to Figure 1 (c).	95
Figure 5.2. (a) CV curves of Ti-substrate and the carbon-free Ni-NiO nanocomposite thin film on Ti-substrate, (b) Charge-discharge curves of one cycle at different current densities, (c) Cycling performance after 800 cycles at 20 A/g.....	98
Figure S5.1. Deposition profiles of carbon-free Ni-NiO nanocomposite thin film on Ti-substrate: (a) Cyclic voltammetry (CV) followed by (b) Pulse reverse potential (PRP).	101
Figure S5.2. (a) SEM image (b & c) Particle size distribution of the Carbon-free Ni-NiO nanocomposite thin film on Ti-substrate.....	102
Figure S5.3. (a) Nyquist plots and (b) polarization curves of Ni/NiO coating on Ti substrate and pristine Ti substrate (Inset shows the Nyquist plot of Ni/NiO coating on Ti).	103
Figure S5.4. TEM image of the Carbon-free Ni-NiO nanocomposite thin film	104
Figure S5.5. Specific capacitance variation with pulse reverse potential (PRP) deposition time of the Carbon-free Ni-NiO nanocomposite thin film on Ti substrate electrode.....	105
Figure 6.1. (A) XRD patterns collected on titanium (Ti) substrate, (B) XRD crystallites size analysis, and (C) Co ₃ O ₄ /Co XRD peak intensity ratio analysis of Co-Co ₃ O ₄ nanocomposite thin films prepared by the molar ratio variation of cobalt acetate and cobalt chloride precursors (represented as cobalt acetate (Ac) and cobalt chloride (Cl)).	114
Figure 6.2. (A) ATR-FTIR spectra of nickel foam (NF) substrate, and (B) area under the two IR absorption bands at 650 cm ⁻¹ and 550 cm ⁻¹ of Co-Co ₃ O ₄ nanocomposite thin films prepared by varying the molar ratios of Ac and Cl.	117
Figure 6.3. Graph of the ratio of the two IR absorption bands at 650 cm ⁻¹ and 550 cm ⁻¹ of the Co-Co ₃ O ₄ nanocomposite thin films prepared by varying the molar ratios of Ac and Cl.	118
Figure 6.4. SEM micrographs of the as-synthesized Co-Co ₃ O ₄ nanocomposite thin films on NF substrate prepared by the different molar ratios of cobalt precursors (a) 100Ac0Cl, (b) 80Ac20Cl, (c) 50Ac50Cl, (d) 20Ac80Cl and (e) 0Ac100Cl respectively.....	120

Figure 6.5. EDX spectra of Co-Co ₃ O ₄ nanocomposite thin films deposited on NF substrate using precursors with varied molar concentrations of Ac (100 % to 0 %) and Cl (0 % to 100 %).	122
Figure 6.6 (A) Cyclic voltammetry curves at 5 mV/s, (B) Charge-discharge curves at 1 A/g, (C) Optimization graph of the molar ratio variation of cobalt precursors, (D) variation of specific capacitance at the different specific current graph of Co-Co ₃ O ₄ nanocomposite thin films deposited using 100Ac0Cl, 80Ac20Cl, 50Ac50Cl, 20Ac80Cl, and 0Ac100Cl precursors.	124
Figure 6.7. Cycling performance for 500 cycles at a specific current of 20 A/g of Co-Co ₃ O ₄ nanocomposite thin films deposited using 100Ac0Cl, 80Ac20Cl, 50Ac50Cl, 20Ac80Cl, and 0Ac100Cl precursors.	128
Figure 6.8 Nyquist plots of Co-Co ₃ O ₄ nanocomposite thin films on NF substrate using 100Ac0Cl, 80Ac20Cl, 50Ac50Cl, 20Ac80Cl, and 0Ac100Cl precursors with inset showing a magnified plot of the film deposited using 20Ac80Cl.	129
Figure 6S.1. Cyclic voltammetry (CV) curves of (A) 100Ac0Cl (B) 80Ac20Cl, (C) 50Ac50Cl (D) 20Ac80Cl and (E) 0Ac100Cl Co-Co ₃ O ₄ nanocomposite thin films on nickel foam (NF) substrates at different scan rates.	136
Figure 6S.2. Galvanostatic charge-discharge (GCD) curves of (A) 100Ac0Cl (B) 80Ac20Cl (C) 50Ac50Cl (D) 20Ac80Cl (E) 0Ac100Cl Co-Co ₃ O ₄ nanocomposite thin film on NF electrodes at different specific current.	137
Figure 6S.3. Variation of mass and specific capacitance with pulse reverse potential (PRP) electrodeposition time for the 20Ac80Cl Co-Co ₃ O ₄ nanocomposite thin film electrode.	138
Figure 7.1. Individual profiles of electrodeposition modes for the preparation of the Co-Co ₃ O ₄ nanocomposite thin films on NF: (a) cyclic voltammetry (CV, 2 scans), (b) potentiostatic at +1.0V (PS +1.0V), (c) potentiostatic at -1.4 V (PS -1.4V), (d) pulse reverse potential (PRP) (inset of (d) shows the current vs. time graph of the first three cycles).	147
Figure 7.2. XRD patterns of Type 1, 2, 3, and 4 Co-Co ₃ O ₄ nanocomposite thin films synthesized by CV, CVPS +1.0V, CVPS -1.4V, and CVPRP electrodeposition modes on Ti-substrate.	148
Figure 7.4. SEM micrographs of the as-synthesized Co-Co ₃ O ₄ nanocomposite thin films on NF substrate prepared by the four different electrodeposition modes: (a) Type 1 (CV), (b) Type 2 (CVPS +1.0V), (c) Type 3 (CVPS -1.4V) and (d) Type 4 (CV PRP).	151
Figure 7.5. EDX spectra of NF substrate and Type 1 (CV), Type 2 (CV PS +1.0V), Type 3 (CV PS -1.4V) and Type 4 (CV PRP) Co-Co ₃ O ₄ nanocomposite thin films on NF substrate.	153
Figure 7.6. (a) Cyclic voltammetry curves at 5mV/s, (b) Charge-discharge curves at 1 A/g, (c) Variation of specific capacitance at different specific current graph, (d) Cycling performance for 500 cycles at a specific current of 20 A/g of the Type 1 (CV), Type 2 (CV PS +1V), Type 3 (CV PS -1.4V) and Type 4 (CV PRP) Co-Co ₃ O ₄ nanocomposite thin films on NF substrate.	155
Figure 7.7. Variation of specific capacitance as a function of O/Co atomic ratio obtained from EDX analysis for Type 1 (CV), Type 2 (CV PS +1V), Type 3 (CV PS -1.4V) and Type 4 (CV PRP) Co-Co ₃ O ₄ nanocomposite thin films on NF substrate.	158
Figure 7.8. (a) Nyquist plots, (b) Bode plot of the frequency's dependence on the impedance magnitude (Z), (c) Bode plots of the frequency's dependence on the phase angle of the Type 1 (CV), Type 2 (CV PS +1V), Type 3 (CV PS -1.4V) and Type 4 (CV PRP) Co-Co ₃ O ₄ nanocomposite thin films synthesized on NF substrate.	160
Figure S7.1. EDX analysis of (a,c) sponge-like material (b,d) matrix (film) of Type 4 (CV PRP) Co ₃ O ₄ nanocomposite thin on NF substrate.	165
Figure S7.2. Cyclic voltammetry curves of (a) Type 1 (CV) (b) Type 2 (CV PS +1V) (c) Type 3 (CV PS -1.4V) (d) Type 4 (CV PRP) Co-Co ₃ O ₄ nanocomposite thin films on NF substrate at different scan rates.	166
Figure S7.3. (a) SEM image (b) Comparison of the before and after cycle cyclic voltammetry (CV) curves of Type 4 (CV PRP) Co-Co ₃ O ₄ nanocomposite thin film on NF substrate after 500 charge-discharge (GCD) cycles.	166
Figure S7.4. TEM image of Type 4(CV PRP) Co-Co ₃ O ₄ nanocomposite thin film.	167

Figure 8.1. (a) XRD patterns and (b) ATR-FTIR spectra of (I) Nickel foam (NF) substrate, (II) Ag thin film on NF, (III) Co-Co ₃ O ₄ , and (IV) Ag/Co-Co ₃ O ₄ composite thin films on NF.	177
Figure 8.2. SEM micrographs of (a) Nickel foam (NF) substrate, (b) Ag thin film on NF, (c) Co-Co ₃ O ₄ , and (d) Ag/Co-Co ₃ O ₄ composite thin films on NF, red circles identify the Ag nanoparticles in the composite film.	180
Figure 8.3. (a) EDX spectra of (I) nickel (NF) substrate (II) Ag thin film on NF, (III) Co-Co ₃ O ₄ /NF, and (IV) Ag/Co-Co ₃ O ₄ /NF composite thin films. (b) SEM image of Ag/Co-Co ₃ O ₄ /NF composite thin film and (c-f) elemental mapping of Ag/Co-Co ₃ O ₄ /NF composite thin film showing the distribution of (c) Co (d) O (e) Ag (f) Ni.....	182
Figure 8.4. Cyclic voltammetry (CV) curves of (a) Co-Co ₃ O ₄ /NF (b) Ag/Co-Co ₃ O ₄ /NF composite thin film electrodes at different scan rates (c) Comparison CV curves of NF substrate, Co-Co ₃ O ₄ /NF, and Ag/Co-Co ₃ O ₄ /NF electrodes at 5 mV/s.	185
Figure 8.5. Galvanostatic charge-discharge (GCD) curves of (a) Co-Co ₃ O ₄ /NF, (b) Ag/Co-Co ₃ O ₄ /NF composite thin film electrodes at different specific currents, (c) Comparison (GCD) curves NF substrate, Co-Co ₃ O ₄ /NF, and Ag/Co-Co ₃ O ₄ /NF electrodes at 1 A/g, (d) variation of specific capacitance at different specific currents, (e) cycling performance with inset showing the last 17 GCD cycles of Ag/Co-Co ₃ O ₄ /NF tested for 1000 cycles at a specific current of 20 A/g, and (g) Ragone plot of Co-Co ₃ O ₄ /NF and Ag/Co-Co ₃ O ₄ /NF electrodes.....	187
Figure 8.6 Nyquist plots (a) full range, and (b) between 0 and 20 Ω.cm ² , Bode plots of the frequency's dependence on the (c) impedance magnitude (Z), and (d) phase angle of the NF substrate, Co-Co ₃ O ₄ /NF, and Ag/Co-Co ₃ O ₄ /NF electrodes.	192
Figure S8.1 (a) XRD patterns of (I) Titanium (Ti) substrate (II) Ag thin film on Ti, (III) Co-Co ₃ O ₄ , and (IV) Ag/Co-Co ₃ O ₄ composite thin films on Ti (b, c) deconvoluted XRD peaks of Ag/Co-Co ₃ O ₄ composite thin film on Ti at 2θ positions of 38.5° and 44.5° respectively.	199
Figure S8.2 (a) XRD pattern Ag/Co-Co ₃ O ₄ composite thin films on Ti substrate prepared from only cobalt acetate and silver nitrate (0.1 M CoAc + 0.1 M AgNO ₃), (b, c) deconvoluted XRD peaks of at 2θ positions of 38.5° and 44.5° respectively.	200
Figure S8.3 EDX elemental mapping of Co-Co ₃ O ₄ composite thin film on NF substrate (a) SEM image (b) Co (c) O (d) Ni arising from the nickel foam (NF) substrate.	201
Figure S8.4 Cycling performance with inset showing the last 18 GCD cycles of Ag/Co-Co ₃ O ₄ /NF tested for 3000 cycles at a specific current of 20 A/g.	201
Figure S8.5. Optimization graph of the volume of AgNO ₃ in the electrolyte solution for the electrodeposition of Ag/Co-Co ₃ O ₄ nanocomposite thin films.	202
Figure 9.1. (a) Attenuated total reflection–Fourier transform infrared spectra, (b) energy-dispersive X-ray spectroscopy spectra of (i) polypyrrole- coated nickel- modified aluminum mesh (Ppy-Ni-Al), and (ii) polypyrrole-coated steel mesh (Ppy-steel), (c,d) scanning electron microscope micrographs of polypyrrole- coated nickel- modified and polypyrrole-coated steel meshes respectively.	207
Figure S9.1. Nyquist plots of the Ppy- coated Ni- modified-aluminum (Ppy-Ni-Al) mesh, and Ppy-coated steel (Ppy-Steel) mesh electrodes.	213

LIST OF SYMBOLS AND ABBREVIATIONS

C_s : Specific capacitance

C : Capacitance

P_s : Specific power

E_s : Specific energy

I : Current

E : Potential

V_{IR} : Voltage drop

Z' : Real impedance

Z'' : Imaginary impedance

R_{ES} : Equivalent series resistance

Δt : Discharge time

A/g : Ampere per gram

m : mass

Ω : Ohm

S : Seimens

s : Seconds

cm^2 : Centimetre square

g : grams

μm : Micrometre

R_s : Solution resistance

R_{ct} : Charge transfer resistance

F : Farad

F/g : Farad per gram

A : Ampere

V: voltage
W: Watt
Wh: Watt hour
n: number of cycles
D: crystallite size
 β : Full width at half maxima
Ag/AgCl: Silver/silver chloride
Hg/HgO: Mercury/mercury oxide
SCs: Supercapacitors
EDLC: Electrical double-layer capacitor
PC: Pseudocapacitor
TMOs: Transition metal oxides
AC: Activated Carbon
CNTs: Carbon nanotubes
XRD: X-ray diffraction
SEM: Scanning electron microscope
ED: Electrodeposition
EP: Electrophoretic deposition
ELD: Electrolytic deposition
ATR-FTIR: Attenuated total reflectance-Fourier transform infrared spectroscopy
EDS: Energy dispersive X-ray spectroscopy
CV: Cyclic voltammetry
PS: Potentiostatic
PRP: Pulse reverse potential
GCD: Galvonostatic charge-discharge
EIS: Electrochemical impedance spectroscopy
Ppy: Polypyrrole
Al: Aluminum

Ni-NiO: Nickel-nickel oxide

Co-Co₃O₄: Cobalt-Cobalt oxide

Ag/ Co-Co₃O₄: Silver/ Cobalt-Cobalt oxide

CoAc: Cobalt acetate

CoCl₂: Cobalt chloride

NF: Nickel foam

DEDICATION

Dedicated

To

my father of blessed memory, mother, and family

ACKNOWLEDGEMENTS

I take this moment to first and foremost thank the almighty God and his son Jesus Christ for the life and strength and guidance for the entire journey of my Ph.D.

I would also like to express my profound gratitude to my supervisor, Prof. Dilip Sarkar for the opportunity to work with him on this intriguing research and for his constructive criticism, guidance, and encouragement throughout this journey. Without his immense contribution, I would not have been able to reach this far in this Ph.D. journey and become an independent graduate researcher and scientist.

Another heartfelt appreciation to Dr. Saleema Noormohammed for making time to review and give constructive comments for improving the quality of my research articles, and thesis. Further, I would like to thank my former supervisor, Prof. David Doodo-Arhin, Department of Materials Science and Engineering, University of Ghana, and Dr. Henry, University of Laval, for their recommendation and support for this Ph.D. opportunity.

A special appreciation to Dr. Zhang Zhan for training me on the usage of the Scanning Electron Microscope (SEM). And also to Mr. Dany Racine, and Mr. Samuel Dessureault for their technical support. I am exceptionally grateful to Prof. Duygu Kcaefe, UQAC, Dr Saleema Noormohammed, and Dr. Zhang Zhan for taking the time out of their busy schedules to serve as jury members for the doctoral examination and seminar.

I acknowledge the financial support from the Natural Sciences and Engineering Research Council of Canada (NSERC) for this Ph.D. research. I would like to appreciate all the staff at the Department of applied science, CURAL, and my colleagues for their support and friendship during this journey. Without forgetting the visiting master's students, Anthony, Elodie, Jealoup, and Alexis for their contributions to my research work.

Last but not least, I express profound gratitude to my family for their prayers, love, and emotional support during this arduous journey.

CHAPTER 1: INTRODUCTION

This chapter introduces the quest for clean and renewable energy and the potential solution of addressing these issues via higher energy storage technology such as supercapacitors. The objectives, the novelty of the research, and the methodology are provided in this chapter.

1.1 Introduction

The rapid development of the global economy coupled with the depletion of fossil fuels and increasing environmental concerns of global warming requires the switch to alternative energy sources which are clean and renewable. Green energy sources such as solar, hydroelectric, and wind energy are important energy sources to replace traditional fossil fuels. However, most of these renewable energy sources are typically periodic [1]. Thus, the fabrication of energy storage devices capable of storing intermittent renewable energy for future use has become one of the key approaches to the practical application of renewable energy sources. In recent times, electrochemical energy storage devices in the form of electrochemical supercapacitors (ES) have received much attention as they can produce a large amount of energy in a short period and are used in many application areas such as emergency doors on the airbus, low-emission hybrid electric vehicles and consumer electronics [2-4]. Several factors affect the efficiency of energy storage and conversion devices, but their overall performance relies strongly on the structure and properties of the

electrode materials [3]. The major electrode materials that are used in current supercapacitors are those made of graphene and carbonaceous materials (Carbon nanotubes, activated carbon, etc.) [5]. The desire to use carbon materials comes from the fact that they store the charges electrostatically using reversible adsorption of ions of the electrolyte onto active materials that are electrochemically stable and have high surface area [5]. However, they have low specific charge storage and energy density, and thus, the research into other electrode materials such as transition metal oxides (RuO_2 , NiO , Co_3O_4 , MnO_2 , etc.), transition metal sulfides (NiS , CoS , MoS_2 , etc.), and conducting polymers (Polypyrrole (Ppy), polyaniline (PANI), etc.). Among them, noble transition metal oxides such as RuO_2 have exhibited the best energy and power performance however, their high cost and toxicity have limited their commercialization as a supercapacitor electrode material [6-8]. On the other hand, base transition metal oxides including NiO and Co_3O_4 are preferred due to their high storage capacity (High theoretical capacitance), environmental friendliness, and low cost [1, 3, 9]. However, drawbacks such as poor conductivity and high capacitance fading (resulting from large volume expansion leading to the pulverization and deterioration during cycling) of these metal oxides have limited their commercialization as supercapacitor electrode materials [1, 7].

Various strategies have been probed to improve the performance of these materials and one effective strategy is to design nanostructured electrode materials (nanoparticles, nanowires, nanosheets, nanorods, etc) using techniques such as hydrothermal, chemical precipitation, sol-gel, spray pyrolysis, and electrodeposition [10-13]. Nanostructured electrodes are advantageous as they give rise to porous structures to facilitate electron, ion

transport, and electrolyte diffusion. They also offer large surface areas favorable for increased redox reactions [9].

This research addresses the advances in the engineering of nanostructured supercapacitor electrode materials by hydrothermal and electrodeposition techniques for energy storage. More emphasis has been placed on the electrodeposition technique as it has been found to provide materials with superior performance.

1.2 Problem statement

The imminent ban on gasoline-dependent automobiles in 2035 by the Quebec government in Canada for non-emission electric cars has further heightened the quest for high-performing energy storage devices [14]. Supercapacitor energy storage devices present a practical approach for the storage of sporadic renewable energy sources to mitigate the burgeoning energy demand and environmental pollution. However, the key limitation for the wider application of supercapacitor energy storage devices is their limited energy density (E) which is expressed in equation (1.1)

$$E = \frac{1}{2}CV^2 \quad (1.1)$$

where C is the capacitance and V is the cell voltage. The two main approaches to increasing the energy density are by developing electrode material with high Capacitance (C) and developing electrolytes with a wide potential window to increase the cell voltage (V). Most research in the field of supercapacitors is centered on developing new electrode materials with high capacitance however, despite the enormous research efforts commercialization of

these materials is still limited by low experimental capacitance, poor conductivity, limited surface area, low energy density, poor cycle life, and complexity in synthesis processes. Therefore, it is essential to find materials and reproducible techniques for practical and sustainable supercapacitor energy storage.

After careful consideration of the state of the art in the field for supercapacitors, the originality of the research, objectives, and the appropriate methodology are provided below.

1.3 Originality Statement

Non-stop rising demand for long-lasting environment-friendly energy production and storage keeps the research world under constant pressure in finding solutions. Supercapacitance is one of the fields of research, however, with challenges in finding materials with high capacitance and long durability. While the choice of materials is an important factor, considered for exploration in this research work proposed, the role of surface features, especially, a high apparent surface area on capacitance and electrochemical performance of an electrode necessitates strategical approaches in its realization. In this research work, novel electrode surface preparation techniques have been applied to achieve a highly electrochemically active surface with enhanced surface features to improve electrode performance.

The originality of this research is in the approach of combining pulse reverse potential (PRP) and cyclic voltammetry (CV) modes of electrodeposition to achieve high surface, carbon-free, and binder-free materials. Since a negative potential can be used to deposit metal and a positive potential a metal oxide, a pulse reverse potential deposition mode employing

both negative and positive potentials deposits multilayers of metals and metal oxides to achieve nanostructured composite materials with an increased surface area from appropriate metal precursor solutions chosen carefully based on an extensive literature review. The metal in the composite serves as a conduction path for electron transport to enhance conductivity while the metal oxide provides the charge storage site during the supercapacitor charge storage and delivery processes.

One additional novel approach to obtaining enhanced nanostructured morphology leading to increased surface area and activity involves the fabrication of cobalt-based nanoelectrodes by a single electrodeposition electrolyte of cobalt salts where ionic radii of the constituent anions play a significant role in the nucleation and growth processes in a controlled manner. This approach explored as a potential alternate, also provides optimum coating thickness and mass loading, in addition to the increased surface area resulting from the nanostructured morphology obtained. Indeed, surface characterization and electrochemical performance evaluation are carried out at all stages of the fabrication for parametrical optimization as a default procedure to the novel approaches used in this research work.

1.4 Objectives

The electrode material for a supercapacitor is of significance as it is the site for energy storage. The specific surface area resulting from the morphology plays an important role hence techniques to develop electrode materials with high surface area and high performance have been the focus of recent research. By careful engineering through optimization of

synthesis parameters, materials with desired properties can be obtained. The global objective of this thesis is to engineer nanostructured electrode materials for supercapacitor energy applications via different synthesis techniques. The specific objectives to attain global objective are as follows:

1. Synthesis of nanostructured supercapacitor electrode materials by chemical precipitation route.
2. Synthesis of nanostructured supercapacitor electrode materials including metal oxides and composite metal oxide thin films by electrodeposition.
3. Valorization of aluminum as a substrate for nanostructured supercapacitor electrode materials by synthesizing conductive polymer coatings on a nickel-modified aluminum mesh.
4. Investigating the influence of microstructure and chemical composition on electrochemical performance including capacitance, cyclic stability, and impedance of the engineered supercapacitor electrode materials.

1.5 Methodology

Major procedures for achieving the objectives of this research consist of the following steps below. However, A comprehensive description of the experimental procedures has been provided in Chapter 3 and also in the contributing chapters (4, 5, 6, 7, 8, and 9) of the thesis.

1. Engineering of nanomaterials through materials synthesis

(a) Chemical precipitation synthesis: NiO and Co₃O₄ electrode materials were synthesized by the addition of an alkaline solution to relevant salt precursors and subsequent

hydrothermal treatment of the solutions in an autoclave. The as-synthesized materials were then fabricated into single-cell electrodes through the conventional slurry coating method.

(b) Electrodeposition synthesis: Nanostructured Ni-NiO, Co-Co₃O₄, and Ag/Co-Co₃O₄ electrode materials were synthesized through the electrodeposition process by optimization of precursor electrolyte molar (100, 80:20, 50:50) and electrodeposition mode (cyclic voltammetry, positive and negative potentiostatic modes)

(c) Aluminum (Al) mesh as a substrate was valorized by creating nickel coatings on Al to protect the mesh from electrolyte attack via potentiostatic (+1 V) electrodeposition process. Polypyrrole coatings are then potentiostatically deposited on the nickel-modified aluminum mesh from a pyrrole monomer solution.

2. Characterization of the engineered nanomaterials

(a) Physical, compositional, and structural analysis: the morphological and elemental studies of the engineered nanostructured electrode materials were performed using scanning electron microscopy (SEM) equipped with energy-dispersive X-ray spectroscopy (EDX). The X-ray diffraction (XRD) analyses were carried out for crystallographic studies and an attenuated total reflection – Fourier transform infrared spectroscopy (ATR-FTIR) was used to confirm and quantify the resulting functional groups.

(b) Electrochemical characterization: The performance of the engineered nanomaterials as potential supercapacitor electrode materials was evaluated using electrochemical techniques including Cyclic voltammetry (CV), Charge-discharge, and Electrochemical impedance studies to evaluate the charge storage mechanism, capacitance, cycle stability, and charge transfer kinetics.

The rest of the thesis is organized as follows: Chapter 2 provides a detailed literature review on the state of the art in supercapacitor energy storage, the types of supercapacitor energy storage mechanisms, various supercapacitor electrode materials, fabrication, and challenges with current electrode materials, among others. Detailed experimental methods used for the fabrication of supercapacitor electrode materials are provided in Chapter 3. Chapter 4 focuses on the preparation of NiO and Co₃O₄ electrode materials using the chemical precipitation synthesis route. Chapter 5 presents the result of a published article focusing on the electrochemical properties of carbon-free Ni-NiO electrode material. Chapter 6 elaborates on the optimization of the molar ratio of cobalt precursors (Cobalt acetate and cobalt chloride) for the electrochemical preparation of Co-Co₃O₄ nanocomposite electrode material. Chapters 7 and 8 present the result of published articles focusing on electrochemical properties of Co-Co₃O₄, and Ag/Co-Co₃O₄ thin film nanocomposite electrode materials for supercapacitor energy storage respectively. Further, the electrochemical properties of polypyrrole electrode material on different substrates are highlighted in Chapter 9. Finally, Chapter 10 provides overall conclusions on the findings of the contributing chapters, and future recommendations, though each contributing chapter (chapters 4 through 7) is accompanied by its respective conclusions.

1.6 References

- [1] F. Ali, N.R. Khalid, Facile synthesis and properties of chromium-doped cobalt oxide (Cr-doped Co_3O_4) nanostructures for supercapacitor applications, *Appl. Nanosci.*, 10 (2020) 1481-1488.
- [2] M.A.A. Mohd Abdah, N.H.N. Azman, S. Kulandaivalu, Y. Sulaiman, Review of the use of transition-metal-oxide and conducting polymer-based fibres for high-performance supercapacitors, *Mater. Des.*, 186 (2020) 108199.
- [3] S.J. Uke, V.P. Akhare, D.R. Bambole, A.B. Bodade, G.N. Chaudhari, Recent Advancements in the Cobalt Oxides, Manganese Oxides, and Their Composite As an Electrode Material for Supercapacitor: A Review, *Front. Mater.*, 4 (2017) 21.
- [4] P. Sivakumar, C.J. Raj, D.O. Opar, J. Park, H. Jung, Two dimensional layered nickel cobaltite nanosheets as an efficient electrode material for high-performance hybrid supercapacitor, *Int. J. Energy Res.*, 45 (2021) 1–11.
- [5] A. Muzaffar, M.B. Ahamed, K. Deshmukh, J. Thirumalai, A review on recent advances in hybrid supercapacitors: Design, fabrication and applications, *Renewable and Sustainable Energy Reviews*, 101 (2019) 123-145.
- [6] D. Majumdar, T. Maiyalagan, Z. Jiang, Recent Progress in Ruthenium Oxide-Based Composites for Supercapacitor Applications, *ChemElectroChem*, 6 (2019) 4343-4372.
- [7] A. González, E. Goikolea, J.A. Barrena, R. Mysyk, Review on supercapacitors: Technologies and materials, *Renewable and Sustainable Energy Reviews*, 58 (2016) 1189-1206.
- [8] S. Najib, E. Erdem, Current progress achieved in novel materials for supercapacitor electrodes: mini review, *Nanoscale Advances*, 1 (2019) 2817-2827.
- [9] R. Liang, Y. Du, P. Xiao, J. Cheng, S. Yuan, Y. Chen, J. Yuan, J. Chen, Transition Metal Oxide Electrode Materials for Supercapacitors: A Review of Recent Developments, *Nanomaterials* 11 (2021) 1248.
- [10] A. García-Gómez, S. Eugénio, R.G. Duarte, T.M. Silva, M.J. Carmezim, M.F. Montemor, Electrodeposited reduced-graphene oxide/cobalt oxide electrodes for charge storage applications, *Appl. Surf. Sci.*, 382 (2016) 34-40.
- [11] S.J. Uke, V.P. Akhare, D.R. Bambole, A.B. Bodade, G.N. Chaudhari, Recent Advancements in the Cobalt Oxides, Manganese Oxides, and Their Composite As an Electrode Material for Supercapacitor: A Review, *Front. Mater.*, 4 (2017).
- [12] P.E. Lokhande, U.S. Chavan, A. Pandey, Materials and Fabrication Methods for Electrochemical Supercapacitors: Overview, *Electrochemical Energy Reviews*, 3 (2019) 155-186.
- [13] J.N. Tiwari, R.N. Tiwari, K.S. Kim, Zero-dimensional, one-dimensional, two-dimensional and three-dimensional nanostructured materials for advanced electrochemical energy devices, *Progress in Materials Science*, 57 (2012) 724-803.
- [14] (2022).

CHAPTER 2: LITERATURE REVIEW

This chapter provides a review of the current understanding of recent advances in supercapacitor energy storage application with areas such as the charge storage mechanisms, electrode materials, techniques for evaluating electrode performance, and fabrication process presented and discussed.

2.1 Introduction to supercapacitors

The ever increase in demand for renewable and sustainable energy production and storage urges researchers to search for new materials and processes to develop highly efficient, environmentally friendly, and improved energy storage devices (batteries, fuel cells, supercapacitors, etc.). Supercapacitors (SC) which are also known as electrochemical capacitors or ultracapacitors are energy storage devices that convert and store chemical energy into electrical energy. They have recently received massive attention from researchers due to their high power density ($>10^4$ W/kg), long lifecycle ($\sim 10^6$), and bridging function for the power and energy gap between traditional dielectric capacitors (which have high power output) and batteries and fuel cells (which have high energy storage) (Figure 2.1) [1-4]. A typical supercapacitor is made up of three major parts; working electrodes (with a high specific surface area) which contain active materials, an electrolyte, and a separator that electrically separates the two electrodes [5-7].

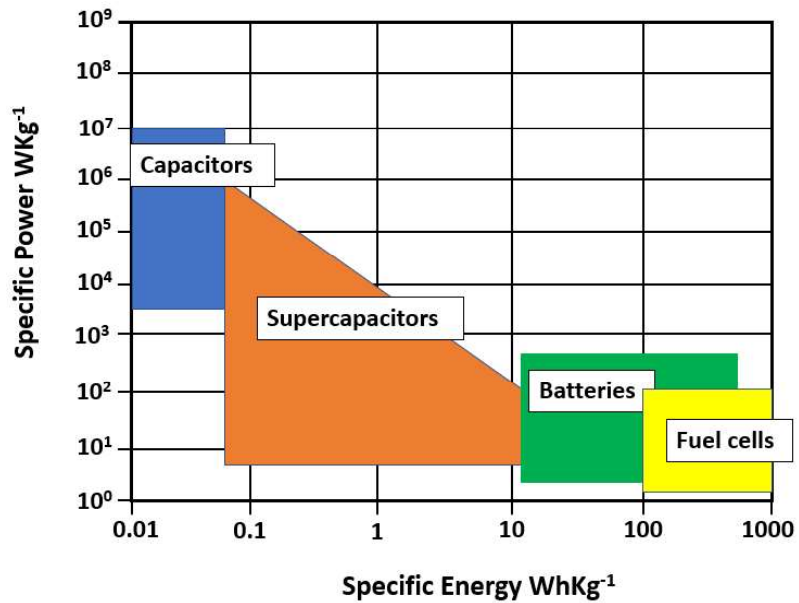


Figure 2.1 Ragone plot for different energy storage systems: capacitors, supercapacitors, batteries, and fuel cells (Specific power against specific energy). Reproduced with permission from reference [3]. Copyright © 2019 Springer Nature.

2.2 Types of supercapacitors

Based on the choice of electrode material, charge storage mechanism, and electrolyte, supercapacitors can be classified into three main groups: Electric Double-Layer Capacitors (EDLCs), Pseudocapacitors (PCs), and Hybrid Capacitors.

2.2.1 Electrochemical double-layer capacitors (EDLCs)

EDLCs comprise two electrodes made of carbon materials immersed in an electrolyte with a separator isolating the two electrodes [7]. They store electric energy through non-faradaic processes or the electrostatic accumulation of charges at the electrode/electrolyte interface leading to the formation of electrical double [8]. The double-layer capacitance (C_{dl}) can be estimated using equation 2.1:

$$C_{dl} = \frac{\epsilon_r \epsilon_0 A}{d} \quad (2.1)$$

where ϵ_r is the relative dielectric constant in the double layer, ϵ_0 is the permittivity of free space, A is the surface area of the electrode, and d (5-10 Å) is the thickness of the double layer [8]. The double layers are connected to an increase in surface area and a reduction in the electrode distance. Due to this reason, EDLCs can obtain higher energy densities compared to conventional capacitors [9]. When a voltage is applied, electrons travel from the negative electrode to the positive electrode through an external load and within the electrolyte, cations migrate towards the negative electrode while anions move towards the positive electrode. In this type of supercapacitor, there are no charge transfers across the electrode/electrolyte interface, and no ion exchanges occur between the electrode and the electrolyte (Figure 2.1). This implies that no chemical or compositional change occurs in the system therefore, EDLCs can sustain longer charge-discharge cycles up to 10^6 cycles compared to batteries which are limited to 10^3 cycles [5, 7-9].

Additionally, carbon-based materials such as activated carbon (AC), carbon nanotubes (CNTs), and graphene are used as EDLC electrode materials owing to their properties such as low cost, high surface area, and environmental friendliness [9, 10]. Despite

the long cycle life of EDLCs, the selection of electrode materials is restricted because of the requirement for very conductive electrodes. Therefore, recent research is geared toward developing ionic conducting electrolytes particularly solid ionic electrolytes [10, 11].

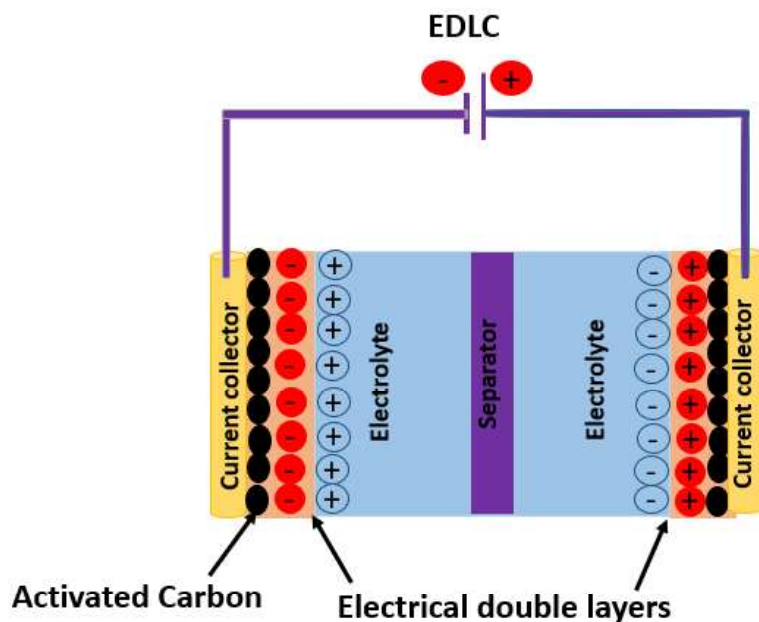


Figure 2.2 Schematic presentation of an Electrochemical double-layer capacitor (EDLC). Reproduced with the permission of reference [12]. Copyright © 2019 MDPI

2.2.2 Pseudocapacitors (PCs)

Pseudocapacitors (PCs) are another type of supercapacitor, however, unlike EDLCs, they store energy mainly by fast and reversible faradaic redox reactions occurring on the electrode material as shown in Figure 2.3. Materials that undergo redox reactions such as conducting polymers and transition metal oxides including RuO₂, NiO, MnO₂, and Co₃O₄ are used in Pseudocapacitors [5, 6, 13].

The three types of faradaic processes occurring at the electrodes of pseudocapacitors are reversible surface adsorption of electrolyte ions, redox reactions occurring in metal oxides, and electrochemical doping-de-doping of conducting polymers [3, 6]. The faradaic process taking place on both the surface and in the bulk of the electrode material allows for pseudocapacitors to achieve higher specific capacitance (10-100 times higher) and energy densities compared to EDLCs and the theoretical capacitance of pseudocapacitors can be estimated using equation 2.2:

$$C = \frac{nF}{MV} \quad 2.2$$

Where n is the number of electrons transferred in the faradaic reaction, F is the Faraday constant, M is the molar mass of the active material and V is the voltage window [3]. However, due to the redox reactions occurring on the electrode material as in the case of batteries, they suffer from poor cyclic stability and low power density [5, 6, 8, 14].

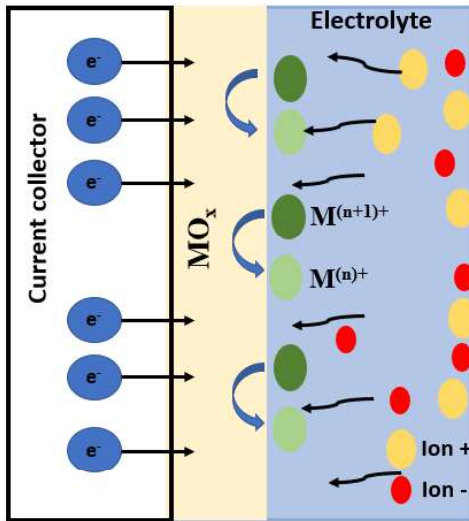


Figure 2.3 Schematic diagram of the charge storage mechanism of a Pseudocapacitor. Reproduced with the permission of reference [13]. Copyright © 2019 John Wiley and Sons.

2.2.3 Hybrid supercapacitors

Hybrid supercapacitors combine Faradaic and non-Faradaic charge storage processes. Therefore, they exploit the high power density, long cycle life of EDLCs, and the high energy densities of pseudocapacitors [5]. Furthermore, maximum operating voltage together with lower equivalent series resistance is an additional benefit of hybrid supercapacitors [3]. Although both electrical double-layer capacitance and faradaic capacitance occur simultaneously, only one plays a greater role [6]. Current research is focused on three different types of hybrid supercapacitors which are composite, asymmetric, and battery-type.

2.3 Supercapacitor electrode materials

Electrodes are one of the critical components of SCs as the electrochemical performance of SCs is strongly dependent on the properties of the electrode materials. To enhance the capacitive performance of SCs, the selection of appropriate electrode material and the fabrication process play a critical role [15]. Furthermore, SC electrode materials must have a high specific surface area (SSA), thermal stability, high electrical conductivity, be environmentally friendly, and have corrosion resistance [6]. Based on the capacitance and charge storage used in SCs, electrode materials can be classified into different types: (1) materials that use double-layer capacitance (carbon materials); (2) redox pseudocapacitive materials (transitional metal oxides and hydroxides, transition metal sulfides, and conducting polymers), and (4) composite materials [6, 8].

2.3.1 Carbon materials

Carbon materials (activated carbon, carbon nanotubes, and graphene) are the most used supercapacitor electrode materials as they have high electrical conductivity, large surface area, good corrosion resistance, high-temperature stability, and moderate cost [5]. The charge storage in carbon materials is by the electrical double-layer mechanism and therefore the capacitance depends on the surface area accessible to the ions of the electrolyte [6]. In addition, factors such as pore-size distribution, pore structure, and shape, specific surface area, and surface functionality influence their electrochemical performance [3].

2.3.1.1 Activated Carbon materials (ACs)

Among all the carbon materials activated carbons (ACs) are widely used as they have a high specific surface area and are less expensive compared to other carbon materials. They are produced by physical or chemical activation of carbonaceous materials such as wood, rice husks, and coconut shell to produce a porous structure with a large surface area (300 m²/g) [8, 16]. The pores of activated carbon are classified according to their size namely, micropores (diameter < 2 nm), mesopores (diameter from 2 – 50 nm), and macropores (diameter > 50 nm) as shown in Figure 2.4. Empirically, it has been observed that a high surface area does not necessarily translate into a high capacitance due to the inability of electrolyte ions to diffuse into them to contribute to the charge storage [16, 17]. It has been observed that in addition to a large surface area, surface functionalization of carbon materials can improve the adsorption of electrolyte ions resulting in increased wettability and rapid ion transport. The functional groups may also increase the total capacitance by inducing faradaic redox reactions [6, 16]. For example, the specific capacitance of an Ac-based supercapacitor was increased from 66 F/g to 106 F/g by nitric acid treatment [18]. Similarly, Lee *et al.* reported a high specific capacitance of 1089 F/g for a Sulphur functionalized graphene aerogel [17].

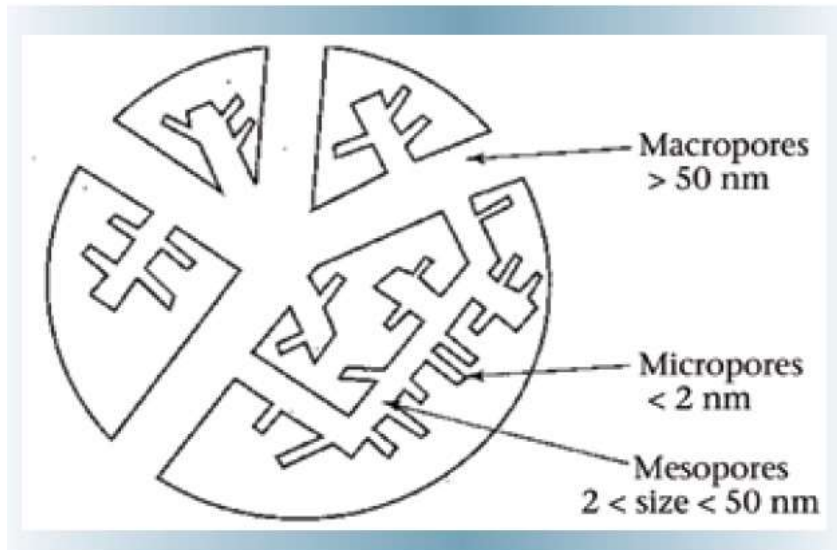


Figure 2.4. Schematic representation of the pore size network of activated carbon grain. Adapted from the reference [19] with permission. Copyright © 2008 The Electrochemical Society.

2.3.1.2 Carbon nanotubes (CNTs)

CNTs electrodes are also carbon materials which have been explored as SC electrode materials as a result of their accessible external structure which offers a high specific surface area (SSA), high mechanical strength, low densities, high electrical conductivity, and an internal network of mesopores [15]. CNTs can be conceptualized as ordered hollow tubes of rolled-up two-dimensional graphene sheets with diameters in the nanometer range and length typically on the micrometer scale [20]. Based on the tubular morphology, CNTs can be categorized into single-walled carbon nanotubes (SWNTs) and multi-walled carbon nanotubes (MWCNTs) as shown in Figure 2.5. SWNTs normally have their diameter in the range of 1-2 nm and length in tens of microns. However, despite the desirable properties of CNTs, their commercialization as SC electrode material is restricted by their high cost.

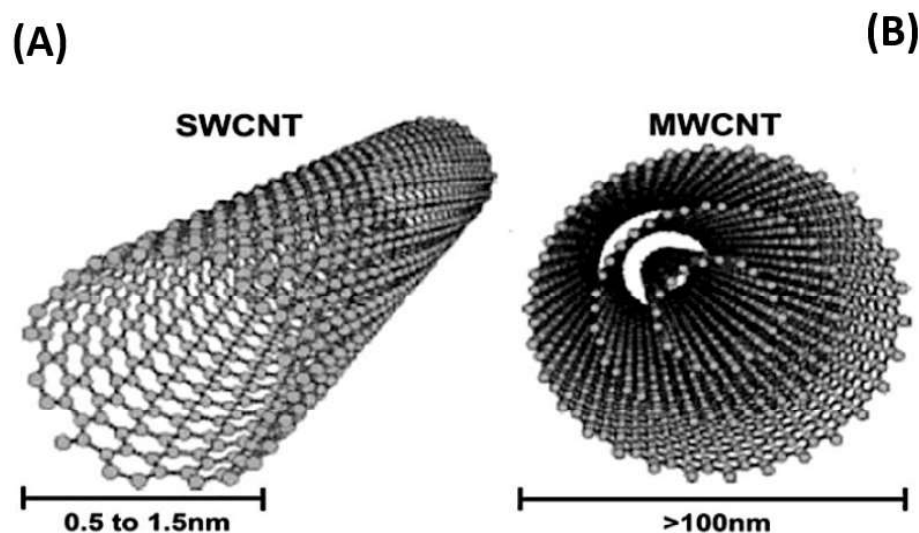


Figure 2.5. Schematic diagram of (A) single-walled carbon nanotube (SWCNT) and (B) multi-walled carbon nanotube. Adapted from reference [21] with permission. Copyright © 2013 SAGE Publications.

MWCNTs on the other hand are made up of concentric cylindrical layers of carbon with an interlayer distance of approximately 0.36 nm and a diameter usually on the order of 10-20 nm [22]. CNTs are prepared by catalytic decomposition of some hydrocarbons using processes such as laser ablation, electric arc, and chemical vapor deposition (CVD) of which CVD is the most suitable method for producing large quantities of CNTs and the length, diameter, and the number of walls can be tuned during the growth process as reported by Li et al in their review of the mechanical properties and structural health monitoring performance of carbon nanotube-modified Fiber-reinforced polymer (FRP) composites [23]. Moreover, CNTs with large surface area (SWNTs $>1600\text{m}^2\text{g}^{-1}$, MWNTs $>430\text{m}^2\text{g}^{-1}$) together with good electrical ($\sim 5000\text{S cm}^{-1}$) properties have been studied as the active electrode materials in supercapacitors [24].

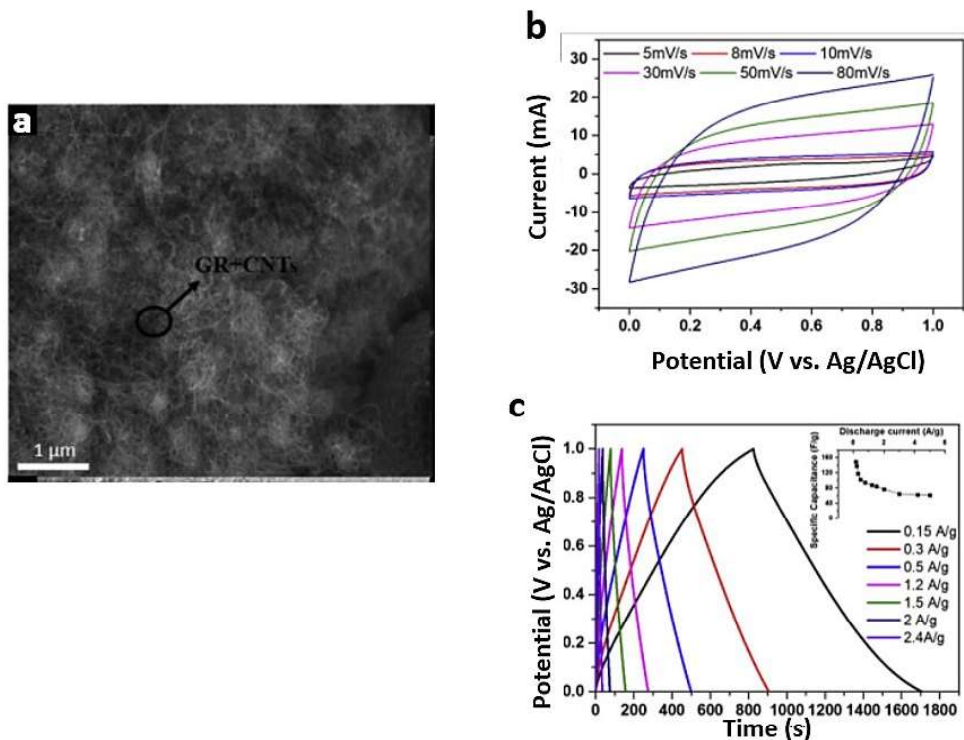


Figure 2.6 (a) SEM micrograph (b) cyclic voltammetry curves at different scan rates (CV), (c) galvanostatic charge-discharge profiles at different specific currents of 3DG/CNT composite material. Adapted from reference [25] with permission. Copyright © 2020 Elsevier.

The specific capacitance (C_s) of MWCNTs electrodes is found to be in the range of 4-135 F/g while a maximum of 180 F/g has been recorded for SWCNTs electrodes [26]. For example, Zhang *et al.* reported a C_s value of 197.2 F/g for their three-dimensional graphene/carbon nanotube (3DG/CNT) synthesized via a CVD process (Figure 2.6) [25]. Like all carbon materials, the CVs of the 3DG/CNT in Figure 2.6(b) present a nearly rectangular shape indicating EDLC charge storage mechanism. Also, the absence of IR drop in the discharge curves indicates the high conductivity of CNTs [25].

2.3.1.3 Graphene

Graphene is a 2D structure allotrope composed of a one-atom-thick layer of sp^2 -bonded carbon atoms which are arranged in a honeycomb-like crystal structure [15, 24]. Graphene like other carbon materials exhibits excellent properties including large surface area, high electrical conductivity, and high carrier mobility. Also, graphene is regarded as the basic building block for carbon materials of all other dimensionalities including 0D fullerene, 1D nanotubes, and 3D graphite [11]. Due to the unique 2D structure which reduces the thickness leading to a larger potential window, higher flexibility, and thermal and chemical stability, graphene-based electrodes have been explored as a powerful candidate for supercapacitor energy storage application. In addition, unlike ACs and CNTs, graphene electrodes do not depend on the pore distribution in the solid state and both exterior surfaces of the graphite sheet are accessible by the electrolyte [16, 24]. Up until now, several processes have been used to produce various types of graphene including micromechanical, exfoliation, chemical vapor deposition, and arch discharge [15, 27]. A specific capacitance of 141 F/g was reported by Yang *et al.* for their graphene electrode prepared by laser irradiation reduction of graphite oxide dissolved in an aqueous solution [28]. Additionally, another study by Li *et al.* reported a specific capacitance value of 100 F/g for their porous graphene paper electrode prepared by a modified Hummers method (for preparation of graphene oxide paper) and subsequent application of thermal shock to the graphene oxide paper [29]. The SEM micrograph together with the electrochemical characteristics of the graphene paper has been presented in Figure 2.7.

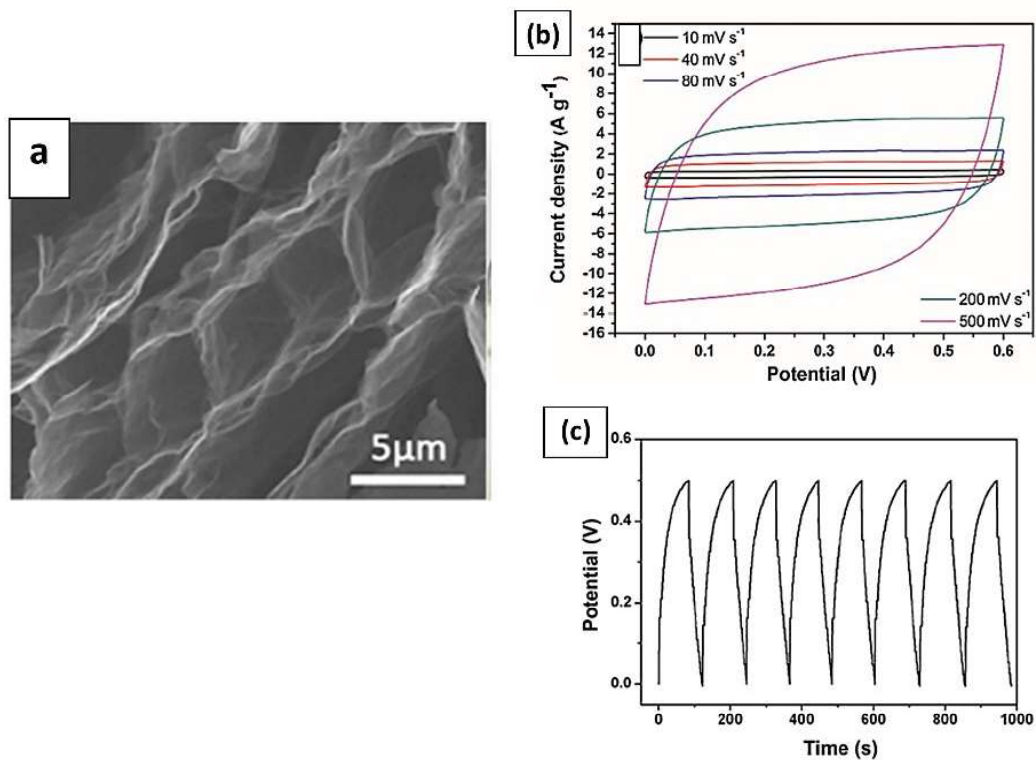


Figure 2.7. (a) SEM image (b) cyclic voltammetry curves at different scan rates (c) Galvanostatic charge-discharge curves of graphene paper. Adapted from reference [29] with permission. Copyright © 2017 Elsevier.

2.3.2 Pseudocapacitive electrode materials

2.3.2.1 Transition metal oxides

Transition metal oxides such as RuO_2 , MnO_2 , NiO , V_2O_5 , and Co_3O_4 have been widely investigated as potential supercapacitor electrode materials as they possess high theoretical specific capacitance. The capacitive behavior of some transition metal oxides has been discussed in the subsequent sections.

I. Ruthenium oxide (RuO₂)

RuO₂ is the most promising and extensively studied due to its high theoretical specific capacitance (~2000 F/g), excellent rate capacity, high conductivity, long cycle life, large voltage window, as well as highly reversible redox reactions [30, 31]. In acidic electrolytes, the charging mechanism for RuO₂ is presented in equation (2.3) [6]. The pseudocapacitive charge storage mechanism shown in equation (2.3) suggests that fast reversible electron transfer accompanied by adsorption of protons on the surface, where the oxidation state of Ru can change from Ru(II) to Ru(IV) [6]



It has been reported that the hydrous form of RuO₂ (RuO₂.xH₂O) exhibits higher specific capacitance than its crystalline form in acidic electrolytes. This observation could be attributed to the high electronic and protonic conductivity of the hydrous form which enhances the electrochemical redox reactions [6, 32]. The specific capacitance of RuO₂.0.5 H₂O achieved a specific capacitance (C_s) of 900 F/g in 1 M H₂SO₄ electrolyte [30]. Similarly, Thangappan *et al.* reported a specific capacitance (C_s) of 301.4 F/g and high cycle stability of 94 % after 1000 cycles for their RuO₂ nanoparticles anchored on graphene nanosheets electrode prepared by an in-situ reduction method (Figure 2.8).

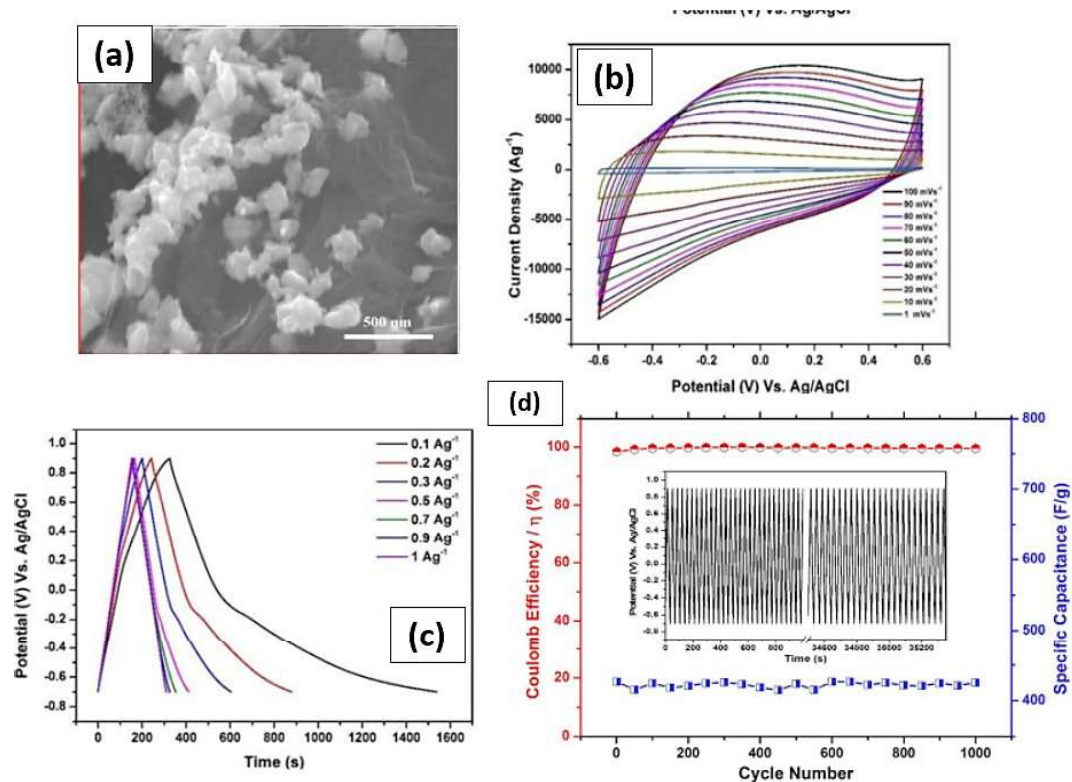


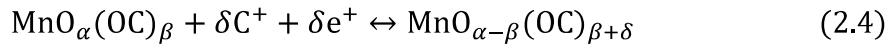
Figure 2.8 (a) SEM image (b) cyclic voltammetry curves at different scan rates (c) Galvanostatic charge-discharge curves of graphene paper (d) cycle performance of RuO₂ nanoparticles anchored on graphene nanosheets. Adapted from reference [33] with permission. Copyright © 2018 Elsevier.

Figures 2.8(b) and (c) are typical CV and GCD curve shapes observed for RuO₂ electrode materials and their resemblance of the curves to those of EDLC electrode materials indicates ideal capacitive behavior [33].

Despite the numerous advantages of RuO₂ electrode material, its practical application is limited due to its high cost and toxicity.

II. Manganese dioxide (MnO₂)

Manganese dioxide is one of the prospective pseudocapacitor electrode materials in place of RuO₂ due to its high theoretical capacitance of 1370 F/g, low cost, availability, and environmental friendliness [34, 35]. The pseudocapacitance charge storage of MnO₂ is assigned to reversible redox transitions which involve the exchange of protons and/ or cations with the electrolyte in addition to the transitions between Mn(III)/Mn(II), Mn(IV)/Mn(III), and Mn(VI)/Mn(IV) in the potential window of the electrolyte. The suggested charge storage mechanism is presented in equation (2.4):



Where C^{+} signifies the protons and the electrolyte's alkali metal cations (Na^{+} , K^{+} , Li^{+}), $\text{MnO}_{\alpha}(\text{OC})_{\beta}$ and $\text{MnO}_{\alpha-\beta}(\text{OC})_{\beta+\delta}$ represents $\text{MnO}_{2.n}\text{H}_2\text{O}$ in high and low oxidation states respectively [6, 36]. An advantage of MnO₂ is its ability to operate in mild aqueous electrolytes such as Na₂SO₄, KCl and NaCl compared to RuO₂ which requires strong acid or base electrolytes [37]. Furthermore, different crystalline phases of MnO₂ (α , β , γ , λ , and λ -MnO₂) present differences in pseudocapacitive properties [6, 37]. Similar to RuO₂, the degree of crystallinity affects the pseudocapacitance. A high crystallinity eliminates the protonation/deprotonation reaction although it gives rise to higher conductivity [6]. Various specific capacitance values and electrochemical performance have been reported for MnO₂ electrode materials with different structures prepared using synthesis methods such as

hydrothermal, electrodeposition, sol-gel, and chemical exfoliation [12, 17, 38]. For instance, Davoglio et al synthesized α - MnO_2 nanoneedles with 1 μm length using microwave synthesis. The α - MnO_2 nanoneedles exhibited a specific capacitance value of 289 F/g with a stability of 88 % after 10000 charge-discharge cycles in a 1M Na_2SO_4 electrolyte [39].

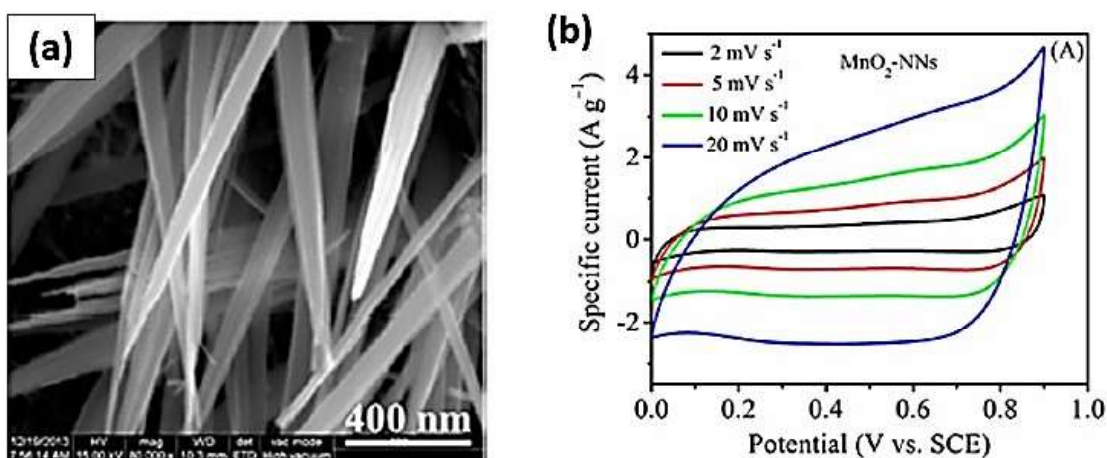


Figure 2.9 (a) SEM micrograph of β - MnO_2 nanoneedles (b) electrochemical performance of β - MnO_2 nanoneedles (NNs) presented by CV at different scan rates. Adapted from reference [40] with permission. Copyright © 2018, American Chemical Society.

Similarly, a specific capacitance of 331.3 F/g was reported by Cueller-Herrera et al. for their γ - MnO_2 nanorods prepared by a hydrothermal process in a 0.1 M Na_2SO_4 electrolyte [41]. Umeshbabu et al also synthesized β - MnO_2 with different nanostructures (nanoneedles and hollow tubes) using a chemical precipitation technique. The nanoneedles (Figure 2.9(a)) delivered a specific capacitance (C_s) of 365 F/g with a stability of 86 % against C_s value of 245 F/g and stability of 75 % for the hollow tubes [40]. The signature of the cyclic voltammetry (CV) curves in Figure 2.9 (b) indicates that MnO_2 can also exhibit typical

rectangular-shaped CV curves comparable to non-faradaic energy storage mechanisms despite the redox nature of the energy storage mechanism [6].

Despite the high theoretical capacitance of MnO₂, its major challenge like most metal oxides is its poor electrical conductivity (10⁻⁶ to 10⁻⁵ Scm⁻¹) which prevents the realization of the theoretical capacitance [42]. Further, it suffers poor structural stability after cycling processes [43]. To combat this problem, recent investigations have been geared towards fabricating MnO₂ composite with conductive carbonaceous materials and metal ions.

III. NiO

NiO is also another promising electrode material that has been extensively studied because of its ultrahigh theoretical specific capacitance of 2580 F/g, low cost, and environmental friendliness [44]. The charge storage mechanism of NiO in KOH electrolyte is presented in equation (2.4) [3].



So far, various NiO nanostructures with different morphologies including nanowire, nanobelts, porous film, nanorods, nanosheets, and nano/microspheres have been fabricated [45, 46]. For example, hierarchical microspheres prepared by a hydrothermal process exhibited (Figure 2.10) a specific capacitance of 809 F/g with capacitance retention of 85 %

[44]. The asymmetrical CV and GCD curves observed in Figures 2.10(b) and (c) are typical of NiO electrodes compared to the symmetrical curves shown by MnO₂ and RuO₂. Similarly, Zhu et al. also prepared NiO nanoparticles which showed a specific capacitance of 1784 F/g with capacitance retention of 75.8 % by a one-step thermal oxidation method [47]. Further, the electrochemical performance of NiO-based electrodes has highlighted in Table 2.1.

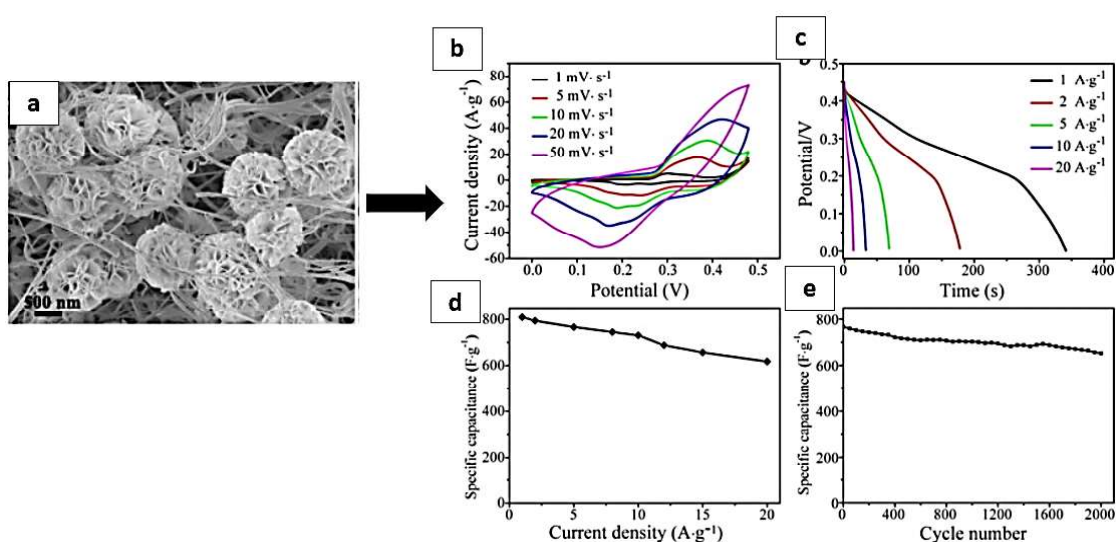


Figure 2.10 (a) SEM of NiO hierarchical microspheres, (b) cyclic voltammetry (CV) at different scan rates (c) galvanostatic charge-discharge (GCD) curves at different specific currents, (d) specific capacitance estimated from the GCD curves, and (e) cyclic performance at 10 A g⁻¹ of the NiO hierarchical microspheres on nickel foam electrode. Adapted from reference [44] with permission. Copyright © 2018, Elsevier.

Although promising achievements have been made, the reported specific capacitance of NiO is still inferior to its theoretical value because of its poor cycle performance and low conductivity. The preparation of NiO-based nanocomposite materials is therefore the current trend in obtaining high-performing and efficient electrodes. Additionally, as the electrochemical performance heavily depends on the specific surface area and porosity,

effective synthesis methods that offer precise morphology formations can enhance its performance.

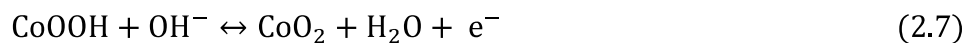
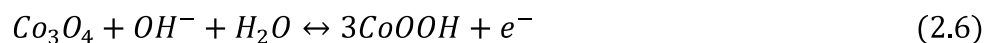
Table 2.1 : Summary of specific capacitance of NiO electrodes

Material	Method of Preparation	Electrolyte	Capacitance	Capacitance Retention	reference
mesoporous NiO nanoflake array	Hydrothermal	1 M KOH	400 F g ⁻¹ at 2 A g ⁻¹	85 % after 5000 cycles	[48]
NiO thin film	Chemical Precipitation	1 M KOH	259.3 F g ⁻¹ at 1 A g ⁻¹		[49]
NiO hierarchical microspheres/nanofibers	Hydrothermal	3 M KOH	809.1 F g ⁻¹ at 1 A g ⁻¹	85 % after 2000 cycles at 5 A g ⁻¹	[50]
NiO nanoflakes	Hydrothermal	2 M KOH	1784 F g ⁻¹ at 5 mV s ⁻¹	75.8 % after 20000 cycles at 5 A g ⁻¹	[51]

porous film	NiO(OH)	Anodic Electrodepositi on	1 M KOH	2302 F g ⁻¹ at 1 A g ⁻¹	95 % after 1000 cycles at 10 mV s ⁻¹	[52]
NiO nanoparticles	Hydrothermal		1 M KOH	132 F g ⁻¹ at 5 mV s ⁻¹	75 % after 500 cycles at 100 mV s ⁻¹	[53]

IV. Co₃O₄

Cobalt oxide belonging to the spinel family is another promising alternative pseudocapacitive electrode material for supercapacitors due to its high theoretical capacitance (3560 F/g), environmentally benign, and low cost [54]. The crystal structure of Co₃O₄ comprises a cubic closed-packed array of oxygen anions whereby 1/8 of the tetrahedral interstices are occupied by Co²⁺ cations, while half of the octahedral interstices are occupied by Co³⁺ cations as depicted in Figure 2.11 [42, 55]. In alkaline electrolytes, the charge storage mechanism involves two steps as presented in equations (2.6) and (2.7) [54, 56]



Because of its numerous advantages, cobalt oxides with different morphologies have been synthesized using various methods (Table 2.2). For example, Kumar *et al.* synthesized ultralayered Co_3O_4 nanosheets with a specific capacitance of 548 F/g and capacitance retention of 66 % after 2000 cycles via a hydrothermal process.

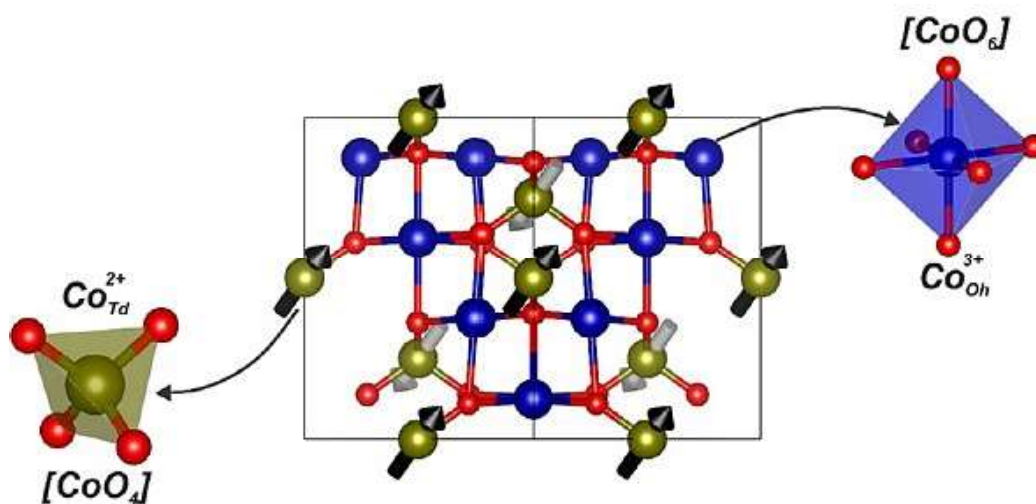


Figure 2.11 Cubic crystal structure of Co_3O_4 exhibiting Co^{2+} and Co^{3+} cations tetrahedrally and octahedrally coordinated to oxygen anions respectively. Adapted from [55] with permission. Copyright © 2018, Elsevier

The ultralayered morphology offered a larger electroactive surface area and easy accessibility of OH^- ions for enhanced redox reactions to increase specific capacitance [57]. Likewise in a report by Fan *et al.*, thin-wall hollow Co_3O_4 spheres prepared by a hydrothermal synthesis delivered a specific capacitance of 988 F/g at a specific current of 1 A/g and capacitance retention of 96.6 % after 6000 cycles in a 2 M KOH electrolyte (Figure 2.12) [58].

However, it has been noticed that like other metal oxides, cobalt oxide electrodes are still plagued with the drawbacks of low conductivity, low experimental capacitance values, and high volume expansion which affects its cycling stability [56, 57]. Effective ways to

improve its capacitive characteristics are growing different nanostructures with enhanced electroactive surface area, combining cobalt oxide with other transition metal oxides, and integrating high-conductivity materials.

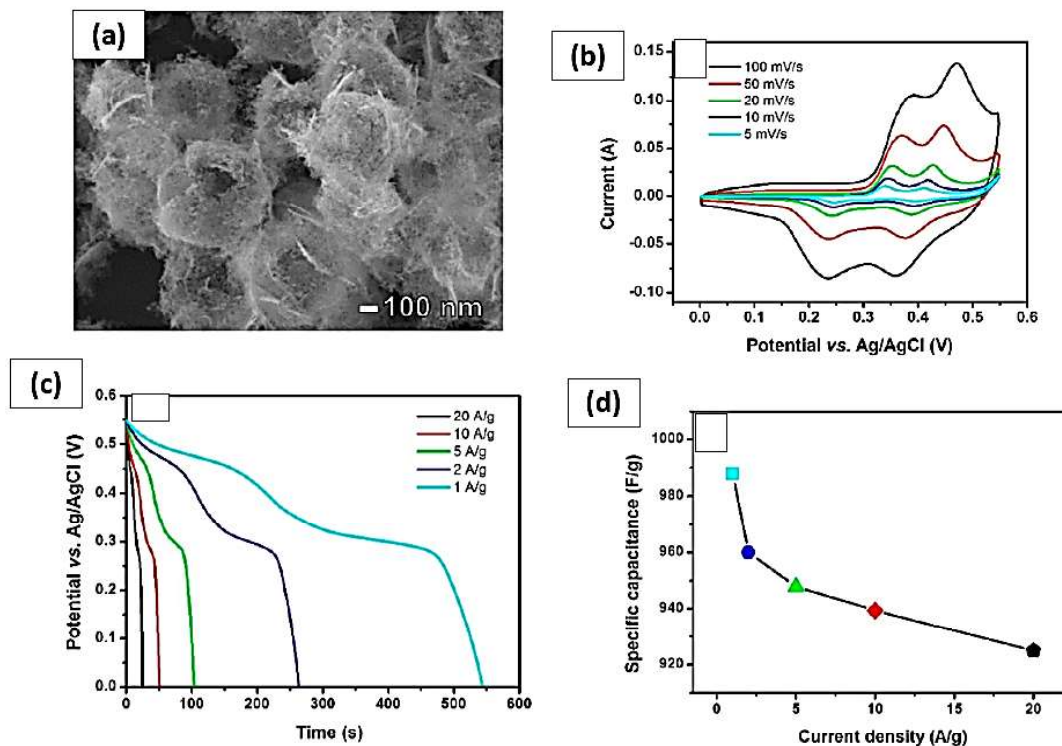


Figure 2.12 (a) SEM image of thin-wall Co_3O_4 spheres (b) cyclic voltammograms (c) galvanostatic charge-discharge profiles (d) specific capacitance values calculated from charge-discharge curves at different current densities of the thin-wall Co_3O_4 spheres.

Adapted from [58] with permission. Copyright © 2018, MDPI.

Table 2.2 : Summary of specific capacitance of Cobalt oxide electrodes

Material	Method of Preparation	Electrolyte	Capacitance	Capacitance retention	reference
cobalt oxide (Co ₃ O ₄) nanotubes	Chemical bath deposition	6 M KOH	574 F g ⁻¹ at 0.1 A g ⁻¹	95 % after 1000 cycles	[59]
Er-GO/CoOx	Pulsed electrodeposition	1 M KOH	430 F g ⁻¹ at 1 A g ⁻¹	76 % after 3500 cycles	[60]
Porous cobalt oxide (Co ₃ O ₄) nanoflakes	Potentiostatic electrodeposition	1 M KOH	248 F g ⁻¹ at 5 mV s ⁻¹	98 % at 1000 cycles	[61]
thin-wall hollow Co ₃ O ₄	Hydrothermal	2 M KOH	988 F g ⁻¹ at 1 mA cm ⁻²	96 % after 6000 cycles	[3]
Mesoporous Co ₃ O ₄ film	Electrodeposition	1 M NaOH	491 F/g at 1 A/g	-	[62]
Co ₃ O ₄ hollow boxes	Chemical precipitation	3 % KOH	278 F/g at 0.5 A/g	-	[63]

2.3.2.2 Conducting polymers

Conducting polymers including polypyrrole (Ppy), polyaniline (PANI), polythiophene (PTH), and poly(3,4-ethylene dioxythiophene) (PEDOT) is also a promising class of pseudocapacitive materials as a result of their high conductivity (10^4 S cm^{-1}), low cost, and ease of fabrication [64]. The charge storage in conducting polymers is based on the reduction-oxidation process. During the oxidation process (doping), ions from the electrolyte solution are transferred to the polymer backbone, and during the reduction process (de-doping) the ions are released back into the solution (Figure 2.13) [5] [65]. In conducting polymers, factors such as dopant ions, electrolytes, substrates, and the type of monomer significantly affect the capacitance [5].

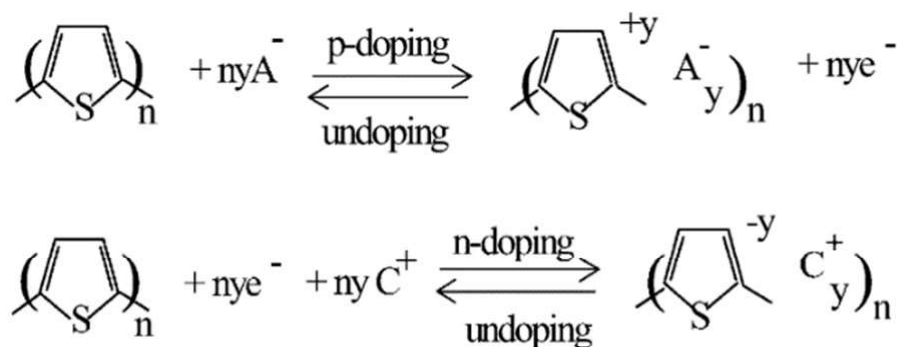


Figure 2.13 Schematic diagram of the p-and n-doping-dedoping process of PTH. Adapted from reference [65] with permission. Copyright © 2001, Elsevier.

Despite the numerous attractive properties of conducting polymers, their commercialization is limited due to poor cycle stability as a result of the doping and the dedoping process. To overcome this limitation, combining conducting polymers with carbon materials ensures mechanical stability, as well as capacitance, increasing the capacitance. For example, a reduced graphene oxide/polypyrrole (rGO/Ppy) composite film achieved a specific capacitance of 361 F/g with a capacitance of 80 % after 5000 cycles compared to pure Ppy (12 F/g and 40 % after 100 cycles) [66].

2.3.3 Composite materials

Composite materials combine pure materials (carbon-based and redox pseudocapacitive materials) for supercapacitors. The rationale behind composite materials is to exploit the advantages of individual pure materials in a single electrode material. When carbon materials merge with redox pseudocapacitive materials, the overall capacitance is increased due to the contribution of both double-layer capacitance and pseudocapacitance [5, 6]. In a study by Lee *et al.*, a composite manganese oxide-carbon nanotube prepared by electrophoresis deposition exhibited a high specific capacitance of 415 F/g compared to that of pure manganese oxide (233 F/g) [67]. Similarly, a polypyrrole-carbon cloth composite showed a high specific capacitance of 701 F/g with enhanced capacitance retention of 58.3 % after 5000 cycles due to the synergetic interaction between polypyrrole and carbon to enhance electrochemical performance [68].

2.4 Electrolytes

Electrolytes are an equally important component of the supercapacitor as their properties affect the electrochemical behavior of supercapacitors. Furthermore, the power density, as well as the energy density of supercapacitors, are controlled by the resistance and the operating voltage of the electrolytes respectively [6]. Different types of electrolytes are used in supercapacitors: (i) aqueous (ii) organic and ionic liquids. Aqueous electrolytes like KOH, Na₂SO₄, NaOH, and H₂SO₄ have advantages of high ionic conductivity, minimum pore size requirements low cost, and can provide more capacitance (due to higher concentration and small ionic radius). However, due to the decomposition of water at 1.23 V, their cell voltage is typically limited to 1 V [69]. Organic electrolytes (acetonitrile and propylene carbonate) on the other hand have a large cell voltage of 2.7 V and higher specific resistance which affects the power capability. Ionic liquids are also of interest because of their nonvolatility, heat resistance, and high cell voltage (4 - 6 V). However, they have the limitation of low conductivity and high cost [3, 8, 38].

2.5 Current collector/Substrates

Another component crucial to the performance of supercapacitors is current collectors as they serve as electron pathways from the active electrode material to the external circuit. Supercapacitor current collectors must have good conductivity, adhesive contact with the electrode material, good corrosion resistance, and stability during cycling processes.

Materials such as aluminum, copper, nickel, graphite, and stainless steel are usually employed as current collectors due to their high conductivity [10, 38]. Adherence of the active material to the current collector is of critical importance, as high resistance and detachment of the electrode material would cause poor electrochemical performance [38].

2.6 Parameters and electrochemical techniques for supercapacitor electrode material evaluation

The performance evaluation of electrode materials entails the determination of specific capacitance, energy and power density, efficiency, and stability. The techniques used in assessing these parameters include cyclic voltammetry (CV), galvanostatic charge/discharge (GCD), and electrochemical impedance spectroscopy studies.

2.6.1 Cyclic voltammetry

The cyclic voltammetry test is conducted by applying a potential between a counter and working electrode for a two-electrode system or between working and reference for a three-electrode system. From the profile of the CV curves (Figure 2.14), the capacitance nature of the electrode material can be determined as EDLC materials give rectangular curves while battery type or intercalated pseudocapacitor materials yield curves with redox peaks

with the former having well-separated peaks while the latter shows diffuse peaks [7]. From the CV analysis, the specific capacitance can be determined using the equation (2.8) [38]:

$$C_s = \left(\frac{1}{m s \Delta V} \right) \int_{V_i}^{V_n} i dV \quad (2.8)$$

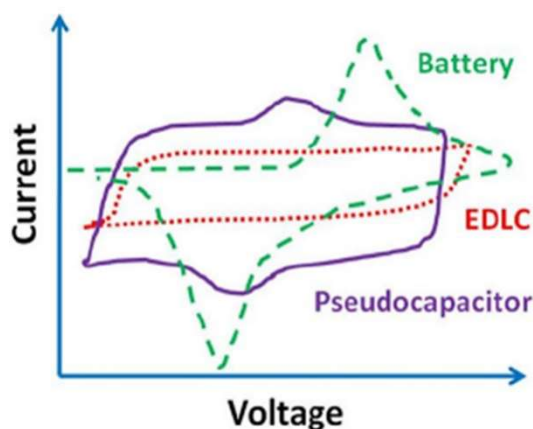


Figure 2.14. Typical cyclic voltammetry signatures for EDLC (red curve), pseudocapacitor (violet curve), and battery-like (green curve) electrode materials. Adapted from reference [38] with permission. Copyright © 2020, Springer Nature.

where C_s is the specific capacitance, $\int i dV$ is the integrated CV curve area, s is the potential scan rate (V/s), ΔV is the potential window (V), V_i and V_n are the extreme limiting values of the voltage scans, and m is the mass of the electrode's active material (g).

2.6.2 Galvanostatic charge-discharge (GCD)

The galvanostatic charge/discharge measurement is carried out by applying a constant current to the working electrode to charge and discharge at a peak voltage that is specified in

the voltage window. The result is potential against time graph from which, the capacitance, energy, and power performance can be estimated using equations (2.9) to (2.11):

$$C_s = \frac{I\Delta t}{m\Delta V} \quad (2.9)$$

$$E_s = \frac{1}{2} C_s (\Delta V)^2 \quad (2.10)$$

$$P_s = \frac{E_s}{\Delta t} \quad (2.11)$$

Where E_s (Wh/kg) is the specific energy, P_s (W/kg), and Δt (s) is the discharge time [3, 38].

The typical GCD curves for the various charge storage mechanisms are highlighted in Figure 2.15.

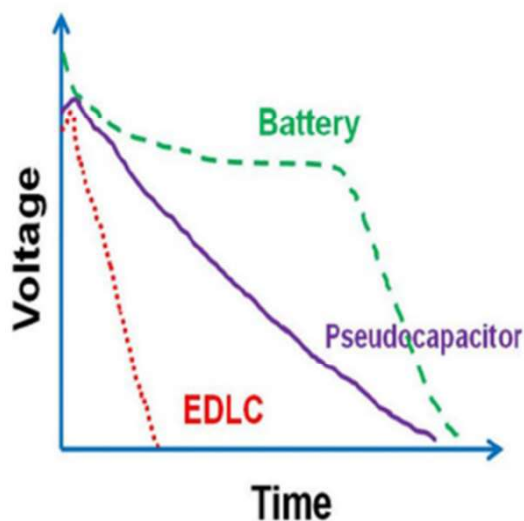


Figure 2.15. Typical galvanostatic charge-discharge (GCD) profiles for EDLC (red curve), pseudocapacitor (violet curve), and battery-like (green curve) electrode materials. Adapted from reference [38] with permission. Copyright © 2020, Springer Nature.

2.6.3 Electrochemical Impedance Spectroscopy (EIS)

In addition to CV and GCD measurements, EIS is another technique to access the performance of electrode materials. The EIS run by applying a small voltage amplitude (5 to 10 mV) over a wide frequency range at open circuit potential gives information about the impedance of the material. The result is often displayed as Nyquist (Figure 2.16) and Bode plots. The Nyquist graphs where the imaginary impedance ($Z(f)''$) is plotted against the real impedance (Z') comprises three regions: intercept at the real axis (high-frequency region), semicircle (medium-frequency region) which is due to charge transfer resistance and a straight line (low-frequency region) representing capacitive behavior. From the Bode plot, the capacitance (C) can be calculated from the imaginary impedance ($|Z|$) and frequency (f) using the equation (2.12) [6, 7, 38].

$$C = \frac{1}{2\pi f |Z|} \quad (2.12)$$

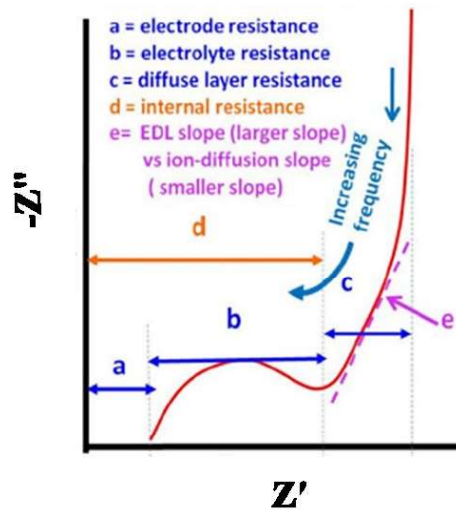


Figure 2.16 Nyquist plot of electrode material for supercapacitors. Adapted from reference [38] with permission. Copyright © 2020, Springer Nature.

2.7 Synthesis of supercapacitor electrode materials

The morphology of electrode materials plays a crucial role in the electrochemical performance and as a result controlling synthesis parameters such as temperature, time, and concentration is needed to tailor materials with optimum properties. Synthesis techniques such as chemical precipitation, sol-gel, hydrothermal, electrodeposition, spray pyrolysis, and chemical vapor deposition among others have extensively been used to fabricate supercapacitor electrode materials with desired characteristics. Therefore in this section, major methods for electrodes have been highlighted.

2.7.1 Electrodeposition

Electrodeposition comprising electrolytic deposition (ELD) and electrophoretic deposition (EPD) is favored to fabricate the film electrodes due to the low capital investment costs, ability to control film thickness, morphology, uniformity, and deposition rate by optimizing deposition parameters. It also offers the advantage of direct deposition of materials onto substrates without the need for binders [7]. In ELD, the deposited film is obtained when charged particles achieved from electrochemical reactions from solutions of precursor metal salts move to an electrode surface under an applied electric field. Cathodic or anodic deposition can be achieved depending on the nature of the particle or ionic charge.

EPD on the other hand involves the movement of charged particles suspended in liquid media towards an electrode under the influence of an applied electric field. The deposits are therefore achieved by the coagulation of the particles on the surface of the electrode. It is worth noting that the deposition rate of EPD process is faster compared to that of ELP, thereby resulting in higher deposit thickness. For this reason, EPD is normally used to produce thick films while ELD allows the fabrication of thin nanostructured films. Even though compared to other synthesis methods, ELD deposited films have low material loading and thus are far from large-scale production, it remains one of the best synthesis methods for the evaluation of the electrochemical capacitance properties of electrode materials [70, 71].

Under electrodeposition synthesis, cyclic voltammetry, galvanostatic, potentiostatic, and pulse deposition are the most widely investigated techniques for nanostructured

supercapacitor electrode materials [61, 72]. The processes are usually executed in electrolytic cells powered by electrochemical workstations. Depending on the number of electrodes involved, the setup can be grouped into two types: two-electrode and three-electrode configurations [73]. The two-electrode system (Figure 2.17(a)) consists of positive and negative electrodes immersed in electrolytes containing the ion of the material to be deposited. An electrochemical workstation or power source supplies voltage across the two electrodes. Thus, the measured voltage is the overall cell voltage. Similarly, the three-electrode system (Figure 2.17(b)) includes a working electrode (WE), a counter electrode (CE), and a reference electrode (RE). In this setup, current flows only between CE and WE, and the voltage of WE is referenced to that of RE. The measured voltage is therefore the real-time potential of WEs. Hg/HgO, saturated calomel, and Ag/AgCl are common REs [73]. Rahimi *et al.* [74] synthesized intertwined nanostructured Co(OH)₂-reduced graphene oxide composite (Co(OH)₂-rGO) by cathodic electrodeposition in a two-electrode system onto nickel foam substrate from graphene oxide and cobalt chloride electrolyte solution (Figure 2.18). The composite delivered a specific capacitance of 734 F/g at a specific current of 1 A/g and stability of 95 % after 1000 charge-discharge cycles. In another study by Aboelazm *et al.* [75] hierarchical Co₃O₄ nanostructures were synthesized via a potentiostatic deposition in a three-electrode system. The Co₃O₄ nanostructures delivered a specific capacitance (C_s) of 1273 F/g at 1 A/g and capacitance retention of 96 % after 5000 cycles. Nady *et al.* [76] also synthesized polypyrrole/NiO composite (Ppy/NiO) from an electrolyte solution consisting of nickel chloride, nickel sulfate, and pyrrole monomer using galvanostatic electrodeposition in a three-electrode system. The Ppy/NiO composite showed a C_s of 679 at 1 A/g and it retained 83.9 % of its initial capacitance after 1000 cycles.

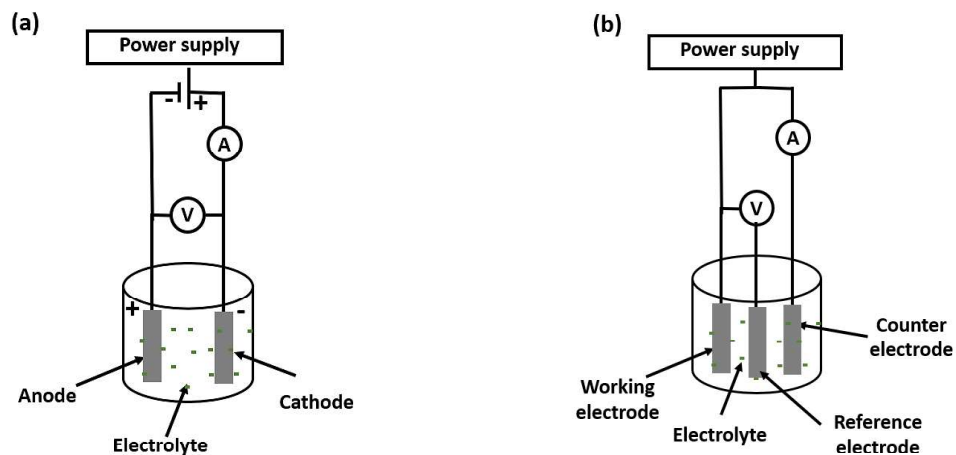


Figure 2.17 Schematic representation of (a) two-electrode (b) three-electrode electrodeposition cell configurations.

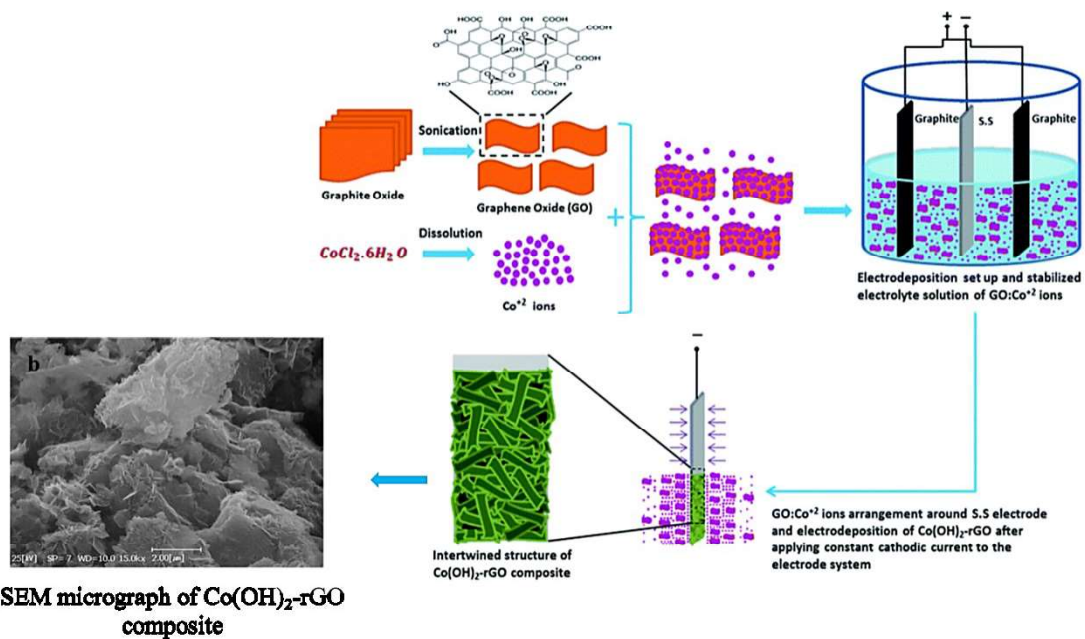


Figure 2.18. Schematic illustration of the cathodic electrodeposition synthesis of $\text{Co}(\text{OH})_2\text{-rGO}$ composite. Adapted from [74] with permission from the Royal Society of Chemistry.

2.7.2 Sol-gel

The sol-gel and chemical precipitation are simple and low-cost wet chemical synthesis techniques that involve the production of colloidal particles of metal oxides from reacting chemical solutions at low temperatures. The steps to the sol-gel synthesis of nanomaterials first involve the hydrolysis of the metal oxide in the presence of water or with the assistance of alcohol to form a sol. Condensation then takes place, increasing viscosity to form porous structures that are to age. Additionally, hydroxo- (M-OH-M) or oxo- (M-O-M) bridges form during the polycondensation or condensation process. Subsequently, drying takes place to remove the water and organic solvents from the gel. Finally, the nanoparticles are obtained by calcination [3, 77]. Thin films or coatings are achieved by dip or drop coating colloidal materials directly onto substrates. Powders of the materials can also be obtained by drying and annealing processes and after which coatings are made by mixing powders with conductive additives and binders to get slurries which are then pasted on substrates.

These fabrication methods have potential industrial applications as they allow high material loading of active materials [27]. In a report by Wu *et al.* Ni(OH)₂ nanoplatelets synthesized by a chemical precipitation method were further annealed to obtain NiO with enhanced conductivity and specific capacitance of 108 F/g [3]. In another study by Mustafa *et al.* [78], Mn₂O₃/graphene composite synthesized by the sol-gel process delivered a specific capacitance of 391 F/g at a scan rate of 5 mV/s in 1 M K₂SO₄ electrolyte.

2.7.3 Hydrothermal

The hydrothermal technique is also another generally accepted one-pot synthesis method for the synthesis of transition metal oxides. It involves chemical reactions in the presence of solvents above room temperature and high pressures. Materials are typically prepared by a combination of reaction precursors heated in a sealed Teflon-lined stainless steel autoclave, kept above 100 °C. The high temperatures and pressures cause the dissolution and recrystallization of reactants into desired materials and factors such as reaction time, temperature, and amount of solvents have a critical impact on the structure and morphology of the resulting product [3, 27]. The advantage of hydrothermal over other methods includes the ability to develop materials with improved purity, crystallinity, and quality [27]. Furthermore, the hydrothermal method is practical for fabricating nanostructures of electrode materials, including nanosheets, nanowalls, nanorods, and nanoneedles among others [15, 27, 58, 79-81]. Figure 2.19 shows the schematic representation of fabricating different nanostructured electrode materials from different precursor solutions using the hydrothermal process.

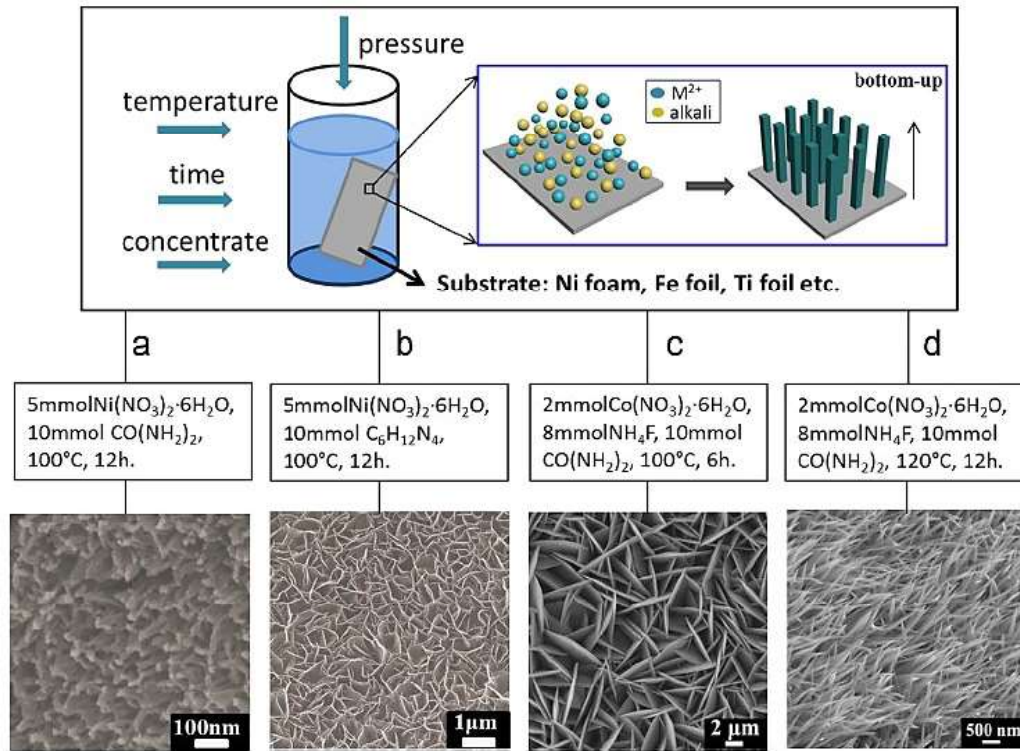


Figure 2.19 Schematic illustration of hydrothermal synthesis of (a) NiO nanorods, (b) Ni(OH)₂ nanowall, (c) Co₃O₄ nanosheet, and (d) Co₃O₄ nanowire. Adapted from [81] with permission. Copyright © 2013, Elsevier.

2.7.4 Chemical precipitation.

Chemical precipitation is another facile process to fabricate nanosized supercapacitor electrode materials (transition metals and hydroxides) on a commercial scale in powder form. During the chemical precipitation process, the concentrations of the solute in the solution are maintained above the solubility limits to allow the occurrence of precipitation as a result of supersaturation whereby the metal ions of interest form salts that are coprecipitated from alkaline/base media. Subsequently, the precipitate is collected from the solution, washed with

distilled water, and dried at the necessary temperatures in suitable conditions to obtain the final product [3]. In a report by Raj *et al.*, [82] a chemical precipitation process was used to prepare Mn₃O₄ nanoparticles from Cl₂.4H₂O and NaOH aqueous solutions and coated onto a stainless steel substrate according to equations (2.14)-(2.16). The Mn₃O₄ nanoparticles offered a C_s of 322 F/g at a current density of 0.5 mA/cm² and a cycle stability of 77 % after 1000 charge-discharge cycles. Additionally, Zhou *et al.*, [83] synthesized Ni₂P₂O₇ nanowires through a chemical precipitation process. The Ni₂P₂O₇ nanowires showed a specific capacitance of 772.5 F/g at 1 A/g and capacitance retention of 94 % after 3000 charge-discharge cycles.



2.8 Applications of supercapacitors

Supercapacitors are used in a wide range of applications such as backup power sources. They are connected in parallel with the main power source such as batteries so that during the disconnection or interruption of the main power, supercapacitors can still supply energy to the system. Thus they are used as backup sources for memories, clocks, system boards, and microcomputers [84]. They are also used as the main power source in portable consumer electronics mobile phones, smart watches, drones, forklifts, and cranes. In the transportation industry, SCs because of their fast high power density are used together with batteries and fuel cells for regenerative braking in electric vehicles to reduce 15 % of fuel consumption [85-87].

2.9 References

- [1] Y. Zhang, J. Wang, H. Wei, J. Hao, J. Mu, P. Cao, J. Wang, S. Zhao, Hydrothermal synthesis of hierarchical mesoporous NiO nanourchins and their supercapacitor application, *Mater. Lett.*, 162 (2016) 67-70.
- [2] M. Aghazadeh, Nickel oxide Nano-Rods/Plates as a High Performance Electrode Materials for Supercapacitors; Electrosynthesis and Evolution of Charge Storage Ability, *Int. J. Electrochem.*, (2016) 11002-11015.
- [3] P.E. Lokhande, U.S. Chavan, A. Pandey, Materials and Fabrication Methods for Electrochemical Supercapacitors: Overview, *Electrochemical Energy Reviews*, 3 (2019) 155-186.
- [4] M. Aadil, S. Zulfiqar, M. Shahid, S. Haider, I. Shakir, M.F. Warsi, Binder free mesoporous Ag-doped Co₃O₄ nanosheets with outstanding cyclic stability and rate capability for advanced supercapacitor applications, *J. Alloys Compd.*, 844 (2020) 156062.
- [5] Z. S. Iro, A Brief Review on Electrode Materials for Supercapacitor, *Int. J. Electrochem.*, (2016) 10628-10643.

- [6] G. Wang, L. Zhang, J. Zhang, A review of electrode materials for electrochemical supercapacitors, *Chemical Society reviews*, 41 (2012) 797-828.
- [7] A. Muzaffar, M.B. Ahamed, K. Deshmukh, J. Thirumalai, A review on recent advances in hybrid supercapacitors: Design, fabrication and applications, *Renewable and Sustainable Energy Reviews*, 101 (2019) 123-145.
- [8] A. González, E. Goikolea, J.A. Barrena, R. Mysyk, Review on supercapacitors: Technologies and materials, *Renewable and Sustainable Energy Reviews*, 58 (2016) 1189-1206.
- [9] M.S. Yadav, Metal oxides nanostructure-based electrode materials for supercapacitor application, *Journal of Nanoparticle Research*, 22 (2020).
- [10] M. Yaseen, M.A.K. Khattak, M. Humayun, M. Usman, S.S. Shah, S. Bibi, B.S.U. Hasnain, S.M. Ahmad, A. Khan, N. Shah, A.A. Tahir, H. Ullah, A Review of Supercapacitors: Materials Design, Modification, and Applications, *Energies*, 14 (2021).
- [11] S. Najib, E. Erdem, Current progress achieved in novel materials for supercapacitor electrodes: mini review, *Nanoscale Advances*, 1 (2019) 2817-2827.
- [12] S.H. Nagarajarao, A. Nandagudi, R. Viswanatha, B.M. Basavaraja, M.S. Santosh, B.M. Praveen, A. Pandith, Recent Developments in Supercapacitor Electrodes: A Mini Review, *ChemEngineering*, 6 (2022).
- [13] Y. Jiang, J. Liu, Definitions of Pseudocapacitive Materials: A Brief Review, *Energy & Environmental Materials*, 2 (2019) 30-37.
- [14] Q. Zhang, E. Uchaker, S.L. Candelaria, G. Cao, Nanomaterials for energy conversion and storage, *Chemical Society reviews*, 42 (2013) 3127-3171.
- [15] P. Forouzandeh, V. Kumaravel, S.C. Pillai, Electrode Materials for Supercapacitors: A Review of Recent Advances, *Catalysts*, 10 (2020).
- [16] R. Dubey, V. Guruviah, Review of carbon-based electrode materials for supercapacitor energy storage, *Ionics*, 25 (2019) 1419-1445.
- [17] M.A.A. Mohd Abdah, N.H.N. Azman, S. Kulandaivalu, Y. Sulaiman, Review of the use of transition-metal-oxide and conducting polymer-based fibres for high-performance supercapacitors, *Mater. Des.*, 186 (2020) 108199.
- [18] K.S. Lee, Y.J. Seo, H.T. Jeong, Capacitive behavior of functionalized activated carbon-based all-solid-state supercapacitor, *Carbon Letters*, 31 (2021) 1041-1049.
- [19] P. Simon, A. Burke, Nanostructured Carbons_Double-Layer Capacitance and More.pdf, *The Electrochemical Society Interface*, 17 (2008) 38-43.
- [20] C. Liu, H.-M. Cheng, Carbon nanotubes for clean energy applications, *Journal of Physics D: Applied Physics*, 38 (2005) R231-R252.
- [21] P.A. Martins-Junior, C.E. Alcantara, R.R. Resende, A.J. Ferreira, Carbon nanotubes: directions and perspectives in oral regenerative medicine, *Journal of dental research*, 92 (2013) 575-583.
- [22] S. Iijima, Helical microtubules of graphitic carbon, 354 (1991) 56-58.
- [23] J. Li, Z. Zhang, J. Fu, Z. Liang, K.R. Ramakrishnan, Mechanical properties and structural health monitoring performance of carbon nanotube-modified FRP composites: A review, *Nanotechnology Reviews*, 10 (2021) 1438-1468.
- [24] L. Dai, D.W. Chang, J.B. Baek, W. Lu, Carbon nanomaterials for advanced energy conversion and storage, *Small*, 8 (2012) 1130-1166.
- [25] Z. Niu, Y. Zhang, Y. Zhang, X. Lu, J. Liu, Enhanced electrochemical performance of three-dimensional graphene/carbon nanotube composite for supercapacitor application, *J. Alloys Compd.*, 820 (2020).

- [26] T. Chen, L. Dai, Carbon nanomaterials for high-performance supercapacitors, *Materials Today*, 16 (2013) 272-280.
- [27] P. Forouzandeh, P. Ganguly, R. Dahiya, S.C. Pillai, Supercapacitor electrode fabrication through chemical and physical routes, *J. Power Sources*, 519 (2022).
- [28] D. Yang, C. Bock, Laser reduced graphene for supercapacitor applications, *J. Power Sources*, 337 (2017) 73-81.
- [29] Q. Li, X. Guo, Y. Zhang, W. Zhang, C. Ge, L. Zhao, X. Wang, H. Zhang, J. Chen, Z. Wang, L. Sun, Porous graphene paper for supercapacitor applications, *Journal of Materials Science & Technology*, 33 (2017) 793-799.
- [30] D. Majumdar, T. Maiyalagan, Z. Jiang, Recent Progress in Ruthenium Oxide-Based Composites for Supercapacitor Applications, *ChemElectroChem*, 6 (2019) 4343-4372.
- [31] S. Deng, X. Xiao, G. Chen, L. Wang, Y. Wang, Cd doped porous Co_3O_4 nanosheets as electrode material for high performance supercapacitor application, *Electrochim. Acta*, 196 (2016) 316-327.
- [32] <- Supercapacitors_ Materials, Systems, and Applications-Wiley-VCH Verlag GmbH & Co. KGaA (2013).pdf>.
- [33] R. Thangappan, M. Arivanandhan, R. Dhinesh Kumar, R. Jayavel, Facile synthesis of RuO_2 nanoparticles anchored on graphene nanosheets for high performance composite electrode for supercapacitor applications, *Journal of Physics and Chemistry of Solids*, 121 (2018) 339-349.
- [34] J. Xiao, S. Yang, L. Wan, F. Xiao, S. Wang, Electrodeposition of manganese oxide nanosheets on a continuous three-dimensional nickel porous scaffold for high performance electrochemical capacitors, *J. Power Sources*, 245 (2014) 1027-1034.
- [35] Y.X. Fang Xiao, Pulse Electrodeposition of Manganese Oxide for High-Rate Capability Supercapacitors, *Int. J. Electrochem. Sci*, 7 (2012) 7440 - 7450.
- [36] T.B. Mathieu Toupin, and Daniel Be'langer, Charge Storage Mechanism of MnO_2 Electrode Used in Aqueous Electrochemical Capacitor, *Chem. Mater.*, 16 (2004) 3184-3190.
- [37] W. Wei, X. Cui, W. Chen, D.G. Ivey, Manganese oxide-based materials as electrochemical supercapacitor electrodes, *Chemical Society reviews*, 40 (2011) 1697-1721.
- [38] D. Majumdar, M. Mandal, S.K. Bhattacharya, Journey from supercapacitors to supercapatteries: recent advancements in electrochemical energy storage systems, *Emergent Materials*, 3 (2020) 347-367.
- [39] R.A. Davoglio, G. Cabello, J.F. Marco, S.R. Biaggio, Synthesis and characterization of α - MnO_2 nanoneedles for electrochemical supercapacitors, *Electrochim. Acta*, 261 (2018) 428-435.
- [40] E. Umeshbabu, P. Justin, G.R. Rao, Tuning the Surface Morphology and Pseudocapacitance of MnO_2 by a Facile Green Method Employing Organic Reducing Sugars, *ACS Applied Energy Materials*, 1 (2018) 3654-3664.
- [41] L. Cuéllar-Herrera, E. Arce-Estrada, A. Romero-Serrano, J. Ortiz-Landeros, R. Cabrera-Sierra, C. Tirado-López, A. Hernández-Ramírez, J. López-Rodríguez, Microwave-Assisted Synthesis and Characterization of γ - MnO_2 for High-Performance Supercapacitors, *Journal of Electronic Materials*, 50 (2021) 5577-5589.
- [42] V. Quispe-Garrido, G.A. Cerron-Calle, A. Bazan-Aguilar, J.G. Ruiz-Montoya, E.O. López, A.M. Baena-Moncada, Advances in the design and application of transition metal oxide-based supercapacitors, *Open Chemistry*, 19 (2021) 709-725.
- [43] J. Zhu, J. He, Facile synthesis of graphene-wrapped honeycomb MnO_2 nanospheres and their application in supercapacitors, *ACS Appl. Mater. Interfaces*, 4 (2012) 1770-1776.

- [44] X. Guo, K. Yan, F. Fan, Y. Zhang, Y. Duan, J. Liu, Controllable synthesis of a NiO hierarchical microspheres/nanofibers composites assembled on nickel foam for supercapacitor, *Mater. Lett.*, 240 (2019) 62-65.
- [45] S. Chatterjee, S.K. Bhattacharya, A review of NiO based composite electrode materials for electrochemical energy storage, *IOP Conference Series: Materials Science and Engineering*, 1080 (2021).
- [46] U.K. Chime, A.C. Nkele, S. Ezugwu, A.C. Nwanya, N.M. Shinde, M. Kebede, P.M. Ejikeme, M. Maaza, F.I. Ezema, Recent progress in nickel oxide-based electrodes for high-performance supercapacitors, *Current Opinion in Electrochemistry*, 21 (2020) 175-181.
- [47] S. Zhu, Y. Dai, W. Huang, C. Zhang, Y. Zhao, L. Tan, Z. Wang, In situ preparation of NiO nanoflakes on Ni foams for high performance supercapacitors, *Mater. Lett.*, 161 (2015) 731-734.
- [48] <09 electrosynthesis and characterization of nickel oxide thin films.pdf>.
- [49] R. Hang, Y. Liu, L. Zhao, A. Gao, L. Bai, X. Huang, X. Zhang, B. Tang, P.K. Chu, Fabrication of Ni-Ti-O nanotube arrays by anodization of NiTi alloy and their potential applications, *Sci Rep*, 4 (2014) 7547.
- [50] P.A. Nikolaychuk, THE POTENTIAL – pH DIAGRAM FOR Ni – H₂O SYSTEM.
- [51] N.N. Adarsh, Metal–Organic Framework (MOF)–Derived Metal Oxides for Supercapacitors, in: *Metal Oxides in Supercapacitors*, 2017, pp. 165-192.
- [52] Š. Trafela, J. Zavašnik, S. Šturm, K.Ž. Rožman, Formation of a Ni(OH)₂/NiOOH active redox couple on nickel nanowires for formaldehyde detection in alkaline media, *Electrochim. Acta*, 309 (2019) 346-353.
- [53] S.D. Dhas, P.S. Maldar, M.D. Patil, A.B. Nagare, M.R. Waikar, R.G. Sonkawade, A.V. Moholkar, Synthesis of NiO nanoparticles for supercapacitor application as an efficient electrode material, *Vacuum*, 181 (2020).
- [54] F. Ali, N.R. Khalid, G. Nabi, A. Ul-Hamid, M. Ikram, Hydrothermal synthesis of cerium-doped Co₃O₄ nanoflakes as electrode for supercapacitor application, *Int. J. Energy Res.*, 45 (2020) 1999-2010.
- [55] R.A.P. Ribeiro, S.R. de Lazaro, L. Gracia, E. Longo, J. Andrés, Theoretical approach for determining the relation between the morphology and surface magnetism of Co₃O₄, *Journal of Magnetism and Magnetic Materials*, 453 (2018) 262-267.
- [56] F. Ali, N.R. Khalid, Facile synthesis and properties of chromium-doped cobalt oxide (Cr-doped Co₃O₄) nanostructures for supercapacitor applications, *Appl. Nanosci.*, 10 (2020) 1481-1488.
- [57] S.K. Meher, G.R. Rao, Ultralayered Co₃O₄ for High-Performance Supercapacitor Applications, *J. Phys. Chem. C*, 115 (2011) 15646-15654.
- [58] X. Fan, Y. Sun, P. Ohlckers, X. Chen, Porous Thin-Wall Hollow Co₃O₄ Spheres for Supercapacitors with High Rate Capability, *Appl. Sci.*, 9 (2019).
- [59] J. Xu, L. Gao, J. Cao, W. Wang, Z. Chen, Preparation and electrochemical capacitance of cobalt oxide (Co₃O₄) nanotubes as supercapacitor material, *Electrochim. Acta*, 56 (2010) 732-736.
- [60] A. García-Gómez, S. Eugénio, R.G. Duarte, T.M. Silva, M.J. Carmezim, M.F. Montemor, Electrodeposited reduced-graphene oxide/cobalt oxide electrodes for charge storage applications, *Appl. Surf. Sci.*, 382 (2016) 34-40.
- [61] A.D. Jagadale, V.S. Kumbhar, R.N. Bulakhe, C.D. Lokhande, Influence of electrodeposition modes on the supercapacitive performance of Co₃O₄ electrodes, *Energy*, 64 (2014) 234-241.

- [62] J.K. Lee, G.P. Kim, K.H. Kim, I.K. Song, S.H. Baeck, Fabrication of mesoporous cobalt oxide (Co₃O₄) film by electrochemical method for electrochemical capacitor, *Journal of nanoscience and nanotechnology*, 10 (2010) 3676-3679.
- [63] W. Du, R. Liu, Y. Jiang, Q. Lu, Y. Fan, F. Gao, Facile synthesis of hollow Co₃O₄ boxes for high capacity supercapacitor, *J. Power Sources*, 227 (2013) 101-105.
- [64] R.B. Choudhary, S. Ansari, B. Purty, Robust electrochemical performance of polypyrrole (PPy) and polyindole (PIn) based hybrid electrode materials for supercapacitor application: A review, *J. Energy Storage*, 29 (2020) 101302.
- [65] M. Mastragostino, C. Arbizzani, F. Soavi, Polymer-based Supercapacitors, *J. Power Sources*, 98 (2001) 812-815.
- [66] J. Chen, Y. Wang, J. Cao, Y. Liu, Y. Zhou, J.H. Ouyang, D. Jia, Facile Co-Electrodeposition Method for High-Performance Supercapacitor Based on Reduced Graphene Oxide/Polypyrrole Composite Film, *ACS Appl. Mater. Interfaces*, 9 (2017) 19831-19842.
- [67] C.Y. Lee, H.M. Tsai, H.J. Chuang, S.Y. Li, P. Lin, T.Y. Tseng, Characteristics and Electrochemical Performance of Supercapacitors with Manganese Oxide-Carbon Nanotube Nanocomposite Electrodes, *Journal of The Electrochemical Society*, 152 (2005).
- [68] R. Devi, K. Tapadia, T. Maharana, Casting of carbon cloth enrobed polypyrrole electrode for high electrochemical performances, *Heliyon*, 6 (2020) e03122.
- [69] A. Burke, R&D considerations for the performance and application of electrochemical capacitors, *Electrochim. Acta*, 53 (2007) 1083-1091.
- [70] I. Zhitomirsky, Cathodic electrodeposition of ceramic and organoceramic materials. Fundamental aspects, 97 (2002) 279-317.
- [71] I. Zhitomirsky, A. Petric, M. Niewczas, Nanostructured ceramic and hybrid materials via electrodeposition, *JOM*, 54 (2002) 31-34.
- [72] F. Pagnanelli, P. Altimari, M. Bellagamba, G. Granata, E. Moscardini, P.G. Schiavi, L. Toro, Pulsed electrodeposition of cobalt nanoparticles on copper: influence of the operating parameters on size distribution and morphology, *Electrochim. Acta*, 155 (2015) 228-235.
- [73] R.G. Kelly, J.R. Scully, D. Shoesmith, R.G. Buchheit, *Electrochemical Techniques in Corrosion Science and Engineering*, 2002.
- [74] S.A. Rahimi, P. Norouzi, M.R. Ganjali, One-step cathodic electrodeposition of a cobalt hydroxide-graphene nanocomposite and its use as a high performance supercapacitor electrode material, *RSC Adv*, 8 (2018) 26818-26827.
- [75] E.A.A. Aboelazm, G.A.M. Ali, H. Algarni, H. Yin, Y.L. Zhong, K.F. Chong, Magnetic Electrodeposition of the Hierarchical Cobalt Oxide Nanostructure from Spent Lithium-Ion Batteries: Its Application as a Supercapacitor Electrode, *J. Phys. Chem. C*, 122 (2018) 12200-12206.
- [76] J. El Nady, A. Shokry, M. Khalil, S. Ebrahim, A.M. Elshaer, M. Anas, One-step electrodeposition of a polypyrrole/NiO nanocomposite as a supercapacitor electrode, *Sci Rep*, 12 (2022) 3611.
- [77] N. Baig, I. Kammakam, W. Falath, Nanomaterials: a review of synthesis methods, properties, recent progress, and challenges, *Materials Advances*, 2 (2021) 1821-1871.
- [78] G. Mustafa, G. Mehboob, S.N. Khisro, M. Javed, X. Chen, M.S. Ahmed, J.M. Ashfaq, G. Asghar, S. Hussain, A.U. Rashid, G. Mehboob, Facile Synthesis and Electrochemical Studies of Mn₂O₃/Graphene Composite as an Electrode Material for Supercapacitor Application, *Frontiers in chemistry*, 9 (2021) 717074.

- [79] X. Hu, L. Wei, R. Chen, Q. Wu, J. Li, Reviews and Prospectives of Co_3O_4 -Based Nanomaterials for Supercapacitor Application, *ChemistrySelect*, 5 (2020) 5268-5288.
- [80] J. Iqbal, A. Numan, R. Jafer, S. Bashir, A. Jilani, S. Mohammad, M. Khalid, K. Ramesh, S. Ramesh, Ternary nanocomposite of cobalt oxide nanograins and silver nanoparticles grown on reduced graphene oxide conducting platform for high-performance supercapattery electrode material, *J. Alloys Compd.*, 821 (2020) 153452.
- [81] Q. Yang, Z. Lu, J. Liu, X. Lei, Z. Chang, L. Luo, X. Sun, Metal oxide and hydroxide nanoarrays: Hydrothermal synthesis and applications as supercapacitors and nanocatalysts, *Prog. Nat. Sci.: Mater. Int.*, 23 (2013) 351-366.
- [82] B. Gnana Sundara Raj, A.M. Asiri, J.J. Wu, S. Anandan, Synthesis of Mn_3O_4 nanoparticles via chemical precipitation approach for supercapacitor application, *J. Alloys Compd.*, 636 (2015) 234-240.
- [83] Y. Zhou, C. Liu, X. Li, L. Sun, D. Wu, J. Li, P. Huo, H. Wang, Chemical precipitation synthesis of porous $\text{Ni}_2\text{P}_2\text{O}_7$ nanowires for supercapacitor, *J. Alloys Compd.*, 790 (2019) 36-41.
- [84] M.C. R. Kořtz Principles and applications of electrochemical capacitors, *Electrochim. Acta*, 45 (2000) 2483–2498.
- [85] L.T. Lam, R. Louey, Development of ultra-battery for hybrid-electric vehicle applications, *J. Power Sources*, 158 (2006) 1140-1148.
- [86] F.S. Garcia, A.A. Ferreira, J.A. Pomilio, Control Strategy for Battery-Ultracapacitor Hybrid Energy Storage System, in: 2009 Twenty-Fourth Annual IEEE Applied Power Electronics Conference and Exposition, 2009, pp. 826-832.
- [87] M.I.A. Abdel Maksoud, R.A. Fahim, A.E. Shalan, M. Abd Elkodous, S.O. Olojede, A.I. Osman, C. Farrell, A.a.H. Al-Muhtaseb, A.S. Awed, A.H. Ashour, D.W. Rooney, Advanced materials and technologies for supercapacitors used in energy conversion and storage: a review, *Environ. Chem. Lett.*, 19 (2020) 375-439.

CHAPTER 3: EXPERIMENTAL PROCEDURE

In this chapter, the materials, synthesis, and characterization techniques employed for the engineering of nanostructured materials for supercapacitor energy storage applications are discussed. This chapter is divided into two sections-Materials syntheses and Materials analysis (Physicochemical and electrochemical characterization).

3.1 Materials synthesis

3.1.1 Chemicals and Materials

The chemicals and materials which have been used in this research have been given in Table 3.1 below.

Table 3.1 : List of chemicals and materials used

Chemical or Material	Molecular Formula	Specifications	Supplier
Cobalt (II) acetate tetrahydrate	$\text{Co}(\text{OOCCH}_3)_2$	98 %	Alfa Aesar
Cobalt (II) chloride hexahydrate	$\text{CoCl}_2 \cdot 6\text{H}_2\text{O}$	98 %	Alfa Aesar

Silver Nitrate	AgNO ₃		VWR
Potassium Hydroxide	KOH		Millipore
Pyrrole	C ₄ H ₅ N	98 %	Alfa Aesar
Sodium perchlorate monohydrate	ClH ₂ NaO ₅	97 +%	Alfa Aesar
Nickel (II) sulfate hexahydrate	NiSO ₄ .6H ₂ O	98 %	Alfa Aesar
Poly(vinylidene fluoride) (PvdF)	(-CH ₂ CF ₂ -) _n		Alfa Aesar
Carbon black, acetylene	-	50 % compressed, 99.9 +%, 75 m ² /g, Bulk density: 80-120g/L	Alfa Aesar
N-methyl pyrrolidinone (NMP)	C ₅ H ₉ NO	99.5 %	Alfa Aesar
Hydrochloric acid	HCl	36.5-38 %	VWR
Titanium foil	-	99.7 %, 0.25 mm thickness, 42.0 Ω.cm resistivity	Sigma Aldrich

Ethyl alcohol	C ₂ H ₅ OH	95 % vol	Commercial Alcohols, Greenfield Global
Nickel foam	-	420 g/m ² density, 450 μm pore size, >99 %, 1.6 mm thickness, 110 PPI cell size	Heze Jiaotong group, China
Aluminum mesh	-	AA6061	-
Stainless-steel mesh	-	-	-
Silicon carbide (SiC) waterproof paper	-	240 grit	-

3.1.2 Substrate preparation

Titanium (Ti) foil substrate: Before any deposition or coating process, Ti foils with dimensions of 4 cm x1 cm were polished with Silicon carbide (SiC) waterproof paper and washed in deionized water via an ultrasonic bath for 15 mins. The polished Ti foils were then etched in concentrated HCl for 5 mins to remove surface contaminants after which they were washed in deionized water, ethanol, and deionized water in turn for 10 mins using an ultrasonic bath before drying on a hot plate at 60 °C for 6 hrs.

Nickel foam (NF) substrate: Similar to the Ti foils, NF substrates (4 cm x1 cm) were etched in 3 M HCl for 15 mins and washed in deionized water via an ultrasonic bath. The etched substrates were then washed in ethanol and deionized for 15 mins each and dried on a hot plate at 60 °C for 24 hrs.

Stainless steel and aluminum mesh substrates: Stainless steel and aluminum mesh substrates (4 cm x1 cm) were polished with SiC paper and washed in laboratory detergent solution for 15 mins and rinsed in deionized water for 10 mins after which the substrates were dried in air for 10 mins for the coating processes.

3.1.3 Chemical precipitation synthesis

NiO and Co₃O₄ electrode material was synthesized via a chemical precipitation route by the addition of a base (NaOH) solution to individual NiSO₄.6H₂O and Co(CH₃CO₂)₂.4H₂O precursor solutions respectively and subsequent hydrothermal treatment. In the preparation process of NiO particles, 10ml of 1 M NaOH solution was added dropwise to 30 ml of 0.1 M NiSO₄.6H₂O while stirring at 3000 rpm using a magnetic stirrer on a hot plate maintained at room temperature until the entire volume of NaOH was consumed. The reaction between NaOH causes the transparent green solution of NiSO₄.6H₂O to become cloudy which is an indication of the formation of Ni(OH)₂ precipitates as expressed in equation (3.1). The resulting solution after the base addition was stirred for an extra 15 mins before it was transferred into 50 ml capacity Teflon-lined autoclave heated at 120 °C for 24 hrs. Subsequently, the solutions are then allowed to cool to room temperature before the resulting

precipitates were washed severally with deionized water via centrifugation at 4000 rpm for 15 mins and dried at 100 °C for 24 hrs to obtain NiO particles.

Likewise, Co₃O₄ particles were also prepared by repeating the preparation processes for NiO particles. However, the precursor used was 30ml of 0.1 M Co(CH₃CO₂)₂.4H₂O and the pink color of the precursor turned purple upon the addition of 10ml of 1 M NaOH solution. The formation mechanism of Co(OH)₂ precipitates is expressed in equation (3.2). Both mechanisms for the formation of the Ni(OH)₂ and Co(OH)₂ expressed in equations (3.1) and (3.2) have been well established by other studies in the literature [1, 2].

Electrode fabrication: The as-synthesized materials were fabricated into a single electrode by mixing 80 wt.% of the as-synthesized materials with carbon black (15 wt.%), and polyvinylidene fluoride (PVDF, 5 wt.%) in N-Methylpyrrolidone (NMP) to form a slurry. The slurry was then coated on a 1 cm² area of nickel foam and titanium substrates, dried at 70 °C for 18 hrs and weighed. The schematic representation of the synthesis and fabrication processes have been provided in Figure 3.1.



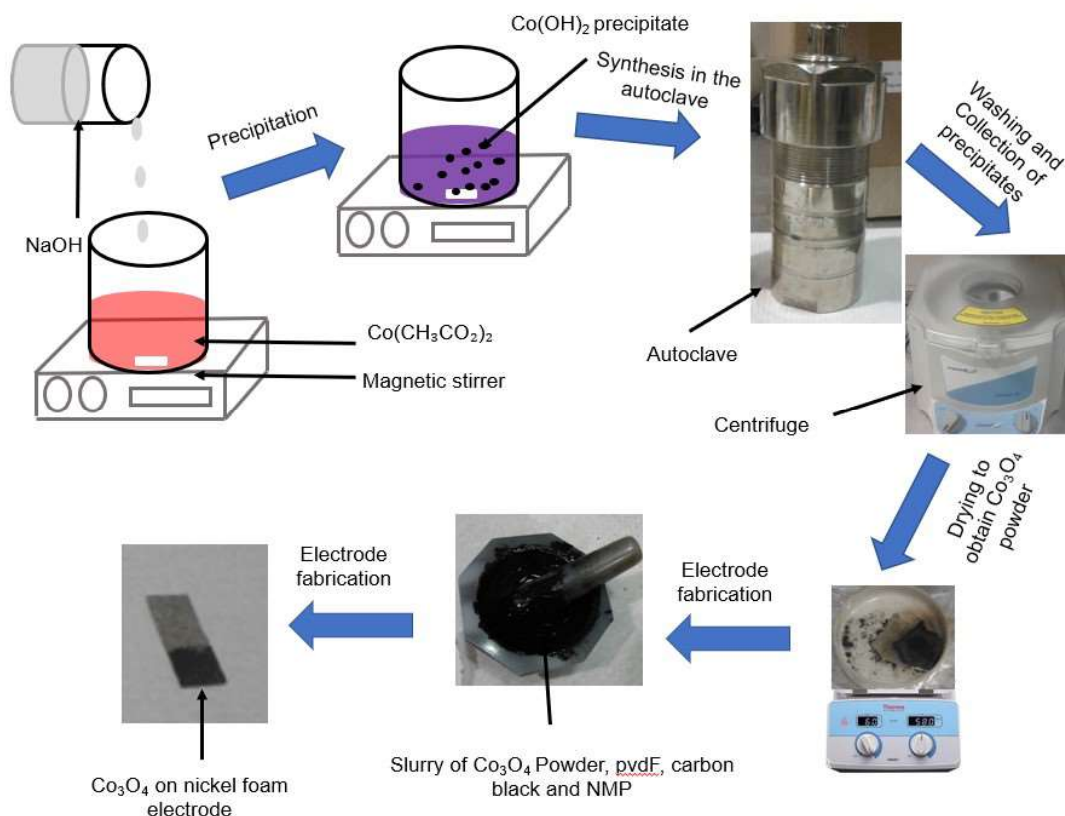
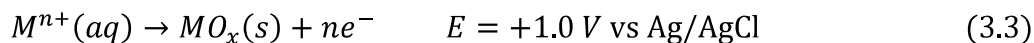
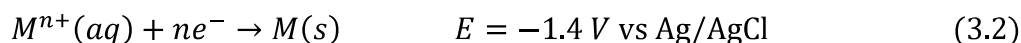


Figure 3.1. Schematic diagram of the hydrothermal synthesis and electrode fabrication process of Co_3O_4 electrode material.

3.1.4 Electrodeposition synthesis

In the research for this thesis, nanostructured supercapacitor electrode materials consisting of metal and metal oxide composites (Ni-NiO , $\text{Co-Co}_3\text{O}_4$, $\text{Ag/Co-Co}_3\text{O}_4$) were prepared on different treated substrates by a combination of cyclic voltammetry (CV) and pulse reverse potential (PRP) electrodeposition techniques from various electrolyte solutions using the three-electrode system whereby platinum wire, and Ag/AgCl , and the substrate served as counter, reference, and working electrodes respectively. In a typical synthesis, the cyclic voltammetry (CV) process is first used to nucleate the metal (M) and metal oxide (MO_x)

on a substrate. It started with a negative potential so that a metal coating will be deposited on the metallic substrate (nickel foam and titanium foil) and that would increase the adhesion of the M-MO_x nanocomposite thin film (due to the mismatch of the surface energy of metal and metal oxide which leads to a weak interface that makes the coating unstable in terms of interfacial adhesion). The pulse reverse potential (PRP) is subsequently applied by conducting the cathodic and anodic deposition to deposit a layer of M and MO_x in sequence. In our experiment, a maximum negative (cathodic) potential of -1.4 V was used to deposit metallic film and a +1.0 V (anodic) was used to deposit metal oxide according to the proposed mechanism given in equations (3.2) and (3.3).



Electrodeposition synthesis of nanostructured Ni-NiO: Ni-NiO nanocomposite thin film was deposited on the treated Ti-substrate by a combined CV and PRP electrodeposition techniques from an electrolyte consisting 0.1 M NiSO₄.6H₂O (30 ml) and 0.2 M NaClO₄.H₂O (30 ml) of pH of 4.5. Initially, CV was performed in a potential range of -1.4 V to +1.0 V vs Ag/AgCl at a scan rate of 20 mVs⁻¹ for 2 cycles. The CV process was then followed with a PRP deposition by first applying a negative voltage of -1.4 V for 0.5 s and a positive voltage of +1 V for 0.5 s for 60 cycles. The deposition process was performed in a standard three-electrode glass cell with a platinum wire, Ti-substrate and Ag/AgCl as the counter, working and reference electrodes, respectively. After electrodeposition, the Ni-NiO

nanocomposite thin film electrode was rinsed in deionized water and dried on a hot plate maintained at 100° C for 10 hrs in air before performing physical and electrochemical characterizations. To optimize the deposition process, the PRP cycles were varied (60, 300, 600 and 900, and 1800 cycles). Furthermore, the mass of the electrodeposited film was determined by the mass difference between the bare NF substrates before and after the deposition process using an analytical microbalance (Sartorius CP124S, max 120g, 0.1 mg of resolution).

Electrodeposition synthesis of nanostructured Co-Co₃O₄ by modulating the molar ratios of two cobalt precursors: Similar to the preparation of the Ni-NiO composite, Co-Co₃O₄ nanocomposite thin films were deposited on nickel foam (NF) substrate by a combination cyclic voltammetry (CV) and pulse reverse potential (PRP) electrodeposition techniques using the three-electrode system where the counter, reference, and working electrodes are platinum wire, Ag/AgCl, and nickel foam respectively. In a typical synthesis, CV is first performed in a potential range of -1.4 to +1.0 V vs Ag/AgCl at a scan rate of 20 mVs⁻¹ for 2 cycles, followed by 60 cycles of PRP deposition conducted at a cathodic potential of -1.4 V for 0.5 s and an anodic potential of +1.0 V for 0.5 s in sequence. The electrolyte solutions used for the electrodeposition consist of a combined solution of 0.1 M cobalt acetate Co(CH₃COO)₂ and 0.1 M cobalt chloride (CoCl₂) in different molar ratios (100:0, 20:80, 40:60, 50:50) together with 0.2 M NaClO₄.H₂O. The deposition process was conducted in a standard three-electrode glass cell with a platinum wire, NF substrate, and Ag/AgCl as the counter, working, and reference electrodes, respectively. The distance between the electrodes was kept at 2 cm throughout the deposition process. After the electrodeposition process, the as-prepared Co-Co₃O₄ nanocomposite thin film electrodes were rinsed in deionized water

and dried on a hot plate at 200 °C for 45 minutes in air before further characterization. Additionally, the mass of the electrodeposited films was determined by first weighing the bare NF substrates before and after the deposition process using an analytical microbalance (Sartorius CP124S, max 120 g, 0.1 mg of resolution), and the difference in mass gives the mass of the deposited film. Figure 3.7 shows the setup for the electrodeposition process.

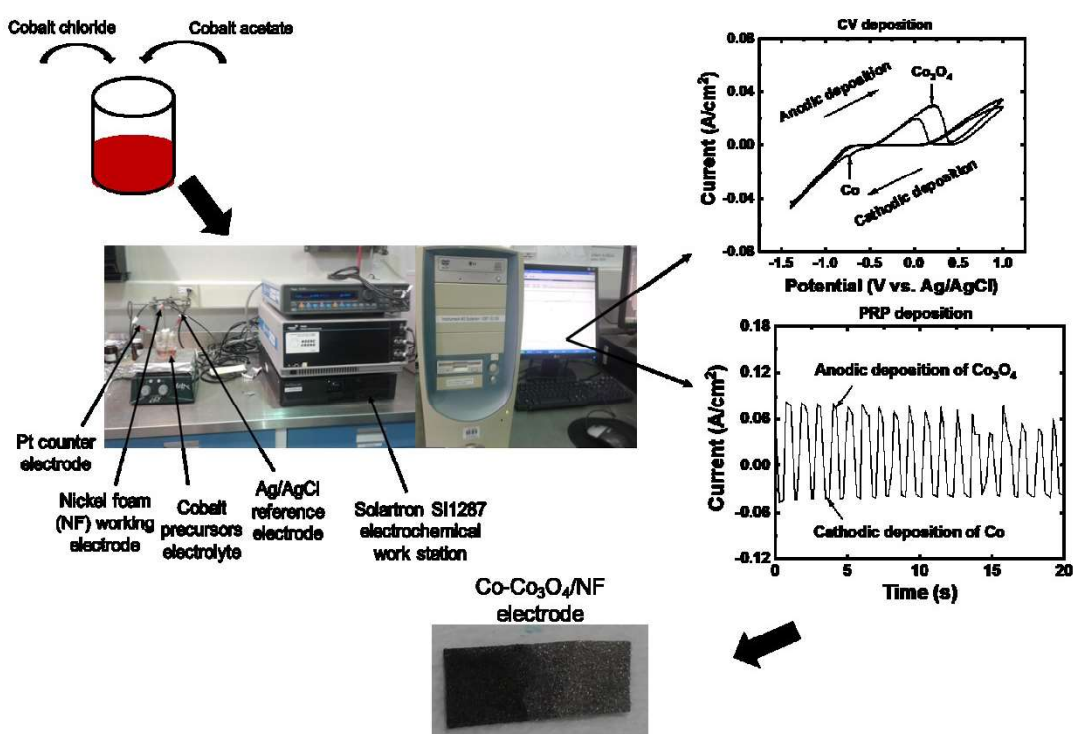


Figure 3.2 Three-electrode system setup for the electrodeposition synthesis of Co-Co₃O₄ nanocomposite electrode material.

Electrodeposition synthesis of nanostructured Co-Co₃O₄ via different electrodeposition techniques: In addition to modulating the molar ratio of cobalt precursors, the electrodeposition techniques were also optimized to obtain Co-Co₃O₄ electrode materials with superior performance. In this experiment, Co-Co₃O₄ composite materials were prepared

on nickel foam (NF) substrates from an electrolyte solution consisting of the optimum molar ratio of cobalt precursors with a pH of 6.5; 0.1 M cobalt acetate ($\text{Co}(\text{CH}_3\text{CO}_2)_2 \cdot 4 \text{H}_2\text{O}$, 6 ml), 0.1 M cobalt chloride (CoCl_2 24 ml) and 0.2 M sodium perchlorate ($\text{NaClO}_4 \cdot \text{H}_2\text{O}$, 30 ml). The electrodeposition process involved the use of four techniques of electrodeposition: (1) Cyclic voltammetry (CV), (2) CV followed by potentiostatic (PS) at +1.0 V (CV PS +1.0 V), (3) CV followed by PS at -1.4 V (CV PS -1.4V) and (4) CV followed by pulse reverse potential (CV PRP) cycled between -1.4V and +1.0V. CV mode was conducted in a potential range of -1.4 to +1.0 V vs Ag/AgCl at a scan rate of 20 mVs^{-1} for 2 cycles. For the CVPS +1V mode, CV was initially conducted in a potential range of -1.4 to +1.0 V vs Ag/AgCl at a scan rate of 20 mVs^{-1} for 2 cycles, and was followed by potentiostatic deposition at +1 V for 30 s. A similar condition was repeated for the CV PS -1.4V mode, however with a negative constant potential of -1.4 V. For the CV PRP mode, CV was initially performed in a potential range of -1.4 to +1.0 V vs Ag/AgCl at a scan rate of 20 mVs^{-1} for 2 cycles, followed by 60 cycles of PRP deposition conducted at a cathodic potential of -1.4 V for 0.5 s and an anodic potential of +1.0 V for 0.5 s in sequence. The deposition process was conducted in a standard three-electrode glass cell with a platinum wire, NF substrate, and Ag/AgCl as the counter, working, and reference electrodes, respectively. After electrodeposition, the as-prepared Co-CoO_x nanocomposite thin film electrodes were rinsed in deionized water and dried in air on a hot plate at 200° C for 45 minutes before performing characterization and electrochemical analyses.

Electrodeposition synthesis of nanostructured Ag/Co-Co₃O₄ composite: (Ag/Co-Co₃O₄ nanocomposite thin films were synthesized onto nickel foam (NF) substrates by cyclic voltammetry (CV) followed by pulse reverse potential (CV PRP) cycled between -1.4 V and

+1.0 V. A standard three-electrode system with a platinum wire, NF substrate, and Ag/AgCl as the counter, working and reference electrodes, respectively was employed for the deposition process. Initially, CV was performed in a potential range of -1.4 to $+1.0$ V vs Ag/AgCl at a scan rate of 20 mVs^{-1} for 2 cycles, followed by pulse reverse potential (PRP) of 60 cycles at -1.4 V and 1 V with $0.5 \text{ s}/0.5 \text{ s}$ time interval for a total duration of 60 s . The electrolyte solutions used for the electrodeposition consist of 0.1 M cobalt acetate ($\text{Co}(\text{CH}_3\text{CO}_2)_2 \cdot 4 \text{ H}_2\text{O}$, 6 ml), 0.1 M cobalt chloride (CoCl_2 24 ml), 0.1 M silver nitrate (AgNO_3 , 2 ml) and 0.2 M sodium perchlorate ($\text{NaClO}_4 \cdot \text{H}_2\text{O}$, 30 ml). In the electrochemical deposition process, the applied negative potential reduces the Co^{2+} and Ag^+ ions into metallic Co and Ag films. Similarly, the applied positive potential results in the deposition of a layer of Co_3O_4 . After the electrodeposition process, the as-prepared Ag/Co- Co_3O_4 /NF nanocomposite thin film electrodes were rinsed in deionized water and dried in air on a hot plate at $200 \text{ }^\circ\text{C}$ for 45 minutes before further characterization and electrochemical analyses. The mass of the electrodeposited material was estimated from the difference in the mass of the NF substrate before the electrodeposition process and with material loading after drying using an analytical microbalance (Sartorius CP124S, max 120 g , 0.1 mg of resolution). To optimize the electrodeposition process, the volume (ml) of silver nitrate was varied ($1, 2, 3, 6, 12 \text{ ml}$).

Electrodeposition synthesis of polypyrrole coatings on nickel-modified aluminum and stainless-steel mesh: Aluminum mesh was valorized as a substrate for polypyrrole electrode material coating. Firstly, the treated aluminum mesh was modified with nickel coating by a potentiostatic electrodeposition from an electrolyte solution of 0.5 M $\text{NiSO}_4 \cdot 6\text{H}_2\text{O}$ (30 ml) and 0.2 M $\text{NaClO}_4 \cdot \text{H}_2\text{O}$ (30 ml), by applying a constant voltage of -1.4

V for 120 mins. Polypyrrole coating was then deposited on the nickel-modified aluminum mesh from an aqueous precursor solution consisting of 0.6 M pyrrole (30 ml) and 0.2 M $\text{NaClO}_4 \cdot \text{H}_2\text{O}$ (30 ml) by applying a constant potential of 0.8 V for 10 min. The formation of the polypyrrole coating is a two-step process that begins with the loss of electrons and the formation of radical cations by the pyrrole monomer when an oxidation potential is applied (Initiation step). Subsequently, the formed radical cation couples with the monomer unit to form a dimer radical cation which in turn reacts with other monomer molecules to form trimer radical cations and so on to form a polymer chain of pyrrole units (Propagation step) [3, 4]. The mechanism for the electropolymerization process of the pyrrole monomer is given in Figure 3.3. The treated steel mesh was also coated with polypyrrole for comparison to elucidate the effect of the nickel modification. All depositions were carried out at room temperature using a standard three-electrode glass cell with a platinum wire, the nickel-modified aluminum mesh/stainless-steel mesh, and Ag/AgCl as the counter, working, and reference electrodes respectively. The fabricated electrodes were dried in air before further analysis.

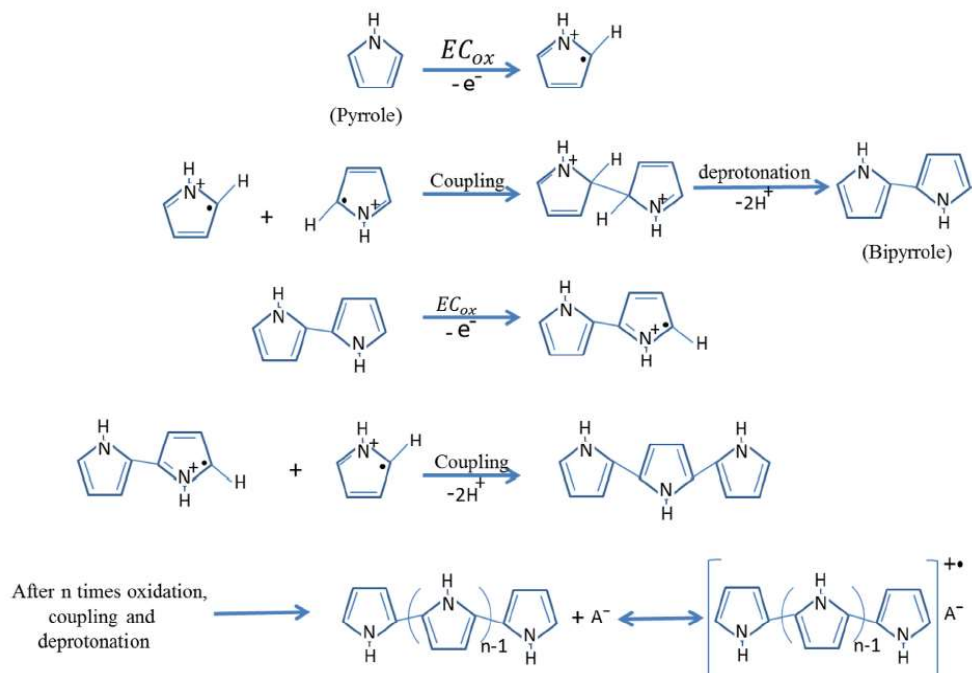


Figure 3.3 Electropolymerization process of pyrrole. Adapted from [3] with permission.

3.2 Materials Analysis

3.2.1 Microstructural analysis by scanning electron microscopy

The surface morphological features and chemical composition of the nanostructured electrode materials were studied using scanning electron microscopy (SEM, JEOL, JSM 6480 LV) equipped with energy dispersive X-ray spectroscopy (EDS) as shown in Figure 3.4. Compared to an ordinary optical microscope, the SEM is a more powerful imaging technique capable of producing three-dimensional images and it combines higher magnification, greater resolution, and higher depth focus. It works on the basic principle of the interaction of an accelerated monoenergetic electron beam emanating from an electron gun via a field emission or thermionic emission process, with the atoms of the material's surface. Typically, the electrons are focused and accelerated by an applied voltage of 20 kV. Subsequently, the secondary and backscattered electrons which result from the interaction are collected by a detector, regulated, and amplified to create an exact reconstruction of the surface of the sample and the particle profile while the X-rays provide the elemental composition. The precondition for successful viewing of samples is that the surface should be electrically conductive.

3.2.2 Fourier transform infrared spectroscopy

In this research, the molecular fingerprints of the nanostructured materials were analyzed with an attenuated total reflectance-Fourier transform infrared spectroscopy (ATR-FTIR, Agilent Technologies Cary 360) shown in Figure 3.5 within the wavenumber range of $4000\text{-}450\text{ cm}^{-1}$.



Figure 3.4. Scanning electron microscope (model SEM JEOL JSM 6480LV), CURAL, UQAC.

In FTIR spectroscopy, when the frequency of an incident infrared radiation corresponds to the normal stretching or bending vibrational modes of the molecules in the material, the molecular bonds absorb some of the radiation while the rest gets transmitted in the transition mode of the FTIR spectroscopy. As the vibrational frequency changes linearly with the bonding force (k) and with the reduced mass of the atom (μ) as depicted in Equation

3.5 [5], the emerging signal detected gives the molecular fingerprint specific molecules within the material.

$$\omega = \frac{1}{2\pi} \sqrt{\frac{k}{\mu}} \quad (3.5)$$

where ω is the vibration frequency (cm^{-1}) and k is the bond strength (dyne.cm^{-1}). For this reason, FTIR spectroscopy can result in qualitative analysis of different materials and the size of the spectrum peaks indicates the amount of material present (Quantitative analysis). Conversely to transmission mode FTIR, with ATR-FTIR, the infrared beam is entirely reflected.



Figure 3.5. ATR-FTIR spectroscopy apparatus (Agilent Technologies Cary 360), CURAL, UQAC.

Usually, in the ATR mode, a high refractive index (RI) diamond-ATR crystal (2.41) is used and due to the high refractive index of the crystal, the IR beam is completely reflected at the sample-crystal interface inside the crystal. Nevertheless, as a result of the wave-like characteristic, the IR radiation penetrates the few layers of the material giving rise to a diminishing wave. As the intensity of the wave decays exponentially, the attenuated reflected signals conveying the absorption details of the materials are collected at the detector and are subsequently Fourier transformed and displayed as ATR-FTIR spectra.

3.2.3 X-ray diffractometry

XRD is an analytical procedure to identify and quantify the phases of crystalline materials. In this research, XRD was used to identify the faces of metal and metal oxides in the nanostructured electrode materials. XRD works on the principle of constructive interference of monochromatic X-rays with atoms in the material. The fundamental principle of XRD is based on the path difference between the X-ray beams scattered by atoms within a material from adjacent lattice planes (hkl) of spacing d_{hkl} [6]. The resulting intensity peaks on the XRD pattern at each measured angle give the condition of the constructive interference satisfying Bragg's law according to Equation (3.6):

$$n\lambda = 2d_{hkl} \sin \theta \quad (3.6)$$

Where n is an integer, λ is the wavelength of the incident monochromatic X-ray beam, and θ is the angle between the incidence and diffraction to the lattice planes [6].

In the research for this thesis, the crystal structure analysis of the developed nanostructured electrode materials was conducted using D8 Discover system (Bruker Corporation) equipped with Cu K α X-ray source ($\lambda=0.15406$ nm) as shown in Figure 3.6.



Figure 3.6 X-ray diffractometer, Bruker D8 Discover system, CURAL, UQAC.

3.2.4 Electrochemical Characterization

The electrochemical assessment of the nanostructured materials as supercapacitor electrode materials were conducted using a three-electrode system with a platinum wire, Hg/HgO, and the fabricated electrodes as counter, reference, and working electrodes

respectively in a 1 M KOH and 1 M Na₂SO₄ electrolytes. Three different techniques namely cyclic voltammetry (CV), galvanostatic charge-discharge (GCD), and electrochemical impedance spectroscopy have been used for the electrochemical studies. In the research of this thesis, the Solartron SI1287 electrochemical interface with the Solartron 1254A frequency analyzer running on the Corrware computer software was used for the electrochemical measurements. A depiction of the electrochemical measurement setup has been given in Figure 3.7.

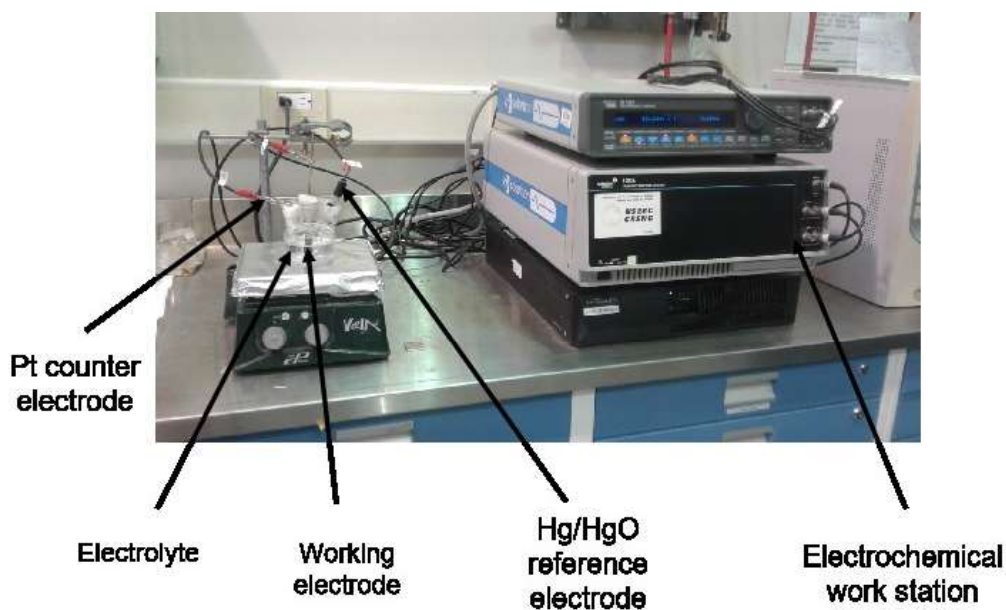


Figure 3.7. Three-electrode setup with the Solartron SI1287 electrochemical interface and the Solartron 1254A frequency analyzer.

Cyclic voltammetry (CV): The CV works on the principle of measuring the instantaneous current which results from applying a linear voltage to an electrode between two predefined voltage limits. The speed at which the potential changes is defined as the scan rate while the range of potential change is the potential window [7]. The CV measurements

for this study were conducted by sweeping a potential typically within the potential range of -0.1 to 0.6 V vs. Hg/HgO for our electrode materials at various scan rates of 100, 50, 20, 10, and 5 mV/s for qualitative analysis of redox reactions as well as determining the voltage window of the electrode materials. From the CV profiles, the specific capacitance of the fabricated electrodes was determined using equation (3.7):

$$C_s = \frac{1}{mv(V_a - V_c)} \int_{V_a}^{V_c} IVdV \quad (3.7)$$

Where C_s denotes the specific capacitance (F/g), m is the mass of the electroactive material (m), v is the applied scan rate (mV/s), $V_a - V_c$ is the potential window and $\int_{V_a}^{V_c} IVdV$ is the integrated area under the CV curve [1].

Galvanostatic charge-discharge (GCD): The GCD test is regarded as the most accurate and versatile technique for determining the capacitance and cycle stability of electrodes and devices. It is conducted by charging and discharging an SC device or working electrode repetitively at a constant current and the output is a plot of potential (E) vs. time (s) [7]. For our work, the GCD tests have been carried out at different current densities from 1 to 20 A/g within a preset potential range of -0.1 to 0.5 V vs. Hg/HgO. From the resulting charge-discharge profiles parameters such as specific capacitance, equivalent series resistance (ESR, Ω), capacitance retention, specific energy and power have been estimated using equations (3.8) to (3.12) respectively:

$$C_s = \frac{I_D \Delta t}{m \Delta V} \quad (3.8)$$

$$ESR = \frac{V_{IR}}{I_D} \quad (3.9)$$

$$C_R = \frac{C_{nth}}{C_{1st}} \quad (3.10)$$

$$E_s = \frac{1}{2} C_s (\Delta V)^2 \quad (3.11)$$

$$P_s = \frac{E_s}{\Delta t} \quad (3.12)$$

Where I_D is the discharge current, Δt is the discharge current (s), ΔV is the potential window (V), V_{IR} (V) is the voltage drop between the charge and discharge curve, C_R (F/g) is the capacitance retention, C_{nth} (F/g) denotes the capacitance retention after the nth cycle, C_{1st} (F/g) designates the capacitance retention after the first cycle, E_s (Wh/kg) and P_s (W/kg) represents the specific energy and power respectively [2] [3].

Electrochemical impedance spectroscopy (EIS): The EIS work works based on determining the impedance of an electrochemical system by applying a low-amplitude alternating voltage V to a steady-state potential V_s with the applied voltage expressed as:

$$V(\omega) = V_{max} e^{j\omega t} \quad (3.14)$$

where ω denotes the oscillation and V_{max} signifies the amplitude's signal. The input signal results in a sinusoidal output current I , with

$$I(\omega) = I_{max} e^{j(\omega t + \varphi)} \quad (3.15)$$

where φ represents the phase angle of the current versus the voltage and I_{\max} the amplitude of the signal. The electrochemical impedance $Z(\omega)$ is expressed

$$Z(\omega) = V/I = |Z(\omega)|e^{-j\varphi} = Z' + jZ'' \quad (3.16)$$

where Z' and Z'' represent the real and the imaginary parts of the impedance, respectively, expounded as [8]:

$$|Z(\omega)|^2 = Z'^2 + Z''^2 \quad (3.17)$$

The EIS data is expressed in Nyquist plots whereby the data from each frequency point is plotted by the imaginary part on the y-axis and the real part on the x-axis observed in Figure 3.8(I). Additionally, the data can also be interpreted as Bode plots in which the magnitude of the impedance and phase angle are plotted against frequency.

For the research work of this thesis, the EIS has been used to determine the charge transfer resistance (R_{ct}), equivalent series resistance (R_{ES}), and the diffusion resistance of the electrode materials [9]. EIS experiments for this research were conducted by applying a sinusoidal voltage of 10 mV in the frequency range from 10 mHz to 100 kHz at an open circuit potential.

3.3 References

- [1] N.K. Yetim, Hydrothermal synthesis of Co_3O_4 with different morphology: Investigation of magnetic and electrochemical properties, *Journal of Molecular Structure*, 1226 (2021).
- [2] A.K. Mondal, D. Su, Y. Wang, S. Chen, G. Wang, Hydrothermal synthesis of nickel oxide nanosheets for lithium-ion batteries and supercapacitors with excellent performance, *Chemistry, an Asian journal*, 8 (2013) 2828-2832.
- [3] R.B. Choudhary, S. Ansari, B. Purty, Robust electrochemical performance of polypyrrole (PPy) and polyindole (PIIn) based hybrid electrode materials for supercapacitor application: A review, *J. Energy Storage*, 29 (2020) 101302.
- [4] M. Gvozdenovic, B. Jugovic, J. Stevanovic, B. Grgur, Electrochemical synthesis of electroconducting polymers, *Hemijaska industrija*, 68 (2014) 673-684.
- [5] C. Berthomieu, R. Hienerwadel, Fourier transform infrared (FTIR) spectroscopy, *Photosynthesis research*, 101 (2009) 157-170.
- [6] C.B. Gary Attard, *Surfaces* Oxford University Press, New York, (1998).
- [7] S. Zhang, N. Pan, Supercapacitors Performance Evaluation, *Adv. Energy Mater.*, 5 (2015).
- [8] P.L. Taberna, P. Simon, J.F. Fauvarque, Electrochemical Characteristics and Impedance Spectroscopy Studies of Carbon-Carbon Supercapacitors, *Journal of The Electrochemical Society*, 150 (2003).
- [9] D. Majumdar, M. Mandal, S.K. Bhattacharya, Journey from supercapacitors to supercapatteries: recent advancements in electrochemical energy storage systems, *Emergent Materials*, 3 (2020) 347-367.

CHAPTER 4: CHEMICAL PRECIPITATION SYNTHESIS OF NiO AND Co₃O₄ SUPERCAPACITOR ELECTRODE MATERIALS

Rania Afia Nuamah, Saleema Noormohammed, Dilip Kumar Sarkar

Department of Applied Science, University of Quebec at Chicoutimi, Aluminum Research
Center-REGAL, Chicoutimi, Quebec, G7H 2B1, Canada

4.1 Abstract

NiO and Co₃O₄ supercapacitor electrode materials have been synthesized by a facile chemical precipitation route. The acquired attenuated total reflection–Fourier transform infrared (ATR-FTIR) spectra have confirmed the presence of Ni-O and Co-O bonds. While the energy-dispersive X-ray spectroscopy spectra (EDX) confirmed the presence of the appropriate elements. The morphological features revealed by the scanning electron microscope (SEM) correspond with the electrochemical behavior of the electrode materials. The capacitive performance assessed using the galvanostatic charge-discharge technique revealed maximum specific capacitance values of 40 F/g and 28 F/g at a specific current of 1 A/g for the NiO and Co₃O₄ electrodes respectively.

4.2 Introduction

High-performing electrochemical energy storage devices are extremely beneficial for today's world of advanced technological devices including smart watches, mobile phones,

laptops, regenerative braking systems, and hybrid electric vehicles. Supercapacitors, of all the various energy storage devices such as batteries and fuel cells, exhibit potential as efficient energy storage devices as a result of their high-power density, long cycle life, lightweight, and environmental friendliness [1-3]. In the operations of supercapacitors, the electrode material is one of the most critical components controlling the electrochemical performance. Up until now, carbon materials (graphene, activated carbon, carbon nanotubes) transition metal oxides (RuO_2 , MnO_2 , NiO , Co_3O_4), and conducting polymers (Polypyrrole, polyaniline) have been identified as supercapacitor electrode materials. Among these, base transition metal oxides including NiO , Co_3O_4 are particularly attractive due to their high theoretical capacitance values of 2573 and 3560 F/g respectively, earth abundance, low cost, high redox activity, and environmental friendliness [2, 4-6].

In the past few decades, great advances have been made to develop NiO , Co_3O_4 materials various morphological features and structures including nanotubes, nanospheres, nanowires, and nanoflowers to improve electrochemical performance [7-10]. However, recorded experimental specific capacitance values are still low compared to theoretical values due to low conductivity and less electrochemically active surface area [5]. Studies have shown that the morphology, surface area, and structure play a critical role in enhancing the electrochemical performance of NiO and Co_3O_4 electrode materials [5, 10]. Moreover, it is well established in the literature that nanostructured materials exhibit interesting properties better than bulk materials [1, 11]. Therefore, NiO and Co_3O_4 with nanoscale features would exhibit high specific surface areas which would result in more electroactive species for enhanced redox reactions, resulting in outstanding capacitive performance.

Numerous preparation techniques including thermal decomposition, chemical bath deposition, sol-gel method, chemical precipitation, and hydrothermal have been investigated for the fabrication of nanostructured NiO and Co₃O₄ materials [3, 12, 13]. In comparison to these synthesis routes, chemical precipitation synthesis presents a facile approach for the large-scale fabrication of high-purity nanostructured materials [14-16].

In this work, NiO and Co₃O₄ electrode materials have been fabricated using the chemical precipitation synthesis route. The electrochemical behavior of the electrodes has been assessed by cyclic voltammetry (CV) and the galvanostatic charge-discharge cycles. The NiO and Co₃O₄ electrodes exhibited specific capacitance values of 40 F/g and 28 F/g respectively.

4.3 Experimental procedure

In the experimental process for the synthesis of NiO and Co₃O₄ electrode materials, 10ml of 1 M NaOH solution was added dropwise to 30 ml of individual solutions of 0.1 M NiSO₄·6H₂O and 0.1 M Co(CH₃CO₂)₂·4H₂O respectively under magnetic stirring at 3000 rpm until the NaOH is consumed and precipitates are formed. The solution was then stirred for 15 mins to achieve homogeneity. Subsequently, the resulting solutions were then transferred into 50 ml capacity Teflon-lined autoclaves, and heated in an oven at 120 °C for 24 hrs. The precipitates were allowed to cool down to room temperature and then washed repeatedly with distilled water via centrifugation. The resulting precipitates were collected and dried at 100 °C for 24 hrs.

The morphological and elemental studies of the samples were conducted using a scanning electron microscope (SEM, JEOL JSM-6480 LV), equipped with energy-dispersive X-ray spectroscopy (EDX). An attenuated total reflection – Fourier transform infrared spectroscopy (ATR-FTIR, Agilent Technologies Cary 630) was used to confirm the metal oxides (Ni-O, and Co-O).

The electrochemical studies namely, cyclic voltammetry (CV) and galvanostatic charge-discharge (GCD) were conducted using a three-electrode glass cell with platinum wire, and Hg/HgO as counter and reference electrodes respectively. The electrochemical measurements were carried out in a 1 M KOH aqueous electrolyte using a Solartron SI1287 electrochemical workstation. The CV and GCD measurements were carried out at different scan rates and specific currents in a potential window of -0.2 to 0.6 V and -0.1 to 0.5 V respectively. The working electrodes were fabricated by mixing the as-prepared active materials (NiO or Co₃O₄) materials with polyvinylidene fluoride (PVDF) and carbon black in a ratio of 85:10:5 in N-Methylpyrrolidone (NMP) to form a homogeneous slurry. The slurry was then coated on a 1 cm² area of titanium substrates, dried at 70 °C for 18 hrs, and weighed.

4.4 Results and discussion

4.4.1 Structural, morphological, and chemical analysis

The ATR-FTIR spectra (Figure 4.1) recorded in the range of 1500-500 cm⁻¹ have been used to give details about phase composition and different chemical bonding states of the

NiO and Co₃O₄ electrode materials. In the IR spectrum of NiO (Figure 4.1(b)), the strong peak at 559 cm⁻¹ corresponds to the stretching bond of Ni-O. Additionally, the IR bands at 928, 1021, and 1211 cm⁻¹ are assigned to C-O stretching vibration which could be a result of the incorporation of carbon particles during the electrode making and absorbed atmospheric CO₂ molecules by the sample [3, 17, 18]. Similarly, the sharp bands observed at 555 and 654 cm⁻¹ in the FTIR spectrum of the Co₃O₄ material in Figure 4.1(b) are attributed to the stretching vibrations of Co-O where Co is tetrahedrally and octahedrally coordinated to oxygen respectively [19].

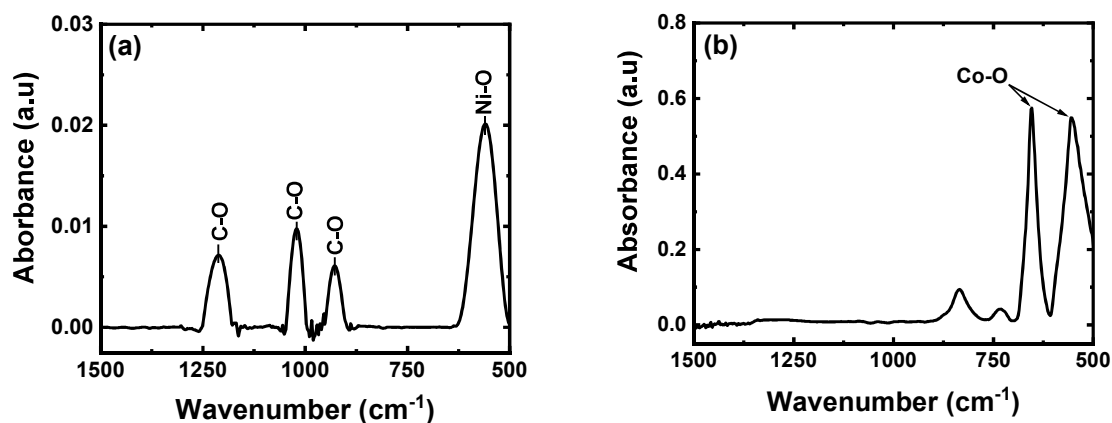


Figure 4.1. FTIR spectra of (a) NiO and (b) Co₃O₄ electrode materials on titanium (Ti) substrates

The formation of the spinel cobalt oxide (Co₃O₄) is confirmed by these absorption bands. Furthermore, the peaks at 734 cm⁻¹ and 834 cm⁻¹ could be attributed to $\delta(\text{CO}_3)$ and $\delta(\text{OCO})$ respectively [20]. The interested absorption bands for both electrode materials fall within wavenumbers ranges that have been reported by other studies [21-25].

In addition to the oxide identification, studies have shown that the specific surface area which results from morphological features has a significant impact on the

electrochemical behavior specifically the capacitive behavior of metal oxide-based electrodes [3, 26, 27]. Hence, morphological investigations of the NiO and Co₃O₄ electrode materials have been conducted using SEM imaging and presented in Figure 4.2.

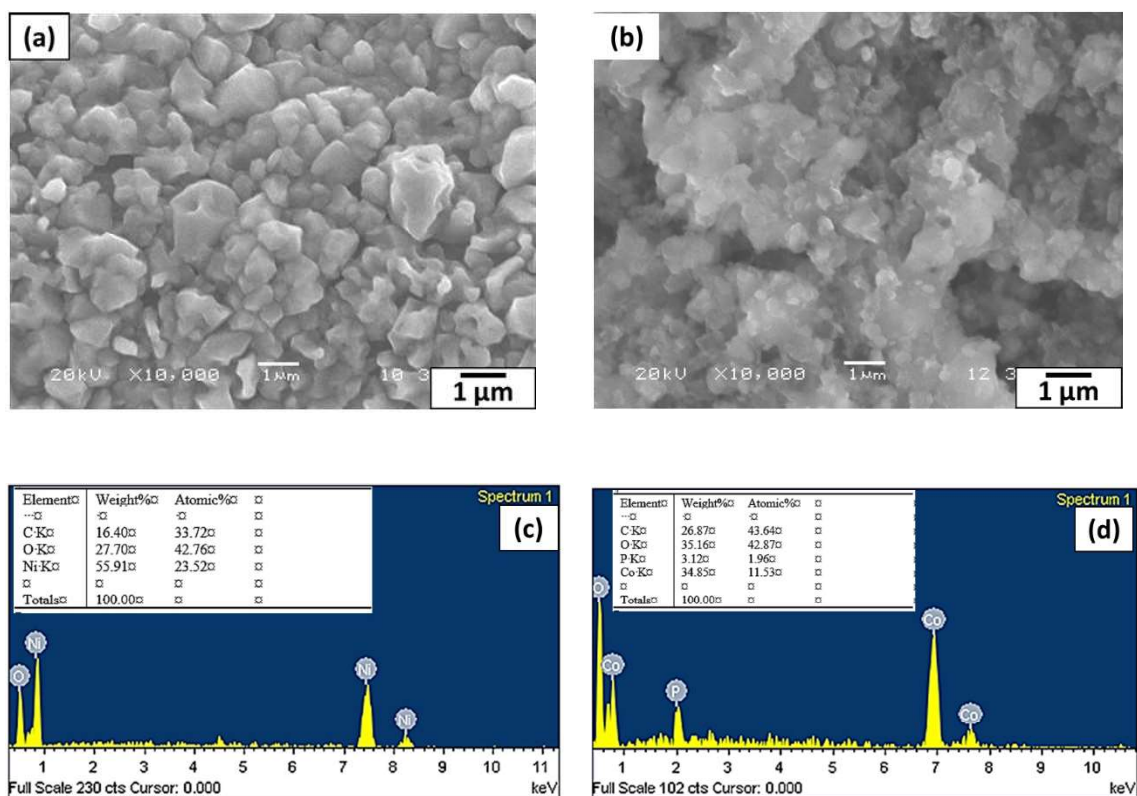


Figure 4.2. SEM micrographs and EDX images (a, c) NiO, (b, d) Co₃O₄ electrode materials on titanium substrates.

The SEM image of NiO electrode material in Figure 4.2(a) shows highly dense, well arranged, porous free irregularly shaped particles of different sizes. On the other hand in Figure 4.2(b), the Co₃O₄ electrode material shows non-uniform spherical particles agglomerated to form clusters with a ribbon-like morphology.

Furthermore, the EDX spectra collected during the SEM analysis to corroborate the FTIR spectral analysis for the presence of oxides in the electrode materials are presented in Figures 4.2 (c) and (d) for the NiO and Co₃O₄ electrode materials respectively. The presence of nickel (Ni) and oxygen (O) peaks in the EDX spectrum of the NiO electrode in Figure 4.2(c) confirms the formation of the NiO electrode material. Additionally, the peak of carbon (C) confirms the incorporation of carbon in the electrode making to increase conductivity. Similarly, in Figure 4.2(d) the peaks of cobalt (Co) and oxygen (O) further confirm the formation of the cobalt oxide material with the presence of C belonging to the carbon used in the electrode making. The EDX studies show a higher concentration of oxygen in both materials which could as a result of the surface adsorbed oxygen due to the hydrophilic nature of the surface [17].

4.3.2 Electrochemical analysis

The electrochemical performance of the NiO and Co₃O₄ electrodes as potential supercapacitor electrodes was investigated by conducting cyclic voltammetry (CV) and charge-discharge measurements (Figure 4.3). The cyclic voltammetry curves of the NiO and Co₃O₄ electrodes in Figures 4.3(a) and (c) respectively at different scan rates show a deviation from the ideal rectangular shape of Electrical double-layer capacitor electrode materials and the presence of redox peaks indicating the charge storage is mainly due to faradaic redox reactions of both electrodes [9, 28, 29]. The possible redox reactions occurring on the surface of NiO and Co₃O₄ are expressed in equations (4.1) for the NiO electrode, and equations (4.2) and (4.3) for the Co₃O₄ electrode [3, 8, 9]. In addition, it can be observed that with the

increase in scan rate, the magnitude of the current increased accordingly and this is a result of the increase in the rate of diffusion compared to the rate of reaction.

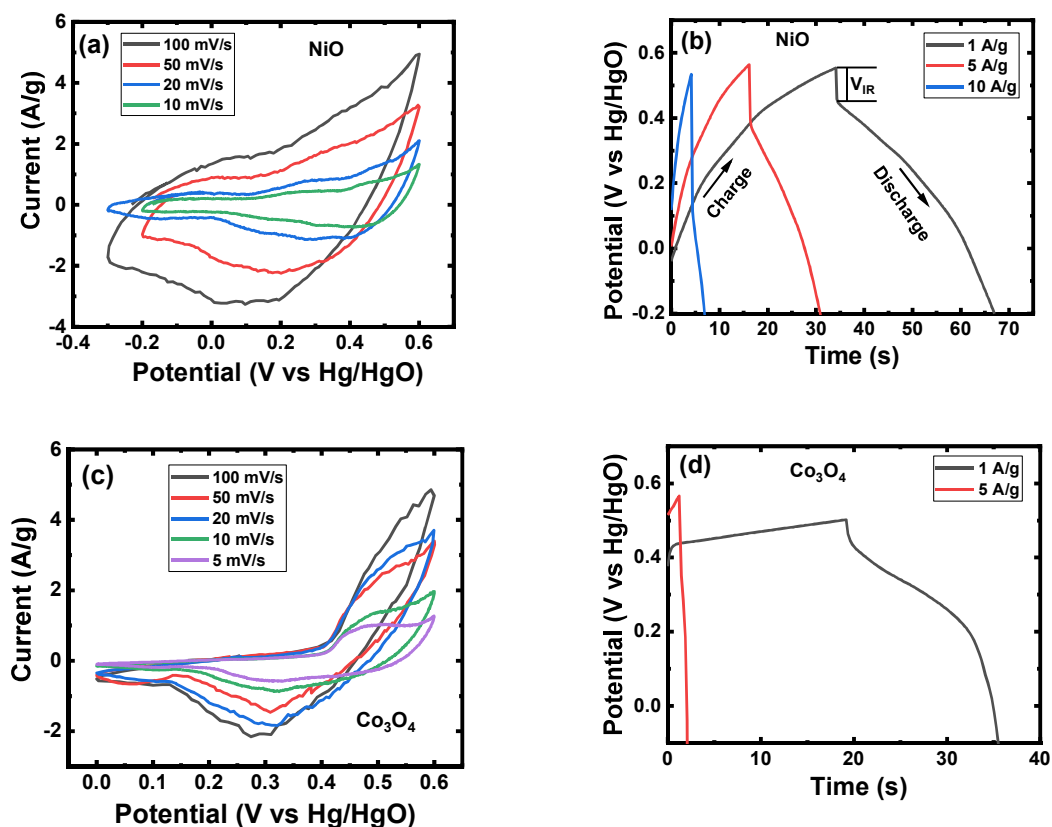
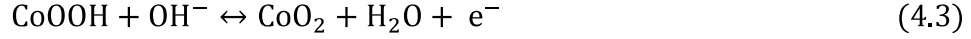
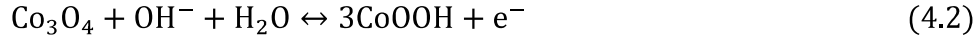


Figure 4.3 (a,c) Cyclic voltammetry (CV) curves of NiO and Co₃O₄ on titanium (Ti) substrate electrodes at different scan rates respectively (b,d) Galvanostatic charge-discharge (GCD) curves of NiO and Co₃O₄ on Ti substrate electrodes at different specific currents respectively.

More electrolyte ions (OH⁻) gain access to the electrode-electrolyte interface though very few ions engage in the charge transfer reaction. Hence, the current at a higher scan rate increases [30, 31].



Subsequently, the galvanostatic charge-discharge (GCD) studies presented in Figures 4.3 (b) and (d) were further used to assess the capacitive performance of the NiO and Co₃O₄ electrodes. The shape of both NiO and Co₃O₄ deviated from the triangular shape of EDLC materials, further corroborating the faradaic redox reaction charge storage as suggested by the CV studies [32]. From the GCD profiles, the specific capacitance of the NiO and Co₃O₄ electrodes were estimated as 40 and 28 F/g for the electrodes respectively at 1 A/g using equation (4.4):

$$C = \frac{I\Delta t}{m\Delta V} \quad (4.4)$$

where C denotes the specific capacitance, I is the specific current, Δt signifies the discharge time, m is the mass of the electroactive material, and ΔV is the potential change during discharge. The obtained specific capacitance values are lower compared to recent values published for NiO and Co₃O₄ based-electrodes [33-36]. For example, a specific capacitance value of 132 F/g has been obtained by Dhas *et al.* for their NiO nanoparticles prepared by a hydrothermal method on a carbon cloth substrate [17]. Similarly, Yadav *et al.* reported a specific capacitance value of 127 F/g for their Co₃O₄ nanowires electrode prepared via a

chemical bath deposition route on stainless steel substrate [9]. In addition, it is to be noted that both electrodes exhibit a large potential drop between the charge and discharge curves, indicating poor conductivity.

The inferior capacitance performance exhibited by the NiO and Co₃O₄ electrodes could be attributed to porous free agglomerated morphology which impedes the electrolyte access to electroactive sites thereby leading to less surface area utilization and hence reduced redox reactions for charge storage. Furthermore, the high mass loading of the active materials NiO(12.2 mg) and Co₃O₄(17.5 mg) due to the inability to control mass during the conventional electrode fabrication process may contribute to poor performance. A thicker mass loading prevents the electrolyte ions from accessing all the inner electroactive surface areas of the electrode, therefore capacitance value reduces [12, 37].

4.4 Conclusions

NiO and Co₃O₄ electrode materials on titanium substrates have been prepared through a facile chemical precipitation route. The chemical signature of the electrodes has been confirmed by the presence of NiO and Co₃O₄ absorption bands and strong peaks of Ni, Co, and O on the FTIR and EDX spectra. The SEM micrographs have revealed highly porous-free, irregular, and aggregated morphological features, unfortunately not attaining the critical standard of contributing to large specific surface areas. The NiO and Co₃O₄ electrodes obtained maximum specific capacitance values of 40 and 28 F/g.

In parallel to the chemical precipitation synthesis, electrode materials were prepared by electrodeposition and they show promising properties, hence the subsequent chapters of this thesis are predominantly focused on nanostructured electrode materials engineered through electrodeposition synthesis.

4.5 References

- [1] X.-h. Xia, J.-p. Tu, Y.-q. Zhang, Y.-j. Mai, X.-l. Wang, C.-d. Gu, X.-b. Zhao, Freestanding Co_3O_4 nanowire array for high performance supercapacitors, *RSC Adv.*, 2 (2012).
- [2] C. Wang, Y. Meng, L. Wang, F. Zhu, Y. Zhang, One Step Hydrothermal Synthesis of Flower-shaped Co_3O_4 Nanorods on Nickel Foam as Supercapacitor Materials and Their Excellent Electrochemical Performance, *Chemical Research in Chinese Universities*, 34 (2018) 882-886.
- [3] P. Lamba, P. Singh, P. Singh, P. Singh, Bharti, A. Kumar, M. Gupta, Y. Kumar, Recent advancements in supercapacitors based on different electrode materials: Classifications, synthesis methods and comparative performance, *J. Energy Storage*, 48 (2022).
- [4] W. Yang, Z. Gao, J. Ma, J. Wang, B. Wang, L. Liu, Effects of solvent on the morphology of nanostructured Co_3O_4 and its application for high-performance supercapacitors, *Electrochim. Acta*, 112 (2013) 378-385.
- [5] Y. Zhang, J. Wang, H. Wei, J. Hao, J. Mu, P. Cao, J. Wang, S. Zhao, Hydrothermal synthesis of hierarchical mesoporous NiO nanourchins and their supercapacitor application, *Mater. Lett.*, 162 (2016) 67-70.
- [6] Z. S. Iro, A Brief Review on Electrode Materials for Supercapacitor, *Int. J. Electrochem.*, (2016) 10628-10643.
- [7] K.R.M.a.M.E.-S. Farrukh Iqbal Dar, Morphology and property control of NiO nanostructures for supercapacitor applications, *Nanoscale Research Letters*, 8 (2013) 363.
- [8] Z. Yang, F. Xu, W. Zhang, Z. Mei, B. Pei, X. Zhu, Controllable preparation of multishelled NiO hollow nanospheres via layer-by-layer self-assembly for supercapacitor application, *J. Power Sources*, 246 (2014) 24-31.
- [9] A.A. Yadav, Y.M. Hunge, S.B. Kulkarni, Chemical synthesis of Co_3O_4 nanowires for symmetric supercapacitor device, *J. Mater. Sci.: Mater. Electron*, 29 (2018) 16401-16409.
- [10] H. Che, A. Liu, Hierarchical Co_3O_4 nanoflowers assembled from nanosheets: facile synthesis and their application in supercapacitors, *J. Mater. Sci.: Mater. Electron*, 26 (2015) 4097-4104.
- [11] T. Meng, P.-P. Ma, J.-L. Chang, Z.-H. Wang, T.-Z. Ren, The Electrochemical Capacitive Behaviors of NiO Nanoparticles, *Electrochim. Acta*, 125 (2014) 586-592.

- [12] P. Forouzandeh, P. Ganguly, R. Dahiya, S.C. Pillai, Supercapacitor electrode fabrication through chemical and physical routes, *J. Power Sources*, 519 (2022).
- [13] D. Majumdar, M. Mandal, S.K. Bhattacharya, Journey from supercapacitors to supercapatteries: recent advancements in electrochemical energy storage systems, *Emergent Materials*, 3 (2020) 347-367.
- [14] J.W. Lang, L.B. Kong, W.J. Wu, Y.C. Luo, L. Kang, Facile approach to prepare loose-packed NiO nano-flakes materials for supercapacitors, *Chem Commun (Camb)*, (2008) 4213-4215.
- [15] D.V. Leontyeva, I.N. Leontyev, M.V. Avramenko, Y.I. Yuzyuk, Y.A. Kukushkina, N.V. Smirnova, Electrochemical dispersion as a simple and effective technique toward preparation of NiO based nanocomposite for supercapacitor application, *Electrochim. Acta*, 114 (2013) 356-362.
- [16] P.E. Lokhande, U.S. Chavan, A. Pandey, Materials and Fabrication Methods for Electrochemical Supercapacitors: Overview, *Electrochemical Energy Reviews*, 3 (2019) 155-186.
- [17] S.D. Dhas, P.S. Maldar, M.D. Patil, A.B. Nagare, M.R. Waikar, R.G. Sonkawade, A.V. Moholkar, Synthesis of NiO nanoparticles for supercapacitor application as an efficient electrode material, *Vacuum*, 181 (2020).
- [18] S.T. Navale, V.V. Mali, S.A. Pawar, R.S. Mane, M. Naushad, F.J. Stadler, V.B. Patil, Electrochemical supercapacitor development based on electrodeposited nickel oxide film, *RSC Adv.*, 5 (2015) 51961-51965.
- [19] M. Khalaj, A. Sedghi, H.N. Miankushki, S.Z. Golkhatmi, Synthesis of novel graphene/Co₃O₄/polypyrrole ternary nanocomposites as electrochemically enhanced supercapacitor electrodes, *Energy*, 188 (2019).
- [20] Y. Wang, Y. Lei, J. Li, L. Gu, H. Yuan, D. Xiao, Synthesis of 3D-nanonet hollow structured Co₃O₄ for high capacity supercapacitor, *ACS Appl. Mater. Interfaces*, 6 (2014) 6739-6747.
- [21] S. Raj, S.K. Srivastava, P. Kar, P. Roy, In situ growth of Co₃O₄ nanoflakes on reduced graphene oxide-wrapped Ni-foam as high performance asymmetric supercapacitor, *Electrochim. Acta*, 302 (2019) 327-337.
- [22] C.I. Priyadharsini, G. Marimuthu, T. Pazhanivel, P.M. Anbarasan, V. Aroulmoji, V. Siva, L. Mohana, Sol-Gel synthesis of Co₃O₄ nanoparticles as an electrode material for supercapacitor applications, *Journal of Sol-Gel Science and Technology*, 96 (2020) 416-422.
- [23] S.A. Pawar, D.S. Patil, J.C. Shin, Hexagonal sheets of Co₃O₄ and Co₃O₄-Ag for high-performance electrochemical supercapacitors, *J. Ind. Eng. Chem*, 54 (2017) 162-173.
- [24] M. Khalaj, S.Z. Golkhatmi, A. Sedghi, High-performance supercapacitor electrode materials based on chemical co-precipitation synthesis of nickel oxide (NiO)/cobalt oxide (Co₃O₄)-intercalated graphene nanosheets binary nanocomposites, *Diamond and Related Materials*, 114 (2021).
- [25] Y. Ghalmi, F. Habelhames, A. Sayah, A. Bahloul, B. Nessark, M. Shalabi, J.M. Nunzi, Capacitance performance of NiO thin films synthesized by direct and pulse potentiostatic methods, *Ionics*, 25 (2019) 6025-6033.
- [26] A. Muzaffar, M.B. Ahamed, K. Deshmukh, J. Thirumalai, A review on recent advances in hybrid supercapacitors: Design, fabrication and applications, *Renewable and Sustainable Energy Reviews*, 101 (2019) 123-145.
- [27] G. Wang, L. Zhang, J. Zhang, A review of electrode materials for electrochemical supercapacitors, *Chemical Society reviews*, 41 (2012) 797-828.

- [28] S. Chatterjee, S.K. Bhattacharya, A review of NiO based composite electrode materials for electrochemical energy storage, IOP Conference Series: Materials Science and Engineering, 1080 (2021).
- [29] N.K. Yetim, Hydrothermal synthesis of Co_3O_4 with different morphology: Investigation of magnetic and electrochemical properties, Journal of Molecular Structure, 1226 (2021).
- [30] A.D. Jagadale, V.S. Kumbhar, R.N. Bulakhe, C.D. Lokhande, Influence of electrodeposition modes on the supercapacitive performance of Co_3O_4 electrodes, Energy, 64 (2014) 234-241.
- [31] F.I. Dar, K.R. Moonoswamy, M. Es-Souni, Morphology and property control of NiO nanostructures for supercapacitor applications, Nanoscale Research Letters, 8 (2013) 363.
- [32] F. Ali, N.R. Khalid, G. Nabi, A. Ul-Hamid, M. Ikram, Hydrothermal synthesis of cerium-doped Co_3O_4 nanoflakes as electrode for supercapacitor application, Int. J. Energy Res., 45 (2020) 1999-2010.
- [33] M.I.A. Abdel Maksoud, R.A. Fahim, A.E. Shalan, M. Abd Elkodous, S.O. Olojede, A.I. Osman, C. Farrell, A.a.H. Al-Muhtaseb, A.S. Awed, A.H. Ashour, D.W. Rooney, Advanced materials and technologies for supercapacitors used in energy conversion and storage: a review, Environ. Chem. Lett., 19 (2020) 375-439.
- [34] J. Zhao, Y. Tian, A. Liu, L. Song, Z. Zhao, The NiO electrode materials in electrochemical capacitor: A review, Materials Science in Semiconductor Processing, 96 (2019) 78-90.
- [35] U.K. Chime, A.C. Nkele, S. Ezugwu, A.C. Nwanya, N.M. Shinde, M. Kebede, P.M. Ejikeme, M. Maaza, F.I. Ezema, Recent progress in nickel oxide-based electrodes for high-performance supercapacitors, Current Opinion in Electrochemistry, 21 (2020) 175-181.
- [36] X. Wang, A. Hu, C. Meng, C. Wu, S. Yang, X. Hong, Recent Advance in Co_3O_4 and Co_3O_4 -Containing Electrode Materials for High-Performance Supercapacitors, Molecules, 25 (2020) 269.
- [37] R. Paulose, R. Mohan, V. Parihar, Nanostructured nickel oxide and its electrochemical behaviour—A brief review, Nano-Structures & Nano-Objects, 11 (2017) 102-111.

CHAPTER 5: PULSED REVERSE POTENTIAL ELECTRODEPOSITION OF CARBON-FREE Ni-NiO NANOCOMPOSITE THIN FILM ELECTRODE FOR ENERGY STORAGE SUPERCAPACITOR ELECTRODES

Rania Afia Nuamah, Saleema Noormohammed, Dilip Kumar Sarkar

Department of Applied Science, University of Quebec at Chicoutimi, Aluminum Research
Center-REGAL, Chicoutimi, Quebec, G7H 2B1, Canada

This article has been published in:

Coatings 11, 7 (2021) 780

5.1 Abstract

A combined cyclic voltammetry and pulse reverse potential electrodeposition technique has been used to synthesize carbon-free Ni-NiO nanocomposite thin film supercapacitor electrode. The structural and morphological analyses have revealed the presence of crystalline phases of both Ni and NiO in the form of nanospheres of size ~ 50 nm. The electrochemical analysis of the Ni-NiO nanocomposite electrode has shown a remarkable performance by delivering a high specific capacitance of 2000 Fg^{-1} at an applied current load of 1 Ag^{-1} and capacitance retention of 98.6 %, after over 800 cycles under a high current load of 20 Ag^{-1} .

5.2 Introduction

Supercapacitors (SCs) have received much attention as important energy storage devices in recent times as a result of their high-power densities and longer cycle life compared to batteries, and high energy densities compared to dielectric capacitors [1]. Based on their charge storage mechanism, SCs can be classified as electric double-layer capacitors (EDLCs) or pseudocapacitors (PCs). PCs are known to provide higher specific capacitance and energy density than EDLCs due to the multiple oxidation states of their electroactive materials, which favor fast faradaic reactions [2-4]. Transition metal oxides such as NiO [1], RuO₂ [3], Co₃O₄ [5], and MnO₂ [4] are mainly used as PC electrode materials. Among them, NiO has received much attention in the past few years because of its low cost, environmental friendliness, and high theoretical specific capacitance (2573 F/g) [1]. Nanostructured NiO coatings have also been found to be useful in other types of applications such as the one recently reported by Yu-Ling Hsieh *et al.* in bio-applications [6].

In this work, we report a novel approach of electrodeposition technique that combines the modes of cyclic voltammetry (CV) and pulse reverse potential (PRP) to deposit carbon-free conducting Ni-NiO nanocomposite thin film supercapacitor on a chemically inert conducting Ti- substrate.

5.3 Experimental Section

The carbon-free Ni-NiO nanocomposite thin film was deposited on Ti-substrate by CV in a potential range of -1.4 to +1.0 V vs Ag/AgCl at a scan rate of 20 mVs⁻¹ for 2 cycles, followed by pulse reverse potential (PRP) of 60 cycles of width of 1 s for the duration of 60 s. The minimum and the maximum pulse heights were chosen to be -1.4 V and +1 V, respectively. The details of this deposition mechanism can be found in the supplementary data in Figure S5.1. The electrolyte solutions, namely, 0.1 M NiSO₄·6H₂O and 0.2 M NaClO₄·H₂O with a pH of 4.5 were used for the deposition of the Ni-NiO nanocomposite thin film. The deposition process was conducted in a standard three-electrode glass cell with a platinum wire, Ti-substrate, and Ag/AgCl as the counter, working, and reference electrodes, respectively. After electrodeposition, the as-prepared carbon-free Ni-NiO nanocomposite thin film electrode was rinsed in deionized water and dried on a hot plate at 100° C for 10 hrs in air before performing physical and electrochemical tests.

The morphological and elemental analyses of the carbon-free Ni-NiO nanocomposite thin film were studied by a scanning electron microscope (SEM, JEOL JSM-6480 LV), equipped with the function of energy-dispersive X-ray spectroscopy (EDX). The X-ray diffraction (XRD) analyses were carried out by Bruker D8 Discover system. The electrochemical properties (cyclic voltammetry (CV), and galvanostatic charge-discharge (GCD) were evaluated using Solartron SI1287 electrochemical workstation in a 1 M KOH aqueous solution.

5.4 Results and discussion

5.4.1 Structural, morphological, and chemical analysis

Figure 5.1(a) shows the XRD spectrum of the carbon-free Ni-NiO nanocomposite thin film deposited on a Ti-substrate and the inset shows the deconvoluted peak observed around 44.5° . The diffraction spectrum shows two small peaks at (111) and (200) at 2θ of 37.2° and 43.2° , respectively, can be assigned to cubic NiO structure with lattice constant $a = 4.1717 \text{ \AA}$ corresponding well with the standard crystallographic data for NiO (JCPDS Card: # 65-5745). The deconvoluted peak in the inset shows the presence of metallic Ni(111) peak at 2θ of 44.5° . The truncated peaks corresponding to Ti are assigned by an asterisk (*) symbol in the main graph. The Ti peak has also been labeled as B in the inset. The calculated mean crystallite sizes of NiO and Ni using Scherrer's equation are found to be 7 nm and 5 nm, respectively. The broad and low-intensity XRD peaks of Ni and NiO can be attributed to the amorphous nature and the small size of the Ni and NiO nanostructures [7, 8]. Similar small size of NiO crystallites of 5.6 nm has been reported by Atalay et al on NiO nanostructures deposited by chemical precipitation onto fungi substrates [8]. The distribution of the small nanosize crystallites of Ni and NiO in the composite thin film can contribute to the large specific surface area [9].

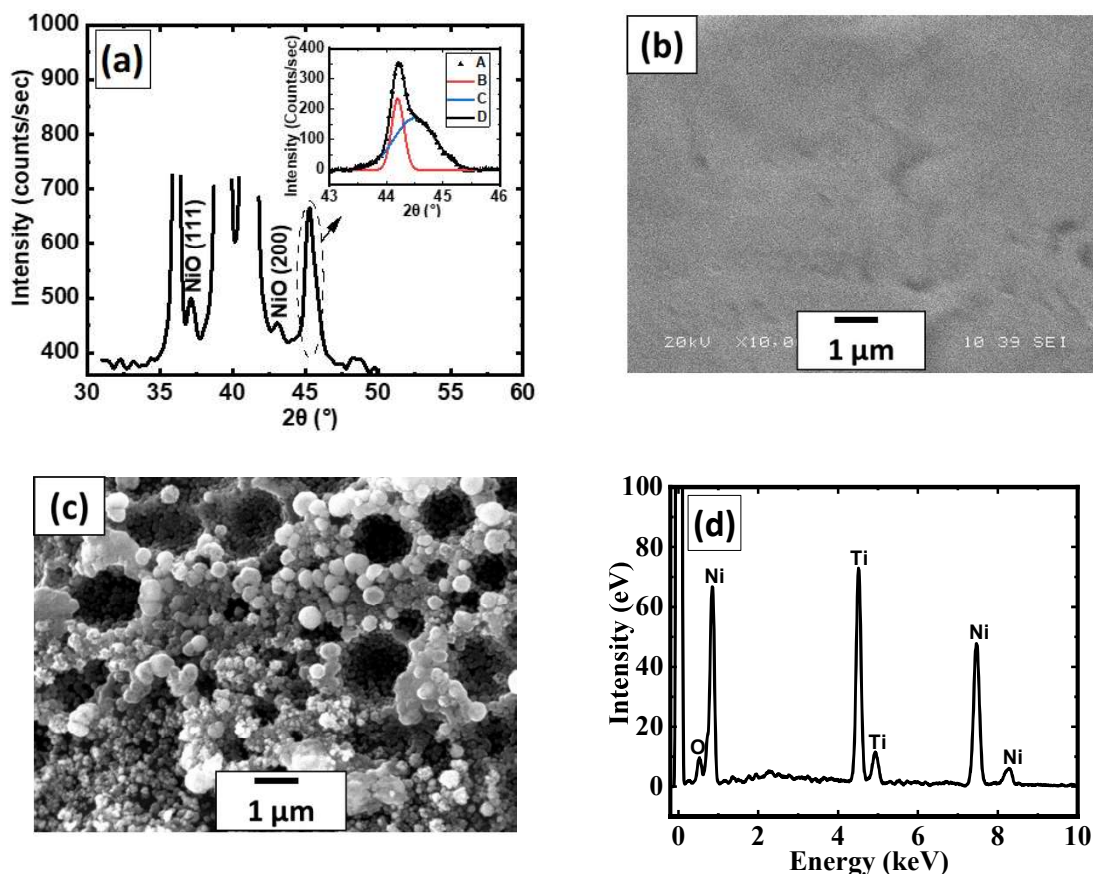


Figure 5.1. (a) XRD spectrum of the carbon-free Ni-NiO nanocomposite thin film on Ti-substrate. Table 200. C-fitted peak of Ni (111), D-smoothened data, (b, c) SEM images of Ti-substrate and carbon-free Ni-NiO nanocomposite thin film (d) EDX spectrum corresponding to Figure 1 (c).

Figure 5.1(b) shows the SEM image of the Ti substrate presenting a smooth surface. However, the SEM image in Figure 5.1(c) shows the morphology of the as-deposited carbon-free Ni-NiO composite thin film revealing a porous interconnected nanospherical structure. Figure 5.1(c), confirms a uniform distribution of loosely packed nanospherical particles with an average size of ~ 50 nm, randomly deposited within and between the pores indicating complete deposition coverage. The particle size (~ 50 nm) distribution was confirmed by

image analysis as presented in supplementary data (Figure S5.2). The EDX spectrum in Figure 5.1(d) shows the peaks of O and Ni in addition to the substrate peaks of Ti indicating the formation of NiO nanostructures with an adequate Ni/O ratio of 1.5.

5.4.2 Electrochemical measurements

The electrochemical and energy storage properties of the carbon-free Ni-NiO nanocomposite thin film electrode were studied and have been presented in Figure 5.2. The Nyquist plots and the polarization curves of Ni/NiO coating on Ti substrate as well as the Ti substrate can also be found in the Figure S5.3(a,b) of supplementary data. The CV curve of the bare Ti-substrate in Figure 5.2(a) shows a horizontal line that signifies no capacitance behavior arising from Ti-substrate. Interestingly, on the carbon-free Ni-NiO nanocomposite thin film, an oxidation peak is observed at +0.55 V, which is related to Ni oxidation state from Ni(II) to Ni(III) where NiO is oxidized to NiOOH and a reduction peak at +0.35 V is related to the reduction of NiOOH to NiO. This is a typical faradaic pseudocapacitive behavior for NiO and these reduction and oxidation peaks correspond to the reversible reaction following the redox reaction [10]:



Apart from CV, galvanostatic charge-discharge (GCD) was performed at different current densities and has been presented in Figure 5.2(b). The specific capacitances of the carbon-free Ni-NiO nanocomposite thin film electrode have been calculated to be 2000, 1820,

1770, 1640, and 1440 Fg^{-1} at the respective current densities of 1, 2, 3, 4, and 5 Ag^{-1} . These values, revealing high energy storage capacities, are much higher than previously reported values on Ni-based energy storage materials [1, 11]. For example, Joaquin *et al.* reported 755 Fg^{-1} at 1 Ag^{-1} on electrophoretic deposited core-shell nanowire arrays of Ni-NiO [12] while Navale *et al.* reported 458 Fg^{-1} at 1 Ag^{-1} corresponding to potentiostatic electrodeposited NiO thin films on stainless steel [11]. However, Farrukh *et al.* have previously reported a similar high capacitance value of 2093 F/g on their NiO nanotubes electrochemically deposited on anodized aluminum (AAO) [13]. The large specific capacitance of our carbon-free Ni-NiO composite thin film electrode may be attributable to the nanostructured morphology of the electrode composed of nanospherical structures of Ni-NiO contributing to the increased surface area as evident from the SEM images in Figure 5.1(c). Such a high surface area-oriented morphology arising from the nanospherical patterns can be responsible for the high capacitive behavior of the Ni-NiO thin film electrode. This behavior could be attributed to better accessibility of the electrolyte to the surface of the electrode to facilitate the Faradic reaction as presented in equation (4.1) [13, 14].

Figure 5.2(c) shows the long-term galvanostatic cycling performance of our Ni-NiO composite electrode. The capacitance retention of our electrode over 800 cycles at a high current density of 20 Ag^{-1} is 97.4 %. The inset of Figure 5.2(c) shows the specific capacitance performance during the last eight charge-discharge cycles.

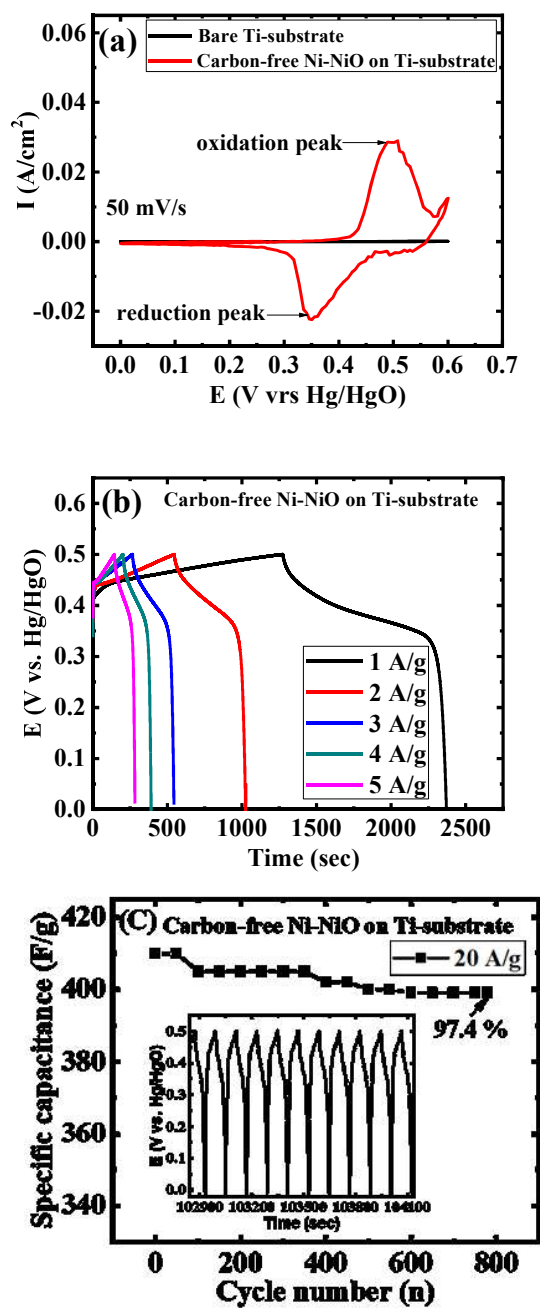


Figure 5.2. (a) CV curves of Ti-substrate and the carbon-free Ni-NiO nanocomposite thin film on Ti-substrate, (b) Charge-discharge curves of one cycle at different current densities, (c) Cycling performance after 800 cycles at 20 A/g.

5.5 Conclusions

Carbon-free Ni-NiO nanocomposite thin film supercapacitor electrode material composed of nanospherical features of size ~50 nm has been synthesized and deposited on Ti substrate surface by a simple combined cyclic voltammetry and pulse reverse electrodeposition technique. A very high specific capacitance of 2000 Fg⁻¹ at a current density of 1 Ag⁻¹ with excellent galvanostatic cycling stability over 800 cycles has been achieved on our Ni-NiO electrodes presenting great potential for a long-term supercapacitive application.

5.6 References

- [1] L. Gu, Y. Wang, R. Lu, L. Guan, X. Peng, J. Sha, Anodic electrodeposition of a porous nickel oxide–hydroxide film on passivated nickel foam for supercapacitors, *J. Mater. Chem. A*, 2 (2014) 7161-7164.
- [2] S.H. Lee, H. Lee, M.S. Cho, J.-D. Nam, Y. Lee, Morphology and composition control of manganese oxide by the pulse reverse electrodeposition technique for high performance supercapacitors, *J. Mater. Chem. A*, 1 (2013) 14606.
- [3] D. Majumdar, M. Mandal, S.K. Bhattacharya, Journey from supercapacitors to supercapatteries: recent advancements in electrochemical energy storage systems, *Emergent Materials*, 3 (2020) 347-367.
- [4] Rusi, S.R. Majid, Effects of Electrodeposition Mode and Deposition Cycle on the Electrochemical Performance of MnO₂-NiO Composite Electrodes for High-Energy-Density Supercapacitors, *PLoS one*, 11 (2016) e0154566.
- [5] I.G. Casella, Electrodeposition of cobalt oxide films from carbonate solutions containing Co(II)–tartrate complexes, *J. Electroanal. Chem.*, 520 119–125.
- [6] Y.-L. Hsieh, C.-W. Chen, W.-H. Lin, B.-R. Li, Construction of the nickel oxide nanocoral structure on microscope slides for total self-assembly-oriented probe immobilization and signal enhancement, *ACS Applied Bio Materials*, 3 (2020) 3304-3312.
- [7] S. Ci, Z. Wen, Y. Qian, S. Mao, S. Cui, J. Chen, NiO-Microflower Formed by Nanowire-weaving Nanosheets with Interconnected Ni-network Decoration as Supercapacitor Electrode, *Sci Rep*, 5 (2015) 11919.

- [8] F.E. Atalay, D. Asma, H. Kaya, A. Bingol, P. Yaya, Synthesis of NiO Nanostructures Using Cladosporium Cladosporioides Fungi for Energy Storage Applications, *Nanomaterials and Nanotechnology*, 6 (2016) 28.
- [9] Y. Ghalmi, F. Habelhames, A. Sayah, A. Bahloul, B. Nessark, M. Shalabi, J.M. Nunzi, Capacitance performance of NiO thin films synthesized by direct and pulse potentiostatic methods, *Ionics*, 25 (2019) 6025-6033.
- [10] Š. Trafela, J. Zavašnik, S. Šturm, K.Ž. Rožman, Formation of a Ni(OH)₂/NiOOH active redox couple on nickel nanowires for formaldehyde detection in alkaline media, *Electrochim. Acta*, 309 (2019) 346-353.
- [11] S.T. Navale, V.V. Mali, S.A. Pawar, R.S. Mane, M. Naushad, F.J. Stadler, V.B. Patil, Electrochemical supercapacitor development based on electrodeposited nickel oxide film, *RSC Adv.*, 5 (2015) 51961-51965.
- [12] J. Yus, B. Ferrari, A. Sanchez-Herencia, A. Caballero, J. Morales, Z. Gonzalez, In Situ Synthesis and Electrophoretic Deposition of NiO/Ni Core-Shell Nanoparticles and Its Application as Pseudocapacitor, *Coatings*, 7 (2017).
- [13] K.R.M.a.M.E.-S. Farrukh Iqbal Dar, Morphology and property control of NiO nanostructures for supercapacitor applications, *Nanoscale Research Letters*, 8 (2013) 363.
- [14] X. Yan, X. Tong, J. Wang, C. Gong, M. Zhang, L. Liang, Construction of three-dimensional porous nano-Ni/NiO nanoflake composite film for electrochemical energy storage, *Mater. Lett.*, 106 (2013) 250-253.

5.7 Supporting Information

(a) Published supporting information (*Nuamah, R.A.; Noormohammed, S.; Sarkar,*

D.K. Pulsed Reverse Potential Electrodeposition of Carbon-Free Ni/NiO Nanocomposite

Thin Film Electrode for Energy Storage Supercapacitor Electrodes. Coatings 2021, 11, 78)

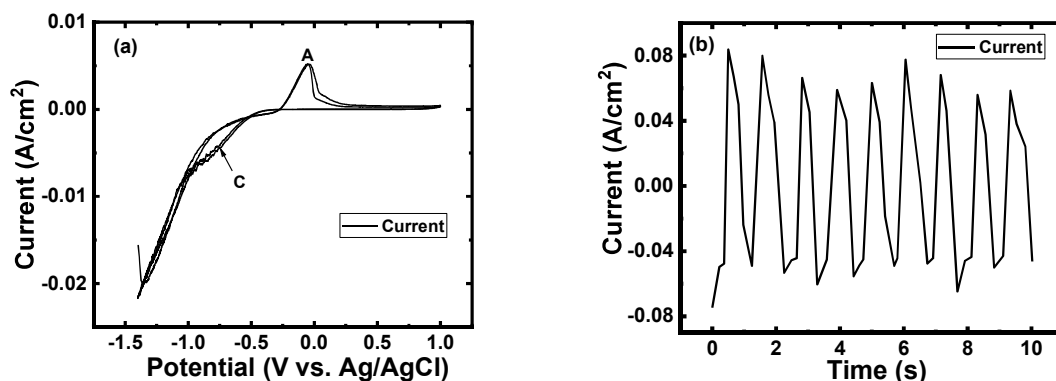


Figure S5.1. Deposition profiles of carbon-free Ni-NiO nanocomposite thin film on Ti-substrate: (a) Cyclic voltammetry (CV) followed by (b) Pulse reverse potential (PRP).

The electrochemical impedance spectroscopy measurement was performed in the frequency range of 100 kHz to 10 mHz for both electrodes in a 1M KOH electrolyte. The Nyquist plots, shown in Figure S4.3(a) demonstrate a large semi-circle corresponding to the Ti substrate. The Ni/NiO coating on Ti substrate, however, is found to have been merged in the lower resistance zone close to zero. The inset of Figure S5.3(a) shows the Nyquist plot of Ni/NiO coating on the Ti substrate. The nature of this plot distinctly shows the capacitive behavior of the coating as compared to the pure resistive behavior of the pristine Ti substrate.

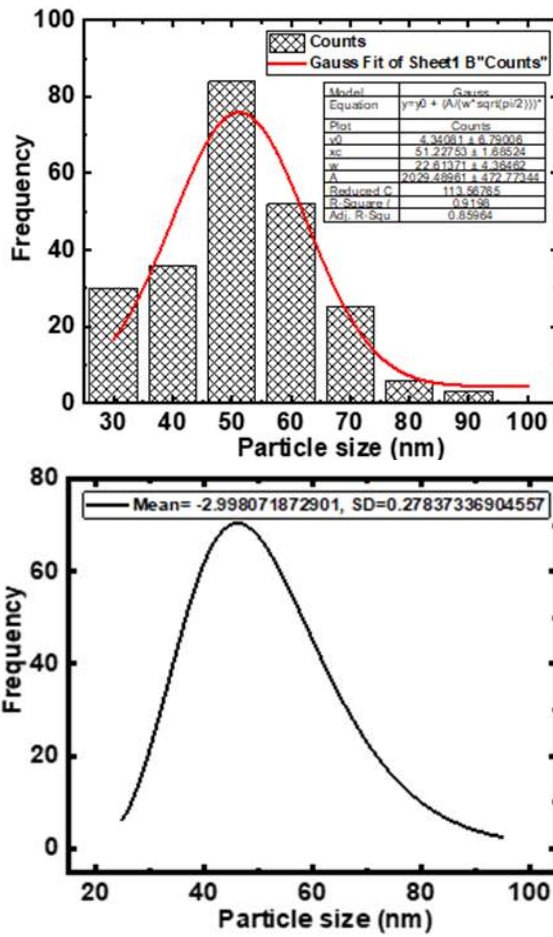
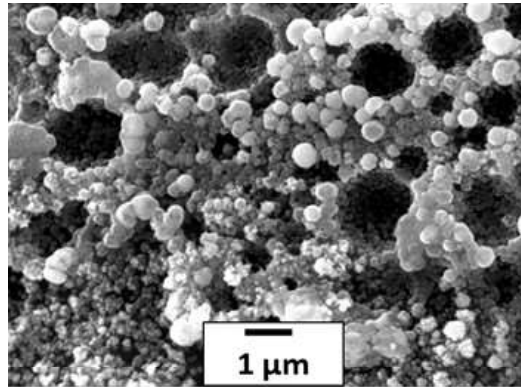


Figure S5.2. (a) SEM image (b & c) Particle size distribution of the Carbon-free Ni-NiO nanocomposite thin film on Ti-substrate.

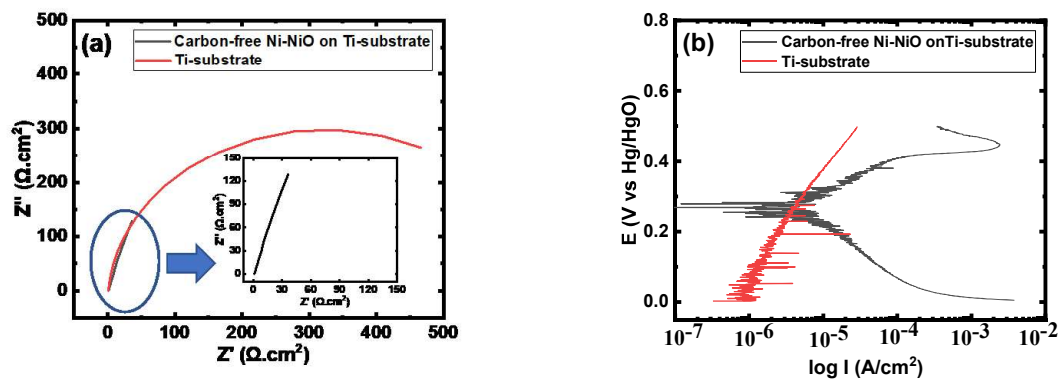


Figure S5.3. (a) Nyquist plots and (b) polarization curves of Ni/NiO coating on Ti substrate and pristine Ti substrate (Inset shows the Nyquist plot of Ni/NiO coating on Ti).

Figure S5.3(b) shows the polarization curves of the Ti substrate and the Ni/NiO coated Ti substrate, in the potential range of 0 to 0.5 V. This potential range was chosen as the CV and charge-discharge experiments were performed in the same range.

(b) Unpublished Supporting Information

The TEM image of the Carbon-free Ni-NiO composite thin film in Figure S5.4 further confirms the porous nanospherical features of the film as observed in the SEM analysis. Also, the multilayered nature of the film is depicted by the image. This confirms the earlier hypothesis of creating multilayers of Ni and NiO with the pulse reverse potential deposition process to enhance the specific surface area.

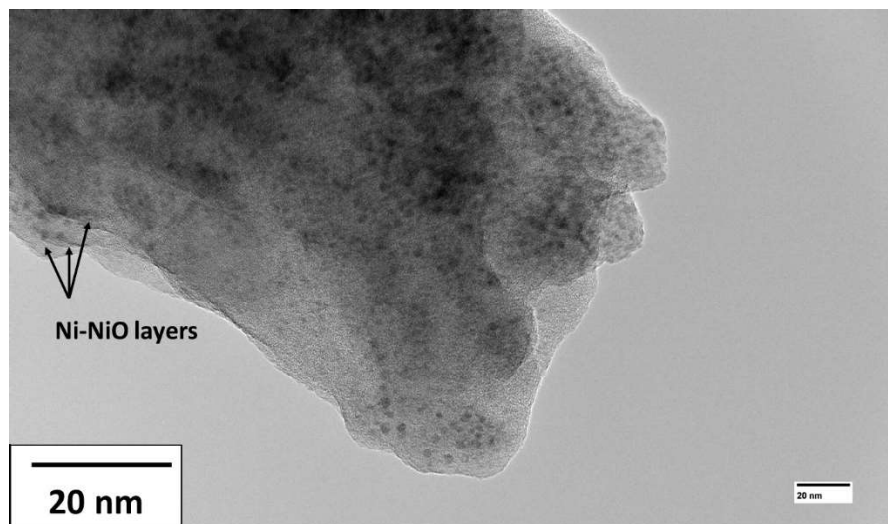


Figure S5.4. TEM image of the Carbon-free Ni-NiO nanocomposite thin film

As part of the optimization process for the synthesis of the Carbon Ni-NiO nanocomposite thin film, the time for the pulse reverse potential electrodeposition process was varied to obtain the optimum specific capacitance (Figure S5.5). The specific capacitance generally decreased with the increase in deposition time with the maximum specific capacitance achieved at 1 min.

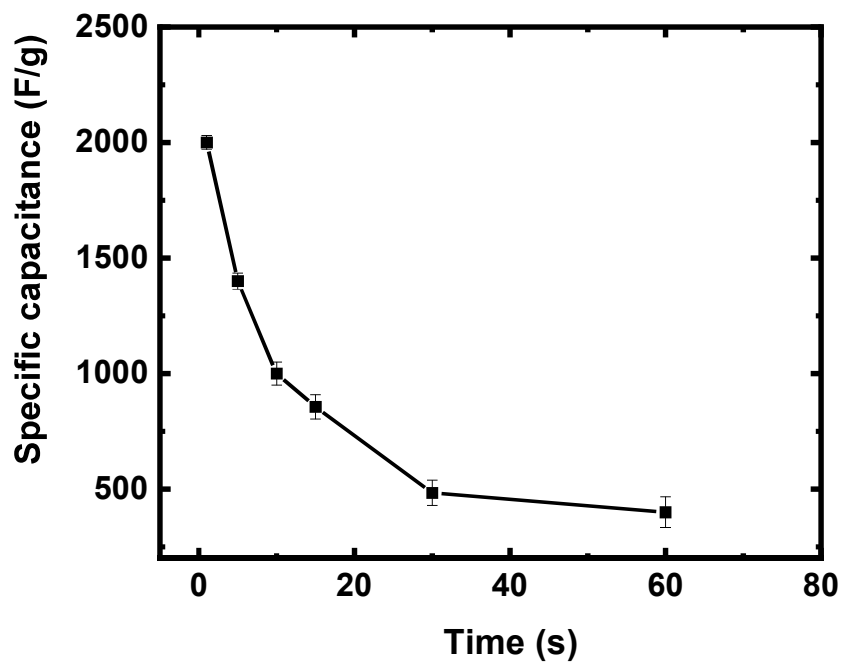


Figure S5.5. Specific capacitance variation with pulse reverse potential (PRP) deposition time of the Carbon-free Ni-NiO nanocomposite thin film on Ti substrate electrode.

CHAPTER 6: EFFECT OF MOLAR RATIO MODULATION OF COBALT PRECURSORS ON SUPERCAPACITOR BEHAVIOR OF ENGINEERED Co- Co₃O₄ NANOCOMPOSITE ELECTRODES

Rania Afia Nuamah, Saleema Noormohammed, Dilip Kumar Sarkar

Department of Applied Science, University of Quebec at Chicoutimi, Aluminum Research
Center-REGAL, Chicoutimi, Quebec, G7H 2B1, Canada

This article has been published in:

ACS Applied Engineering Materials 1, 1 (2023), 241-251

6.1 Abstract

Nanostructured Co-Co₃O₄ composite thin films deposited on nickel foam (NF) using combined cyclic voltammetry (CV) and pulse reverse potential (CV PRP) modes of electrodeposition from an electrolyte composed of CoCl₂ and Co(CH₃COO)₂ precursor salt solutions with varied molar ratios demonstrated a dependency of the supercapacitance performance over the precursor components' molar ratios. The specific capacitance and their retention were found to increase with increasing CoCl₂ in the electrolyte with a starting value of 791 F/g at an applied current load of 1A/g for a molar ratio of Co(CH₃COO)₂:CoCl₂ of 100:0. High specific capacitance (2580 F/g) and large retention (90.5%) were obtained at a critical molar ratio of Co(CH₃COO)₂:CoCl₂ of 20:80. However, with 100% CoCl₂ in the electrolyte, the specific capacitance lowered to 460 /g with poor retention of only 60%.

Crystallinity and morphological features driven by the electrolyte concentration with molar variations of the deposited films have been found to influence the specific capacitance performance. The degree of crystallinity, and the presence of Co and Co₃O₄ phases for the different molar ratios have been revealed by X-ray diffraction (XRD) studies. The diverse morphological features obtained by the scanning electron microscope (SEM) and the varying quantities of Co and O in the Co-Co₃O₄ nanocomposite thin films as confirmed by energy-dispersive X-ray spectroscopy (EDX) spectra correlate well with the electrochemical performance. The phase composition was further confirmed by the presence of Co-O bonds via the attenuated total reflection–Fourier transform infrared (ATR–FTIR) spectra obtained on these films.

6.2 Introduction

Supercapacitors (SCs) have drawn much attention in the past few decades as green energy storage devices owing to their important properties such as high-power density, lightweight, easy and safe operation, fast charge-discharge rates, and long cycle stability. Due to their excellent properties, they are used in portable electronics such as smart watches, mobile phones, laptops, and low-emission hybrid vehicles [1-4]. In the operations of SCs, one of the critical components is the electrode material as it drives the performance and energy of SCs [5]. Transition metal oxides (TMOs) consisting of NiO, RuO₂, Co₃O₄, and Vn₂O₅ have been extensively studied as promising SC electrodes among the different electrode materials including carbon materials (graphene, activated carbon, carbon nanotubes), conducting polymers (polypyrrole, polyaniline) as a result of their higher specific

capacitance and high energy density in contrast to carbon materials and their high chemical stability in contrast to conducting polymers [6-8]. Among this array of TMOs, Co_3O_4 which is a base which TMO with a high theoretical capacitance of 3560 F/g, low cost, and environmentally benign has shown promising potential for substituting noble TMOs such as RuO_2 which although are ideal pseudocapacitive electrode materials, however, are expensive and toxic [9-12]. Furthermore, Co_3O_4 -based materials have been widely explored in other applications such as catalysts for oxygen evolution, gas sensors, and biosensors due to their high electrochemical activity and multiple oxidation states [13-15].

However, despite its high theoretical capacitance, the practical utilization of Co_3O_4 as an electrode material is still hindered due to limited surface area for effective redox reactions resulting in lower experimental specific capacitance values in contrast to the theoretical capacitance, poor reversibility, poor conductivity, and poor rate capability at higher current density [4, 16, 17]. Reports from various studies have shown that the structure, morphology, and microscopic dimensions of Co_3O_4 can be easily tuned by controlling the preparative parameters of the fabrication method used [18-20]. This is a very critical step in supercapacitor performance as the electrochemical performance specifically the specific capacitance of Co_3O_4 strongly relies on the surface area, morphology, and size distribution contributing to an improvement in the active surface area by facilitating electron and ion transport in the material [21, 22]. Hence, Co_3O_4 with morphological characteristics in the nanosized range can substantially lead to tunable specific surface area in enhancing the experimental specific capacitance values.

So far, a myriad of techniques including chemical precipitation, sol-gel, hydrothermal, chemical bath deposition, spray pyrolysis, direct magnetron sputtering and electrodeposition

have been explored to develop nanostructured Co_3O_4 materials [23-27]. Among these deposition techniques, the electrodeposition method is found to be a simple, low temperature, and cost-effective technique for growing well-adhered Co_3O_4 nanostructures with desired morphological features and composition directly onto conductive substrates without the use of binders and conductive additives. Furthermore, in electrodeposition, factors such as the composition of the electrolyte, type of electrodeposition mode, and duration of the process can be regulated to achieve the desired morphology and texture including, nanoplates, nanoflowers, nanosheets, and nanotubes [5, 23, 24, 28, 29]. Subsequently, previous studies have reported a variation in morphological features, microstructure, and corresponding electrochemical performance of Co_3O_4 materials when different types of cobalt precursor salts namely, cobalt chloride, cobalt acetate, cobalt sulfate, and cobalt nitrate are used [21, 30, 31]. However, our present study is the first to date where we have attempted to tune the morphological features and correlate the electrochemical behavior of the Co_3O_4 electrode nanocomposite thin films, by varying the molar concentrations of the cobalt salt solutions, namely the cobalt acetate and cobalt chloride, in the electrolyte and selecting the appropriate electrodeposition mode to deposit the electrode thin films.

In this present work, Co- Co_3O_4 nanocomposite thin films on nickel foam (NF) substrate electrodes have been prepared from an electrolyte solution consisting of both cobalt acetate $\text{Co}(\text{CH}_3\text{COO})_2$ and cobalt chloride (CoCl_2) salts, represented at Ac and Cl respectively, using a combined cyclic voltammetry and pulse reverse potential (CV PRP) modes of electrodeposition. The molar ratio of the cobalt precursors (Ac:Cl) has been varied (100:0, 80:20, 50:50, 20:80, and 0:100) and a critical molar ratio of the cobalt precursors providing Co- Co_3O_4 nanocomposites with the highest specific capacitance and stability

attained. The structural, compositional, and morphological studies present a correlation with the electrochemical characteristics, specifically the cyclic voltammetry (CV), electrochemical impedance spectroscopy (EIS), and galvanic charge-discharge (GCD) cycles. The precursor with 20 (Ac):80 (Cl) molar ratio precursor resulted in the deposition of Co-Co₃O₄ nanocomposite thin film presenting a superior capacitance of 2580 F/g and stable cycling performance.

6.3 Experimental section

The Co-Co₃O₄ nanocomposite thin films were deposited on nickel foam (NF) substrate by electrodeposition using cyclic voltammetry (CV) in a potential range of -1.4 to +1.0 V vs Ag/AgCl at a scan rate of 20 mVs⁻¹ for 2 cycles, followed by pulse reverse potential (PRP) of 60 cycles of the width of 1 s for the duration of 60 s. The minimum and the maximum pulse heights were chosen to be -1.4 V and +1 V, respectively. The electrolyte solutions used for the electrodeposition consist of a combined solution of 0.1 M cobalt acetate Co(CH₃COO)₂ represented as Ac and 0.1 M cobalt chloride (CoCl₂) represented as Cl in different molar ratios together with 0.2 M NaClO₄.H₂O as described in Table 6.1. Before the electrodeposition process, the nickel foam was etched in 3 M HCl for 15 min and washed in turn with deionized water and ethanol for 10 min. The deposition process was conducted in a standard three-electrode glass cell with a platinum wire, NF substrate, and Ag/AgCl as the counter, working, and reference electrodes, respectively. After the electrodeposition process, the as-prepared Co-Co₃O₄ nanocomposite thin film electrodes were rinsed in deionized water and dried on a hot plate at 200 °C for 45 minutes in air before performing characterization

and electrochemical tests. For physical characterization by XRD, a separate set of samples was prepared by depositing the thin films on titanium (Ti) substrate.

A scanning electron microscope (SEM, JEOL JSM-6480 LV), equipped with energy-dispersive X-ray spectroscopy (EDX) was used to conduct the morphological and elemental studies of the electrodeposited thin films. A Bruker D8 Discover system was used for crystallographic analysis. The confirmation and quantification of the deposition of the metal oxide (Co-O) were conducted using an attenuated total reflection – Fourier transform infrared spectroscopy (ATR-FTIR, Agilent Technologies Cary 630). The electrochemical properties, consisting of cyclic voltammetry (CV), galvanostatic charge-discharge (GCD), and electrochemical impedance spectroscopy (EIS) characteristics were assessed using a three-electrode glass cell and Solartron SI1287 electrochemical workstation with 1 M KOH aqueous electrolyte.

The as-synthesized Co-Co₃O₄ nanocomposite thin films on NF substrate of the various molar ratios were employed directly as working electrodes, with platinum wire and Hg/HgO as counter and reference electrodes respectively. The CV and GCD measurements were carried out at different scan rates and specific currents in a potential window of 0 to 0.6 V and -0.1 to 0.5 V respectively. In addition, the EIS measurement was conducted in a frequency range from 10 mHz to 100 kHz.

Table 6.1: Summary of electrodeposition electrolyte solutions consisting of different molar ratios of cobalt acetate $\text{Co}(\text{CH}_3\text{COO})_2$ and cobalt chloride (CoCl_2).

Identification	Molar ratio of Ac:Cl	$\text{Co}(\text{CH}_3\text{COO})_2$ (ml)	CoCl_2 (ml)	NaClO_4(ml)
100Ac0Cl	100:0	30	0	30
80Ac20Cl	80:20	24	6	30
60Ac40Cl	60:40	18	12	30
50Ac50Cl	50:50	15	15	30
40Ac60Cl	40:60	12	18	30
30Ac70Cl	30:70	9	21	30
20Ac80Cl	20:80	6	24	30
15Ac85Cl	15:85	4.5	25.5	30
10Ac90Cl	10:90	3	27	30
0Ac100Cl	0:100	0	100	30

* $\text{Co}(\text{CH}_3\text{COO})_2$ - Ac, * CoCl_2 - Cl

6.4 Results and discussion

6.4.1 Structural, morphological, and chemical analysis

The XRD patterns of the Co-Co₃O₄ nanocomposite thin films prepared by the molar ratios of 100Ac0Cl, 80Ac20Cl, 50Ac50Cl, 20Ac80Cl, and 0Ac100Cl on titanium (Ti) substrate are shown in Figure 6.1 (A). The XRD spectra of all the molar ratios show Co (100) and Co (101) planes of the hexagonal crystal structure of cobalt corresponding to the JCPDS card No-00-005-0727 at 2θ angles of 41.7° and 47.5°, respectively. Similarly, the Co₃O₄ (222) and Co₃O₄ (400) planes of the cubic crystal structure of Co₃O₄ (JCPDS card No-42-1467) can be detected at 2θ positions of 38.5° and 44.5°, respectively in all the cases. These peak positions assigned to Co₃O₄ are also in agreement with those reported by Gaikar *et al.* on their Co₃O₄ electrodes synthesized by the chemical deposition method in presence of different cobalt precursors [28] in addition to those reported by Ali *et al.* on their Ce-doped Co₃O₄ nanoflakes prepared by a facile hydrothermal technique [32]. Cheng *et al.* have also reported peak similar peak positions for their porous Co₃O₄ prepared by a chemical precipitation route [31]. In addition to the peaks of Co and Co₃O₄, the peaks originating from the Ti substrate are located at 2θ values 34.4°, 40.2°, and 53.0°.

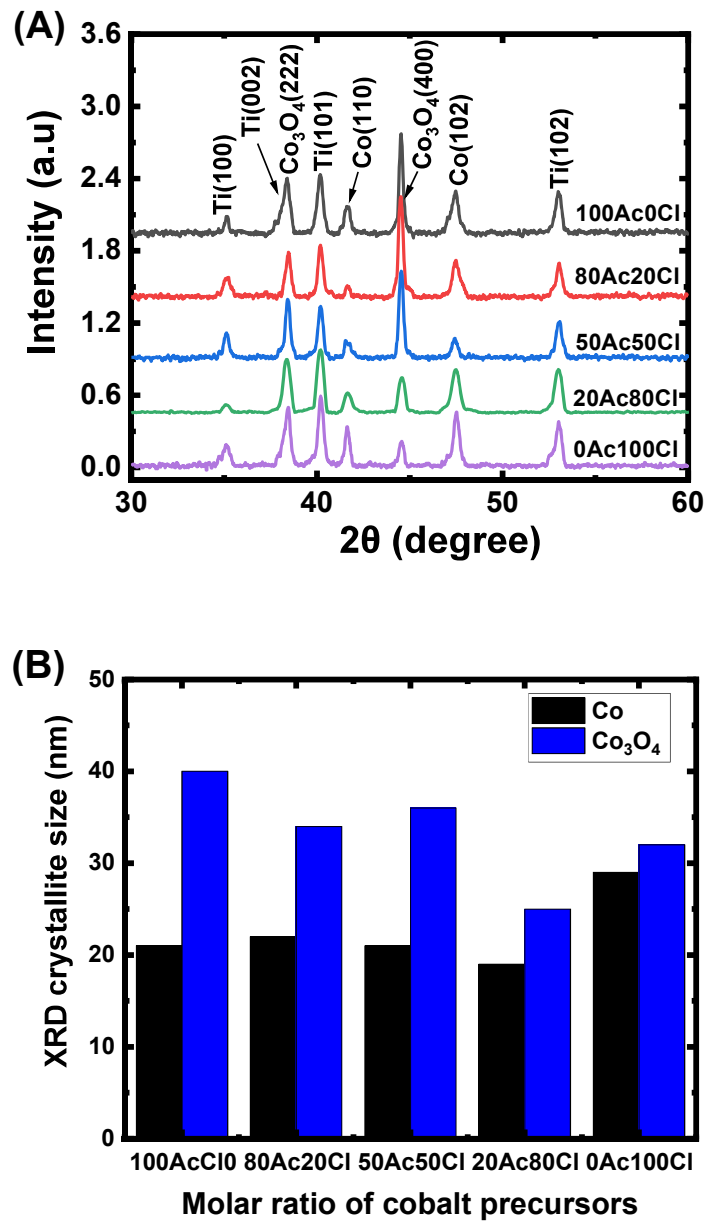


Figure 6.1. (A) XRD patterns collected on titanium (Ti) substrate, (B) XRD crystallites size analysis, and (C) $\text{Co}_3\text{O}_4/\text{Co}$ XRD peak intensity ratio analysis of $\text{Co}-\text{Co}_3\text{O}_4$ nanocomposite thin films prepared by the molar ratio variation of cobalt acetate and cobalt chloride precursors (represented as cobalt acetate (Ac) and cobalt chloride (Cl)).

These peaks are assigned to the Ti (100), Ti (002), and Ti (101) planes of the hexagonal crystal structure of titanium (JCPDS card No-00-005-0682).

The crystallite size analyses of the Co (100), Co (101), and Co₃O₄ (400) planes for the Co-Co₃O₄ thin film composites prepared by the different molar ratios of cobalt acetate and cobalt chloride were estimated by Scherrer's formula in equation (6.1).

$$D = \frac{0.94\lambda}{\beta \cos\theta} \quad (6.1)$$

where 'D' is crystallite size, 'β' is full width at half maxima, 'λ' is the wavelength of X-ray used and 'θ' is diffraction angle [33, 34]. The average crystallite size values of Co are 21.3, 22.2, 21.7, 19.2, and 29.9 nm for 100Ac0Cl, 80Ac20Cl, 50Ac50Cl, 20Ac80Cl, and 0Ac100Cl, correspondingly, as shown in Figure 6.1(B). Also, the crystallite size of Co₃O₄ is 40.6, 34.2, 36.4, 25.2, and 32.2 nm for 100Ac0Cl, 80Ac20Cl, 50Ac50Cl, 20Ac80Cl, and 0Ac100Cl, respectively, as depicted in Figure 6.1(B). The results indicate that Co-Co₃O₄ thin film prepared with the molar ratio of 20Ac80Cl has the smallest crystallite size and may offer a high surface area for enhancing redox reactions to increase charge storage [16].

Furthermore, from the crystallite size analysis of the Co₃O₄(400) peak in Figure 6.1(B), it is observed that the addition of cobalt chloride to cobalt acetate causes the crystallite size to decrease from 40.6 nm (100Ac0Cl) to 25.2 nm (20Ac80Cl) as the chloride content increases. This could be a result of the higher ionic radius (181 pm) of the chloride anion (Cl⁻) compared to the ionic radius of 161 pm of the acetate anion (CH₃COO⁻) which restricts the growth of the acetate ions during the synthesis process. Also, generally, it can be observed from Figure 6.1(A) that the samples with higher cobalt acetate content (100Ac0Cl, 80Ac20Cl, and 50Ac50Cl) show well-defined and high Co and Co₃O₄ peak intensities which is an

indication of high crystallinity and high number of Co and Co₃O₄ atoms compared to samples with low cobalt acetate or higher cobalt chloride content (0Ac100Cl, 20Ac80Cl) which suggests that cobalt acetate precursor causes higher growth of Co-Co₃O₄ nanocomposite material. The XRD result demonstrated that although the combination of different cobalt precursors in different molar ratios does not affect the crystal structure of the final film, the degree of crystallinity is significantly impacted. Therefore, the difference in crystallinity may influence the diversity in the electrochemical properties of Co-Co₃O₄ electrode materials.

The ATR-FTIR spectroscopy recorded in the range of interest between 500 and 1000 cm⁻¹ has been used to provide information about phase composition and different chemical bonding states present in the Co-Co₃O₄ nanocomposite materials of 100Ac0Cl, 80Ac20Cl, 50Ac50Cl, 20Ac80Cl and 0Ac100Cl along with the bonding mechanism of species like oxygen with the metal ions (Figure 6.2). Characteristic peaks shown by all the electrodes at wavenumbers between 650 cm⁻¹ and 550 cm⁻¹ are indicative of the stretching vibrations of the Co-O bond in the tetrahedrally (Co²⁺-O) and octahedrally (Co³⁺-O) coordinated cobalt respectively [35]. It is to be noted that the associated bond lengths are 1.96 Å and 1.93 Å, respectively [36]. The presence of these absorption bands confirms the formation of Co₃O₄ for all the cases of films electrodeposited for the different molar ratios of cobalt acetate and cobalt chloride. The recorded wavenumbers at which these absorption bands appear are consistent with reports in the literature [37-40].

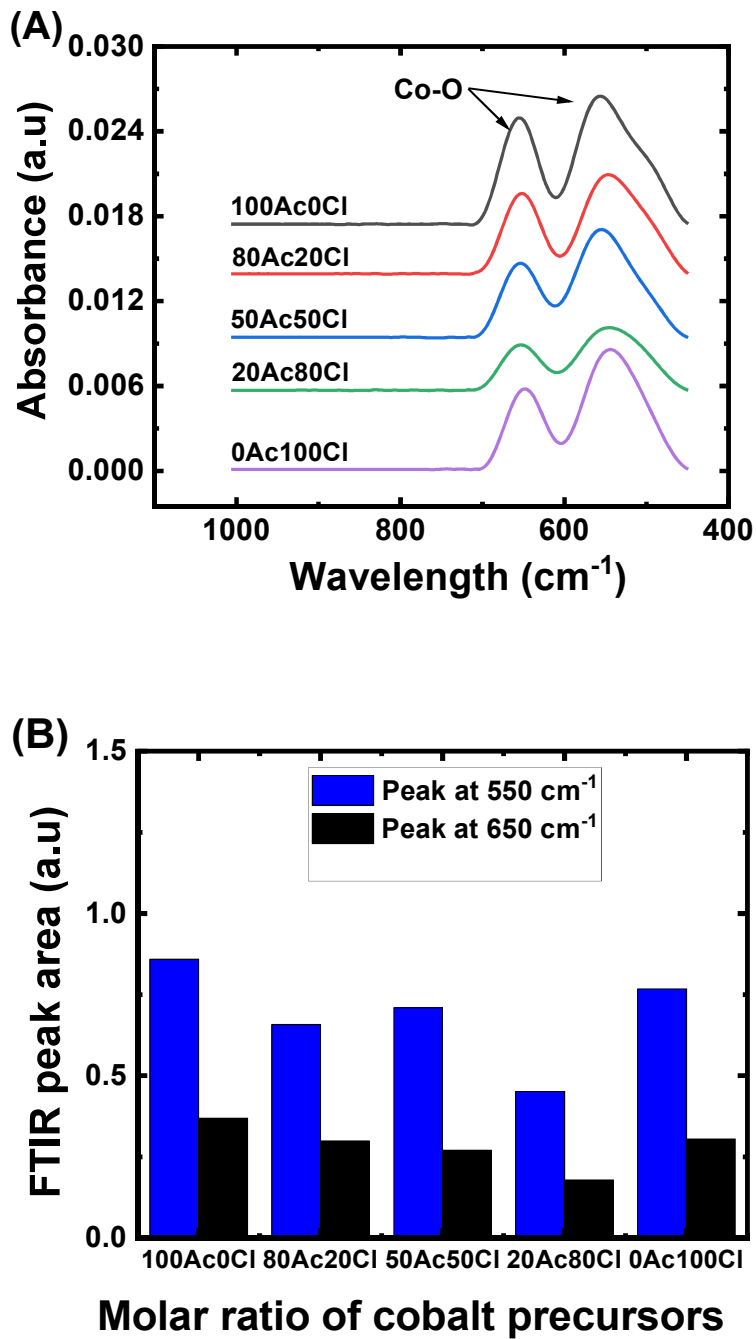


Figure 6.2. (A) ATR-FTIR spectra of nickel foam (NF) substrate, and (B) area under the two IR absorption bands at 650 cm⁻¹ and 550 cm⁻¹ of Co-Co₃O₄ nanocomposite thin films prepared by varying the molar ratios of Ac and Cl.

Although the ATR-FTIR absorption bands support the formation of Co_3O_4 for all the molar ratios of cobalt precursors studied, the intensities of these bands vary. Hence, to understand the oxide peak intensities and their practicable effect on the supercapacitive characteristics of these nanocomposite thin films, the area under the observed characteristic peaks of Co_3O_4 has been investigated and presented in Figure 6.2(B). The area under the peak for the pristine precursors (100Ac0Cl and 0Ac100Cl) is found to be higher than those with the combination of both in varying quantities.

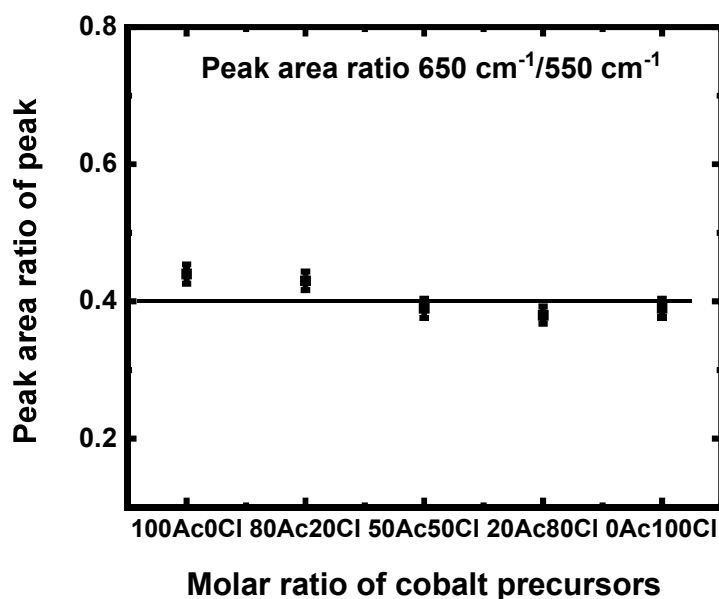


Figure 6.3. Graph of the ratio of the two IR absorption bands at 650 cm^{-1} and 550 cm^{-1} of the Co- Co_3O_4 nanocomposite thin films prepared by varying the molar ratios of Ac and Cl.

The 20Ac80Cl presents the least peak areas due to low growth of material as complemented by the XRD peak analysis. It can, therefore, be expected that the specific capacitance can

vary due to variations in the oxide intensities revealed by the FTIR peak area analysis. On the other hand, the ratio of the area of the two interested bands in Figure 6.3 for all the cases is approximately ~ 0.4 which confirms that the same phase of Co_3O_4 oxide material was formed in all the molar ratios despite the variations in their intensities.

In addition to oxides identification and quantification, reports in the literature have demonstrated that the specific surface area which results from the final morphology has a significant impact on the electrochemical performance of Co_3O_4 -based electrode materials [5, 41, 42]. Therefore, the morphologies of the Co- Co_3O_4 nanocomposite thin films on NF obtained from the different molar ratios of cobalt precursors have been obtained by SEM imaging and presented in Figure 6.4. When pristine cobalt acetate (100Ac0Cl) was used as a precursor, a morphology of dense nanoflakes partly self-assembled into large flower-like structures is observed as evident in Figure 6.4(A). In Figure 6.4(B), complete growth of the large flower-like structures observed in Figure 6.4(A) is observed with some agglomeration over the NF surface when a combination of 20 % of cobalt chloride and 80 % cobalt acetate (80Ac20Cl) was used as the precursor. On the other hand, when an equal amount of cobalt chloride and cobalt acetate (50Ac50Cl) was used, the large flower-like structures are transformed into small homogenous cotton ball-like features with well-defined shapes as shown in Figure 6.4(C). Further, the morphological features are transformed into highly porous interconnected nanoflake morphology with homogeneously distributed flower-like structures with a precursor containing 80 % cobalt chloride and 20 % cobalt acetate (20Ac80Cl) as revealed in Figure 6.4(D).

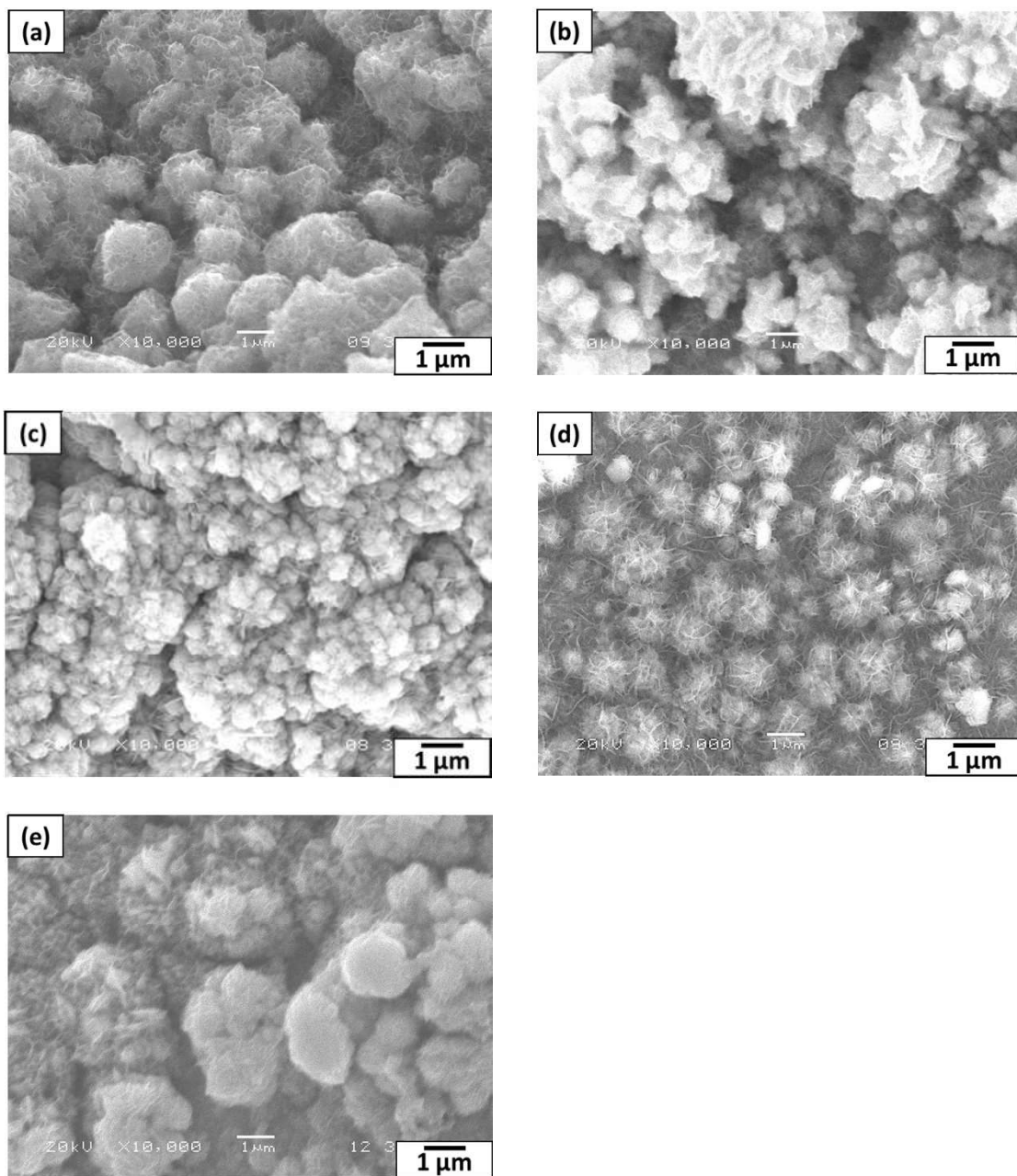


Figure 6.4. SEM micrographs of the as-synthesized Co-Co₃O₄ nanocomposite thin films on NF substrate prepared by the different molar ratios of cobalt precursors (a) 100Ac0Cl, (b) 80Ac20Cl, (c) 50Ac50Cl, (d) 20Ac80Cl and (e) 0Ac100Cl respectively.

The morphological features of the 20Ac80Cl Co-Co₃O₄ nanocomposite thin film is expected to provide an enhanced active surface area favorable for efficient intercalation of electrolyte ions, ultimately enhancing the electrochemical performance [3, 5]. Conversely, when pristine

cobalt chloride (0Ac100Cl) was used as a precursor, dense, non-homogenous, and highly agglomerated flowerlike structures cover the surface of the NF substrate as observed in Figure 6.4(E). Morphological features similar to that of our Co-Co₃O₄ thin films have been reported previously by Waghmode *et al.* for their NiCo₂O₄ thin films prepared by chemical bath deposition using different cobalt precursors [5]. The morphological analysis further supports the idea that the type of cobalt precursor and their different molar ratios when combined, influence variations in size, shape, and morphological features of the final electrodeposited Co-Co₃O₄ nanocomposite films.

Furthermore, the EDX spectra (Figure 6.5) for all the molar ratios used in the Co-Co₃O₄ thin film deposition were also collected as a complementary analysis to the FTIR spectral analysis for the confirmation of the presence of oxide on these films. All the elements of interest were traced on the EDX spectra, including O, Co, and Ni, where Ni originates from the NF substrate. The presence of O in all the thin films confirms the oxide formation on the electrodeposited thin film surfaces. The O/Co atomic ratio extracted from EDX quantification for 100Ac0Cl, 80Ac20Cl, 50Ac50Cl, 20Ac80Cl, and 0Ac100Cl are found to be 1.1, 1.4, 1.5, 2.3, and 1.8, respectively, which are in a close agreement with the stoichiometry of Co₃O₄ as supported by other studies [17, 43]. The film deposited using Ac20Cl80 precursor shows comparably a higher O/Co ratio indicating that this film may provide a higher specific capacitance value.

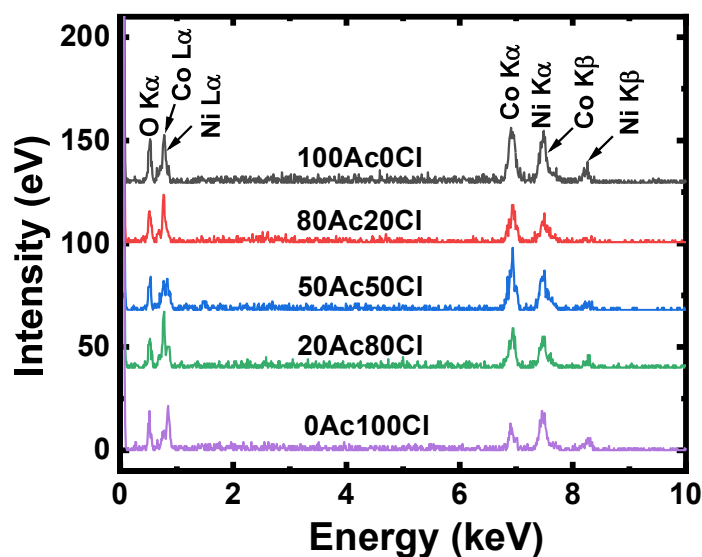
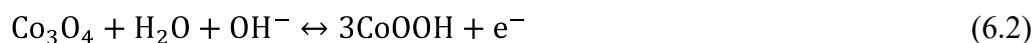


Figure 6.5. EDX spectra of Co-Co₃O₄ nanocomposite thin films deposited on NF substrate using precursors with varied molar concentrations of Ac (100 % to 0 %) and Cl (0 % to 100 %).

6.4.2 Electrochemical measurements

To assess the effect of cobalt precursor molar ratio on the electrochemical properties of the nanocomposite thin films as potential electrode materials for supercapacitor energy storage applications, cyclic voltammetry (CV), galvanostatic charge-discharge (GCD), and the electrochemical impedance studies of the electrodes have been performed. Figure 6.6(A) shows the CV curves of the four types of Co-Co₃O₄ nanocomposite thin films prepared by using the molar ratios of 100Ac0Cl, 80Ac20Cl, 50Ac50Cl, 20Ac80Cl, and 0Ac100Cl of Co(CH₃COO)₂ to CoCl₂ obtained at a scan rate of 5 mV/s. The non-rectangular shape together with the presence of oxidation and reduction peaks observed for all the thin films suggests that the charge storage originates from Faraday redox reactions of battery type

characteristics [2, 44]. The redox peaks can be correlated to the redox reaction of $\text{Co}^{2+}/\text{Co}^{3+}$ and $\text{Co}^{3+}/\text{Co}^{4+}$ as shown in equations (6.2) and (6.3), respectively [18, 28, 45].



The 20Ac80Cl film electrode presents a larger area and current response of the CV curve in comparison to the other molar ratios, indicating a higher accumulation of charges, hence superior capacitive performance. Furthermore, the individual CV curves of various compositions have been provided in the Figure S6.1 of the supplementary data.

The GCD curves of the Co- Co_3O_4 nanocomposite thin films, deposited using various molar ratios of Ac and Cl, at a specific current of 1 A/g are presented in Figure 6.6(B). In addition, the individual GCD curves of the various molar ratios at different specific currents have been presented in Figure S6.2 of the supplementary data. Following the CV analysis, the nonlinear nature of the GCD curves with voltage plateaus further confirms the Faradaic reactions of battery-type behaviors [39, 43, 46]. It is to be noted that all Co- Co_3O_4 nanocomposite thin films prepared using different molar ratios of Ac and Cl do not exhibit a significant potential drop (V_{IR}) between the charge and discharge curves, indicating good conductivity. It can be seen that the thin film electrode obtained from 20Ac180Cl combination possesses longer discharge curves compared to the other molar ratios indicating higher specific capacitance for these electrodes.

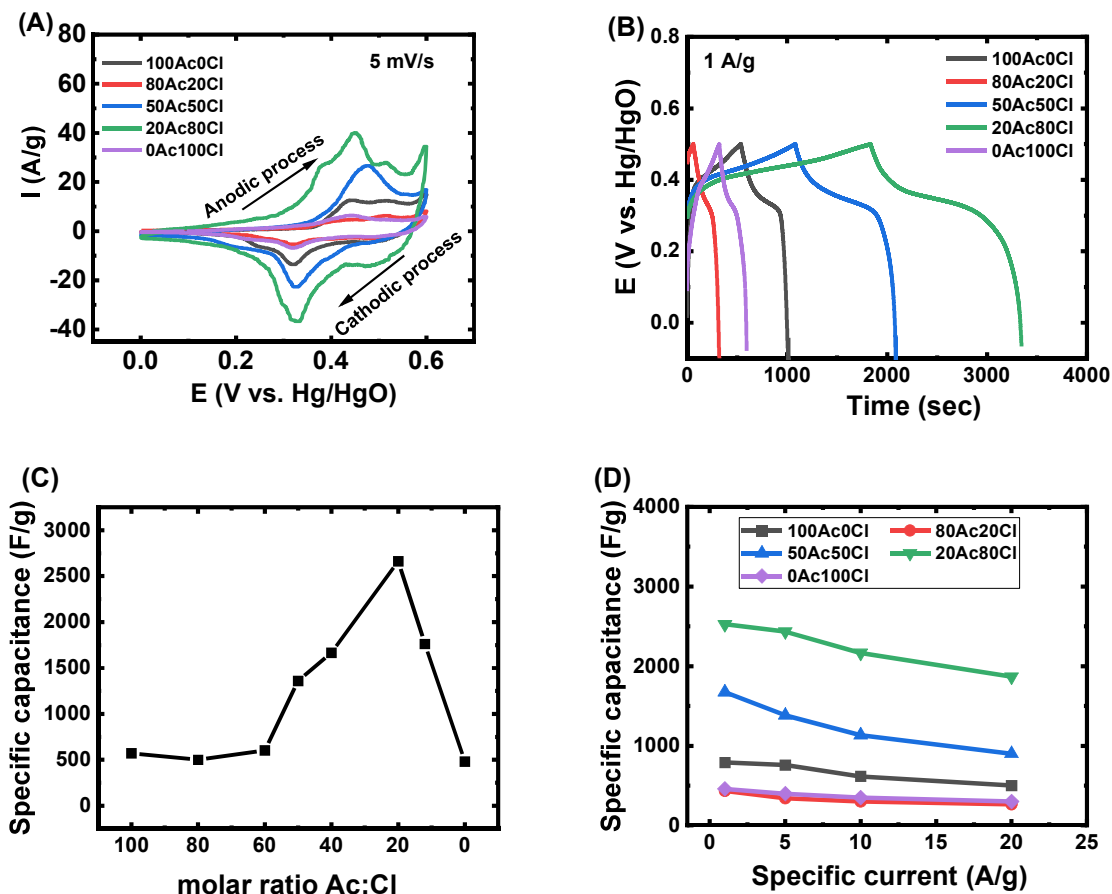


Figure 6.6 (A) Cyclic voltammety curves at 5 mV/s, (B) Charge-discharge curves at 1 A/g, (C) Optimization graph of the molar ratio variation of cobalt precursors, (D) variation of specific capacitance at the different specific current graph of Co-Co₃O₄ nanocomposite thin films deposited using 100Ac0Cl, 80Ac20Cl, 50Ac50Cl, 20Ac80Cl, and 0Ac100Cl precursors.

The specific capacitance values calculated from the charge-discharge (GCD) curves in Figure 6.6 (B) using equation (6.4) at a specific current of 1 A/g are 791, 435, 1673, 2580, and 460 F/g for 100Ac0Cl, 80Ac20Cl, 50Ac50Cl, 20Ac80Cl and 0Ac100Cl, respectively.

$$C_s = \frac{I\Delta t}{m\Delta V} \quad (6.4)$$

where C_s is the specific capacitance, I is the specific current, Δt is the discharge time, m is the electrode mass, and ΔV is the potential change during discharge. The specific capacitance value recorded for 20Ac80Cl is much higher than those reported by other studies on cobalt-based electrodes. For instance, previously Obodo *et al.* reported a specific capacitance value of 1718 F/g at 1 A/g for $\text{Co}_3\text{O}_4/\text{MnO}_2@\text{GO}$ composite electrode synthesized by a hydrothermal process [47]. Liu *et al.* also reported a specific capacitance value of 581F/g at 1 A/g on their $\text{Co}_3\text{O}_4/\text{nitrogen-doped carbon hollow spheres}$ ($\text{Co}_3\text{O}_4/\text{NHCSs}$) with hierarchical structures prepared by a hydrothermal process [48]. In a review reported by Quispe-Garrido *et al.*, much lower specific capacitance values than that obtained for the films deposited using 20Ac80Cl have been obtained by other authors on Co_3O_4 -based electrode materials prepared by various other fabrication techniques [9]. In this study, the GCD measurements were used for the quantitative analysis while the CV measurements in Figure 6.6(A) were used for qualitative understanding of the expected charge storage behavior.

Furthermore, to determine an optimized molar ratio of the cobalt precursors to achieve Co- Co_3O_4 electrode materials with enhanced specific capacitance, a graph of variation of the specific capacitance against the molar ratios of cobalt precursors has been obtained and presented in Figure 6.6(C). Lower specific capacitance values are observed for pristine cobalt acetate (100Ac0Cl) and cobalt chloride (0Ac100Cl) precursors. Introducing a mixture of the precursors in the various molar ratios caused the specific capacitance to increase. However, it can be observed that a higher content of cobalt acetate with respect to

cobalt chloride (80Ac20Cl, and 60Ac40Cl) causes a decrease in the specific capacitance due to aggregation and higher growth of material as shown in the XRD and SEM analysis in Figures 6.1 and 6.4, respectively. This higher growth and aggregation limit the electrolyte ion access to the electroactive sites thereby affecting the capacitive performance. On the other hand, a lower cobalt acetate content with respect to cobalt chloride (15Ac85Cl and 20Ac80Cl) significantly increased the specific capacitance from 460 F/g to 2580 F/g due to controlled growth which results in morphological features with enhanced active surface area for high capacitive performance.

Subsequently, the variation of the specific capacitance of the thin films deposited using Ac, 100Ac0Cl, 80Ac20Cl, 50Ac50Cl, 20Ac80Cl, and 0Ac100Cl combinations at the specific currents of 1, 5, 10, and 20 A/g have been presented in Figure 6.6(D). The specific capacitance values of all the electrodes are found to decrease with increasing specific current attributable to the slow diffusion of charges through the electrodes. At a higher specific current, the ability of electrolyte ions to saturate the bulk of the electroactive surface area becomes limited due to insufficient time, hence the Faraday redox reactions are restricted to only the surface of the material leading to the reduction in the specific capacitance. This phenomenon whereby the specific capacitance decrease when the specific current increases have been regularly observed by other authors [1, 41, 49, 50]. Most importantly, at each specific current, the specific capacitance of the electrode obtained from 20Ac80Cl precursor is higher contrary to the other electrodes indicating superior rate capability.

Such high specific capacitance of the electrode obtained from 20Ac80Cl cobalt precursor as compared to the other molar ratio combinations could be ascribed to its highly porous interconnected nanoflake morphology with homogenous flower-like structures which

provide abundant electrochemical active sites to facilitate more redox reactions and amplify their specific capacitance. In addition, its low crystallinity as studied by XRD could influence its capacitive performance. The XRD results revealed that the different molar ratios of cobalt precursors had a notable impact on the degrees of crystallinity of the final Co-Co₃O₄ nanocomposite thin films. As observed in the results of electrochemical performance, the electrode obtained from 20Ac80Cl precursor with the lowest crystallinity exhibited superior capacitive performance when compared to pristine 100Ac0Cl which presented the highest crystallinity.

Despite the importance of high specific capacitance, long-term cyclic stability is another critical requirement of electrode materials in practical applications of supercapacitors. The cycling performance of the electrodeposited thin films using precursors of 100Ac0Cl, 80Ac20Cl, 50Ac50Cl, 20Ac80Cl, and 0Ac100Cl was, therefore, assessed and is presented in Figure 6.7. The cyclic test was performed by conducting continuous charge-discharge measurements at a current load of 20 A/g for 500 cycles. The specific capacitance retention values were found to be 66.6 %, 56.4, 74.0 %, 90.5 % and 60.0 % for the electrodes obtained from 100Ac0Cl, 80Ac20Cl, 50Ac50Cl, 20Ac80Cl and 0Ac100Cl precursors, respectively, with the 20Ac80Cl combination showing a superior stability with a maximum retention of 90.5% after 500 cycles. In addition, the electrode obtained from 20Ac80Cl precursor has been cycled for 1000 cycles and its capacitance is 78.2 % as reported in our previous work on Co-Co₃O₄ electrodes [51]. Such outstanding stability is attributable to the interconnected porous morphology which promotes rapid electron transport by shortening the diffusion path and offsetting the mechanical stresses induced by volume expansion resulting from the repetitive insertion and removal of electrolyte ions [21, 28].

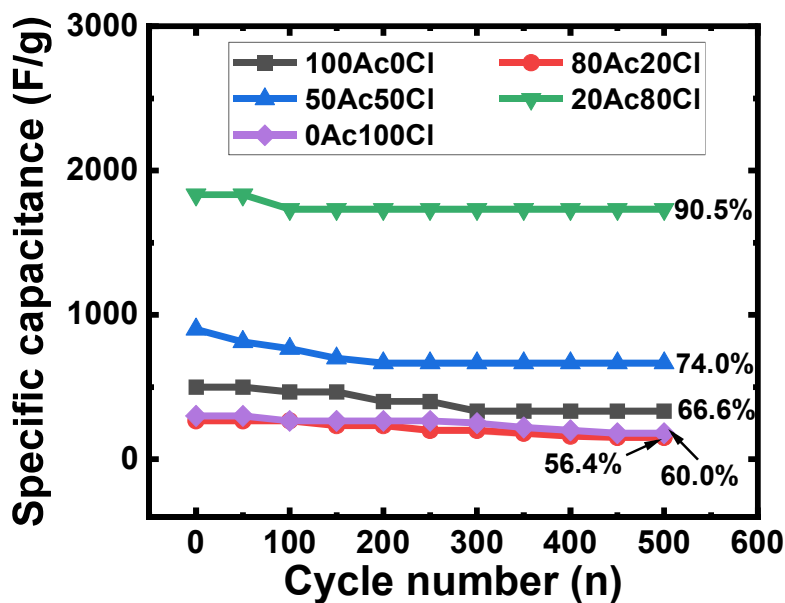


Figure 6.7. Cycling performance for 500 cycles at a specific current of 20 A/g of Co-Co₃O₄ nanocomposite thin films deposited using 100Ac0Cl, 80Ac20Cl, 50Ac50Cl, 20Ac80Cl, and 0Ac100Cl precursors.

To further investigate the electrochemical characteristics of the Co-Co₃O₄ thin film electrodes obtained from the different molar ratios of cobalt precursors, Nyquist plots (Figure 6.8) obtained from conducting electrochemical impedance spectroscopy (EIS) in a frequency range from 10 mHz to 100 kHz were used to investigate the charge transport resistance.

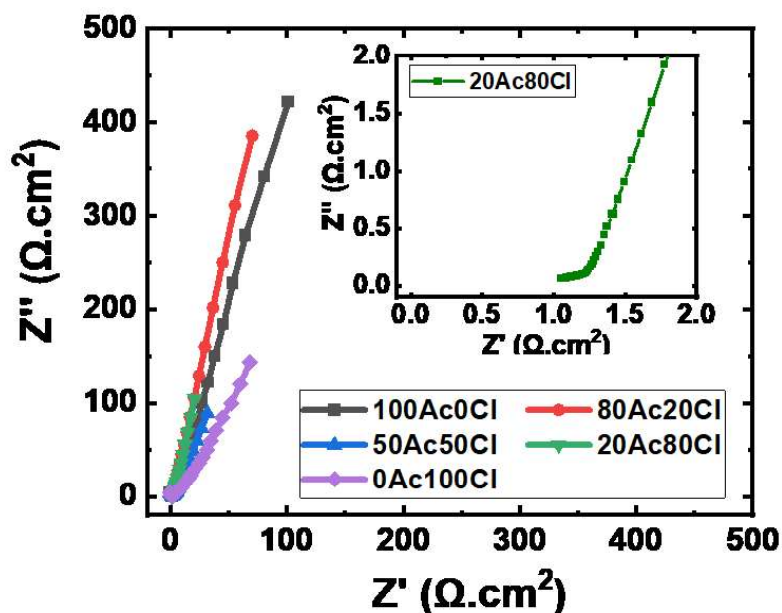


Figure 6.8 Nyquist plots of Co-Co₃O₄ nanocomposite thin films on NF substrate using 100Ac0Cl, 80Ac20Cl, 50Ac50Cl, 20Ac80Cl, and 0Ac100Cl precursors with inset showing a magnified plot of the film deposited using 20Ac80Cl.

The equivalent series resistance (R_s) which includes the resistance of the electrolyte, the internal resistance of the active material, and contact resistance at the electrode-electrolyte interface was evaluated from the intercept of the curves with the real impedance axis of the high-frequency region [16, 28, 29]. The R_s values were estimated to be 1.4, 1.3, 1.2, 1.0 and 1.6 $\Omega\cdot\text{cm}^2$ for electrodes deposited using 100Ac0Cl, 80Ac20Cl, 50Ac50Cl, 20Ac80Cl and 0Ac100Cl, respectively. This result indicates a higher conductivity of the electrode made with 20Ac80Cl compared to the other combinations and is consistent with the higher rate capability as observed from the GCD measurements at different specific currents. Similar R_s values have been reported by other studies for Co₃O₄-based electrodes [5, 46, 52]. In all the Nyquist plots acquired, there was no manifestation of a semicircle signifying the lower charge transfer resistance of the electrodes. Furthermore, in the lower frequency region, the

electrode deposited using 20Ac80Cl exhibits a shorter and more vertical line compared to others, indicating efficient ion diffusion and hence better capacitive performance as supported by the high specific capacitance value [17, 44, 48, 53].

6.5 Conclusions

Co-Co₃O₄ nanocomposite thin film electrode materials on nickel foam substrates have been synthesized by a facile technique that combines cyclic voltammetry and pulse reverse potential (CV PRP) modes of electrodeposition from a single electrolyte composed of CoCl₂ (Ac) and Co(CH₃COO)₂ (Cl) salts in different molar ratios of Ac and Cl, namely 100Ac0Cl (100:0), 80Ac20Cl (80:20), 50Ac50Cl (50:50), 20Ac80Cl (20:80), and 0Ac100Cl (0:100). The formation of both Co and Co₃O₄ phases together with variations in crystallinity for all the electrodes has been confirmed by the XRD spectra. The FTIR and EDX analysis have further confirmed the chemical characteristics of the electrode materials by the presence of Co₃O₄ absorption bands and oxygen and cobalt peak intensities, respectively. Different morphological features exhibited by the various molar ratios of the cobalt precursors have been revealed by the SEM images. The film deposited using 20Ac80Cl combination exhibited a maximum specific capacitance of 2580 F/g as compared to 791, 435, 1673, and 460 F/g for those obtained using 100Ac0Cl, 80Ac20Cl, 50Ac50Cl, and 0Ac100Cl combinations, respectively. Additionally, the respective capacitance retention for the 100Ac0Cl, 80Ac20Cl, 50Ac50Cl, 20Ac80Cl, and 0Ac100 Cl thin film electrodes have been estimated to be 66.6 %, 56.4, 74.0 %, 90.5 % and 60.0 %, after 500 cycles of charging/discharging under a high current load of 20 A/g. This indicates that the electrode

prepared using 20Ac80Cl with 20 % cobalt acetate to 80 % cobalt chloride displays superior electrochemical performance including high specific capacitance and cycle stability. The excellent performance is attributed to its good crystallinity and porous morphological features which offer high electrochemically active surface area. Finally, the type of cobalt precursors has a crucial impact on the morphology and microstructure of Co-Co₃O₄ materials leading to variations in the electrochemical characteristics.

6.6 References

- [1] S. Islam, M.M. Mia, S.S. Shah, S. Naher, M.N. Shaikh, M.A. Aziz, A.J.S. Ahammad, Recent Advancements in Electrochemical Deposition of Metal-Based Electrode Materials for Electrochemical Supercapacitors, *Chem Rec*, 22 (2022) e202200013.
- [2] S.J. Arbaz, S.C. Sekhar, B. Ramulu, J.S. Yu, Binder-free preparation of bimetallic oxide vertical nanosheet arrays toward high-rate performance and energy density supercapacitors, *Int. J. Energy Res.*, 45 (2021) 13999-14009.
- [3] W. Yang, Y. Feng, N. Wang, H. Yuan, D. Xiao, Facile microwave-assisted synthesis of sheet-like cobalt hydroxide for energy-storage application: Effect of the cobalt precursors, *J. Alloys Compd.*, 644 (2015) 836-845.
- [4] X. Fan, P. Ohlckers, X. Chen, Tunable Synthesis of Hollow Co₃O₄ Nanoboxes and Their Application in Supercapacitors, *Appl. Sci.*, 10 (2020) 1208.
- [5] R.B. Waghmode, N.C. Maile, D.S. Lee, A.P. Torane, Chemical bath synthesis of NiCo₂O₄ nanoflowers with nanorods like thin film for flexible supercapacitor application-effect of urea concentration on structural conversion, *Electrochim. Acta*, 350 (2020) 136413
- [6] A. Kim, G. Kalita, J.H. Kim, R. Patel, Recent Development in Vanadium Pentoxide and Carbon Hybrid Active Materials for Energy Storage Devices, *Nanomaterials (Basel)*, 11 (2021) 3213.
- [7] R. Liang, Y. Du, P. Xiao, J. Cheng, S. Yuan, Y. Chen, J. Yuan, J. Chen, Transition Metal Oxide Electrode Materials for Supercapacitors: A Review of Recent Developments, *Nanomaterials* 11 (2021) 1248.
- [8] C. An, Y. Zhang, H. Guo, Y. Wang, Metal oxide-based supercapacitors: progress and perspectives, *Nanoscale Advances*, 1 (2019) 4644-4658.
- [9] V. Quispe-Garrido, G.A. Cerron-Calle, A. Bazan-Aguilar, J.G. Ruiz-Montoya, E.O. López, A.M. Baena-Moncada, Advances in the design and application of transition metal oxide-based supercapacitors, *Open Chemistry*, 19 (2021) 709-725.

- [10] L. Ma, H. Fan, X. Wei, S. Chen, Q. Hu, Y. Liu, C. Zhi, W. Lu, J.A. Zapien, H. Huang, Towards high areal capacitance, rate capability, and tailorable supercapacitors: Co_3O_4 @polypyrrole core-shell nanorod bundle array electrodes, *J. Mater. Chem. A*, 6 (2018) 19058-19065.
- [11] S.J. Uke, V.P. Akhare, D.R. Bambole, A.B. Bodade, G.N. Chaudhari, Recent Advancements in the Cobalt Oxides, Manganese Oxides, and Their Composite As an Electrode Material for Supercapacitor: A Review, *Front. Mater.*, 4 (2017) 21.
- [12] B.D. Tanka Mukhiya, Gunendra Prasad Ojha, Kisan Chhetri, Minju Lee, Taewoo Kim, Su-Hyeong Chae, Arjun Prasad Tiwari, Alagan Muthurasu, Hak Yong Kim, Silver nanoparticles entrapped cobalt oxide nanohairs/electrospun carbon nanofibers nanocomposite in apt architecture for high performance supercapacitors, *Composites, Part B*, 178 (2019) 107482.
- [13] Z. Xiao, Y.C. Huang, C.L. Dong, C. Xie, Z. Liu, S. Du, W. Chen, D. Yan, L. Tao, Z. Shu, G. Zhang, H. Duan, Y. Wang, Y. Zou, R. Chen, S. Wang, Operando Identification of the Dynamic Behavior of Oxygen Vacancy-Rich Co_3O_4 for Oxygen Evolution Reaction, *Journal of the American Chemical Society*, 142 (2020) 12087-12095.
- [14] X. Fan, Y. Xu, C. Ma, W. He, In-situ growth of Co_3O_4 nanoparticles based on electrospay for an acetone gas sensor, *J. Alloys Compd.*, 854 (2021) 157234.
- [15] X. Liu, L. Yan, H. Ren, Y. Cai, C. Liu, L. Zeng, J. Guo, A. Liu, Facile synthesis of magnetic hierarchical flower-like Co_3O_4 spheres: Mechanism, excellent tetra-enzyme mimics and their colorimetric biosensing applications, *Biosensors & bioelectronics*, 165 (2020) 112342.
- [16] K. Prasad, G.R. Reddy, B.D.P. Raju, Surfactant assisted morphological transformation of rod-like ZnCo_2O_4 into hexagonal-like structures for high-performance supercapacitors, *Indian Journal of Science and Technology*, 14 (2021) 676-689.
- [17] Y. Tao, Y. Wu, H. Chen, W. Chen, J. Wang, Y. Tong, G. Pei, Z. Shen, C. Guan, Synthesis of amorphous hydroxyl-rich Co_3O_4 for flexible high-rate supercapacitor, *Chemical Engineering Journal*, 396 (2020) 125364.
- [18] C.V. Niveditha, R. Aswini, M.J. Jabeen Fatima, R. Ramanarayan, N. Pullanjiyot, S. Swaminathan, Feather like highly active Co_3O_4 electrode for supercapacitor application: a potentiodynamic approach, *Mater. Res. Express*, 5 (2018) 065501.
- [19] S.A. Pawar, D.S. Patil, J.C. Shin, Hexagonal sheets of Co_3O_4 and Co_3O_4 -Ag for high-performance electrochemical supercapacitors, *J. Ind. Eng. Chem*, 54 (2017) 162-173.
- [20] M.A.A. Mohd Abdah, N.H.N. Azman, S. Kulandaivalu, Y. Sulaiman, Review of the use of transition-metal-oxide and conducting polymer-based fibres for high-performance supercapacitors, *Mater. Des.*, 186 (2020) 108199.
- [21] Y. Li, X. Li, Z. Wang, H. Guo, T. Li, Distinct impact of cobalt salt type on the morphology, microstructure, and electrochemical properties of Co_3O_4 synthesized by ultrasonic spray pyrolysis, *J. Alloys Compd.*, 696 (2017) 836-843.
- [22] H. Xuan, R. Wang, J. Yang, G. Zhang, X. Liang, Y. Li, Z. Xie, P. Han, Synthesis of NiMoO_4 @ Co_3O_4 hierarchical nanostructure arrays on reduced graphene oxide/Ni foam as binder-free electrode for asymmetric supercapacitor, *J. Mater. Sci.*, 56 (2021) 9419-9433.
- [23] X. Wang, A. Hu, C. Meng, C. Wu, S. Yang, X. Hong, Recent Advance in Co_3O_4 and Co_3O_4 -Containing Electrode Materials for High-Performance Supercapacitors, *Molecules*, 25 (2020) 269.
- [24] E.M. Abebe, M. Ujihara, Influence of Temperature on $\text{ZnO}/\text{Co}_3\text{O}_4$ Nanocomposites for High Energy Storage Supercapacitors, *ACS omega*, 6 (2021) 23750-23763.

- [25] P.S. Gaikar, A.P. Angre, G. Wadhawa, P.V. Ledade, S.H. Mahmood, T.L. Lambat, Green synthesis of cobalt oxide thin films as an electrode material for electrochemical capacitor application, *Current Research in Green and Sustainable Chemistry*, 5 (2022) 100265.
- [26] M. Sharma, R. Adalati, A. Kumar, V. Chawla, R. Chandra, Elevated performance of binder-free Co_3O_4 electrode for the supercapacitor applications, *Nano Express*, 2 (2021) 010002.
- [27] S.S. Gavande, P.S. Kulkarni, V.B. Patil, B.R. Karche, S.S. Gavande, An Assay of Electrodeposited Cobalt Oxide Thin Film as a Supercapacitor Electrode, *Macromol. Symp.*, 393 (2020) 2000169.
- [28] P.S. Gaikar, S.T. Navale, V.V. Jadhav, P.V. Shinde, D.P. Dubal, P.R. Arjunwadkar, F.J. Stadler, M. Naushad, A.A. Ghfar, R.S. Mane, A simple wet-chemical synthesis, reaction mechanism, and charge storage application of cobalt oxide electrodes of different morphologies, *Electrochim. Acta*, 253 (2017) 151-162.
- [29] B. Sun, S. Lou, W. Zheng, Z. Qian, C. Cui, P. Zuo, C. Du, J. Xie, J. Wang, G. Yin, Synergistic engineering of defects and architecture in $\text{Co}_3\text{O}_4@\text{C}$ nanosheets toward Li/Na ion batteries with enhanced pseudocapacitances, *Nano Energy*, 78 (2020) 105366.
- [30] K. Tian, J.-t. Wang, L. Xing, Z.-y. Li, B.-b. Kuang, Y.-a. Sun, Nanostructure modulation of Co_3O_4 films by varying anion sources for pseudocapacitor applications, *Solid State Ionics*, 371 (2021) 115756.
- [31] J.P. Cheng, X. Chen, J.-S. Wu, F. Liu, X.B. Zhang, V.P. Dravid, Porous cobalt oxides with tunable hierarchical morphologies for supercapacitor electrodes, *CrystEngComm*, 14 (2012) 6702–6709.
- [32] F. Ali, N.R. Khalid, G. Nabi, A. Ul-Hamid, M. Ikram, Hydrothermal synthesis of cerium-doped Co_3O_4 nanoflakes as electrode for supercapacitor application, *Int. J. Energy Res.*, 45 (2020) 1999-2010.
- [33] A.D. Jagadale, V.S. Kumbhar, R.N. Bulakhe, C.D. Lokhande, Influence of electrodeposition modes on the supercapacitive performance of Co_3O_4 electrodes, *Energy*, 64 (2014) 234-241.
- [34] S.Y. Shajaripour Jaber, A. Ghaffarinejad, Z. Khajehsaeidi, The effect of annealing temperature, reaction time, and cobalt precursor on the structural properties and catalytic performance of CoS_2 for hydrogen evolution reaction, *Int. J. Hydrog. Energy*, 46 (2021) 3922-3932.
- [35] C.I. Priyadharsini, G. Marimuthu, T. Pazhanivel, P.M. Anbarasan, V. Aroulmoji, V. Siva, L. Mohana, Sol–Gel synthesis of Co_3O_4 nanoparticles as an electrode material for supercapacitor applications, *Journal of Sol-Gel Science and Technology*, 96 (2020) 416-422.
- [36] T.M. Project, Materials Data on Co_3O_4 by Materials Project, in, United States, 2020.
- [37] R. Samal, B. Dash, C.K. Sarangi, K. Sanjay, T. Subbaiah, G. Senanayake, M. Minakshi, Influence of Synthesis Temperature on the Growth and Surface Morphology of Co_3O_4 Nanocubes for Supercapacitor Applications, *Nanomaterials (Basel)*, 7 (2017) 356.
- [38] Y. Zhao, Y. Liu, J. Du, X. Zhang, J. Zhou, X. Li, C. Wu, Z. Zhu, E. Xie, X. Pan, Facile synthesis of interconnected carbon network decorated with Co_3O_4 nanoparticles for potential supercapacitor applications, *Appl. Surf. Sci.*, 487 (2019) 442-451.
- [39] S. Raj, S.K. Srivastava, P. Kar, P. Roy, In situ growth of Co_3O_4 nanoflakes on reduced graphene oxide-wrapped Ni-foam as high performance asymmetric supercapacitor, *Electrochim. Acta*, 302 (2019) 327-337.

- [40] K. Gothandapani, A.N. Grace, V. Venugopal, Mesoporous carbon-supported Co_3O_4 derived from Zif-67 metal organic framework (MOF) for hydrogen evolution reaction in acidic and alkaline medium, *Int. J. Energy Res.*, 46 (2021) 3384-3395.
- [41] X. Hu, L. Wei, R. Chen, Q. Wu, J. Li, Reviews and Prospectives of Co_3O_4 -Based Nanomaterials for Supercapacitor Application, *ChemistrySelect*, 5 (2020) 5268-5288.
- [42] G.-S. Jang, S. Ameen, M.S. Akhtar, E. Kim, H.-S. Shin, Electrochemical Investigations of Hydrothermally Synthesized Porous Cobalt Oxide (Co_3O_4) Nanorods: Supercapacitor Application, *ChemistrySelect*, 2 (2017) 8941-8949.
- [43] R. Packiaraj, P. Devendran, K.S. Venkatesh, S. Asath bahadur, A. Manikandan, N. Nallamuthu, Electrochemical Investigations of Magnetic Co_3O_4 Nanoparticles as an Active Electrode for Supercapacitor Applications, *J. Supercond. Nov. Magn.*, 32 (2018) 2427-2436.
- [44] P. Sivakumar, C.J. Raj, D.O. Opar, J. Park, H. Jung, Two dimensional layered nickel cobaltite nanosheets as an efficient electrode material for high-performance hybrid supercapacitor, *Int. J. Energy Res.*, 45 (2021) 1–11.
- [45] H. Zhu, J. Liu, Q. Zhang, J. Wei, High electrochemical performance of metal azolate framework-derived $\text{ZnO}/\text{Co}_3\text{O}_4$ for supercapacitors, *Int. J. Energy Res.*, 44 (2020) 8654-8665.
- [46] M. Gao, W.K. Wang, Q. Rong, J. Jiang, Y.J. Zhang, H.Q. Yu, Porous ZnO -Coated Co_3O_4 Nanorod as a High-Energy-Density Supercapacitor Material, *ACS Appl. Mater. Interfaces*, 10 (2018) 23163-23173.
- [47] R.M. Obodo, E.O. Onah, H.E. Nsude, A. Agbogu, A.C. Nwanya, I. Ahmad, T. Zhao, P.M. Ejikeme, M. Maaza, F.I. Ezema, Performance Evaluation of Graphene Oxide Based $\text{Co}_3\text{O}_4@\text{GO}$, $\text{MnO}_2@\text{GO}$ and $\text{Co}_3\text{O}_4/\text{MnO}_2@\text{GO}$ Electrodes for Supercapacitors, *Electroanalysis*, 32 (2020) 2786-2794.
- [48] T. Liu, L. Zhang, W. You, J. Yu, Core-Shell Nitrogen-Doped Carbon Hollow Spheres/ Co_3O_4 Nanosheets as Advanced Electrode for High-Performance Supercapacitor, *Small*, 14 (2018) e1702407.
- [49] H. Pang, X. Li, Q. Zhao, H. Xue, W.-Y. Lai, Z. Hu, W. Huang, One-pot synthesis of heterogeneous Co_3O_4 -nanocube/ $\text{Co}(\text{OH})_2$ -nanosheet hybrids for high-performance flexible asymmetric all-solid-state supercapacitors, *Nano Energy*, 35 (2017) 138-145.
- [50] J. Li, C. Wei, Y. Sun, Q. Liu, X. Zhang, J. Guo, Hierarchical $\text{Ni}(\text{OH})_2$ - MnO_2 Array as Supercapacitor Electrode with High Capacity, *Advanced Materials Interfaces*, 6 (2018) 1801470.
- [51] R.A. Nuamah, S. Noormohammed, D.K. Sarkar, Specific capacitance behavior of Co- Co_3O_4 nanocomposite thin films synthesized via different electrodeposition modes, *Int. J. Energy Res.*, (2021) 1-11.
- [52] A. Numan, N. Duraisamy, F. Saiha Omar, Y.K. Mahipal, K. Ramesh, S. Ramesh, Enhanced electrochemical performance of cobalt oxide nanocube intercalated reduced graphene oxide for supercapacitor application, *RSC Adv.*, 6 (2016) 34894-34902.
- [53] P. Siwatch, K. Sharma, N. Manyani, J. Kang, S.K. Tripathi, Characterization of nanostructured nickel cobalt oxide-polyvinyl alcohol composite films for supercapacitor application, *J. Alloys Compd.*, 872 (2021) 159409.

6.7 Supplementary information

(a) Supporting information for publication (*Rania Afia Nuamah, Saleema Noormohammed, Dilip Kumar Sarkar, Effect of molar ratio modulation of cobalt precursors on supercapacitor behavior of engineered Co-Co₃O₄ nanocomposite electrodes. ACS Appl. Eng. Mater, 2023, 1(1), 241-251*)

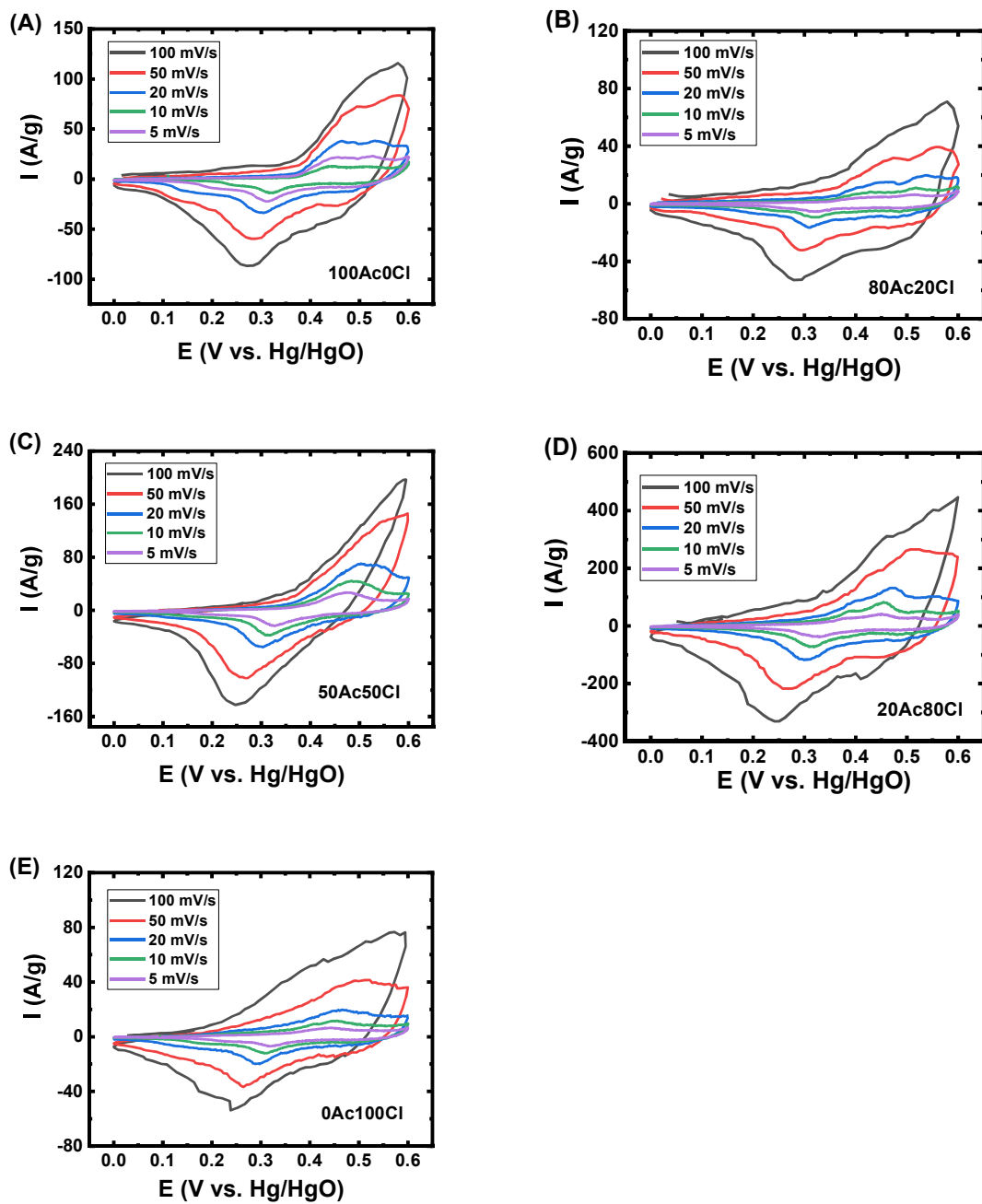


Figure 6S.1. Cyclic voltammetry (CV) curves of (A) 100Ac0Cl (B) 80Ac20Cl, (C) 50Ac50Cl (D) 20Ac80Cl and (E) 0Ac100Cl Co-Co₃O₄ nanocomposite thin films on nickel foam (NF) substrates at different scan rates.

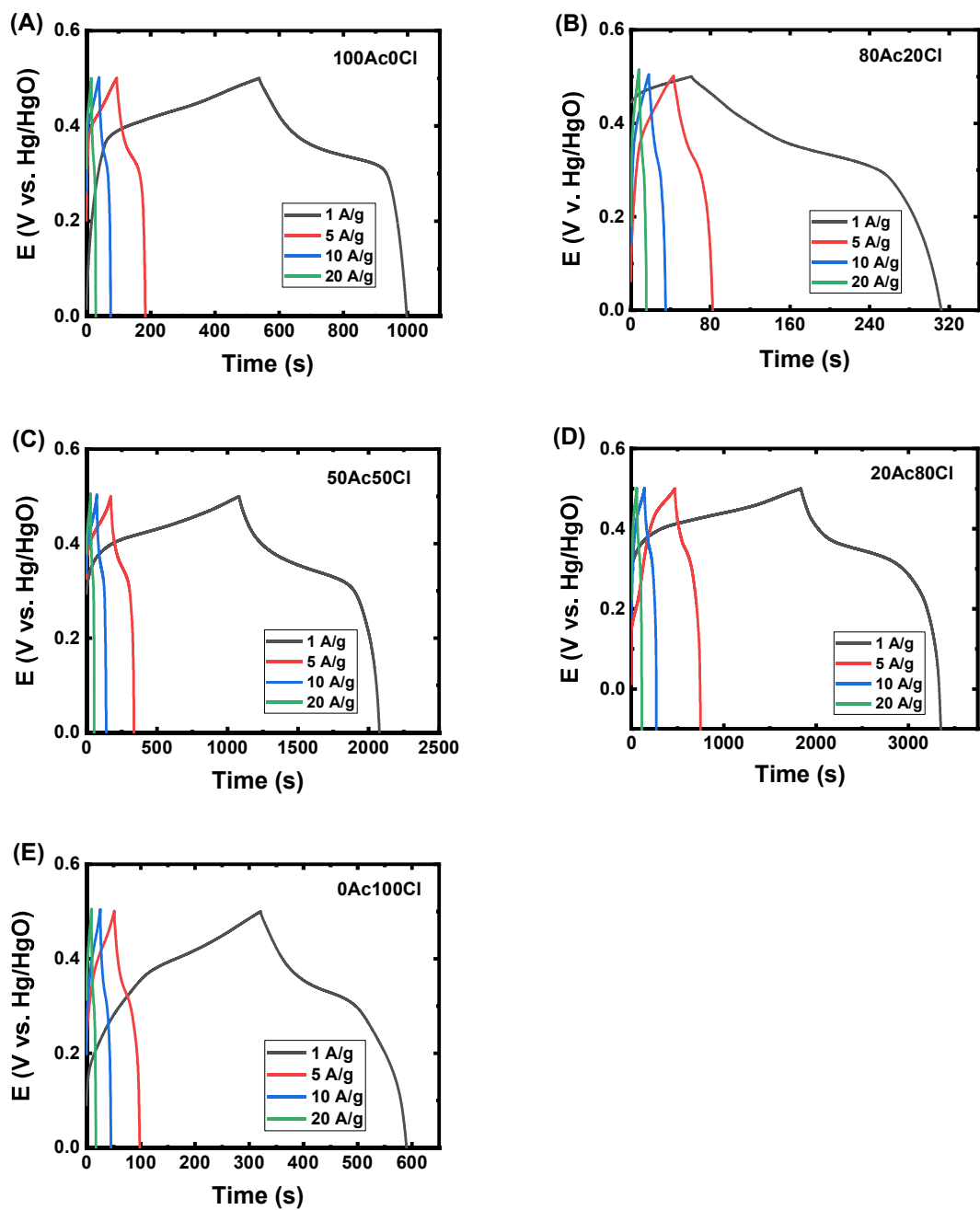


Figure 6S.2. Galvanostatic charge-discharge (GCD) curves of (A) 100Ac0Cl (B) 80Ac20Cl (C) 50Ac50Cl (D) 20Ac80Cl (E) 0Ac100Cl Co-Co₃O₄ nanocomposite thin film on NF electrodes at different specific current.

(b) Unpublished supporting information

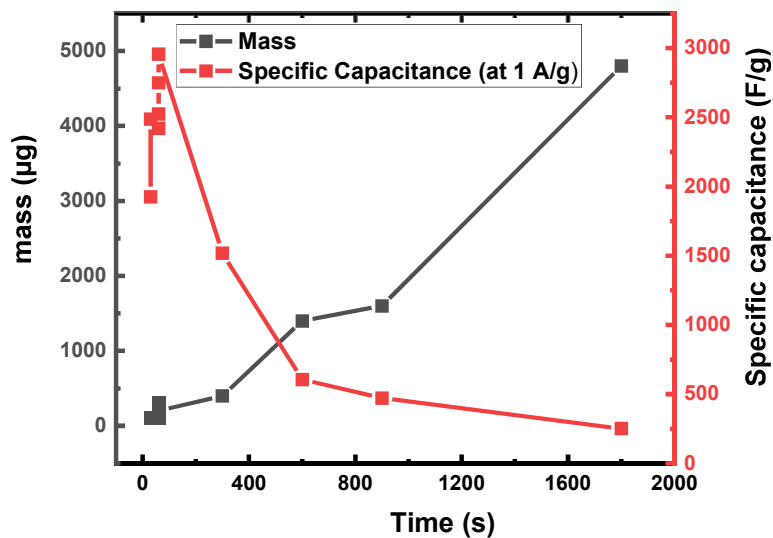


Figure 6S.3. Variation of mass and specific capacitance with pulse reverse potential (PRP) electrodeposition time for the 20Ac80Cl Co-Co₃O₄ nanocomposite thin film electrode.

To further optimize the electrodeposition process, the time for the PRP electrodeposition process was varied for the 20Ac80Cl Co-Co₃O₄ nanocomposite thin film. From Figure 6S.3, it can be observed that the mass increases linearly with the deposition time while there is a general decrease in the specific capacitance as the deposition time increases. Furthermore, Figure 6S.3 revealed the optimum PRP time to produce Co-Co₃O₄ nanocomposite thin film with an optimum mass for superior specific capacitance to be 60 s.

CHAPTER 7: SPECIFIC CAPACITANCE BEHAVIOR OF Co-Co₃O₄ NANOCOMPOSITE THIN FILMS SYNTHESIZED VIA DIFFERENT ELECTRODEPOSITION MODES

Rania Afia Nuamah, Saleema Noormohammed, Dilip Kumar Sarkar

Department of Applied Science, University of Quebec at Chicoutimi, Aluminum Research
Center-REGAL, Chicoutimi, Quebec, G7H 2B1, Canada

This article has been published in:

International Journal for Energy Research 46 (2022) 4434-4444

7.1 Abstract

High capacitance Co-Co₃O₄ nanocomposite thin films have been synthesized on nickel foam (NF) using cyclic voltammetry (CV), combination of cyclic voltammetry and potentiostatic (CV PS -1.4V and CV PS +1V) and combination of cyclic voltammetry and pulse reverse potential (CV PRP) modes of electrodeposition. X-ray diffraction (XRD) studies reveal the presence of Co and Co₃O₄ phases for the four electrodeposition modes. The scanning electron microscope (SEM) revealed an interesting morphology correlating the electrochemical and capacitance behavior while the energy-dispersive X-ray spectroscopy (EDX) spectra confirmed the varying quantities of Co and O in the Co-Co₃O₄ nanocomposite thin films. The presence of Co-O bonds was also confirmed by the attenuated total reflection – Fourier transform infrared (ATR – FTIR) spectra obtained on these films. The capacitance

values of Co-Co₃O₄ composite thin films obtained by CV, CV PS -1.4V, CV PS +1V, and CV PRP, respectively, were found to be 1661, 1400, 1866, 2580 F/g at an applied current load of 1 A/g while the capacitance retentions after 500 cycles under a high current load of 20 A/g for the same were 85.8, 77.8, 87.1, and 90.5 %, respectively. The high capacitance and their retention of the electrodeposited Co-Co₃O₄ nanocomposite thin films show potential as high-performance supercapacitor electrodes.

7.2 Introduction

Advanced technological devices including portable electronics such as mobile phones, tablets, laptops, and smartwatches as well as low emission technologies including hybrid vehicles constantly demand lightweight energy storage systems for easy portability and handling with long service life. Supercapacitors demonstrate high potential as efficient energy storage systems owing to their most essential features such as lightweight, high energy density, high power density, fast charge-discharge rates, easy and safe operation, and long cycle stability [1-3]. Among an array of supercapacitor electrode materials such as activated carbon, conducting polymers, and transition metal oxides (TMOs) [4, 5], TMOs are widely preferred due to their high electronegativity and variable oxidation states of metal ions facilitating redox reactions, charge storage, low cost, environmental friendliness and excellent electrochemical performance [2, 4, 6]. TMOs have higher specific capacitance (100–2000 F/g), higher energy density than carbon materials, and better chemical stability than conductive polymers [7]. Noble TMOs such as RuO₂, exhibit high theoretical capacitance and rapid faraday redox reaction proving as optimal pseudocapacitive electrode

material, however, are very expensive and environmentally unfriendly, limiting industrial scale productions. Base TMOs, on the other hand, including, Co_3O_4 , MnO_2 , Fe_2O_3 , SnO_2 , and ZnO are easy to fabricate and exhibit high theoretical specific capacitance showing potentials as substitutes for RuO_2 [2, 7, 8]. Among these base TMOs, Co_3O_4 has a very high theoretical specific capacitance of 3560 F/g and is relatively low in cost owing to easy fabrication methods [9-11]. Also, nanostructured Co_3O_4 coatings have been found to be useful in other types of applications such electrocatalysts for hydrogen evolution reaction[12] and photocatalysts for discoloration of organic dye contaminants in wastewater and antibacterial treatment [13].

Despite the high theoretical capacitance of Co_3O_4 , this TMO suffers limited practical utility due to low experimental capacitance values of this material compared to the theoretical value [14]. Studies have shown that the morphology, structure, and dimensions of Co_3O_4 features are easily tunable by controlling the preparative parameters of the fabrication method employed [7, 15, 16]. This is a very important factor in supercapacitive performance as the specific capacitance of the cobalt oxide strongly depends on morphology, surface area, and size distribution contributing to enhancement in the specific surface area, facilitating the electrolyte ion transport in the material [2]. Co_3O_4 with morphological features in nanoscale dimensions can essentially lead to tunable specific surface area in enhancing the experimental specific capacitance values.

Generally, nanostructured Co_3O_4 materials have been prepared by techniques such as spray pyrolysis, precipitation, sol-gel, and hydrothermal synthesis. These techniques require the use of binders and conductive materials which increase the electrode resistance affecting their supercapacitive performance [17, 18]. Recently, electrodeposition has become a useful

technique for growing Co-O nanostructures with desired composition and morphology directly onto the substrates without necessitating the use of binders. In electrodeposition, several factors such as electrolyte composition, temperature, type of electrodeposition mode, duration of the electrode deposition process, etc., can be adjusted to obtain the desired morphology and texture such as nanoporous structure, nanocolumnar structure, nanoflower-like structure [19-21]. Studies have also reported variation in surface morphology and respective supercapacitive behavior of Co_3O_4 -based electrodes by performing electrodeposition in different modes, namely, cyclic voltammetry (CV), potentiostatic (PS), galvanostatic (GS), pulse (current or potential) [15, 22]. Optimal electrodeposition modes together with the appropriate cobalt salt precursor for the preparation of Co_3O_4 -based electrodes offering high capacitance closest to the theoretical value as well as low electric resistance, however, need further investigation.

In view of optimizing the mode of electrodeposition in achieving the highest and most stable specific capacitance, we have deposited Co- Co_3O_4 nanocomposite thin films electrodes on nickel foam substrates using CV, CV PS -1.4V, CV PS +1V, and CV combined with pulsed reverse potential (CV PRP) modes from an electrolyte composed of CoCl_2 and $\text{Co}(\text{CH}_3\text{COO})_2$ salts solution. The structural, morphological, and compositional analyses present a correlation with the electrochemical behavior namely the CV, EIS, and charge-discharge cycles. CV PRP mode that led to the deposition of Co- Co_3O_4 nanocomposite thin film is found to present a very high capacitance of 2580 F/g with stable cycling performance.

7.3 Experimental Section

In the electrochemical deposition process, the use of a negative potential reduces the Co^{2+} ions into a metallic Co as a film. Similarly, the use of a positive potential deposits a layer of Co_3O_4 . In our experiment, a maximum negative potential of -1.4V was used to deposit metallic Co film and a $+1.0\text{V}$ was used to deposit Co_3O_4 . Cobalt-cobalt oxide (Co-CoO_x) nanocomposite thin films were electrodeposited on nickel foam (NF) substrates by different modes, namely, (1) Cyclic voltammetry (CV), (2) CV followed by potentiostatic (PS) at $+1.0\text{ V}$ (CV PS $+1.0\text{ V}$), (3) CV followed by PS at -1.4 V (CV PS -1.4V) and (4) CV followed by pulse reverse potential (CV PRP) cycled between -1.4V and $+1.0\text{V}$. The thin films deposited via these four modes have been identified as Type 1 (CV), Type 2 (CV PS $+1.0\text{V}$), Type 3 (CV PS -1.4V) and Type 4 (CV PRP). CV mode was conducted in a potential range of -1.4 to $+1.0\text{ V}$ vs Ag/AgCl at a scan rate of 20 mVs^{-1} for 2 cycles. For the CVPS $+1\text{V}$ mode, CV was initially conducted in a potential range of -1.4 to $+1.0\text{ V}$ vs Ag/AgCl at a scan rate of 20 mVs^{-1} for 2 cycles, and was followed by potentiostatic deposition at $+1\text{ V}$ for 30 s. A similar condition was used for the CV PS -1.4V mode, however with a negative constant potential of -1.4 V . For the CV PRP mode, CV was initially performed in a potential range of -1.4 to $+1.0\text{ V}$ vs Ag/AgCl at a scan rate of 20 mVs^{-1} for 2 cycles, followed by pulse reverse potential (PRP) of 60 cycles of width of 1 s for a total duration of 60 s. The minimum and the maximum of pulse heights were chosen to be -1.4 V and $+1\text{ V}$, respectively. The electrolyte solutions used for the electrodeposition consist of 0.1 M cobalt acetate ($\text{Co}(\text{CH}_3\text{CO}_2)_2 \cdot 4\text{ H}_2\text{O}$, 6 ml), 0.1 M cobalt chloride (CoCl_2 24 ml) and 0.2 M sodium perchlorate ($\text{NaClO}_4 \cdot \text{H}_2\text{O}$, 30 ml). The pH of the electrolyte was 6.5. Prior to the electrodeposition process, the NF substrate was etched in 3 M HCl for 15 minutes and rinsed ultrasonically with ethanol and deionised water for 15 minutes each. The deposition process was conducted in a standard three-electrode glass cell with a platinum wire, NF substrate and

Ag/AgCl as the counter, working and reference electrodes, respectively. After electrodeposition, the as-prepared Co-CoO_x nanocomposite thin film electrodes were rinsed in deionized water and dried in air on a hot plate at 200° C for 45 minutes before performing characterization and electrochemical analyses. The experimental details of the four electrodeposition modes have been summarized in Table 7.1. A separate set of samples were also prepared by depositing the thin films on Ti substrate for the purpose of physical characterization by XRD.

Table 7.1 : Summary of the different modes of electrodeposition

Identification	Electrodeposition mode*	Potential range
Type 1	CV	-1.4V to +1.0V
Type 2	CV PS 1.0V	CV followed by PS at +1.0 V
Type 3	CV PS -1.4V	CV followed by PS at -1.4 V
Type 4	CV PRP	CV followed by PRP of 60 cycles between -1.4V and +1.0V

*CV – Cyclic voltammetry, PS – potentiostatic, PRP – pulse reverse potential

The morphological and elemental analyses of the electrodeposited thin films were studied by a scanning electron microscope (SEM, JEOL JSM-6480 LV), equipped with energy-dispersive X-ray spectroscopy (EDX) for elemental analyses. The X-ray diffraction (XRD) analyses were carried out by Bruker D8 Discover system for crystallographic analysis. An attenuated total reflection – Fourier transform infrared spectroscopy (ATR-FTIR, Agilent

Technologies Cary 630) was used to confirm and quantify the deposition of the metal oxide (Co-O).

The electrochemical properties, namely, cyclic voltammetry (CV) and galvanostatic charge-discharge (GCD), and electrochemical impedance spectroscopy (EIS) characteristics were evaluated using a three-electrode glass cell and Solartron SI1287 electrochemical workstation with 1 M KOH aqueous electrolyte. The as-synthesized Co-Co₃O₄ nanocomposite thin films on NF substrate of the various types were directly employed as working electrodes, with platinum wire and Hg/HgO as counter and reference electrodes respectively. The CV and GCD measurements were performed at different scan rates and specific currents in a potential window of 0 to 0.6 V and -0.1 to 0.5 V respectively. Additionally, the EIS measurement was conducted in a frequency range from 10 mHz to 100 kHz.

7.4 Results and discussion

7.4.1 Electrodeposition of Co-Co₃O₄

Figure 7.1 shows the profiles of electrodeposition modes individually for the preparation of the Co-Co₃O₄ nanocomposite thin films on nickel foam (NF) substrates. Electrodeposition of four types of thin films were realised using individual modes: (1) Type 1 (CV, Figure 6.1(a)), (2) Type 2 (combination of CV and PS (+1.0V), Figure 7.1(b)), (3) Type 3 (combination of CV and PS (-1.4V), Figure (6.1(c)), and (4) Type 4, (combination of

CV and PRP (between +1.0V and -1.4V), Figure (7.1(d)). The Type 1 thin film was deposited on NF by using the CV process alone as shown in Figure 7.1(a). During this process, the potential is swept between -1.4 to +1.0V, and hence it can be assumed that metal (Co) and metal oxides (Co-O) are deposited on NF simultaneously. A negative potential was used in order to initiate the deposition of metallic Co on NF to enhance the adhesion of the nanocomposite thin film layer deposited further by PS and PRP processes. The Type 2 thin film was deposited utilising CV process followed by PS (+1.0V) by combining Figure 7.1(a) and 1(b) processes in order to deposit an additional layer of cobalt oxide after the CV process. Similarly, the Type 3 thin film was deposited by the CV process followed by PS (-1.4V) to deposit an additional layer of metal (Co). This was achieved by combining the processes shown in Figures 7.1(a) and 6.1(c). The Type 4 thin film, on the other hand, was deposited utilizing CV process followed by PRP with the potential cycled between -1.4V and +1.0V to deposit multilayers of cobalt and cobalt oxide in a sequence where metal deposition is followed by metal oxide deposition after the CV process. This was achieved by combining Figures 7.1(a) and 7.1(d).

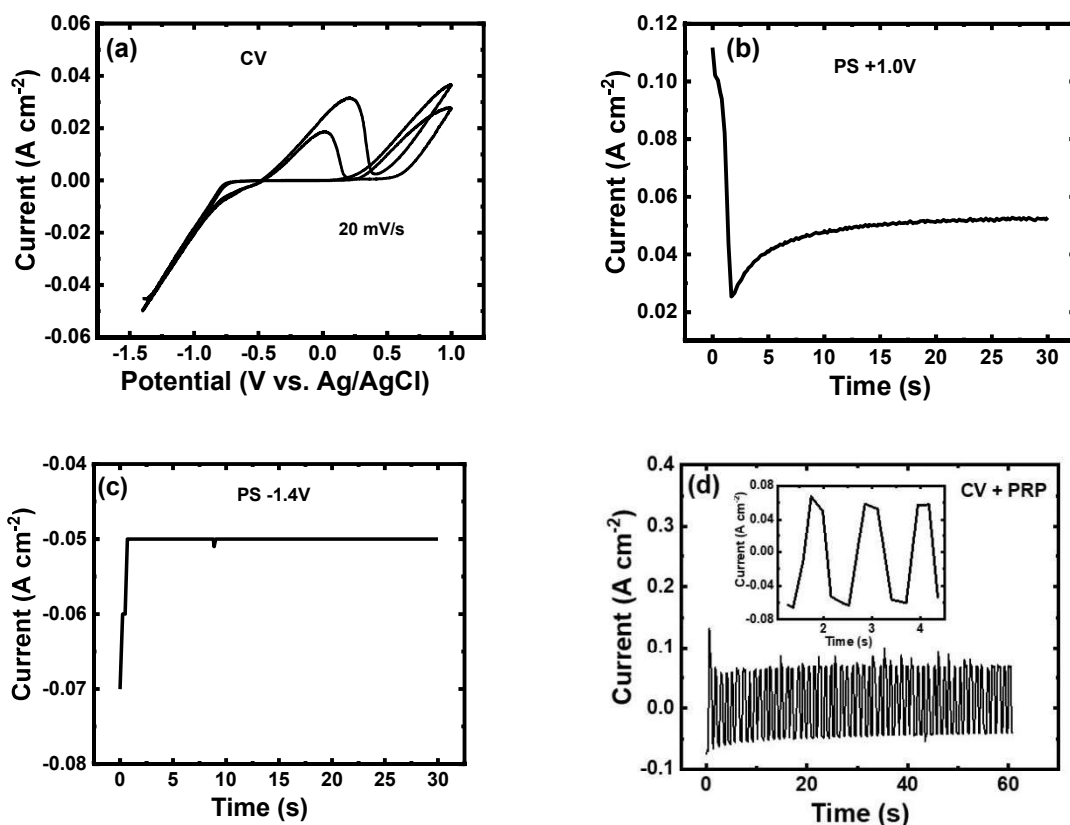


Figure 7.1. Individual profiles of electrodeposition modes for the preparation of the Co-Co₃O₄ nanocomposite thin films on NF: (a) cyclic voltammetry (CV, 2 scans), (b) potentiostatic at +1.0V (PS +1.0V), (c) potentiostatic at -1.4 V (PS -1.4V), (d) pulse reverse potential (PRP) (inset of (d) shows the current vs. time graph of the first three cycles).

7.4.2 Structural, morphological, and chemical analysis

Figure 7.2(a) shows the XRD patterns of the Co-Co₃O₄ nanocomposite thin films prepared by the four electrodeposition modes on Ti-substrate. The diffraction peaks at 2θ angles of 41.7° and 47.5° are assigned to Co (100) and Co (101) planes of hexagonal crystal structure of cobalt (JCPDS card No-00-005-0727). The peak at 44.6° is assigned to

$\text{Co}_3\text{O}_4(400)$ plane of cubic crystal structure of cobalt oxide (Co_3O_4) (JCPDS card No-42-1467).

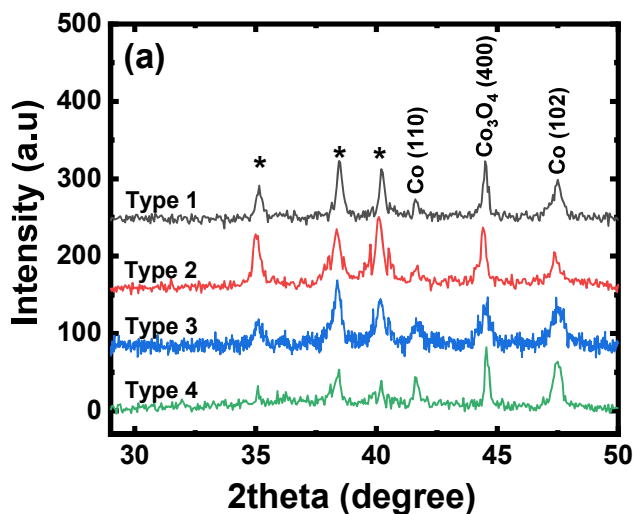


Figure 7.2. XRD patterns of Type 1, 2, 3, and 4 Co- Co_3O_4 nanocomposite thin films synthesized by CV, CVPS +1.0V, CVPS -1.4V, and CVPRP electrodeposition modes on Ti-substrate.

These peak positions assigned to Co_3O_4 are also in agreement with those reported by Zhang *et al.* on their 3d nanosheet arrays of Co- Co_3O_4 prepared by a potentiostatic deposition process [23] as well as those reported by Duraisamy *et al.* on their Co_3O_4 nanoparticles synthesized by a pyrolysis technique [24]. Similar peak positions have also been reported by Bin Qui *et al.* for Co_3O_4 and Co-CoO-C materials prepared by a potentiodynamic mode of electrodeposition [25]. The peaks marked with asterisks ‘*’ originate from the Ti-substrate and are attributable to Ti (100), Ti (002) and Ti (101) planes (JCPDS card No-00-005-0682).

All the four types of thin films electrodeposited on NF substrates were analyzed by FTIR spectrometry for confirming the formation of Co_3O_4 following the deposition processes

employed. The FTIR spectra obtained from these thin films within the range of interest between 500 and 1000 cm^{-1} are presented in Figure 7.3(a). Two absorption bands observed in the wavenumber range of 646-658 cm^{-1} and 530-554 cm^{-1} are attributed to the stretching vibrations of Co-O bond in the tetrahedrally and octahedrally coordinated cobalt, respectively. The presence of these fingerprint absorption bands confirms the formation of Co_3O_4 for all the four types of thin films electrodeposited under the four different modes briefed in Table 7.1. The wavenumber ranges within which these absorption bands appear are also in good agreement with reports in the literature [15, 18, 26-28]. While the formation of Co_3O_4 is evident from the IR absorption bands in Figure 7.3(a), the intensities of these bands are obviously varying. Therefore, in order to understand the oxide peak intensities and their possible effect on the supercapacitive behavior of these thin films, we further investigated the area under these two representative peaks and are presented in Figure 7.3(b). The area under the peaks clearly vary for different electrodeposition modes used and the least area under the peak is observed in particular on Type 3 thin film (CV PS -1.4V). It is possible that in Type 3 thin film, due to the negative potential used in the deposition process, metal layers are deposited resulting in a lower intensity of the oxide. Therefore, it can be expected that the specific capacitance can vary depending on the oxide intensities revealed by the FTIR peak area analysis.

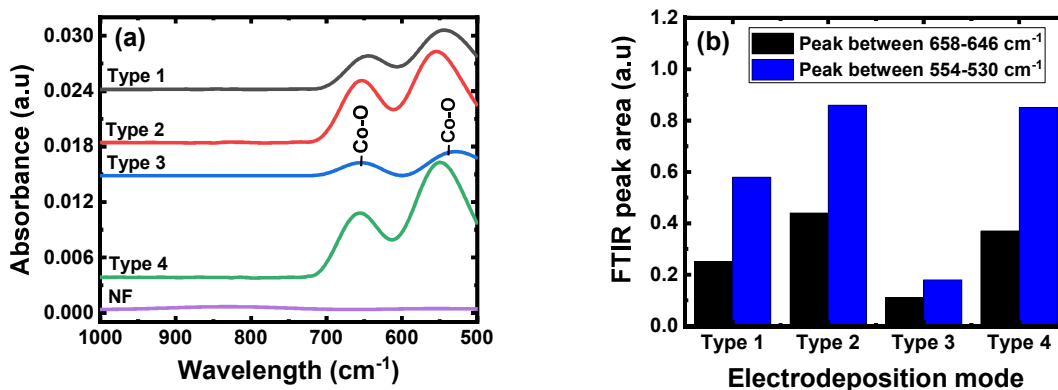


Figure 7.3. (a) FTIR spectra and (b) area under the two IR absorption bands of Type 1, 2, 3, and 4 Co-Co₃O₄ nanocomposite thin films synthesized by Type 1 (CV), Type 2 (CV PS +1.0V), Type 3 (CV PS - 1.4V) and Type 4 (CVPRP) electrodeposition modes on NF substrate

In addition to the type of oxides and their quantities, it has been reported that the specific surface area resulting from the final morphology and structure of the obtained thin films can have a significant impact on the supercapacitive behavior of Co₃O₄-based electrodes [15, 22]. Therefore, morphological investigations on the four types of thin films deposited under different modes on NF were further carried out using SEM imaging and are depicted in Figure 7.4 (a-d). The apparent morphology of all types looks similar; however, a slight variation is certainly visible. In case of Type 1 (CV, Figure 7.4(a)) and Type 2 (CVPS +1.0V, Figure 6.4(d)) thin films, for example, CV process (Type 1) presumably results in the formation of a baseline morphology resembling a network of interconnected nanoflakes while the CVPS +1.0V process (Type 2) maintains the initial baseline produced by the CV process, but with an additional cloudy cluster-like morphology formed over the CV's baseline morphology.

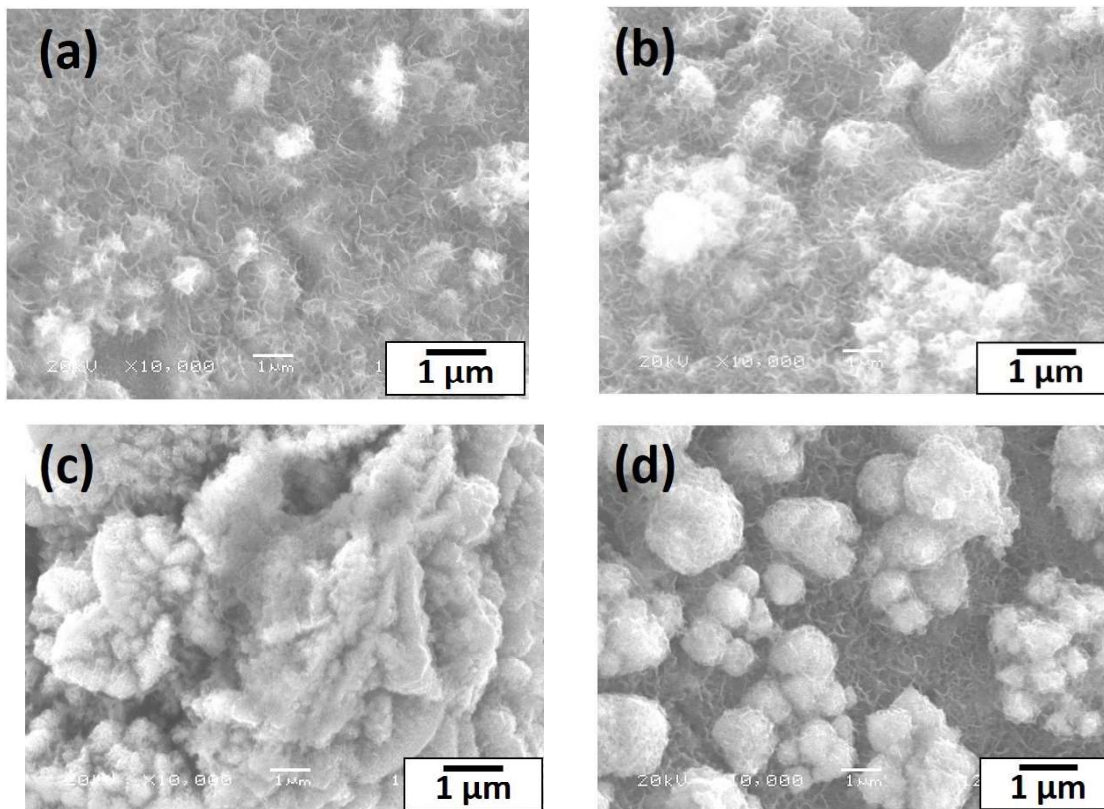


Figure 7.4. SEM micrographs of the as-synthesized Co-Co₃O₄ nanocomposite thin films on NF substrate prepared by the four different electrodeposition modes: (a) Type 1 (CV), (b) Type 2 (CVPS +1.0V), (c) Type 3 (CVPS -1.4V) and (d) Type 4 (CV PRP)

The surface morphology of the Type 3 thin film deposited by CVPS -1.4V process (Figure 7.4(c)), however, shows large agglomeration of spongy cloud-like features which may be attributable to overgrowth of the material. This agglomeration may be expected to limit the electrolyte access to the electroactive sites which in turn may affect the capacitive performance. The Type 4 thin film deposited by CV PRP process presented in Figure 7.4(d), on the other hand, shows well adherent porous interconnected nanoflake morphology decorated with spongy cloud-like features homogeneously dispersed over the porous interconnected nanoflakes formed on the substrate. The Type 4 thin film's morphological features may contribute to enhanced surface area favorable for improved access of electrolyte

to the electroactive sites and hence increase the capacitive ability [11, 29]. Morphological features resembling that of our thin films obtained via the four modes of electrodeposition process have been previously reported by Jagadale *et al.* presenting nanoflake-like mesoporous cobalt oxide film prepared by potentiodynamic, galvanostatic, and potentiostatic modes of electrodeposition [15].

During the SEM image analysis, EDX spectra (Figure 7.5) were also collected on all four types of thin films as well as on the NF substrate in complementing the FTIR spectral analysis for the confirmation of the presence of oxide on these films. All the elements of interest were traced on the EDX spectra, including O, Co, and Ni, where Ni arises from the NF substrate. The presence of O in all the four thin film types and the absence of O on NF substrate confirms the oxide formation on the electrodeposited thin films surfaces. The atomic ratio of O to Co (O/Co) for Type 1, Type 2, Type 3, and Type 4 thin films are found to be 1.9, 2.1, 1.7, and 3.0 respectively, with a close match with the Co_3O_4 stoichiometric as supported by the study of Faisal Ali *et al.* [16]. The Type 4 thin film deposited by CV PRP process, however, shows a reasonably higher O/Co ratio indicating that this thin film may result in a higher specific capacitance value.

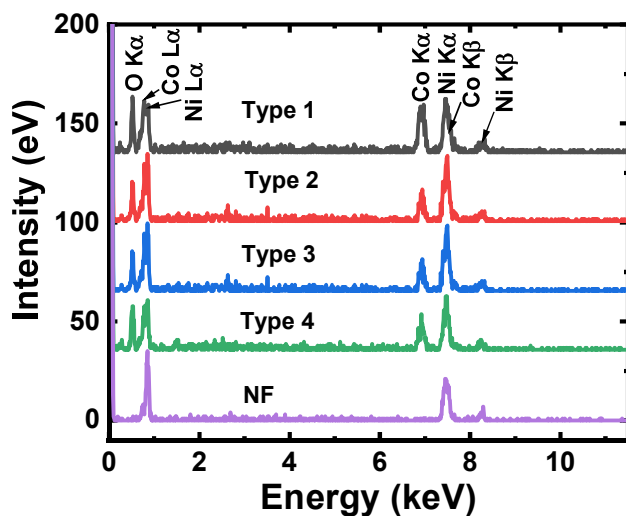


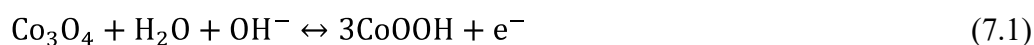
Figure 7.5. EDX spectra of NF substrate and Type 1 (CV), Type 2 (CV PS +1.0V), Type 3 (CV PS -1.4V) and Type 4 (CV PRP) Co-Co₃O₄ nanocomposite thin films on NF substrate.

Additionally, a comparison of the EDX point scans of the film (beneath the sponge-like features) and sponge-like material presented in the Figure S7.1 of the supplementary shows that, the O/Co ratio of 2.4 in the film beneath the sponge-like features is higher compared to O/C ratio of 1.4 on the sponge-like material. The O/Co ratio of Co₃O₄ theoretically is 1.33 (4/3), which is very close to the value obtained on the EDX point scan of the sponge-like features. Therefore, it may be assumed that these sponge-like features are mostly Co₃O₄ and therefore may contribute to high specific capacitance.

7.4.3 Electrochemical measurements

Figure 7.6(a) shows the CV curves of the four types of Co-Co₃O₄ nanocomposite thin films deposited by Type 1 (CV), Type 2 (CV PS +1V), Type 3 (CV PS -1.4V), and Type 4

(CV PRP) modes of electrodeposition on NF substrates at a scan rate of 5 mV/s. Also, the CV curves of the various types of Co-Co₃O₄ nanocomposite thin films at different scan rates (100, 50, 20, 10, and 5 mV/s) have been presented in Figure S7.2 of the supplementary data. The shapes of the CV curves show that the as-synthesized Co-Co₃O₄ nanocomposite thin films deposited by the Type 1, Type 2, Type 3, and Type 4 modes of electrodeposition are strongly governed by faradaic processes and present both anodic (oxidation) and cathodic (reduction) peaks from the Co-Co₃O₄ thin film electrodes [4]. The first redox peak (A1 (0.38V), C1 (0.24V)) and the third redox peaks (A3 (0.52V), C3 (0.51V)) can be correlated to the redox reaction of Co²⁺/Co³⁺ as depicted in Equation (7.1) [30]. The second pair of redox peaks (A2 (0.45V), C2 (0.33V)) is correlated to the redox reaction of Co³⁺/Co⁴⁺ shown in Equation (7.2) [30, 31].



It can be noted that the CV curve of the Type 4 film presents higher area under the CV curve as compared to the other modes of electrodeposition. The larger area indicates a higher accumulation of charge at the CVPRP thin film electrode surface during potential cycling process, and therefore expected to show higher specific capacitance.

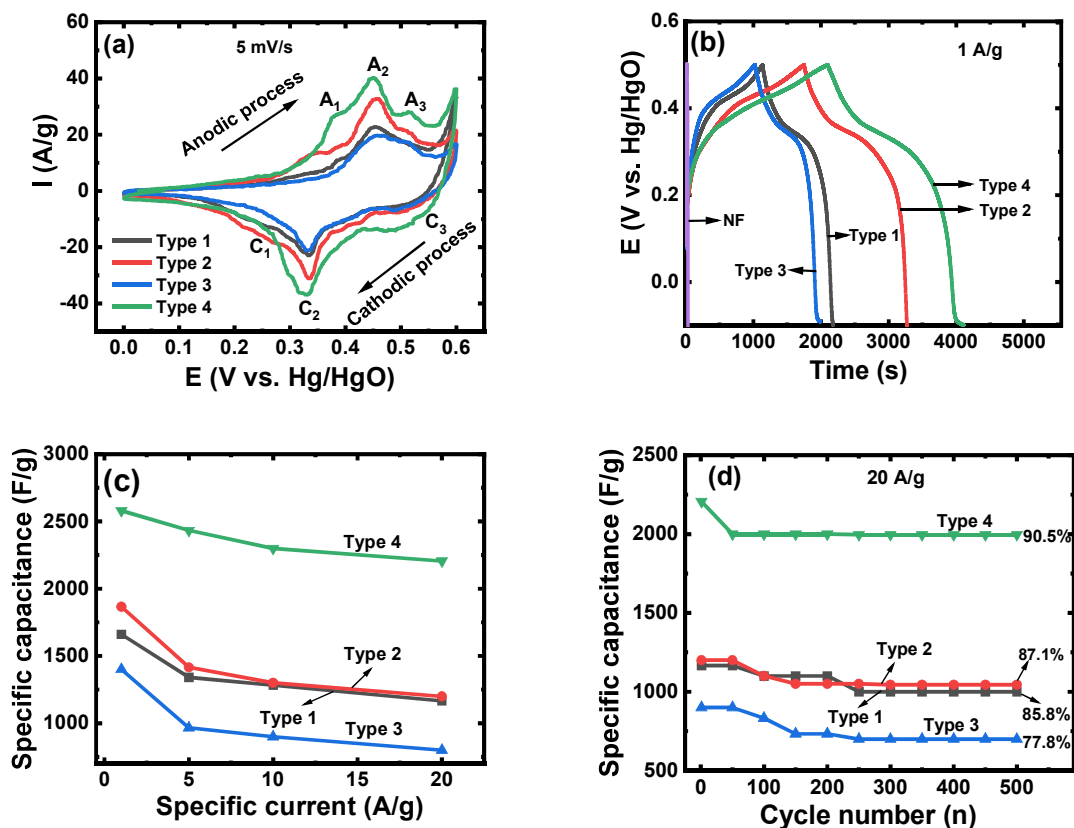


Figure 7.6. (a) Cyclic voltammograms at 5mV/s, (b) Charge-discharge curves at 1 A/g, (c) Variation of specific capacitance at different specific current graph, (d) Cycling performance for 500 cycles at a specific current of 20 A/g of the Type 1 (CV), Type 2 (CV PS +1V), Type 3 (CV PS -1.4V) and Type 4 (CV PRP) Co-Co₃O₄ nanocomposite thin films on NF substrate.

The GCD curves of the four types of Co-Co₃O₄ nanocomposite thin films as well as the bare NF substrate at a specific current of 1 A/g are presented in Figure 7.6(b). The nonlinear nature of the GCD curves shows the pseudocapacitive nature of the Co-Co₃O₄ thin film electrodes. Note that all types of Co-Co₃O₄ nanocomposite thin films do not exhibit significant potential drop (V_{IR}) between the charge and discharge curves, implying good conductivity. It is evident that the Type 4 thin film electrode (CV PRP mode) possesses longer discharge curves compared to the other three types of thin film electrodes indicating that the Type 4 electrode may show higher specific capacitance value. The specific

capacitance estimated from the GCD curves are 1661, 1866, 1400 and 2580 F/g for the Type 1 (CV), Type 2 (CV PS +1.0V), Type 3 (CV PS -1.4V) and Type 4 (CV PRP), respectively at a current load of 1 A/g using equation (7.3),

$$C = \frac{I\Delta t}{m\Delta V} \quad (7.3)$$

where C is the specific capacitance, I is the specific current, Δt is the discharge time, m is the electrode mass, and ΔV is the potential change during discharge. These specific capacitance values for Types 1 to 4 are much higher than previously reported values. Aboelazm *et al.* reported a specific capacitance value of 1273 F/g at 1 A/g for their hierarchical Co_3O_4 nanostructures prepared by magnetic electrodeposition at a constant voltage of -1.0 V for 20 s on nickel foam [32]. Zhang *et al.* reported a specific capacitance value of 1520 F/g at 1 A/g on their Co- Co_3O_4 nanosheet arrays deposited on activated carbon cloth by electrodeposition and a post annealing at 400 °C [23]. Specific capacitance values much lower than these authors have been reported on Co_3O_4 electrodes on different substrate materials prepared by various other fabrication techniques as reported in a review by Uke *et al.* [2]. The GCD curves were used for the quantitative analysis while the CV curves were used (Figure 7.6(a)) for qualitative understanding of the expected specific capacitance behavior.

Figure 7.6(c) shows the capacitance variation of the four types of thin film electrodes at the specific currents of 1, 5, 10 and 20 A/g. The specific capacitance is found to decrease with the increasing current density possibly due the minimum electrolytic contact with the electrode material at higher current densities. At higher constant discharge currents, the OH^-

ions from the electrolyte reach only the outer surface of the electrode; thus, the electrode material at the inner surface does not get fully involved in the electrochemical reactions resulting in lower specific capacitance. This phenomenon where low specific capacitance values are attributed to the poor electrochemical reactivity between the electrolytes and the electrode materials has been commonly observed by other authors [2, 15, 29, 30].

The high capacitance of the Type 4 (CV PRP) thin film electrode could be attributed to the interconnected nanoflake-like morphology decorated with cloudy structures providing maximum surface area at the electrode/electrolyte interface. Additionally, the higher O/Co atomic ratio obtained from the EDX compositional analysis may also contribute to the high charge storage capacity. The dependence of the specific capacitance on the oxide content in the electrode material was confirmed by the EDX compositional analysis as shown in Figure 7.7. It is clear from the graph that higher O/Co atomic ratio indicating higher oxide content in the electrode thin films show higher specific capacitance.

While electrode materials with high specific capacitance are important, long-term cycling stability is another important aspect in practical applications of supercapacitors. The cycling performance of the four types of thin film electrodes deposited on NF substrate under four different electrodeposition modes was, therefore, evaluated and is presented in Figure 7.6(d). The cyclic performance was evaluated by conducting charge-discharge measurements at a current load of 20 A/g for 500 cycles. The specific capacitance retention was found to be 77.8% for Type 1 (CV only), 87.1% for Type 2 (CV +1.0V), and 85.8% for Type 3 (CV - 1.4V) thin films while the Type 4 (CV PRP) shows maximum retention of 90.5% after 500 cycles.

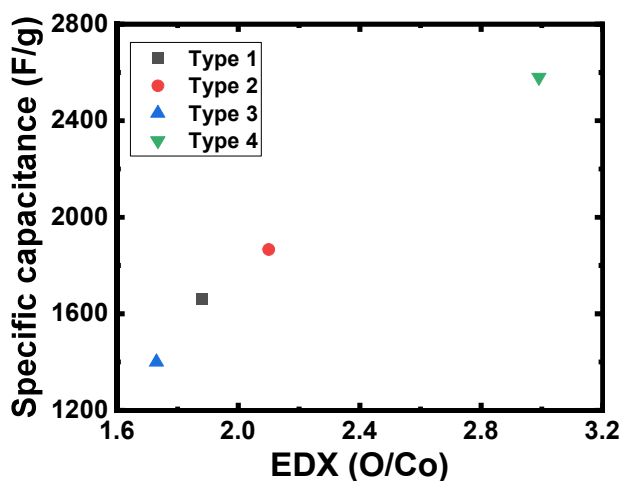


Figure 7.7. Variation of specific capacitance as a function of O/Co atomic ratio obtained from EDX analysis for Type 1 (CV), Type 2 (CV PS +1V), Type 3 (CV PS - 1.4V) and Type 4 (CV PRP) Co- Co₃O₄ nanocomposite thin films on NF substrate.

The high specific capacitance as well as its maximum retention of Type 4 thin films as compared to the other types which show relatively lower specific capacitance and retention demonstrates as an ideal combination for practical applications while the ease of developing these thin film electrodes shows promises to future large-scale manufacturing. The SEM image and the CV curve at 5 mV/s for the Type 4 thin film after 500 GCD cycles have been presented in Figure S7.3 of the supplementary data.

In addition to the specific capacitance investigations, electrochemical impedance spectroscopy (EIS) was also carried out to investigate the charge kinetic properties of the electrode in a frequency range from 10 mHz to 100 kHz. Figure 6.8(a) shows Nyquist plots of the Co-Co₃O₄ nanocomposite thin film electrodes deposited by the four different electrodeposition modes. All four types apparently present almost straight lines with maximum slope for Type 4 (CV PRP) with nearly vertical line. The slopes 1.7, 3.3, 1.9, and 5.4 for Type 1, Type 2, Type 3, and Type 4 respectively change systematically and is found

complementary with the obtained specific capacitance of the electrodes. The electrode with capacitive characteristic shows higher slope, for example in case of Type 4 [14]. Type 4 shows a nearly vertical straight line compared to the others indicating better capacitor behavior. Figure 7.8(b) and (c) show the Bode plots of the four types of the thin film electrodes. At very high frequencies, the intercept of the plot with the X-axis represents the equivalent series resistance (ESR) as shown in Figure 7.8(b), which is a combination of the electrolyte resistance, the intrinsic resistance of the active material, and the contact resistance at the electrode-electrolyte interface [9]. The ESR values of all four types of thin films are found to be very low.

Figure 7.8(b) shows the impedance of the four electrode types. The Type 4 (CV PRP) electrode shows a lower impedance compared to the other three electrode types. The Bode plot in Figure 7.8(c) describes the relationship between phase angle and frequency which shows that the four electrodes electrodeposited by Type 1, Type 2, Type 3 and Type 4 respectively processes exhibit a good capacitive performance at phase angles 55.9 °, 64.9 °, 54.6 ° and 71.7 °, respectively [14]. A phase angle of 90° is typically observed only in EDLCs using carbon materials whereas deviations from 90° are commonly observed in pseudocapacitors. The relaxation time (τ) in seconds (s) was calculated using the following equation (7.4):

$$\tau = \frac{1}{f_o} \quad (7.4)$$

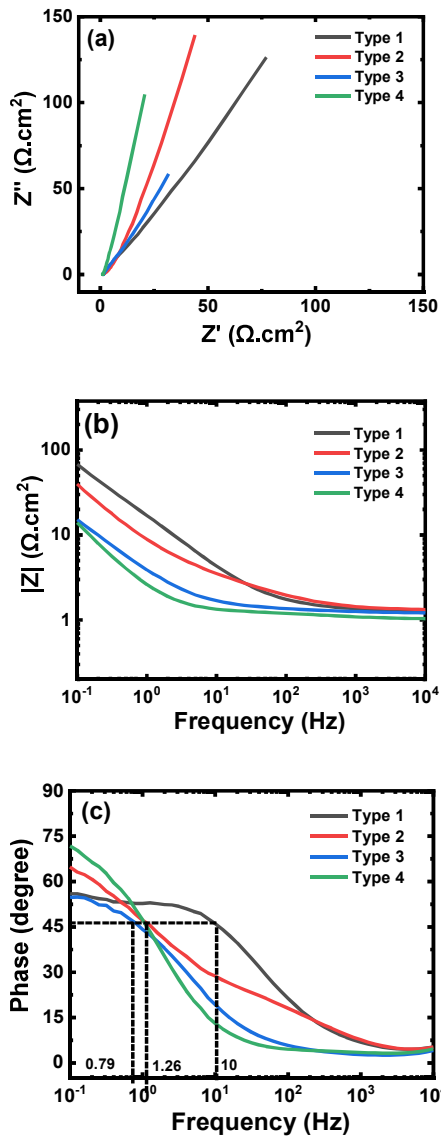


Figure 7.8. (a) Nyquist plots, (b) Bode plot of the frequency's dependence on the impedance magnitude ($|Z|$), (c) Bode plots of the frequency's dependence on the phase angle of the Type 1 (CV), Type 2 (CV PS +1V), Type 3 (CV PS -1.4V) and Type 4 (CV PRP) Co-Co₃O₄ nanocomposite thin films synthesized on NF substrate.

where (f_o) is the frequency at the phase angle of 45° and they were computed to be 0.10, 0.62, 1.10, and 0.60 s for Type 1, Type 2, Type 3, and Type 4, respectively (Figure 7.8(c)). Shorter relaxation time indicates that the electrode could switch more rapidly from resistive behavior to capacitive behavior [32].

7.5 Conclusion

Co-Co₃O₄ nanocomposite thin films electrode materials have been synthesized on nickel foam (NF) substrates using four different electrodeposition modes, namely, cyclic voltammetry (CV), combination of cyclic voltammetry and potentiostatic at -1.4 V (CV PS -1.4V), combination of cyclic voltammetry and potentiostatic at 1.0 V (CV PS +1.0V) and combination of cyclic voltammetry and pulse reverse potential (CV PRP). The XRD patterns have confirmed the presence of Co and Co₃O₄ on all the electrodes. The chemical nature of the electrode thin films has been complemented by the presence of Co₃O₄ absorption bands and strong oxygen peak intensities on the FTIR and EDX spectra respectively. The SEM images have revealed porous microfeatures which changes slightly for different electrodeposition modes, fulfilling the important criterion of its contributing to large specific surface area of the electrode surfaces. The Type 4 film synthesized by combining cyclic voltammetry and pulse reverse potential processes (CV PRP) is found to have resulted in a maximum specific capacitance of 2580 F/g while the Types 1, 2 and 3 thin films deposited by cyclic voltammetry (CV), combination of cyclic voltammetry and potentiostatic at -1.4 V (CVPS -1.4V), combination of cyclic voltammetry and potentiostatic at 1.0 V (CVPS +1.0V) have resulted in specific capacitance values of 1661, 1400, 1866 F/g respectively. Their respective capacitance retention for Type 1, 2, 3 and 4 thin film electrodes have been found to be 85.8, 77.8, 87.1, and 90.5 %, after 500 cycles of charging/discharging under a high current load of 20 A/g. Comparative analysis shows that the Type 4 thin film electrode material electrodeposited by CV PRP process has a greater potential as high-performance

supercapacitor material in terms of high specific capacitance and charging/discharging cycle stability. These results and observations place the Type 4 (CV PRP) electrode as the ideal material for practical applications and show promises for future large-scale manufacturing due to the ease of fabrication of these thin films.

7.6 References

- [1] M.A.A. Mohd Abdah, N.H.N. Azman, S. Kulandaivalu, Y. Sulaiman, Review of the use of transition-metal-oxide and conducting polymer-based fibres for high-performance supercapacitors, *Mater. Des.*, 186 (2020) 108199.
- [2] S.J. Uke, V.P. Akhare, D.R. Bambole, A.B. Bodade, G.N. Chaudhari, Recent Advancements in the Cobalt Oxides, Manganese Oxides, and Their Composite As an Electrode Material for Supercapacitor: A Review, *Front. Mater.*, 4 (2017) 21.
- [3] P. Sivakumar, C.J. Raj, D.O. Opar, J. Park, H. Jung, Two dimensional layered nickel cobaltite nanosheets as an efficient electrode material for high-performance hybrid supercapacitor, *Int. J. Energy Res.*, 45 (2021) 1–11.
- [4] H. Zhu, J. Liu, Q. Zhang, J. Wei, High electrochemical performance of metal azolate framework-derived ZnO/Co₃O₄ for supercapacitors, *Int. J. Energy Res.*, 44 (2020) 8654-8665.
- [5] A.D. Jagadale, V.S. Kumbhar, C.D. Lokhande, Supercapacitive activities of potentiodynamically deposited nanoflakes of cobalt oxide (Co₃O₄) thin film electrode, *J. Colloid Interface Sci.*, 406 (2013) 225-230.
- [6] S.K. Meher, G.R. Rao, Ultralayered Co₃O₄ for High-Performance Supercapacitor Applications, *J. Phys. Chem. C*, 115 (2011) 15646-15654.
- [7] R. Liang, Y. Du, P. Xiao, J. Cheng, S. Yuan, Y. Chen, J. Yuan, J. Chen, Transition Metal Oxide Electrode Materials for Supercapacitors: A Review of Recent Developments, *Nanomaterials* 11 (2021) 1248.
- [8] F. Ali, N.R. Khalid, G. Nabi, A. Ul-Hamid, M. Ikram, Hydrothermal synthesis of cerium-doped Co₃O₄ nanoflakes as electrode for supercapacitor application, *Int. J. Energy Res.*, 45 (2020) 1999-2010.
- [9] S.G. Mohamed, S.Y. Attia, H.H. Hassan, Spinel-structured FeCo₂O₄ mesoporous nanosheets as efficient electrode for supercapacitor applications, *Microporous Mesoporous Mater.*, 251 (2017) 26-33.
- [10] M. Gao, W.K. Wang, Q. Rong, J. Jiang, Y.J. Zhang, H.Q. Yu, Porous ZnO-Coated Co₃O₄ Nanorod as a High-Energy-Density Supercapacitor Material, *ACS Appl. Mater. Interfaces*, 10 (2018) 23163-23173.
- [11] J. Mei, W. Fu, Z. Zhang, X. Jiang, H. Bu, C. Jiang, E. Xie, W. Han, Vertically-aligned Co₃O₄ nanowires interconnected with Co(OH)₂ nanosheets as supercapacitor electrode, *Energy*, 139 (2017) 1153-1158.

- [12] X. Yan, L. Tian, M. He, X. Chen, Three-Dimensional Crystalline/Amorphous Co/Co₃O₄ Core/Shell Nanosheets as Efficient Electrocatalysts for the Hydrogen Evolution Reaction, *Nano Lett*, 15 (2015) 6015-6021.
- [13] S.R. Yousefi, H.A. Alshamsi, O. Amiri, M. Salavati-Niasari, Synthesis, characterization and application of Co/Co₃O₄ nanocomposites as an effective photocatalyst for discoloration of organic dye contaminants in wastewater and antibacterial properties, *J. Mol. Liq.*, 337 (2021) 116405.
- [14] M. Harilal, S.G. Krishnan, B.L. Vijayan, M. Venkatesh Reddy, S. Adams, A.R. Barron, M.M. Yusoff, R. Jose, Continuous nanobelts of nickel oxide–cobalt oxide hybrid with improved capacitive charge storage properties, *Mater. Des.*, 122 (2017) 376-384.
- [15] A.D. Jagdale, V.S. Kumbhar, R.N. Bulakhe, C.D. Lokhande, Influence of electrodeposition modes on the supercapacitive performance of Co₃O₄ electrodes, *Energy*, 64 (2014) 234-241.
- [16] F. Ali, N.R. Khalid, Facile synthesis and properties of chromium-doped cobalt oxide (Cr-doped Co₃O₄) nanostructures for supercapacitor applications, *Appl. Nanosci.*, 10 (2020) 1481-1488.
- [17] A. García-Gómez, S. Eugénio, R.G. Duarte, T.M. Silva, M.J. Carmezim, M.F. Montemor, Electrodeposited reduced-graphene oxide/cobalt oxide electrodes for charge storage applications, *Appl. Surf. Sci.*, 382 (2016) 34-40.
- [18] M.K. Lima-Tenório, C.S. Ferreira, Q.H.F. Rebelo, R.F.B.d. Souza, R.R. Passos, E.A.G. Pineda, L.A. Pocrifka, Pseudocapacitance Properties of Co₃O₄ Nanoparticles Synthesized Using a Modified Sol-Gel Method, *Mater. Res.*, 21 (2018) e20170521.
- [19] J.P. Cheng, X. Chen, J.-S. Wu, F. Liu, X.B. Zhang, V.P. Dravid, Porous cobalt oxides with tunable hierarchical morphologies for supercapacitor electrodes, *CrystEngComm*, 14 (2012) 6702–6709.
- [20] Y. Li, X. Li, Z. Wang, H. Guo, T. Li, Distinct impact of cobalt salt type on the morphology, microstructure, and electrochemical properties of Co₃O₄ synthesized by ultrasonic spray pyrolysis, *J. Alloys Compd.*, 696 (2017) 836-843.
- [21] E. Valatka, I. Kelpšaitė, J. Baltrušaitis, Electrochemical Deposition of Porous Cobalt Oxide Films on AISI 304 Type Steel, *Mater. Sci.*, 17 (2011) 236-243.
- [22] M. Aghazadeh, M. Hosseini-fard, B. Sabour, S. Dalvand, Pulse electrochemical synthesis of capsule-like nanostructures of Co₃O₄ and investigation of their capacitive performance, *Appl. Surf. Sci.*, 287 (2013) 187-194.
- [23] M. Zhang, Y. Xu, H. Fan, N. Zhao, B. Yan, C. Wang, J. Ma, A.K. Yadav, W. Zhang, Z. Du, X. Zheng, M. Li, G. Dong, W. Wang, In situ synthesis of 3D Co@Co₃O₄ nanosheet arrays for hybrid supercapacitors with ultra-high rate performance, *J. Alloys Compd.*, 826 (2020) 154115.
- [24] E. Duraisamy, P. Gurunathan, H.T. Das, K. Ramesha, P. Elumalai, [Co(salen)] derived Co/Co₃O₄ nanoparticle@carbon matrix as high-performance electrode for energy storage applications, *J. Power Sources*, 344 (2017) 103-110.
- [25] B. Qiu, W. Guo, Z. Liang, W. Xia, S. Gao, Q. Wang, X. Yu, R. Zhao, R. Zou, Fabrication of Co₃O₄ nanoparticles in thin porous carbon shells from metal–organic frameworks for enhanced electrochemical performance, *RSC Adv.*, 7 (2017) 13340-13346.
- [26] H. Cai, Q. Wei, H. Xiao, H. Liu, J. Wang, Preparation and microwave absorption properties of petal CoO/CNFs composites, *J. Mater. Sci.: Mater. Electron*, 31 (2020) 7606-7615.

- [27] F. Liu, H. Su, L. Jin, H. Zhang, X. Chu, W. Yang, Facile synthesis of ultrafine cobalt oxide nanoparticles for high-performance supercapacitors, *J. Colloid Interface Sci.*, 505 (2017) 796-804.
- [28] M. Aadil, S. Zulfiqar, M. Shahid, S. Haider, I. Shakir, M.F. Warsi, Binder free mesoporous Ag-doped Co_3O_4 nanosheets with outstanding cyclic stability and rate capability for advanced supercapacitor applications, *J. Alloys Compd.*, 844 (2020) 156062.
- [29] Rusi, P.Y. Chan, S.R. Majid, Layer by Layer Ex-Situ Deposited Cobalt-Manganese Oxide as Composite Electrode Material for Electrochemical Capacitor, *PloS one*, 10 (2015) e0129780.
- [30] M. Mirzaeian, N. Akhanova, M. Gabdullin, Z. Kalkozova, A. Tulegenova, S. Nurbolat, K. Abdullin, Improvement of the Pseudocapacitive Performance of Cobalt Oxide-Based Electrodes for Electrochemical Capacitors, *Energies*, 13 (2020) 5228.
- [31] F. Zhang, C. Yuan, X. Lu, L. Zhang, Q. Che, X. Zhang, Facile growth of mesoporous Co_3O_4 nanowire arrays on Ni foam for high performance electrochemical capacitors, *J. Power Sources*, 203 (2012) 250-256.
- [32] E.A.A. Aboelazm, G.A.M. Ali, H. Algarni, H. Yin, Y.L. Zhong, K.F. Chong, Magnetic Electrodeposition of the Hierarchical Cobalt Oxide Nanostructure from Spent Lithium-Ion Batteries: Its Application as a Supercapacitor Electrode, *J. Phys. Chem. C*, 122 (2018) 12200-12206.

7.7 Supporting information

(a) Published supporting information (*Nuamah RA, Noormohammed S, Sarkar*

DK. Specific capacitance behavior of Co-Co₃O₄ nanocomposite thin films synthesized via different electrodeposition modes. Int J Energy Res. 2022;46(4):4434-4444).

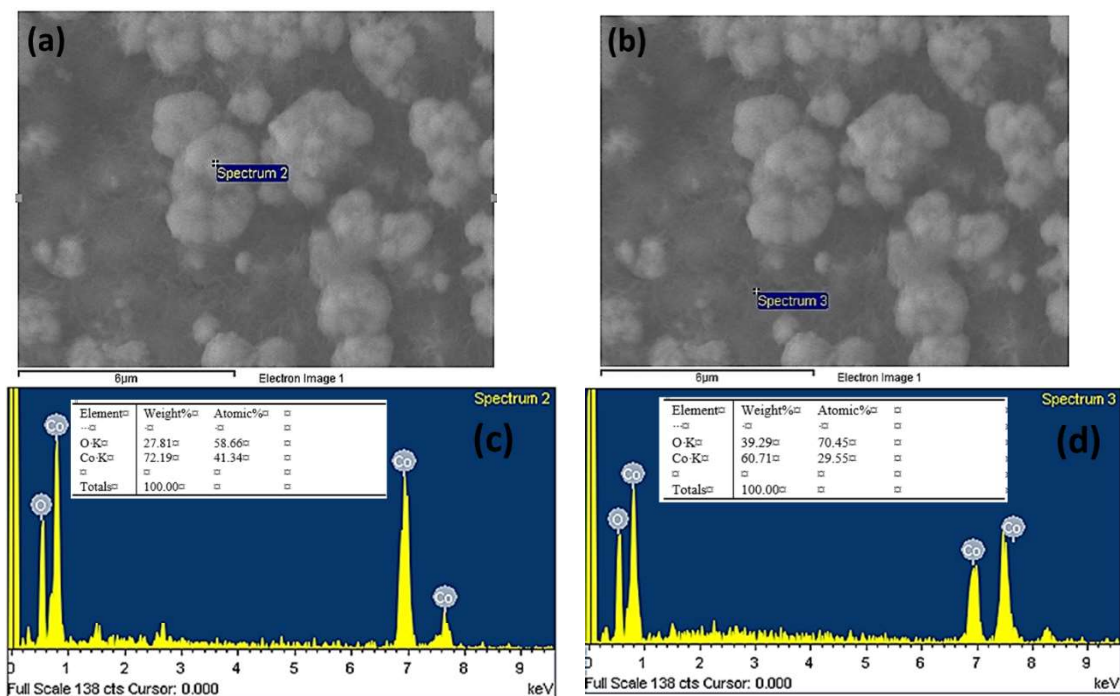


Figure S7.1. EDX analysis of (a,c) sponge-like material (b,d) matrix (film) of Type 4 (CV PRP) Co_3O_4 nanocomposite thin on NF substrate.

The SEM image of Type 4 (CV PRP) Co- Co_3O_4 nanocomposite thin film after 500 GCD cycles in Figure S7.3 (a) shows that the morphology was maintained even after the 500 cycles. In addition, the less loss of area of the after-cycle CV curve in comparison to the before-cycle CV curve in Figure S7.3(b) further corroborates the good stability of the Type 4 film.

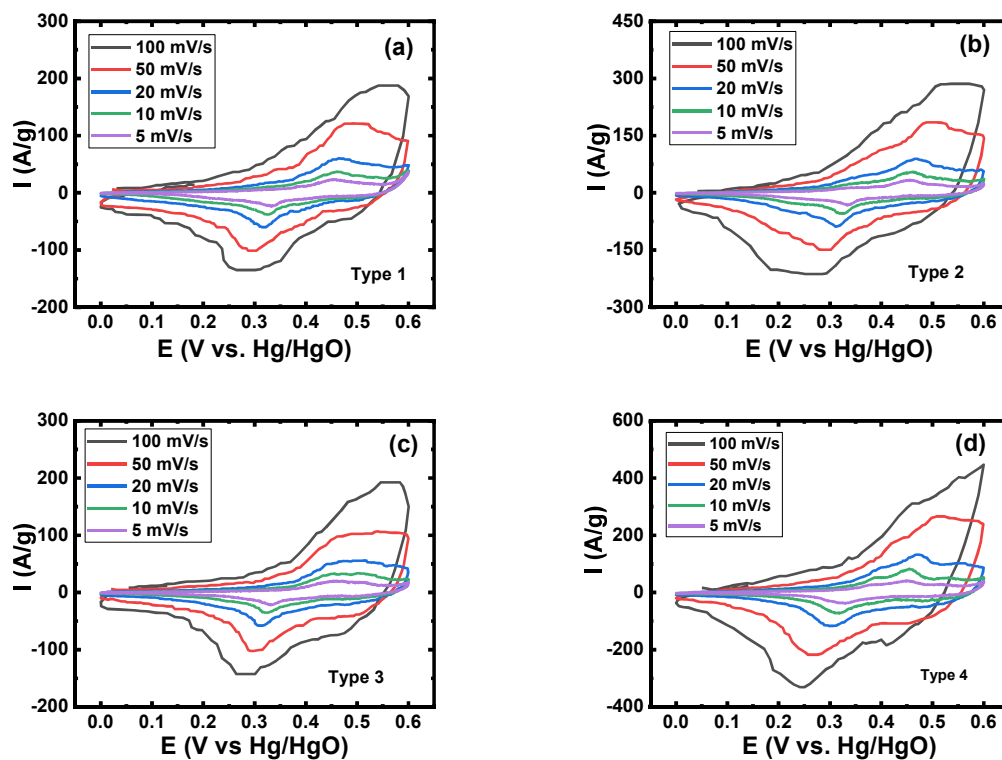


Figure S7.2. Cyclic voltammetry curves of (a) Type 1 (CV) (b) Type 2 (CV PS +1V) (c) Type 3 (CV PS -1.4V) (d) Type 4 (CV PRP) Co-Co₃O₄ nanocomposite thin films on NF substrate at different scan rates.

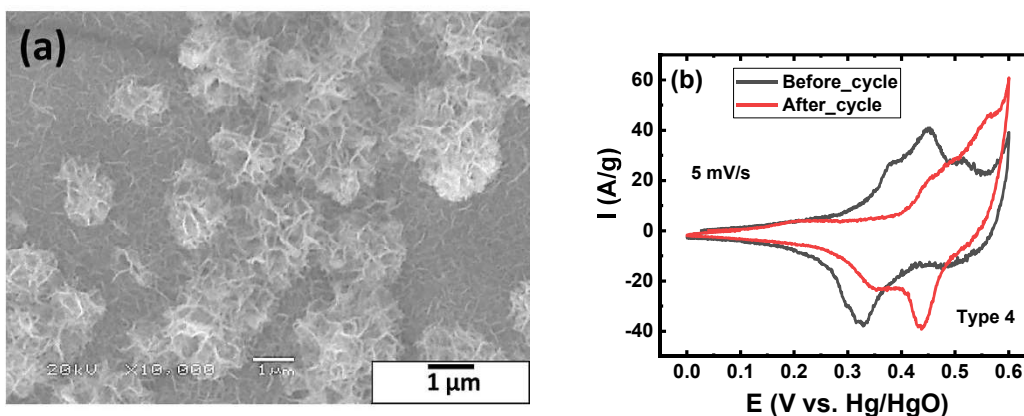


Figure S7.3. (a) SEM image (b) Comparison of the before and after cycle cyclic voltammetry (CV) curves of Type 4 (CV PRP) Co-Co₃O₄ nanocomposite thin film on NF substrate after 500 charge-discharge (GCD) cycles.

(b) Unpublished supporting information

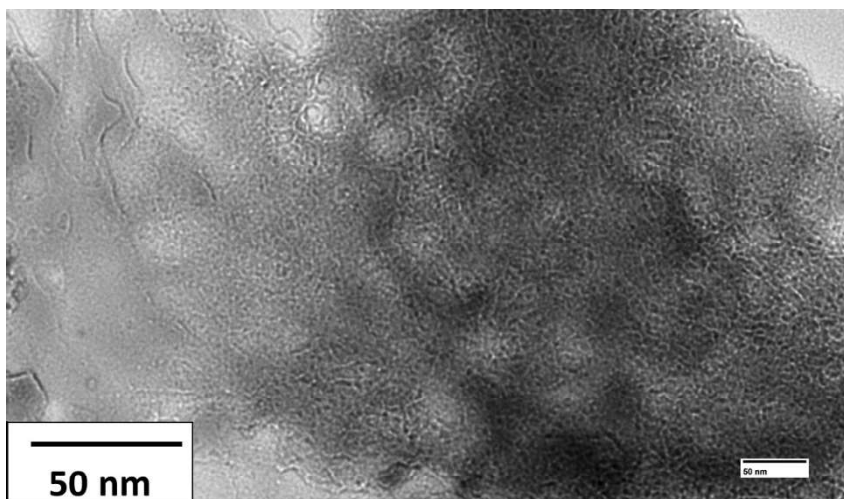


Figure S7.4. TEM image of Type 4(CV PRP) Co-Co₃O₄ nanocomposite thin film.

The porous flake-like morphology of Type 4(CV PRP) Co-Co₃O₄ nanocomposite thin film can be observed clearly in the TEM image of Figure S7.4. This observation is complementary to the SEM observation. Furthermore, the image reveals that the nanoflakes are composed of numerous interconnected particles with particle sizes in the range of 3-5 nm.

Table S7.1. : Crystallite size of the Co (102) and Co₃O₄ (400) planes estimated from the XRD data and thickness of the various types of Co-Co₃O₄ nanocomposite thin films

Electrodeposition mode	Crystallite size (nm)	Crystallite size (nm)	Thickness (nm)
	Co (102)	Co ₃ O ₄ (400)	
CV (Type 1)	18	36	267
CV PS +1.0V (Type 2)	13	29	267
CVPS -1.4V (Type 3)	24	21	200
CVPRP (Type 4)	19	25	200

The average density of (Co, Co₃O₄), area, and mass of the films have been used to estimate the thickness by applying the equation (S7.1):

$$t = \frac{m}{\rho A} \quad (S7.1)$$

where t is thickness, m is mass, ρ is average density and A is area. Also, the crystallite size for the Co-Co₃O₄ thin film composites was estimated from the XRD data by using Scherrer's formula in equation (S7.2),

$$D = \frac{0.94\lambda}{\beta \cos\theta} \quad (S7.2)$$

where 'D' is crystallite size, ' β ' is full width at half maxima, ' λ ' is wavelength of X-ray used and ' θ ' is diffraction angle [15]. The calculated thickness and crystallite size values of the various film types have been presented in table S7.1.

CHAPTER 8: SUPERCAPACITOR PERFORMANCE EVALUATION OF NANOSTRUCTURED Ag-DECORATED Co-Co₃O₄ COMPOSITE THIN FILM ELECTRODE MATERIAL

Rania Afia Nuamah, Saleema Noormohammed, Dilip Kumar Sarkar

Department of Applied Science, University of Quebec at Chicoutimi, Aluminum Research Center-REGAL, Chicoutimi, Quebec, G7H 2B1, Canada

This article has been published in:

International Journal for Energy Research 46 (2022) 13099-13110

8.1 Abstract

Nanostructured Ag-decorated Co-Co₃O₄ composite thin film (Ag/Co-Co₃O₄) synthesized on nickel foam (NF) by a combination of cyclic voltammetry and pulse reverse potential (CV PRP) electrodeposition modes presents higher specific capacitance and its retention. The higher specific capacitance of 2800 F/g on Ag/Co-Co₃O₄/NF composite thin film in comparison with 2580 F/g on Co-Co₃O₄/NF at 1 A/g is attributable to the presence of nanostructured Ag in the composite film enhancing the ionic and electronic conductivity of the material. The morphology revealed by the scanning electron microscope (SEM) correlates the electrochemical and capacitance behavior while the energy-dispersive X-ray spectroscopy (EDX) spectra confirmed the presence of Co, Ag, and O in the Ag/Co-Co₃O₄/NF composite thin film. The attenuated total reflection – Fourier transform infrared (ATR – FTIR) spectra obtained further confirmed the presence of Co-O bonds. The Ag/Co-

Co₃O₄/NF composite thin film presented an amorphous nature as revealed by the X-ray diffraction (XRD) spectra. In addition, the Ag/Co-Co₃O₄/NF electrode exhibited a maximum specific energy of 69.5 Wh/kg, specific power of 6.6 kW/kg and capacitance retention of 82.6 % after 1000 cycles, while the Co-Co₃O₄ electrode (with no Ag) showed lower specific energy of 60.8 Whkg⁻¹, specific power of 5.8 kW/kg, and a capacitance retention of 78.2 % after 1000 cycles. Further, by the incorporation of Ag, the composite electrode showed a reduction in the equivalence series resistance (ESR) value from 1.5 Ω.cm² (Co-Co₃O₄/NF) to 1.0 Ω.cm² (Ag/Co-Co₃O₄/NF) as well as in the charge transfer resistance (R_{ct}) from 2.86 Ω.cm² (Co-Co₃O₄/NF) to 0.96 Ω.cm² (Ag/Co-Co₃O₄/NF) indicating the positive influence of the presence of Ag in the film. The electrochemical evaluation indicates that a synergistic effect between Ag and Co-Co₃O₄ enhances supercapacitor electrode performance.

8.2 Introduction

The shift from the usage of fossil-based fuels towards renewable energy sources due to various environmental concerns coupled with the increase in demand for energy as a result of population growth requires energy storage devices to overcome the renewable energy shortage during their intermittent periods [1]. Supercapacitors particularly have received massive attention in the field of research as energy storage devices due to their high energy density, lightweight, fast charge-discharge rates, long life span, easy and safe operations [1-5]. Among the diverse supercapacitor electrode materials such as carbonaceous materials (activated carbon, graphene, carbon nanotubes, etc.), conducting polymers (polypyrrole, polyaniline), transition metal oxides (TMOs), TMOs are widely attractive due to their high

electronegativity, low cost, environmental friendliness, and multiple oxidation states which enhances redox reactions for high s capacitance [4, 6, 7]. Noble TMOs (for example RuO_2) are optimum pseudocapacitive materials due to their high theoretical capacitance, reversibility, and fast Faradaic reactions. However, they are toxic and expensive thereby limiting their commercialization [7, 8]. On the contrary, base TMOs such as Co_3O_4 , NiO , MnO_2 , and Fe_2O_3 besides their high theoretical capacitance are environmentally friendly, inexpensive, and easy to process [6, 9-11]. Among the base TMOs, cobalt oxide (Co_3O_4) has been considered as one of the promising electrode materials owing to its high theoretical specific capacitance (3560 F/g), low-cost, excellent reversibility, and nontoxicity [11, 12]. Further, nanostructured Co_3O_4 coatings have been found widely useful in other types of applications as well including electrocatalysts for oxygen evolution reaction [13] and biological applications as antibacterial agents [14].

Despite their outstanding properties, Co_3O_4 materials are plagued with low electronic conductivity and limited topographical surface area for effective redox reactions, leading to lower reported specific capacitance values versus their theoretical capacitance, poor reversibility, and poor capacitance retention at higher current densities [1, 15].

In view of overcoming these challenges, several synthesis techniques such as hydrothermal, chemical precipitation, and sol-gel have been and are being experimented constantly to prepare nanostructured cobalt oxide-based materials. These techniques, however, require the inclusion of adhesive binders and conducting agents which increase the “dead volume” of the electrode thereby increasing the electrode resistance and reducing redox-active sites [16-19]. The electrodeposition, on the other hand, poses as a useful method for growing cobalt oxide-based nanostructures directly onto substrates without the need for

adhesive binders, presenting the advantages of obtaining increased apparent surface area owing to the resulting nanofeatures. Studies have shown that by adjusting experimental conditions such as electrodeposition mode, precursor electrolyte composition, time, and temperature, materials with desired composition and morphological properties can be obtained. Our recent work on Co-Co₃O₄ nanostructured supercapacitor electrodes has presented such favorable features leading to increased specific capacitance and high capacitance retention [20]. Other studies have reported arrays of morphologies for Co₃O₄ prepared by electrodeposition method including features such as nanoflowers, nanosheets, and nanocolumnar structure which leads to a general conclusion on the ultimate benefit of having nanostructured morphological features leading to increased surface areas, favorable for increased redox reactions [15, 21, 22].

Subsequently, it can be agreed that the electrical conductivity leading to enhanced total electrochemical performance of Co₃O₄-based materials can be improved extrinsically and intrinsically either by forming composites or by doping with conductive metals (Cd, Mn, Cr, Ag, etc.) or conductive matrixes (carbon nanotube (CNT), reduced graphene oxide (r-GO), etc.) [5, 8, 23]. For example, Du *et al.* showed improved specific capacitance of pure Co₃O₄ from 300 F/g to 894 F/g on a composite of Co₃O₄ nanosheets anchored on reduced graphene oxide with improved conductivity [23]. Similarly, Deng *et al.* also reported an improved specific capacitance of 737 F/g and charge transfer resistance of $1.031 \times 10^{-7} \Omega$ on their Cd-doped Co₃O₄ (Cd-Co₃O₄) nanosheets compared to those of pure cobalt (436 F/g and 0.0109 Ω) [8]. Core-shell nanocomposite structures have also been considered to improve supercapacitor performances as they provide porous channels for efficient and rapid pathways for ion and electron transport, rich accessible electroactive sites, and cycle stability

[24]. In a study by Xia *et al.*, $\text{Co}_3\text{O}_4@\text{NiO}/\text{NF}$ core-shell nanostructure arrays provided a specific capacitance of 853 F/g and excellent cycling stability after 6000 cycles compared to 642 F/g on their Co_3O_4 nanowire arrays and 178 F/g for the NiO nanoflake arrays. It was observed that the NiO nanoflakes were well separated and formed a porous layer surrounding the Co_3O_4 nanowire core thereby making both the shell and core fully reachable for the electrolyte for improved electron and ion diffusion [25]. Similarly, Xu *et al.* fabricated $\text{Co}_3\text{O}_4@\text{NiCo}_2\text{O}_4$ core-shell nanosheets on Ni foam which exhibited much higher capacitance of 1330 F/g and cycle stability 100.7 % after 5000 cycles with comparatively lower capacitance performance on Co_3O_4 electrode alone [26].

In this study, considering the advantages of Co_3O_4 as supercapacitor material and the challenges in enhancing their conductivity and specific capacitance, we have incorporated Ag in- preparing Ag-decorated Co- Co_3O_4 (Ag/Co- Co_3O_4) nanostructured composite thin film on nickel foam (NF) substrates by combining cyclic voltammetry and pulse reverse potential (CV PRP) modes of electrodeposition from an electrolyte composed of AgNO_3 , CoCl_2 , and $\text{Co}(\text{CH}_3\text{COO})_2$ salts solution. To elucidate the enhancement of electrochemical properties by the addition of Ag, Co- Co_3O_4 composite thin films have also been prepared on NF using the same method we recently published and investigated as control counterparts. The morphological, structural, and compositional analyses correlate the electrochemical behavior specifically the CV, EIS, and charge-discharge performance confirming the advantages of the presence of Ag in the films. The Ag/Co- $\text{Co}_3\text{O}_4/\text{NF}$ composite thin film is found to achieve a very high capacitance which is ~12 % more than the Co- $\text{Co}_3\text{O}_4/\text{NF}$ with stable cycling performance and capacitance retention.

8.3 Experimental details

Cobalt-cobalt oxide ($\text{Co-Co}_3\text{O}_4$) and Ag-decorated $\text{Co-Co}_3\text{O}_4$ ($\text{Ag/Co-Co}_3\text{O}_4$) nanocomposite thin films were electrodeposited on nickel foam (NF) substrates by cyclic voltammetry (CV) followed by pulse reverse potential (CV PRP) cycled between -1.4 V and +1.0 V [20]. Initially, CV was performed in a potential range of -1.4 to +1.0 V vs Ag/AgCl at a scan rate of 20 mVs^{-1} for 2 cycles, followed by pulse reverse potential (PRP) of 60 cycles at -1.4 V and 1 V with 0.5 s/0.5 s time interval for a total duration of 60 s. The electrolyte solutions used for the electrodeposition of $\text{Co-Co}_3\text{O}_4/\text{NF}$ consist of 0.1 M cobalt acetate ($\text{Co}(\text{CH}_3\text{CO}_2)_2 \cdot 4 \text{ H}_2\text{O}$, 6 mL), 0.1 M cobalt chloride (CoCl_2 24 mL) and 0.2 M sodium perchlorate ($\text{NaClO}_4 \cdot \text{H}_2\text{O}$, 30 mL). Similarly, the $\text{Ag/Co-Co}_3\text{O}_4/\text{NF}$ thin film was deposited using the same precursor solutions like that of the $\text{Co-Co}_3\text{O}_4$ but with the addition of 0.1 M AgNO_3 (2 mL).

In the electrochemical deposition process, the applied negative potential reduces the Co^{2+} and Ag^+ ions into metallic Co and Ag films. Similarly, the use of a positive potential, results in the deposition of a layer of Co_3O_4 . In the present experiment, a maximum negative potential of -1.4 V was used to deposit metallic Co and Ag films and a +1.0 V was used to deposit Co_3O_4 . The pH of both electrolytes was 6.5. Before the electrodeposition process, the NF substrates were etched in 3 M HCl for 15 minutes and subsequently rinsed ultrasonically with ethanol and deionized water for 15 minutes each. A standard three-electrode system with a platinum wire, NF substrate, and Ag/AgCl as the counter, working and reference electrodes, respectively were employed for the deposition process. After electrodeposition, the as-prepared $\text{Co-Co}_3\text{O}_4/\text{NF}$ and $\text{Ag/Co-Co}_3\text{O}_4/\text{NF}$ nanocomposite thin film electrodes

were rinsed in deionized water and dried in air on a hot plate at 200 °C for 45 minutes before further characterization and electrochemical analyses. The mass of the electrodeposited material estimated from the difference in the mass of the NF substrate before the electrodeposition process and with material loading after drying using an analytical microbalance (Sartorius CP124S, max 120g, 0.1 mg of resolution) is 0.3 mg and 0.5 mg for the Co-Co₃O₄ and Ag/Co-Co₃O₄ composite thin films respectively.

A scanning electron microscope (SEM, JEOL JSM-6480 LV), equipped with energy-dispersive X-ray spectroscopy (EDX) was used to study the morphological and elemental analyses respectively, of the electrodeposited thin films. The X-ray diffraction (XRD) analyses were carried out by the Bruker D8 Discover system for crystallographic analysis. An attenuated total reflection – Fourier transform infrared spectroscopy (ATR-FTIR, Agilent Technologies Cary 630) was used to confirm and quantify the deposition of the metal oxide (Co-O).

The electrochemical properties, specifically, cyclic voltammetry (CV), galvanostatic charge-discharge (GCD), and electrochemical impedance spectroscopy (EIS) characteristics, were assessed using a three-electrode glass cell and Solartron SI1287 electrochemical workstation with 1 M KOH aqueous electrolyte. The as-synthesized Co-Co₃O₄/NF and Ag/Co-Co₃O₄/NF nanocomposite thin films on NF substrates were directly employed as working electrodes, with platinum wire and Hg/HgO as counter and reference electrodes respectively. The CV and GCD measurements were carried out at different scan rates and specific currents in a potential window of -0.1 to 0.6 V and -0.1 to 0.5 V respectively. In addition, the EIS measurement was conducted in a frequency range from 10 mHz to 100 kHz.

8.4 Results and discussion

8.4.1 Structural, morphological, and chemical analysis

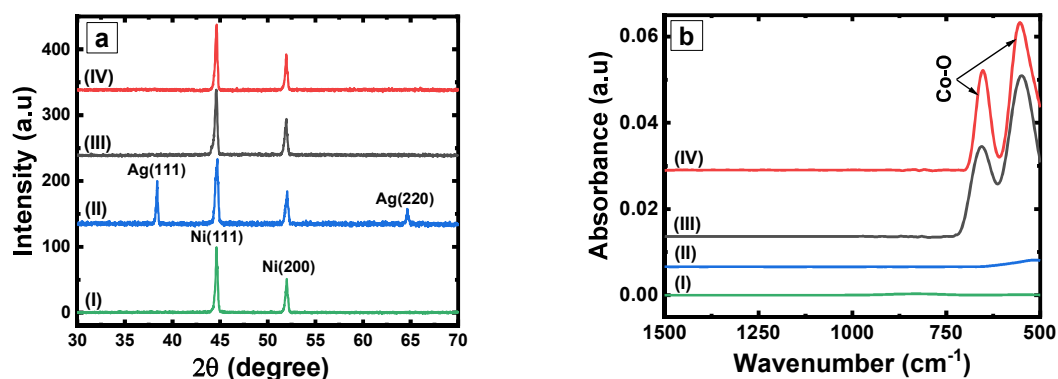


Figure 8.1. (a) XRD patterns and (b) ATR-FTIR spectra of (I) Nickel foam (NF) substrate, (II) Ag thin film on NF, (III) Co-Co₃O₄, and (IV) Ag/Co-Co₃O₄ composite thin films on NF.

The XRD patterns of the NF substrate and the various thin films deposited on the (NF) substrates are presented in Figure 8.1(a), (I)-(IV). The XRD pattern of the NF substrate in Figure 8.1(a)-(I) shows two prominent diffraction peaks at 2θ of 44.5° and 52° which correspond to the Ni(111) and Ni(200) planes of the cubic Ni system (JCPDS card No-00-004-0850). In addition to the Ni(111) plane of the NF substrate, the XRD pattern of Ag thin film on NF substrates in Figure 8.1(a)-(II) revealed two distinct peaks of Ag at 2θ positions of 38.4° and 64.6° . These 2θ positions correspond to the crystal planes of Ag(111) and Ag(220) respectively of the face-centered cubic Ag system (JCPDS card No-00-004-0783). The peaks assigned to Ag are in agreement with those reported by Nagamuthu *et al.* on their

Ag/NiO honeycomb nanostructured arrays prepared by a surfactant-assisted hydrothermal route [11].

In Figures 8.1(a)-(III) and (IV), the XRD patterns of both the Co-Co₃O₄ and Ag/Co-Co₃O₄ composite thin films on NF substrates do not show any visible peaks of Co, Co₃O₄, and Ag apart from the peaks of the NF substrate. This could be a result of the nanostructures being embedded in the pores of the NF substrate, hence the inability in obtaining the signals of the relevant phases. Further, the absence of the peaks could also be attributed to the amorphous nature of both the Co-Co₃O₄/NF and Ag/Co-Co₃O₄/NF composite thin films.

In order to understand the growth mechanism of these films, an investigation was carried out by depositing the same on titanium substrates as reported in our recent work on Ni-NiO and Co-Co₃O₄ [20, 27] and these results have been provided in the supplementary data (Figure S8.1 (a) of the supplementary data). It is to be noted that on titanium substrate (Figure S8.1 (a)), the peaks of Co (100) and Co (101) planes of the hexagonal crystal structure of cobalt (JCPDS card No-00-005-0727), Co₃O₄ (222) and Co₃O₄ (400) plane of the cubic crystal structure of Co₃O₄ (JCPDS card No-42-1467) can be detected at 2θ of 41.7°, 47.5°, 38.5° and 44.5° respectively in the XRD spectrum of the Co-Co₃O₄ composite thin film. The Ag/Co-Co₃O₄ composite on Ti substrate shows similar peaks of Co (100), Co(101), Co₃O₄(222), and Co₃O₄(400) planes together with the Ag (111), Ag (200), and Ag (220) planes. Our Co-Co₃O₄ nanocomposite thin film on Ti substrate by CV PRP mode of electrodeposition further confirms the presence of Co and Co₃O₄ [20]. The deconvoluted peak of Ag/Co-Co₃O₄ at 2θ position of 38.5° clearly shows the Co₃O₄ (222), Ag (111), and Ti(002) (Figure S8.1(b)). Also, the deconvoluted peak at 44.5° shows the merged Co₃O₄ (400) and Ag (200) (Figure S8.1 (c)). It is to be noted that during the addition of AgNO₃ to the

precursor solution of $\text{CoCl}_2 + \text{Co}(\text{CH}_3\text{CO}_2)_2$, a precipitate of AgCl was observed and the EDX analysis showed the presence of Ag in the deposited thin film. However, the coating process was further performed using only $\text{CoCl}_2 + \text{AgNO}_3$ and $\text{CoAc} + \text{AgNO}_3$ separately and the XRD could detect the presence of Ag as evident from the supplementary data (Figure S8.2 (a-c)).

In order to confirm the presence of Co_3O_4 and the incorporation of Ag in Co_3O_4 in the $\text{Ag}/\text{Co}-\text{Co}_3\text{O}_4/\text{NF}$ composite thin film undetected by the XRD analysis, ATR-FTIR spectra were further recorded on these films deposited on the NF substrates, namely, Ag thin film on NF, $\text{Co}-\text{Co}_3\text{O}_4/\text{NF}$, and $\text{Ag}/\text{Co}-\text{Co}_3\text{O}_4/\text{NF}$ composite thin films. These spectra recorded in the range of $1500\text{-}500\text{ cm}^{-1}$ are presented in Figure 8.1(b), (I)-(IV) respectively. The IR spectra for NF substrate (Figure 8.1(b)-I) and Ag thin film on NF substrate (Figure 8.1(b)-II) show no noticeable absorption bands in the given range due to the obvious presence of Ag and Ni in their pure metallic form without any kind of oxygen bonding [28]. On the other hand, the IR spectrum of the $\text{Co}-\text{Co}_3\text{O}_4/\text{NF}$ composite thin film (Figure 8.1(b)-III) shows two prominent peaks at 658 and 559 cm^{-1} . The peak at 658 cm^{-1} is attributed to the stretching mode of $\text{Co}-\text{O}$ of tetrahedrally coordinated Co^{2+} and the peak at 559 cm^{-1} is assigned to the $\text{Co}-\text{O}$ of octahedrally coordinated Co^{3+} [28]. The presence of these peaks confirms the formation of Co_3O_4 . The absorption spectrum of the $\text{Ag}/\text{Co}-\text{Co}_3\text{O}_4/\text{NF}$ composite thin film in (Figure 8.1(b)-IV) is similar to that of the $\text{Co}-\text{Co}_3\text{O}_4/\text{NF}$ composite thin film, indicating the retention of the original Co_3O_4 phase even after the addition of Ag . The observed absorption bands on these spectra are in close agreement with previous reports [3, 19, 28].

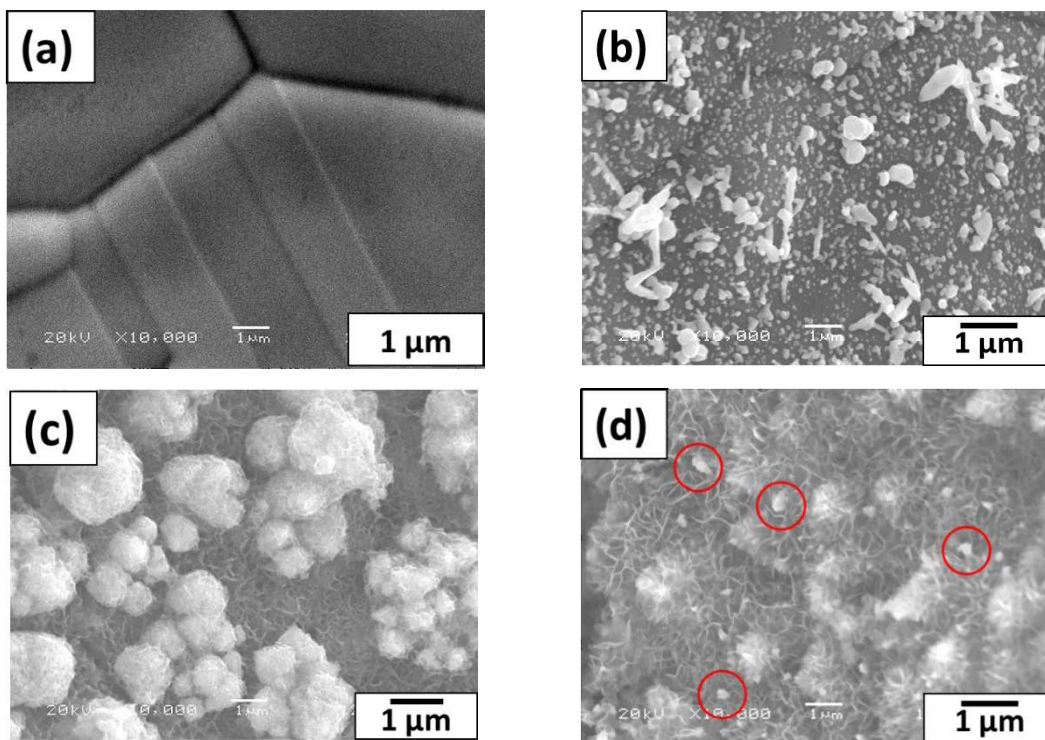


Figure 8.2. SEM micrographs of (a) Nickel foam (NF) substrate, (b) Ag thin film on NF, (c) Co-Co₃O₄, and (d) Ag/Co-Co₃O₄ composite thin films on NF, red circles identify the Ag nanoparticles in the composite film.

Reports in the literature have demonstrated that the specific surface area resulting from the final morphology of thin films has a crucial impact on electrochemical performance, especially the specific capacitance [8, 29]. Hence, the morphologies of the bare nickel foam (NF) substrate, Ag thin film on NF, Co-Co₃O₄/NF, and Ag/Co-Co₃O₄/NF composite thin films have been obtained by SEM imaging and presented in Figure 7.2. The surface morphology of the NF substrate as presented in Figure 8.2 (a) is relatively smooth, whereas the SEM image of the Ag thin film on NF shown in Figure 8.2(b) reveals a rougher morphology of uniformly distributed nanoparticles with the emergence of random clusters over the NF substrate. On the other hand, the SEM image of the Co-Co₃O₄ composite thin film coated on NF shown in Figure 8.2(c) shows an entirely different surface morphology

consisting of porous interconnected nanoflakes decorated with spongy cloudlike features homogeneously dispersed over the porous interconnected nanoflakes. Similar to the Co-Co₃O₄ composite thin film, the SEM image of the Ag/Co-Co₃O₄ composite thin film shows the baseline porous interconnected nanoflake morphology, however, with the presence of Ag nanoparticles distributed over the surface and as well embedded in the pores of the porous nanoflakes (Figure 8.2(d)). The Ag nanoparticles have been marked in red circles for identification in the figure. Further, it can also be noticed that the large clusters of spongy cloudlike features present in the Co-Co₃O₄ (Figure 8.2(c)) have reduced in size upon the addition of Ag. Owing to this higher apparent surface area with the addition of Ag, it may be expected that the Ag/Co-Co₃O₄ thin films offer additional electrochemical active sites and result in enhanced capacitive ability. Close morphological features as obtained on our Co-Co₃O₄ and Ag/Co-Co₃O₄ composite thin films have been reported previously, for instance, by Chen *et al.* on their sandwich-like NiO_x/NiCo₂O₄/Co₃O₄ nanoflakes prepared by a dealloying process [30]. Ali *et al.* also reported a nanoflake-like morphology for their hydrothermally synthesized cerium-doped Co₃O₄ [31].

In addition to the morphological investigation of the thin films, the elemental compositions of the nickel foam (NF) substrate, Ag thin film on NF, Co-Co₃O₄/NF, and Ag/Co-Co₃O₄/NF composite thin films were obtained by EDX studies as presented in Figure 8.3(a), (I)-(IV). The EDX spectrum of the bare NF substrate ((I) in Figure 8.3(a)) presents only the Ni K_α, Ni K_β, and Ni L_α peaks at energies 7.7, 8.5, and 1.1 keV respectively. On the other hand, the Ag thin film coated on the NF substrate in Figure 8.3(a) (II) shows the presence of Ag L_β at 3.2 keV, in addition to the Ni peaks arising from the NF substrate.

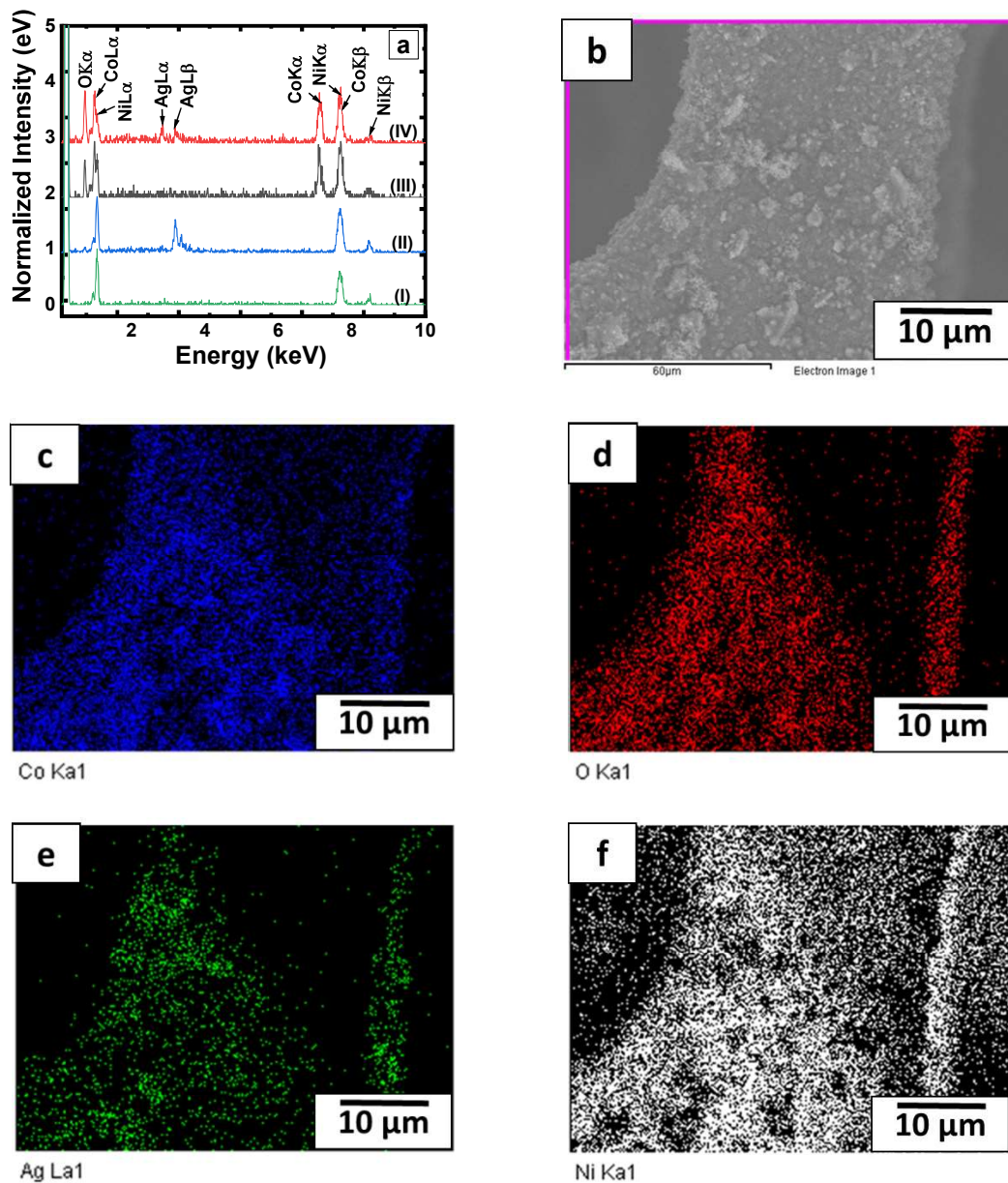


Figure 8.3. (a) EDX spectra of (I) nickel (NF) substrate (II) Ag thin film on NF, (III) Co-Co₃O₄/NF, and (IV) Ag/Co-Co₃O₄/NF composite thin films. (b) SEM image of Ag/Co-Co₃O₄/NF composite thin film and (c-f) elemental mapping of Ag/Co-Co₃O₄/NF composite thin film showing the distribution of (c) Co (d) O (e) Ag (f) Ni.

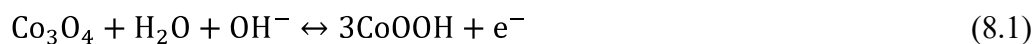
The EDX spectrum of the Co-Co₃O₄/NF (Figure 8.3(a) (III)) confirms the Cobalt oxide formation by exhibiting the peaks of Co K_α, Co K_β, Co L_α, and O K_α at 7.1, 7.7 and 1.0 keV respectively, along with the Ni signature originating from the NF substrate. Similarly, the

EDX spectrum of the Ag/Co-Co₃O₄ in Figure 8.3(a) (IV) reveals the peaks of Ag L_α and Ag L_β at 2.8 and 3.2 keV respectively, along with Co, O, and Ni peaks from the composite thin film on NF. The presence of the Ag peaks in the Ag/Co-Co₃O₄ thin film confirms the effective incorporation of silver into the Co-Co₃O₄ composite. The elemental mapping of the Ag/Co-Co₃O₄ composite thin film on NF substrate showing the distribution of Co, O, Ag, and Ni at a lower magnification has been presented in Figure 7.3(b-f). It is apparent from Figure 8.3(e) that the Ag nanoparticles are dispersed over and within the porous interconnected nanoflake structure of the Co-Co₃O₄ composite. On the other hand, Figure 8.3(c) and Figure 8.3(d) show a uniform distribution of Co and O on the Ni (Figure 8.3(f)).

8.5.2 Electrochemical measurements

To investigate the performance of the thin films as potential electrodes for supercapacitor applications, cyclic voltammetry (CV), galvanostatic charge-discharge (GCD), and electrochemical impedance studies of electrodes have been performed. The CV curves employed in estimating the oxidation and reduction reaction occurring in the Co-Co₃O₄/NF, Ag/Co-Co₃O₄/NF composite electrodes at different scan rates (100, 50, 20, 10, and 5 mV/s) as well as their comparison curves at 5 mV/s is presented in Figure 8.4. The deviation of the shape of all the CV curves from the ideal rectangular shape of electrical double-layer capacitor (EDLC) electrode materials, and the presence of redox peaks suggests that the specific capacitance arises mainly from Faraday redox reactions indicating battery-type storage properties [4, 15, 32, 33]. Also, it can be observed that the CV curves of the Co-Co₃O₄/NF in Figure 8.4(a) are identical to those of the Ag/Co-Co₃O₄/NF composite electrode

(Figure 8.4(b)). However, additional oxidation and reduction peaks (A1/C1) are observed for the CV curves of the Ag/Co-Co₃O₄/NF electrode aside from the (A2/C2) and (A3/C3) redox pairs for the Co-Co₃O₄ thin film. The first redox peaks of both Co-Co₃O₄/NF and Ag/Co-Co₃O₄/NF electrodes (A2 (0.37 V), C2 (0.33 V)) can be correlated to the conversion of Co²⁺/Co³⁺ as shown by equation (8.1) [5, 10, 17, 34]. Similarly, the redox pair (A3(0.47 V), C3 (0.36 V)) is also attributed to the redox reaction of Co³⁺/Co⁴⁺ according to equation (8.2) [3, 10, 15, 35]. The additional redox pair of the Ag/Co-Co₃O₄/NF thin film electrode (A1 (0.29 V), C1 (0.12 V)) which indicates the incorporation of Ag into Co-Co₃O₄ is from the redox reaction of Ag⁰/Ag⁺ as shown by equation (8.3) [15, 36, 37]. This observation complements the EDX analysis confirming the presence of Ag.



Additionally, it can be noticed that there is a peak shift in the oxidation peaks towards higher potential and reduction peaks towards lower potential in all the electrodes as the scan rate increases (Figure 8.4(a-c)). This is a result of limited charge transfer to satisfy electronic neutralization during the redox reaction caused by the increase in the diffusion resistance of the electrolyte ions within the electrodes [3, 36, 38, 39].

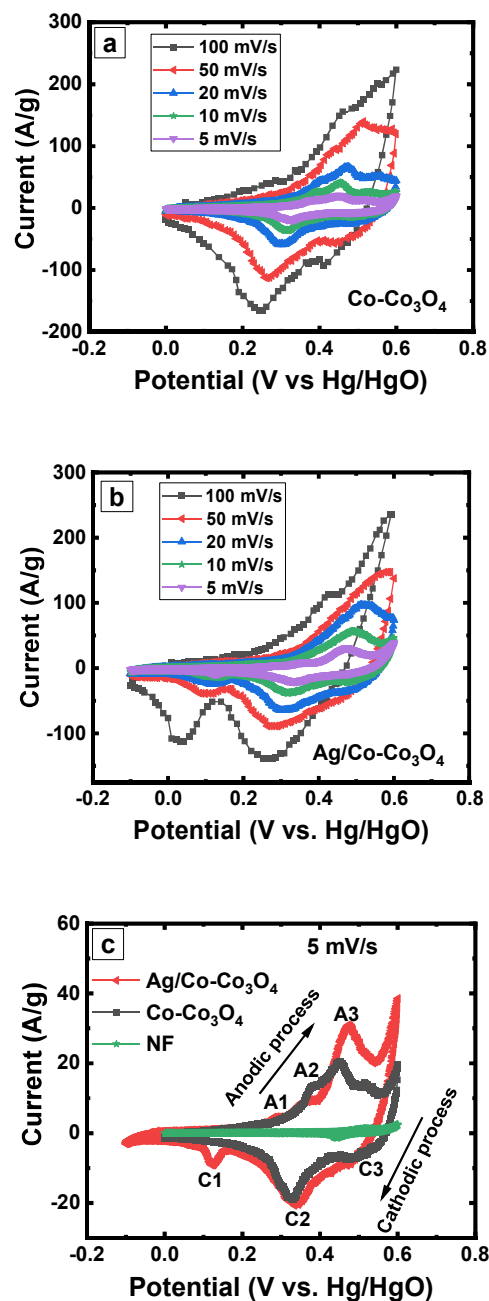


Figure 8.4. Cyclic voltammetry (CV) curves of (a) Co-Co₃O₄/NF (b) Ag/Co-Co₃O₄/NF composite thin film electrodes at different scan rates (c) Comparison CV curves of NF substrate, Co-Co₃O₄/NF, and Ag/Co-Co₃O₄/NF electrodes at 5 mV/s.

The GCD curves of the Co-Co₃O₄/NF electrode (Figure 8(a)) are similar to those of the Ag/Co-Co₃O₄/NF electrode as observed in the CV analysis. The shape of the curves, deviated

from the ideal triangular shape of EDLC electrode materials together with voltage plateaus, further confirms the Faradaic reactions of battery-type behaviors complementing the observations on the CV curves [33, 40-42]. When the specific current was increased from 1 to 20 A/g, the shape of the curves obtained from the individual electrodes remained unchanged, indicating that the as-prepared electrodes have high stability [40]. Furthermore, it can be observed that the discharge times decreased with increasing specific currents in both cases. Comparing the CV curves of the NF, Co-Co₃O₄/NF, and Ag/Co-Co₃O₄/NF electrodes in Figure 8.4(c), the Ag/Co-Co₃O₄/NF electrode exhibit a higher CV area which indicates a larger storage capacity. The CV area of the bare NF electrode shows a nearly horizontal line which implies that the capacitance contribution of the NF substrate is negligible.

Subsequently, the GCD graphs obtained for the Co-Co₃O₄/NF and Ag/Co-Co₃O₄/NF thin films composite electrodes at specific currents of 1, 5, 10, and 20 A/g, as well as their comparison at 1 A/g with NF substrate within the potential window of -0.1 and 0.5 V, has been presented in Figure 5(a-c). In Figure 8.5(c) at 1 A/g, the Ag/Co-Co₃O₄/NF electrode exhibited a longer discharge time revealing its superior capacitive performance compared to the NF substrate and the Co-Co₃O₄/NF electrodes. The specific capacitance of the Co-Co₃O₄/NF and Ag/Co-Co₃O₄/NF electrodes at 1 A/g has been calculated as 2580 and 2800 F/g, respectively, from the GCD curves, using equation (7.4),

$$C_s = \frac{I\Delta t}{m\Delta V} \quad (8.4)$$

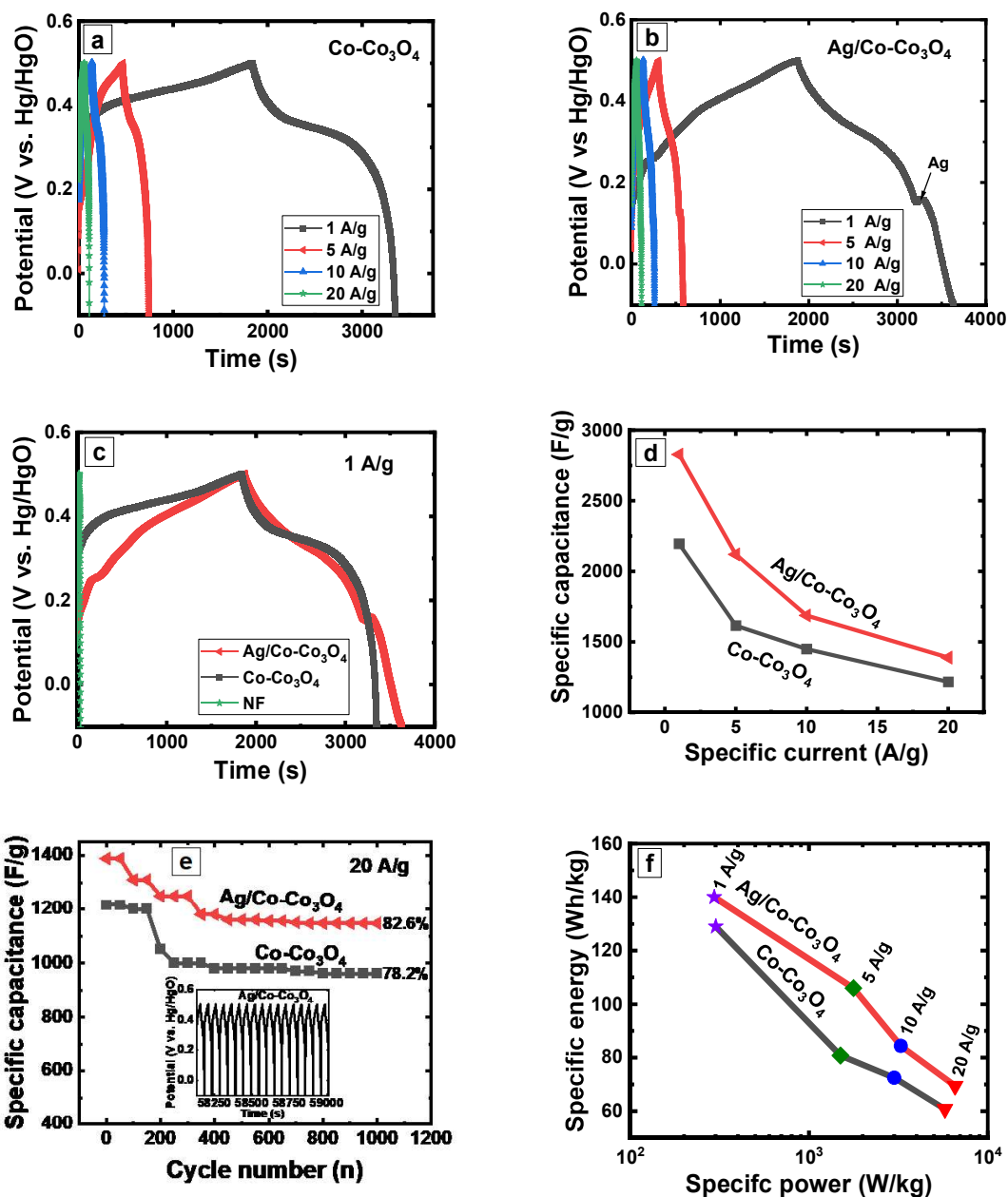


Figure 8.5. Galvanostatic charge-discharge (GCD) curves of (a) Co-Co₃O₄/NF, (b) Ag/Co-Co₃O₄/NF composite thin film electrodes at different specific currents, (c) Comparison (GCD) curves NF substrate, Co-Co₃O₄/NF, and Ag/Co-Co₃O₄/NF electrodes at 1 A/g, (d) variation of specific capacitance at different specific currents, (e) cycling performance with inset showing the last 17 GCD cycles of Ag/Co-Co₃O₄/NF tested for 1000 cycles at a specific current of 20 A/g, and (g) Ragone plot of Co-Co₃O₄/NF and Ag/Co-Co₃O₄/NF electrodes.

where C_s is the specific capacitance, I is the specific current, Δt is the discharge time, m is the electrode mass, and ΔV is the potential change during discharge. It can be noted that the obtained specific capacitance value of the Ag/Co-Co₃O₄/NF electrode is higher than that obtained on the Co-Co₃O₄/NF electrode and much higher than those reported in the literature on similar chemistry prepared by other methods including doping and hydrothermal processes involving multiple steps in their fabrication [20]. For example, Aadil *et al.* reported a specific capacitance value of 1425 F/g for their binder-free mesoporous Ag-doped Co₃O₄ nanosheet prepared on nickel foam by a hydrothermal technique [3]. Also, the specific capacitance value of our Ag/Co-Co₃O₄/NF composite thin film electrode is higher than the specific capacitance value of 103 F/g at 1 A/g of Co₃O₄ nanoparticles prepared by a modified sol-gel synthesis using an organic template as reported by Shaheen *et al.* [17]. Equally, much lower specific capacitance values of Co₃O₄-based electrodes on different substrate materials prepared by various other fabrication techniques have also been previously reported by other authors [1, 8, 15, 42, 43].

Furthermore, the equivalent series resistance (ESR), which comprises the intrinsic resistance of the electroactive material, electrolyte resistance, and the contact resistance at the electrode-electrolyte interface, [35, 44, 45] has been estimated from the GCD curves of the various electrodes by taking the ratio of the potential drop (V_{IR}) between the charge-discharge curves to the discharge current. The ESR values are 1.5 Ω and 1.2 Ω for Co-Co₃O₄/NF and Ag/Co-Co₃O₄/NF electrodes at 1 A/g, respectively, indicating that, the incorporation of Ag into Co-Co₃O₄ has improved its conductivity, thereby enhancing its capacitive performance. Similar ESR values have been reported by Harilal *et al.* for their electrospun Co₃O₄ (1.7 Ω) and hybrid nanobelt NiO-Co₃O₄ (1.2 Ω) electrode material [35].

In the specific capacitance variation with specific current graph in Figure 8.5(d), it is observed that the specific capacitance decreases with increasing scan rates for both electrodes. This phenomenon is due to the inability of the electrolyte ions (OH^- ions) to saturate the bulk of the electroactive material due to insufficient time. Hence, the Faraday redox reaction is limited to only the surface of the electroactive material, consequently reducing the specific capacitance [3, 46, 47].

Although the capacitance of electrode material is important in its practical application in supercapacitors, long-term cycling stability is also a critical requirement. Therefore, the cycling performances of the $\text{Co-Co}_3\text{O}_4/\text{NF}$ and $\text{Ag/Co-Co}_3\text{O}_4/\text{NF}$ electrodes have been studied by repeated charge-discharge cycles up to 1000 cycles at a high specific current of 20 A/g as presented in Figure 8.5(e). The $\text{Ag/Co-Co}_3\text{O}_4/\text{NF}$ electrode demonstrated superior electrochemical stability by maintaining 82.6 % of its initial specific capacitance compared to the capacitance retention of 78.2 % of the $\text{Co-Co}_3\text{O}_4/\text{NF}$ electrodes. Furthermore, the $\text{Ag/Co-Co}_3\text{O}_4/\text{NF}$ electrode has been cycled for 3000 cycles (Figure S8.4 of the supplementary data) and its capacitance retention value is 80.3 % showing high stability. The higher stability of the $\text{Ag/Co-Co}_3\text{O}_4/\text{NF}$ electrode is attributed to the porous structure which accommodates the volume expansion during cycling and the presence of Ag nanoparticles which provides direct and stable conduction pathways for electrons to be transported rapidly [3, 15]

Another important requirement of electrode material for practical supercapacitor application is the specific energy and specific power which is known, in other words, as the Ragone plot (Figure 8.5(f)). The specific energy and power at different specific currents were

also estimated from the GCD curves of the Co-Co₃O₄/NF and Ag/Co-Co₃O₄/NF electrodes using equations (8.5) and (8.6) respectively,

$$E_s = \frac{1}{2} C_s V^2 \quad (7.5)$$

$$P_s = \frac{E}{\Delta t} \quad (7.6)$$

where E_s is the specific energy, C_s is the specific capacitance, V is the potential range, P_s is the specific power and Δt is the discharge time. Figure 8.5(f) depicts that the Ag/Co-Co₃O₄/NF electrode showed maximum specific energy and power of 69.5 Wh/kg and 6.6 kW/kg, respectively, while the Co-Co₃O₄/NF electrode showed specific energy of 60.8 Wh/kg and specific power of 5.8 kW/kg at a high specific current of 20 A/g. The recorded specific energy and power for our Ag/Co-Co₃O₄/NF is higher compared to previously reported values such as those recorded by Shaheen *et al.* (1.9 Wh/kg and 4.7 kW/kg) on their functionalized Co₃O₄ nanoparticles grown on nickel foam by sol-gel synthesis [17]. Similarly, lower specific energy and power values (24.3 Wh/kg and 0.26 kW/kg) compared to that of our work have also been reported by Zhu *et al.* on their solvothermally synthesized Flower-like ZnO/Co₃O₄ on nickel foam [48].

The superior capacitive performance and the lower resistance of the Ag/Co-Co₃O₄/NF thin film electrode could be attributed to the porous structure of Co-Co₃O₄ with embedded Ag nanoparticles which promotes the diffusion of the OH⁻ ions to the electroactive sites combined with the increased redox-active surface area. Additionally, the presence of metallic

silver enhances the electrical conductivity to provide fast electron transport during the Faradaic-redox reaction.

For more insight into the electrical conductivity and ion transfer performance of the electrodes, the EIS measurement has been performed in a frequency range from 10 mHz to 100 kHz as shown in Figure 8.6. The Nyquist plots of the Co-Co₃O₄/NF, Ag/Co-Co₃O₄/NF composite electrodes as well as the NF substrate are presented in Figure 8.6(a). The Nyquist plots consist of a semicircle in the high-frequency region and its diameter gives information on the charge transfer resistance (R_{ct}) of the electrodes [49-52]. The R_{ct} values of the Co-Co₃O₄/NF and Ag/Co-Co₃O₄/NF electrodes were recorded as 2.86 $\Omega\cdot\text{cm}^2$ and 0.96 $\Omega\cdot\text{cm}^2$ respectively. In the case of the bare NF substrate, there is almost no charge transfer resistance as a result of its metallic nature. The intercept of the plots with the x-axis in the higher frequency region presents the ESR of the electrodes [10, 53]. In the present study, the ESR of the Co-Co₃O₄/NF reduced from 1.5 $\Omega\cdot\text{cm}^2$ to 1.0 $\Omega\cdot\text{cm}^2$ by the incorporation of Ag into Co-Co₃O₄. These ESR values are consistent with ESR values estimated from the GCD curves for both the Co-Co₃O₄/NF and Ag/Co-Co₃O₄/NF electrodes. The zoom-in of the Nyquist plots in Figure 8.6(b) depicts the enhancement of the conductivity of the Ag/Co-Co₃O₄/NF electrode compared to Co-Co₃O₄/NF electrode. In addition, the inclined straight line at the lower frequency region of the Nyquist plots is attributed to the process of ions diffusion from the electrolyte into the electrode while also revealing the capacitive nature of the material [29].

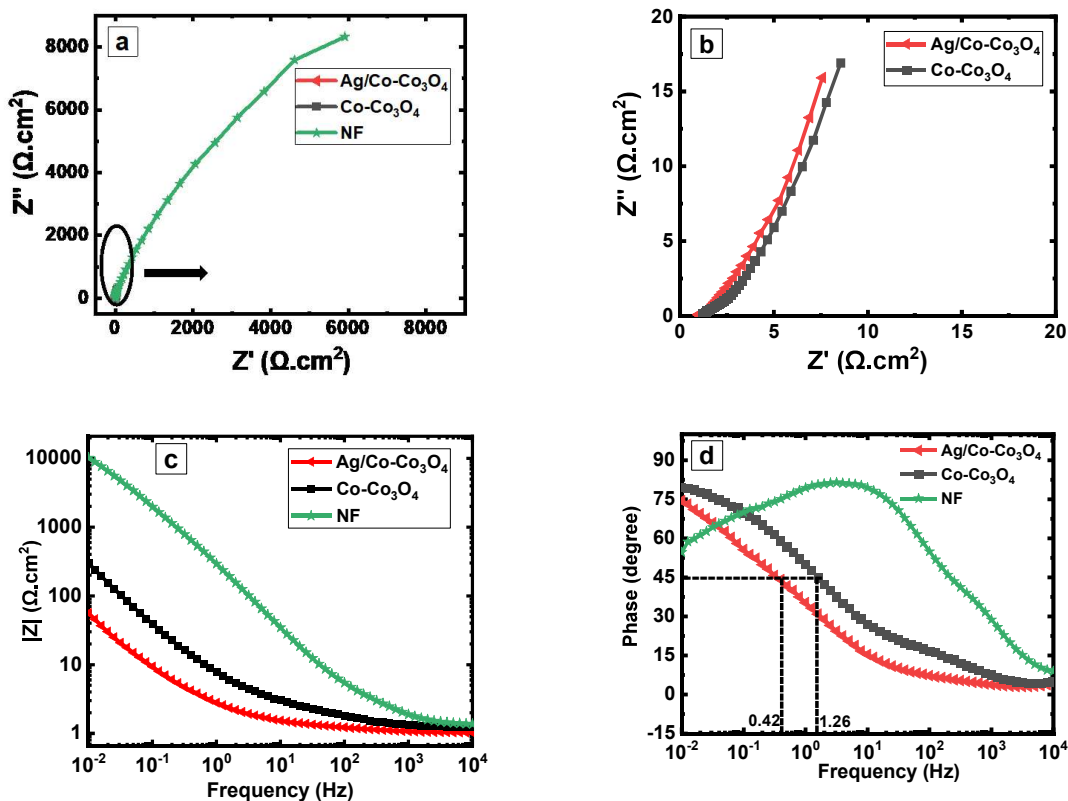


Figure 8.6 Nyquist plots (a) full range, and (b) between 0 and 20 $\Omega\cdot\text{cm}^2$, Bode plots of the frequency's dependence on the (c) impedance magnitude ($|Z|$), and (d) phase angle of the NF substrate, $\text{Co-Co}_3\text{O}_4/\text{NF}$, and $\text{Ag}/\text{Co-Co}_3\text{O}_4/\text{NF}$ electrodes.

The $\text{Ag}/\text{Co-Co}_3\text{O}_4/\text{NF}$ electrode exhibited a shorter and steeper vertical line compared to the $\text{Co-Co}_3\text{O}_4/\text{NF}$ electrode indicating a rapid ion diffusion and hence better capacitive performance as it is expected that the electrode with a more vertical line shows high capacitive characteristics. This observation complements the specific capacitance values obtained. The Bode plots in Figure 8.6(c) showing the relationship between frequency and impedance of the $\text{Co-Co}_3\text{O}_4/\text{NF}$, $\text{Ag}/\text{Co-Co}_3\text{O}_4/\text{NF}$, and NF substrate further support the Nyquist plots findings, with the $\text{Ag}/\text{Co-Co}_3\text{O}_4/\text{NF}$ electrode having a lower impedance due to improved conductivity promoted by the presence of Ag.

Subsequently, the relationship between frequency and phase angle of the Co-Co₃O₄/NF, Ag/Co-Co₃O₄/NF electrodes, and the bare NF substrate is presented by the Bode plots in Figure 8.6(d). A phase angle of 90° is typically observed for EDLCs using carbon materials and 45° when the capacitive resistive impedances are equal whereas for pseudocapacitors phase angles between 45 and 90 are generally observed [35] [49, 54]. Therefore, phase angles of 79° and 75° obtained for the Co-Co₃O₄/NF, and Ag/Co-Co₃O₄/NF electrodes, respectively, further corroborate the CV and GCD analysis of the pseudocapacitive nature of the electrodes. The relaxation time (τ) in seconds (s), which indicates how fast an electrode material switches from resistive to capacitive behavior, is computed to be 2.5 s and 0.6 s for the Co-Co₃O₄/NF and Ag/Co-Co₃O₄/NF electrodes, respectively, using the equation (8.7):

$$\tau = \frac{1}{f_o} \quad (8.7)$$

where (f_o) is the frequency at the phase angle of 45° [54].

8.5 Conclusions

Ag/Co-Co₃O₄ composite thin film electrodes on NF substrate presenting superior capacitive behavior and cycle durability have been prepared effectively by incorporating Ag in the Co-Co₃O₄ by using a simple technique that combines cyclic voltammetry and pulse reverse potential (CV PRP) modes of electrodeposition. The XRD studies have revealed the amorphous nature of both Co-Co₃O₄ and Ag/Co-Co₃O₄/NF composite thin film electrode

materials. The FTIR and EDX analysis have confirmed the chemical signature of the presence of the oxides of cobalt in the prepared electrodes. The porous nanoflakes network of the Co-Co₃O₄ and Ag/Co-Co₃O₄ composite thin films by SEM analysis presented features promoting increased specific surface area upon Ag incorporation which is a favorable parameter for enhanced capacitive behavior of the electrode. The Ag/Co-Co₃O₄/NF electrode exhibited a higher specific capacitance of 2800 F/g compared to the Co-Co₃O₄/NF (2580 F/g) electrode. Additionally, the Ag/Co-Co₃O₄/NF electrode demonstrated outstanding specific energy and power (69.5 Wh/kg and 6.6 kW/kg) with capacitance retention of 82.6 % after 1000 cycles than the Co-Co₃O₄/NF electrode. Furthermore, the conductivity of the Co-Co₃O₄/NF electrode has been improved by the incorporation of Ag nanoparticles as evidenced by the reduction of the charge transfer resistance (R_{ct}) and equivalence series resistance (ESR). The superior electrochemical performance of the Ag/Co-Co₃O₄/NF composite thin film electrode is attributed to the synergistic interaction between Ag and Co-Co₃O₄ to enhance conductivity and specific surface area. This high performance presents potential to the Ag/Co-Co₃O₄/NF as an electrode material for practical applications in a supercapacitor device.

8.6 References

- [1] F. Ali, N.R. Khalid, Facile synthesis and properties of chromium-doped cobalt oxide (Cr-doped Co₃O₄) nanostructures for supercapacitor applications, *Appl. Nanosci.*, 10 (2020) 1481-1488.
- [2] M.I.A. Abdel Maksoud, R.A. Fahim, A.E. Shalan, M. Abd Elkodous, S.O. Olojede, A.I. Osman, C. Farrell, A.a.H. Al-Muhtaseb, A.S. Awed, A.H. Ashour, D.W. Rooney, *Advanced materials and technologies for supercapacitors used in energy conversion and storage: a review*, *Environ. Chem. Lett.*, 19 (2020) 375-439.

- [3] M. Aadil, S. Zulfiqar, M. Shahid, S. Haider, I. Shakir, M.F. Warsi, Binder free mesoporous Ag-doped Co_3O_4 nanosheets with outstanding cyclic stability and rate capability for advanced supercapacitor applications, *J. Alloys Compd.*, 844 (2020) 156062.
- [4] J. Theerthagiri, G. Durai, T. Tatarchuk, M. Sumathi, P. Kuppasami, J. Qin, M.Y. Choi, Synthesis of hierarchical structured rare earth metal-doped Co_3O_4 by polymer combustion method for high performance electrochemical supercapacitor electrode materials, *Ionics*, 26 (2019) 2051-2061.
- [5] G. Li, M. Chen, Y. Ouyang, D. Yao, L. Lu, L. Wang, X. Xia, W. Lei, S.-M. Chen, D. Mandler, Q. Hao, Manganese doped Co_3O_4 mesoporous nanoneedle array for long cycle-stable supercapacitors, *Appl. Surf. Sci.*, 469 (2019) 941-950.
- [6] S.J. Uke, V.P. Akhare, D.R. Bambole, A.B. Bodade, G.N. Chaudhari, Recent Advancements in the Cobalt Oxides, Manganese Oxides, and Their Composite As an Electrode Material for Supercapacitor: A Review, *Front. Mater.*, 4 (2017) 21.
- [7] D. Majumdar, T. Maiyalagan, Z. Jiang, Recent Progress in Ruthenium Oxide-Based Composites for Supercapacitor Applications, *ChemElectroChem*, 6 (2019) 4343-4372.
- [8] S. Deng, X. Xiao, G. Chen, L. Wang, Y. Wang, Cd doped porous Co_3O_4 nanosheets as electrode material for high performance supercapacitor application, *Electrochim. Acta*, 196 (2016) 316-327.
- [9] X. Fan, P. Ohlckers, X. Chen, Tunable Synthesis of Hollow Co_3O_4 Nanoboxes and Their Application in Supercapacitors, *Appl. Sci.*, 10 (2020) 1208.
- [10] M. Mirzaeian, N. Akhanova, M. Gabdullin, Z. Kalkozova, A. Tulegenova, S. Nurbolat, K. Abdullin, Improvement of the Pseudocapacitive Performance of Cobalt Oxide-Based Electrodes for Electrochemical Capacitors, *Energies*, 13 (2020) 5228.
- [11] S. Nagamuthu, K.S. Ryu, Synthesis of Ag/NiO Honeycomb Structured Nanoarrays as the Electrode Material for High Performance Asymmetric Supercapacitor Devices, *Sci Rep*, 9 (2019) 4864.
- [12] X. Hu, L. Wei, R. Chen, Q. Wu, J. Li, Reviews and Prospectives of Co_3O_4 -Based Nanomaterials for Supercapacitor Application, *ChemistrySelect*, 5 (2020) 5268-5288.
- [13] Y. Li, F.-M. Li, X.-Y. Meng, S.-N. Li, J.-H. Zeng, Y. Chen, Ultrathin Co_3O_4 Nanomeshes for the Oxygen Evolution Reaction, *ACS Catalysis*, 8 (2018) 1913-1920.
- [14] M. Hafeez, R. Shaheen, B. Akram, A. Zain ul, S. Haq, S. Mahsud, S. Ali, R.T. Khan, Green synthesis of cobalt oxide nanoparticles for potential biological applications, *Mater. Res. Express*, 7 (2020).
- [15] S.A. Pawar, D.S. Patil, J.C. Shin, Hexagonal sheets of Co_3O_4 and Co_3O_4 -Ag for high-performance electrochemical supercapacitors, *J. Ind. Eng. Chem*, 54 (2017) 162-173.
- [16] A. García-Gómez, S. Eugénio, R.G. Duarte, T.M. Silva, M.J. Carmezim, M.F. Montemor, Electrodeposited reduced-graphene oxide/cobalt oxide electrodes for charge storage applications, *Appl. Surf. Sci.*, 382 (2016) 34-40.
- [17] I. Shaheen, K.S. Ahmad, C. Zequine, R.K. Gupta, A.G. Thomas, M.A. Malik, Modified sol-gel synthesis of Co_3O_4 nanoparticles using organic template for electrochemical energy storage, *Energy*, 218 (2021) 119502.
- [18] H. Pang, X. Li, Q. Zhao, H. Xue, W.-Y. Lai, Z. Hu, W. Huang, One-pot synthesis of heterogeneous Co_3O_4 -nanocube/ $\text{Co}(\text{OH})_2$ -nanosheet hybrids for high-performance flexible asymmetric all-solid-state supercapacitors, *Nano Energy*, 35 (2017) 138-145.
- [19] G. M, S. G, M. A, A. V, In-situ synthesis of Co_3O_4 /graphite nanocomposite for high-performance supercapacitor electrode applications, *Appl. Surf. Sci.*, 403 (2017) 578-583.

- [20] R.A. Nuamah, S. Noormohammed, D.K. Sarkar, Specific capacitance behavior of Co-Co₃O₄ nanocomposite thin films synthesized via different electrodeposition modes, *Int. J. Energy Res.*, (2021) 1-11.
- [21] P.G. Schiavi, P. Altimari, A. Rubino, F. Pagnanelli, Electrodeposition of cobalt nanowires into alumina templates generated by one-step anodization, *Electrochim. Acta*, 259 (2018) 711-722.
- [22] S.S. Gavande, P.S. Kulkarni, V.B. Patil, B.R. Karche, S.S. Gavande, An Assay of Electrodeposited Cobalt Oxide Thin Film as a Supercapacitor Electrode, *Macromol. Symp.*, 393 (2020) 2000169.
- [23] J. Mei, W. Fu, Z. Zhang, X. Jiang, H. Bu, C. Jiang, E. Xie, W. Han, Vertically-aligned Co₃O₄ nanowires interconnected with Co(OH)₂ nanosheets as supercapacitor electrode, *Energy*, 139 (2017) 1153-1158.
- [24] L.-b. Jiang, X.-z. Yuan, J. Liang, J. Zhang, H. Wang, G.-m. Zeng, Nanostructured core-shell electrode materials for electrochemical capacitors, *J. Power Sources*, 331 (2016) 408-425.
- [25] X. Xia, J. Tu, YongqiZhang, XiuliWang, C. Gu, X.-b. Zhao, H. JinFan, High-Quality Metal Oxide Core/Shell NanowireArrays onConductive Substrates for Electrochemical Energy Storage, *ACS Nano*, 6 (2012) 5531–5538
- [26] K. Xu, X. Yang, J. Yang, J. Hu, Synthesis of hierarchical Co₃O₄@NiCo₂O₄ core-shell nanosheets as electrode materials for supercapacitor application, *J. Alloys Compd.*, 700 (2017) 247-251.
- [27] R.A. Nuamah, S. Noormohammed, D.K. Sarkar, Pulsed Reverse Potential Electrodeposition of Carbon-Free Ni/NiO Nanocomposite Thin Film Electrode for Energy Storage Supercapacitor Electrodes, *Coatings*, 11 (2021) 780.
- [28] A. Ashok, A. Kumar, M.A. Matin, F. Tarlochan, Synthesis of Highly Efficient Bifunctional Ag/Co₃O₄ Catalyst for Oxygen Reduction and Oxygen Evolution Reactions in Alkaline Medium, *ACS omega*, 3 (2018) 7745-7756.
- [29] P. Howli, S. Das, S. Sarkar, M. Samanta, K. Panigrahi, N.S. Das, K.K. Chattopadhyay, Co₃O₄ Nanowires on Flexible Carbon Fabric as a Binder-Free Electrode for All Solid-State Symmetric Supercapacitor, *ACS omega*, 2 (2017) 4216-4226.
- [30] J. Chen, Y. Ling, Z. Lu, X. Huai, F. Qin, Z. Zhang, Sandwich-like NiOx/NiCo₂O₄/Co₃O₄ nanoflakes enable efficient oxygen evolution electrocatalysis, *Electrochim. Acta*, 322 (2019) 134753.
- [31] F. Ali, N.R. Khalid, G. Nabi, A. Ul-Hamid, M. Ikram, Hydrothermal synthesis of cerium-doped Co₃O₄ nanoflakes as electrode for supercapacitor application, *Int. J. Energy Res.*, 45 (2020) 1999-2010.
- [32] P. Siwatch, K. Sharma, N. Manyani, J. Kang, S.K. Tripathi, Characterization of nanostructured nickel cobalt oxide-polyvinyl alcohol composite films for supercapacitor application, *J. Alloys Compd.*, 872 (2021) 159409.
- [33] S.J. Arbaz, S.C. Sekhar, B. Ramulu, J.S. Yu, Binder-free preparation of bimetallic oxide vertical nanosheet arrays toward high-rate performance and energy density supercapacitors, *Int. J. Energy Res.*, 45 (2021) 13999-14009.
- [34] X. Wang, Y. Fang, B. Shi, F. Huang, F. Rong, R. Que, M. Shao, Fabrication of Isomorphous Co₃O₄@Co₃O₄ Hierarchical Core-Shell Nanoneedles for High-Performance Supercapacitors, *ChemistrySelect*, 2 (2017) 9267-9276.

- [35] M. Harilal, S.G. Krishnan, B.L. Vijayan, M. Venkatasamy Reddy, S. Adams, A.R. Barron, M.M. Yusoff, R. Jose, Continuous nanobelts of nickel oxide–cobalt oxide hybrid with improved capacitive charge storage properties, *Mater. Des.*, 122 (2017) 376-384.
- [36] Y. Li, P. Ren, W. Wu, C. Chen, M. Wu, Solvothermal synthesis and electrochemical properties of octahedral cobalt oxide decorated with Ag₂O, *J. Wuhan Univ. Technol. Mater.*, 32 (2017) 568-573.
- [37] A.I. Oje, A.A. Ogwu, M. Mirzaeian, N. Tsendzughul, Electrochemical energy storage of silver and silver oxide thin films in an aqueous NaCl electrolyte, *J. Electroanal. Chem.*, 829 (2018) 59-68.
- [38] W. Liu, H. Fan, W. Shen, S. Qu, Facile and Sustainable Synthesis of Co₃O₄@Hollow-Carbon-Fiber for a Binder-Free Supercapacitor Electrode, *ChemistrySelect*, 1 (2016) 6469-6475.
- [39] I. Manohara Babu, J.J. William, G. Muralidharan, AgCoO₂–Co₃O₄/CMC Cloudy Architecture as High Performance Electrodes for Asymmetric Supercapacitors, *ChemElectroChem*, 7 (2020) 535-545.
- [40] P. Sivakumar, C.J. Raj, D.O. Opar, J. Park, H. Jung, Two dimensional layered nickel cobaltite nanosheets as an efficient electrode material for high-performance hybrid supercapacitor, *Int. J. Energy Res.*, 45 (2021) 1–11.
- [41] R.M. Obodo, A.C. Nwanya, M. Arshad, C. Iroegbu, I. Ahmad, R.U. Osuji, M. Maaza, F.I. Ezema, Conjugated NiO-ZnO/GO nanocomposite powder for applications in supercapacitor electrodes material, *Int. J. Energy Res.*, 44 (2020) 3192-3202.
- [42] H. Xuan, R. Wang, J. Yang, G. Zhang, X. Liang, Y. Li, Z. Xie, P. Han, Synthesis of NiMoO₄@Co₃O₄ hierarchical nanostructure arrays on reduced graphene oxide/Ni foam as binder-free electrode for asymmetric supercapacitor, *J. Mater. Sci.*, 56 (2021) 9419-9433.
- [43] M. Zhang, Y. Xu, H. Fan, N. Zhao, B. Yan, C. Wang, J. Ma, A.K. Yadav, W. Zhang, Z. Du, X. Zheng, M. Li, G. Dong, W. Wang, In situ synthesis of 3D Co@Co₃O₄ nanosheet arrays for hybrid supercapacitors with ultra-high rate performance, *J. Alloys Compd.*, 826 (2020) 154115.
- [44] H. Ju, X.D. Liu, C.Y. Tao, F. Yang, X.L. Liu, X. Luo, L. Zhang, A novel edge-rich structure of CuO/Co₃O₄ derived from Prussian blue analogue as a high-rate and ultra-stable electrode for efficient capacitive storage, *Electrochim. Acta*, 366 (2021) 137410.
- [45] S.G. Mohamed, S.Y. Attia, H.H. Hassan, Spinel-structured FeCo₂O₄ mesoporous nanosheets as efficient electrode for supercapacitor applications, *Microporous Mesoporous Mater.*, 251 (2017) 26-33.
- [46] Q. Ziyang, X. Ruidong, Y. Bohao, W. Wenbiny, Y. Zhang, Synthesis and Characterization of Hierarchical NiO/Ni-Co-Mn Oxide Nanocomposite Materials for High Performance Supercapacitors, *Int. J. Electrochem.*, 14 (2019) 2999-3010.
- [47] J. Iqbal, A. Numan, R. Jafer, S. Bashir, A. Jilani, S. Mohammad, M. Khalid, K. Ramesh, S. Ramesh, Ternary nanocomposite of cobalt oxide nanograins and silver nanoparticles grown on reduced graphene oxide conducting platform for high-performance supercapattery electrode material, *J. Alloys Compd.*, 821 (2020) 153452.
- [48] H. Zhu, J. Liu, Q. Zhang, J. Wei, High electrochemical performance of metal azolate framework-derived ZnO/Co₃O₄ for supercapacitors, *Int. J. Energy Res.*, 44 (2020) 8654-8665.
- [49] M. Suksomboon, J. Khuntilo, S. Kalasina, P. Suktha, J. Limtrakul, M. Sawangphruk, High-performance energy storage of Ag-doped Co(OH)₂-coated graphene paper: In situ electrochemical X-ray absorption spectroscopy, *Electrochim. Acta*, 252 (2017) 91-100.

- [50] S.C. Sekhar, G. Nagaraju, B. Ramulu, J.S. Yu, Hierarchically Designed Ag@Ce₆Mo₁₀O₃₉ Marigold Flower-Like Architectures: An Efficient Electrode Material for Hybrid Supercapacitors, ACS Appl. Mater. Interfaces, 10 (2018) 36976-36987.
- [51] R. Xie, H. Huang, X. Qi, G. Wei, Significant enhancement of the electrochemical performance of hierarchical Co₃O₄ electrodes for supercapacitors via architecture design and training activation, J. Energy Storage, 35 (2021) 102258.
- [52] R. Packiaraj, P. Devendran, K.S. Venkatesh, S. Asath bahadur, A. Manikandan, N. Nallamuthu, Electrochemical Investigations of Magnetic Co₃O₄ Nanoparticles as an Active Electrode for Supercapacitor Applications, J. Supercond. Nov. Magn., 32 (2018) 2427-2436.
- [53] K.V.G. Raghavendra, C.V.V.M. Gopi, R. Vinodh, S.S. Rao, I.M. Obaidat, H.-J. Kim, Facile synthesis of nanoparticles anchored on honeycomb-like MnCo₂S₄ nanostructures as a binder-free electroactive material for supercapacitors, J. Energy Storage, 27 (2020) 101159.
- [54] E.A.A. Aboelazm, G.A.M. Ali, H. Algarni, H. Yin, Y.L. Zhong, K.F. Chong, Magnetic Electrodeposition of the Hierarchical Cobalt Oxide Nanostructure from Spent Lithium-Ion Batteries: Its Application as a Supercapacitor Electrode, J. Phys. Chem. C, 122 (2018) 12200-12206.

8.7 Supporting information

(a) Published supporting information (Nuamah RA, Noormohammed S, Sarkar DK.

Supercapacitor performance evaluation of nanostructured Ag-decorated Co-Co₃O₄ composite thin film electrode material. Int J Energy Res. 2022;46(9):13099-13110)

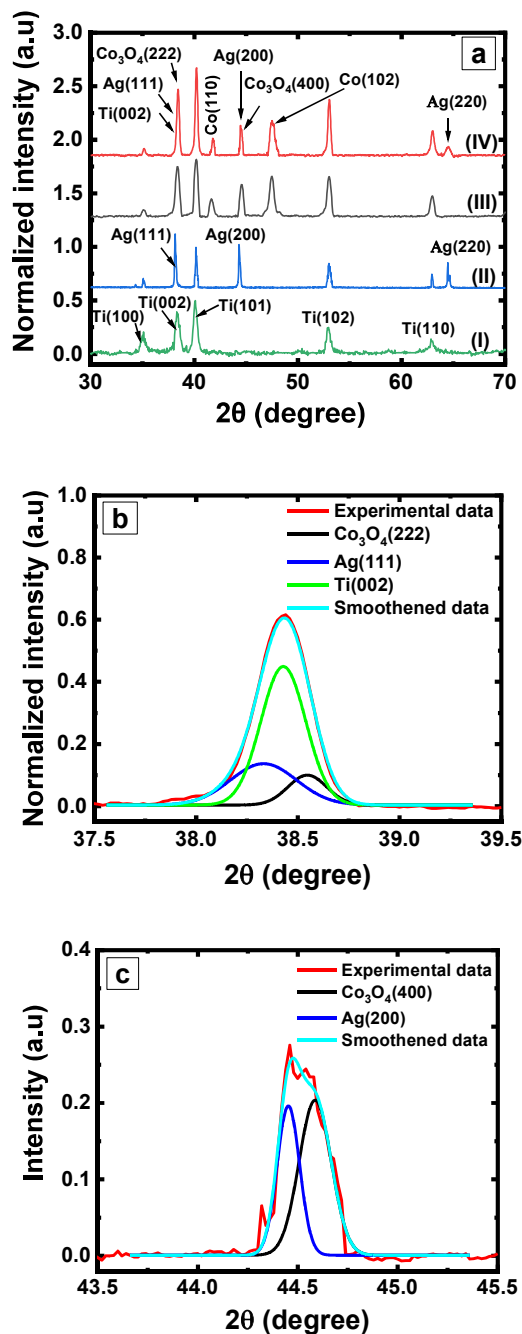


Figure S8.1 (a) XRD patterns of (I) Titanium (Ti) substrate (II) Ag thin film on Ti, (III) Co-Co₃O₄, and (IV) Ag/Co-Co₃O₄ composite thin films on Ti (b, c) deconvoluted XRD peaks of Ag/Co-Co₃O₄ composite thin film on Ti at 2θ positions of 38.5° and 44.5° respectively.

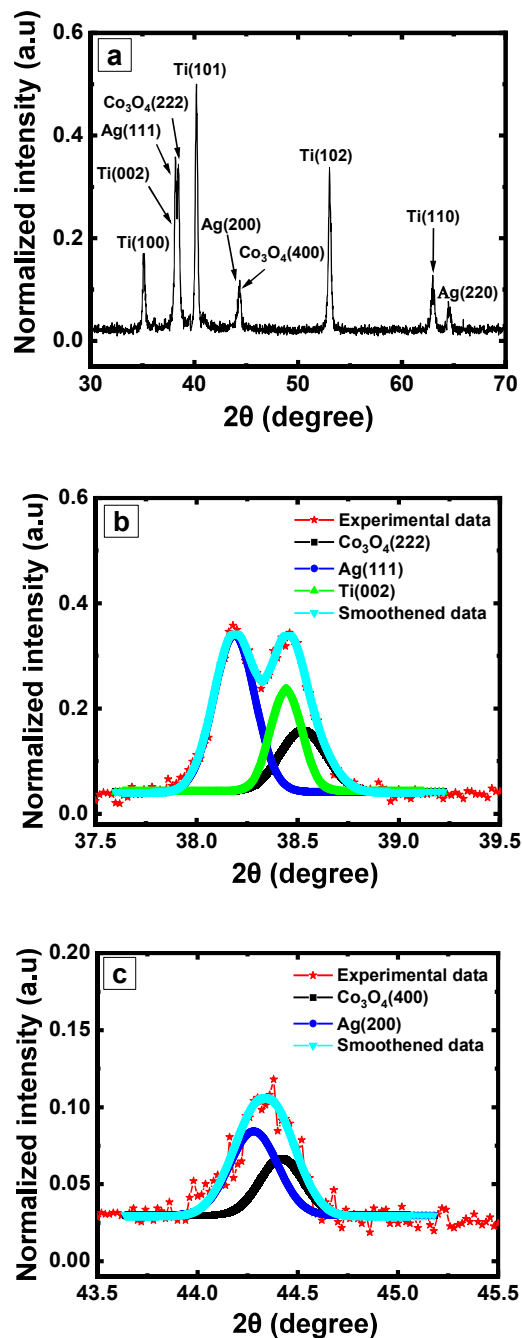


Figure S8.2 (a) XRD pattern Ag/Co-Co₃O₄ composite thin films on Ti substrate prepared from only cobalt acetate and silver nitrate (0.1 M CoAc + 0.1 M AgNO₃), (b, c) deconvoluted XRD peaks of at 2θ positions of 38.5° and 44.5° respectively.

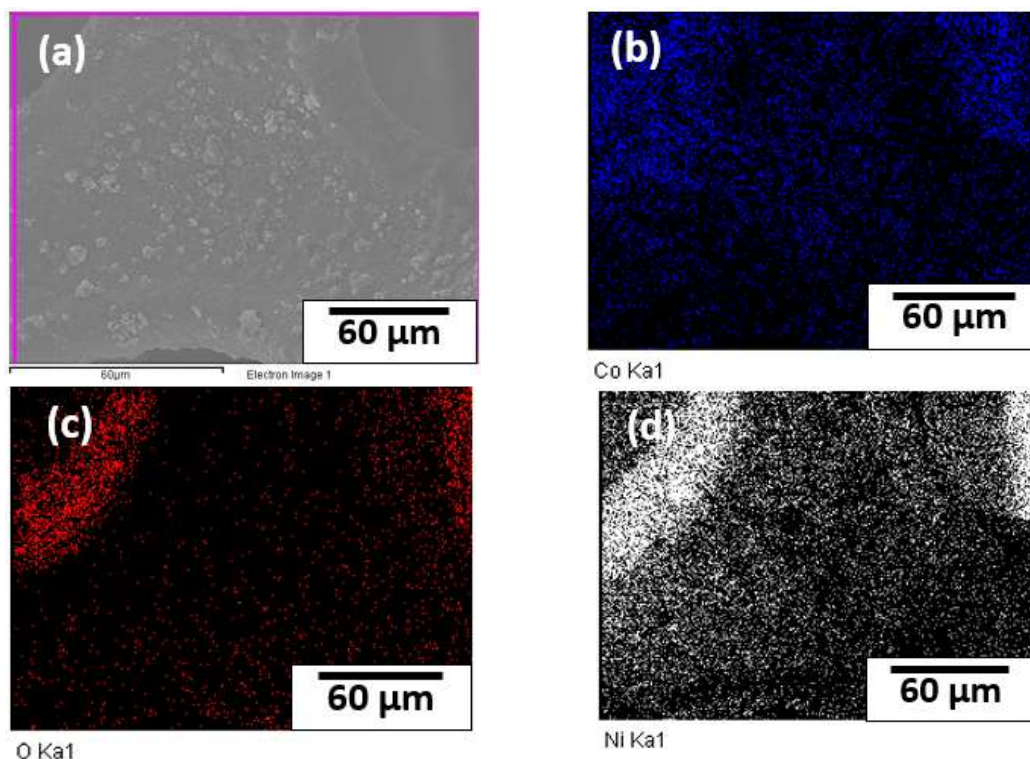


Figure S8.3 EDX elemental mapping of Co-Co₃O₄ composite thin film on NF substrate (a) SEM image (b) Co (c) O (d) Ni arising from the nickel foam (NF) substrate.

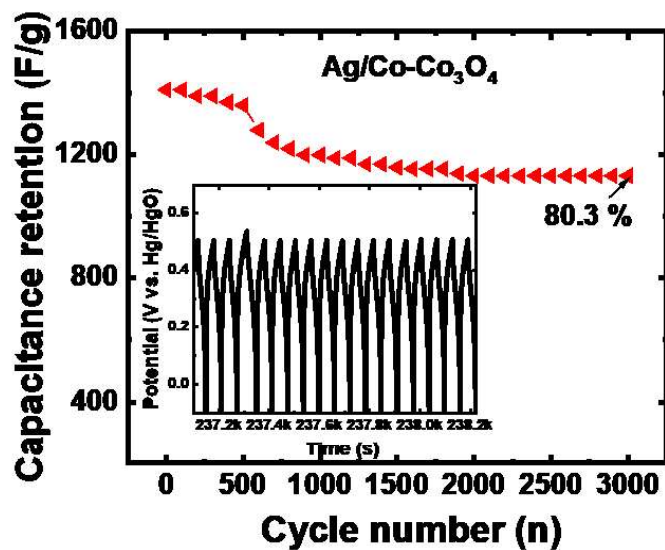


Figure S8.4 Cycling performance with inset showing the last 18 GCD cycles of Ag/Co-Co₃O₄/NF tested for 3000 cycles at a specific current of 20 A/g.

(b) Unpublished supporting information

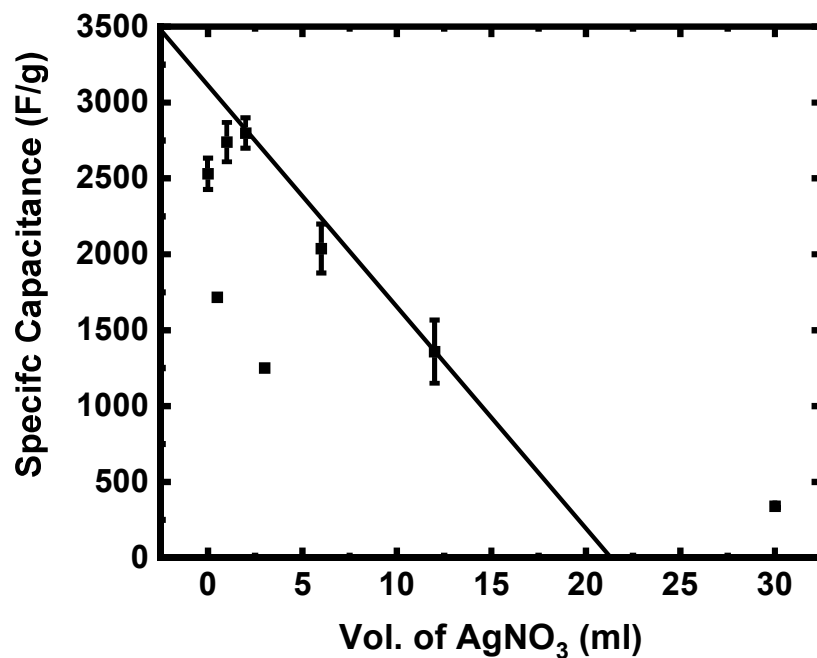


Figure S8.5. Optimization graph of the volume of AgNO₃ in the electrolyte solution for the electrodeposition of Ag/Co-Co₃O₄ nanocomposite thin films.

As part of the optimization process, the volume of AgNO₃ in the electrodeposition electrolyte consisting of cobalt acetate and cobalt chloride was varied to achieve Ag/Co-Co₃O₄ nanocomposites electrodes with maximum specific capacitance (Figure S8.5).

CHAPTER 9: CAPACITIVE BEHAVIOR OF ELECTROCHEMICALLY SYNTHESIZED POLYPYRROLE COATINGS ON NICKEL-MODIFIED ALUMINUM MESH AND STEEL MESH SUBSTRATES

Rania Afia Nuamah, Saleema Noormohammed, Dilip Kumar Sarkar

Department of Applied Science, University of Quebec at Chicoutimi, Aluminum Research Center-REGAL, Chicoutimi, Quebec, G7H 2B1, Canada

This manuscript is under review at:
Materials Science and Engineering Technology

9.1 Abstract

Polypyrrole, which is a conducting polymer is a promising electroactive material for supercapacitors owing to its high electrical conductivity and theoretical capacitance. The type of substrate on which the electroactive material is formed influences the transportation of electrons during charge storage processes as well as the morphology of electroactive materials. In this work, polypyrrole-coated nickel-modified aluminum and steel mesh supercapacitor electrode materials have been fabricated by a simple potentiostatic electrodeposition technique. The morphologies revealed by the scanning electron microscope correlate with the electrochemical and capacitive behavior while the energy-dispersive X-ray spectroscopy spectra confirmed the presence of the relevant elements. The structural composition has also been confirmed by the attenuated total reflection–Fourier transform

infrared spectra obtained. The electrochemical analysis of the polypyrrole-coated nickel-modified aluminum mesh electrode has shown superior performance by delivering a specific capacitance of $\sim 100 \text{ Fg}^{-1}$ at an applied specific current of 1 Ag^{-1} with an excellent conductivity revealed by a small equivalence series resistance of $0.18 \text{ }\Omega\cdot\text{cm}^2$.

9.2 Introduction

The rapid technological advancement in next-generation portable electronics such as mobile phones, laptops, cameras as well as hybrid vehicles, and backup power supplies requires flexible, lightweight, and, long-cycle life energy storage systems. Interestingly, Supercapacitors have gained attention in recent research as potential efficient energy systems as a result of their high-power density, high specific capacitance, safe and easy operation, and ultra-long lifespan [1-3]. Among a variety of electrode materials for supercapacitors such as graphene, activated carbon, transition metal oxides, conducting polymers (e.g., polyaniline, polyacetylene), polypyrrole is particularly attractive due to its environmental stability, easy processing, commercial availability of initial monomers, high specific capacitance and high electrical conductivity [1, 4, 5]. In addition to electrode materials, substrates or current collectors are vital to the performance of supercapacitors as they serve as paths along which electrons are transported during the storage and delivery processes of charges. Particularly, the contact resistance at the interface between the electroactive material and the current collector is consequential in the high-power application of supercapacitors [6]. Furthermore, studies have reported varied surface morphologies of polypyrrole and their respective

supercapacitor behavior by using different substrates such as nickel foam, carbon cloth, and steel mesh [2, 5, 7].

In this present work, an aluminum mesh has been modified with nickel and used as a substrate for the deposition of polypyrrole coating by a potentiostatic electrodeposition technique. The polypyrrole-coated nickel-modified aluminum mesh electrode was compared with a polypyrrole-coated steel mesh electrode to elucidate the effect of the substrate on capacitive performance.

9.3 Experimental details

Polypyrrole thin films were coated on nickel-modified aluminum, and steel meshes by a potentiostatic electrodeposition. Initially, a commercially available aluminum mesh was modified with nickel by a potentiostatic electrodeposition of nickel thin film on the aluminum mesh from an electrolyte solution of 0.5 M $\text{NiSO}_4 \cdot 6\text{H}_2\text{O}$ (30 ml) and 0.2 M $\text{NaClO}_4 \cdot \text{H}_2\text{O}$ (30 ml), by using a constant voltage of -1.4 V for 120 mins. Polypyrrole coatings were then formed on the nickel-modified aluminum mesh, and stainless-steel mesh by applying a constant potential of 0.8 V for 10 min. An aqueous precursor solution consisting of 0.6 M pyrrole (30 ml) and 0.2 M $\text{NaClO}_4 \cdot \text{H}_2\text{O}$ (30 ml) was used as the electrolyte. All depositions were carried out at room temperature using a standard three-electrode glass cell with a platinum wire, the nickel-modified aluminum mesh/stainless-steel mesh, and Ag/AgCl as the counter, working, and reference electrodes respectively.

The surface morphology and elemental composition of the electrodeposited coatings were studied by a scanning electron microscope (SEM, JEOL JSM-6480 LV), equipped with energy-dispersive X-ray spectroscopy respectively. An attenuated total reflection – Fourier transform infrared spectroscopy (ATR-FTIR, Agilent Technologies Cary 630) was used to confirm the chemical nature of the as-prepared polypyrrole coated nickel-modified aluminum mesh, and steel meshes electrodes.

The electrochemical characterization, which consists of cyclic voltammetry, galvanostatic charge-discharge characteristics, and, electrochemical impedance spectroscopy was carried out using Solartron SI1287 electrochemical workstation in a 1 M Na₂SO₄ electrolyte.

9.4 Results and discussion

9.4.1 Structural, morphological, and chemical analysis

The chemical nature of the polypyrrole-coated nickel-modified aluminum mesh (Ppy-Ni-Al) and polypyrrole-coated steel mesh (Ppy-St) has been ascertained by attenuated total reflection – Fourier transform infrared spectroscopy as shown in Figure 9.1(a). The characteristic peaks of polypyrrole located at 900 cm⁻¹ and 765 cm⁻¹ indicate the polymerization of pyrrole. Additionally, the peaks at 1067 cm⁻¹ and 1174 cm⁻¹ are assigned to C-H and C-N deformation vibrations respectively. The peaks at 1520 cm⁻¹ and 1682 cm⁻¹ are also assigned to the C-C and C=C stretching vibrations respectively in the pyrrole ring.

Furthermore, the broad peak at 3000 - 3500 cm^{-1} arises from N-H stretching vibrations of pyrrole units in polymers. The absorption bands around 600 cm^{-1} are assigned to metal-oxide vibration from the substrates. Although, metals do not show any peaks in Fourier transform infrared spectroscopy, the considerable shift in the characteristic peaks of polypyrrole (1520, 1682, and 3200-3500 cm^{-1}) in the polypyrrole-coated nickel-modified aluminum mesh spectrum could be a result of the nickel coating [1-3].

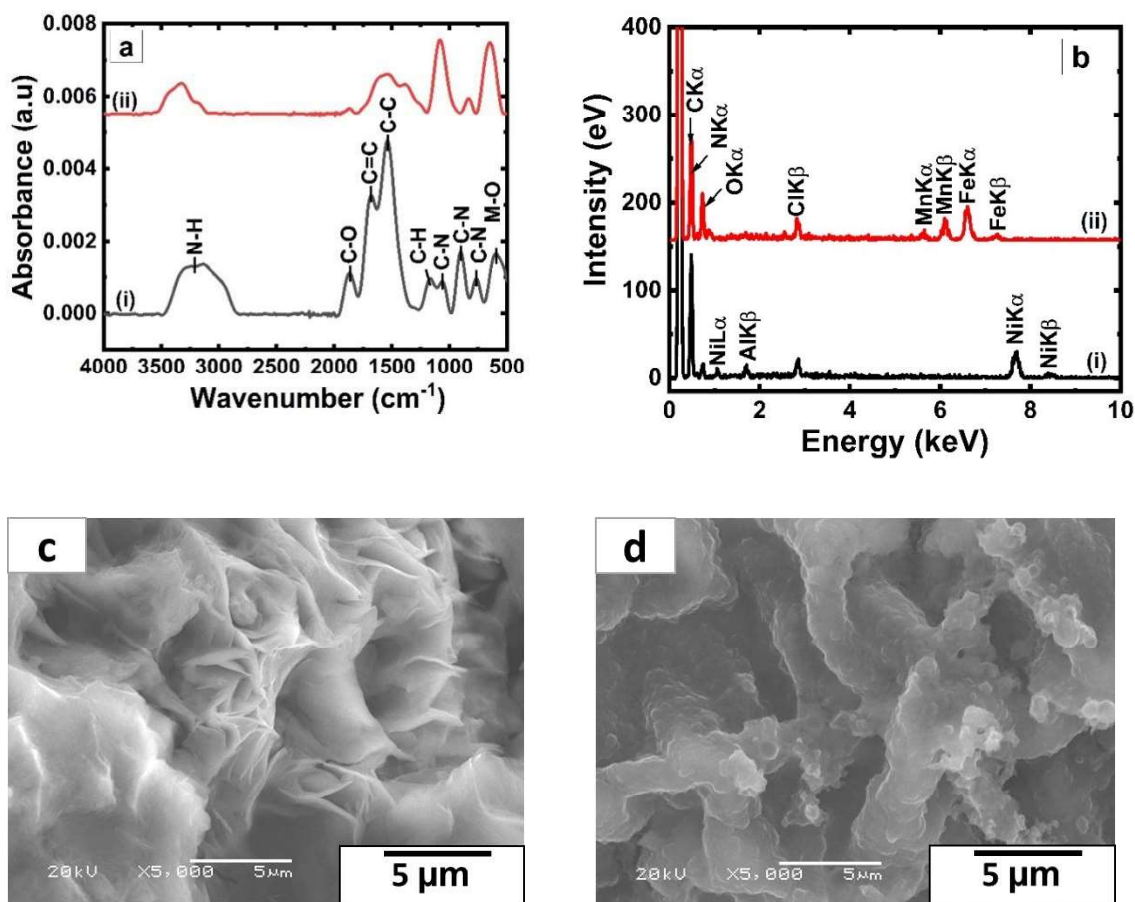


Figure 9.1. (a) Attenuated total reflection–Fourier transform infrared spectra, (b) energy-dispersive X-ray spectroscopy spectra of (i) polypyrrole-coated nickel-modified aluminum mesh (Ppy-Ni-Al), and (ii) polypyrrole-coated steel mesh (Ppy-steel), (c,d) scanning electron microscope micrographs of polypyrrole-coated nickel-modified and polypyrrole-coated steel meshes respectively.

The energy-dispersive X-ray spectroscopy spectra collected during the scanning electron microscope image analysis is presented in Figure 8.1(b). The peaks of carbon and nitrogen in the spectrum of the polypyrrole-coated nickel-modified aluminum mesh (Ppy-Ni-Al mesh) in Figure 9.1(b), (i) confirm the formation of the polypyrrole coating. The peaks of aluminum and nickel arise from the nickel-coated aluminum mesh. Similarly, the Ppy-coated steel mesh (Ppy-steel) in Figure 9.1(b), (ii) shows peaks of manganese and iron which come from the pristine steel mesh along with the peaks of carbon and nitrogen [1, 2, 4].

As the active surface area ensuing from the final morphology and structure of electrode materials have been demonstrated to have a significant impact on capacitance performance, the morphology of the polypyrrole-coated nickel-modified aluminum mesh (Ppy-Ni-Al) and, polypyrrole-coated steel mesh (Ppy-steel) have been obtained by scanning electron microscope imaging and presented in Figure 9.1(c) and (d) [5, 6]. The surface morphology of the polypyrrole-coated nickel-modified aluminum mesh in Figure 9.1(c) depicts a layered structure while that of the polypyrrole-steel mesh in Figure 9.1(d) shows intertwined globules. These morphologies (Figure 9.1(c) and (d)) are typically reported for polypyrrole synthesized by electrochemical polymerization either by potentiostatic or galvanostatic methods [1, 7].

9.4.2 Electrochemical measurements

The cyclic voltammetry curves of the polypyrrole-coated nickel-modified aluminum (Ppy-Ni-Al) mesh, and polypyrrole-coated steel (Ppy-steel) mesh electrodes at 100 mV/s is shown in Figure 9.2(a). The near rectangular shape of the cyclic voltammetry curves of both electrodes shows the pseudocapacitive behavior of the electrodes [2]. It can be observed that the cyclic voltammetry profile of the polypyrrole-coated nickel-modified aluminum mesh electrode is higher than that of the polypyrrole-coated steel mesh electrode, which indicates a higher accumulation of charge and therefore may show a higher specific capacitance.

Furthermore, the galvanostatic charge-discharge curves performed at a specific current of 1 A/g for the polypyrrole-coated nickel-modified aluminum mesh (Ppy-Ni-Al) and, polypyrrole-coated steel (Ppy-steel) mesh electrodes are shown in Figure 9.2(b). The nearly triangular shape of the curves further depicts the pseudocapacitive characteristics of both electrodes as suggested by the cyclic voltammetry curves. The specific capacitance obtained from the galvanostatic charge-discharge curves at an applied specific current of 1 A/g are 91 and 40 F/g for the polypyrrole-coated nickel-modified aluminum mesh and polypyrrole-coated steel mesh electrodes, respectively, using equation (9.1),

$$C_s = \frac{I\Delta t}{m\Delta V} \quad (9.1)$$

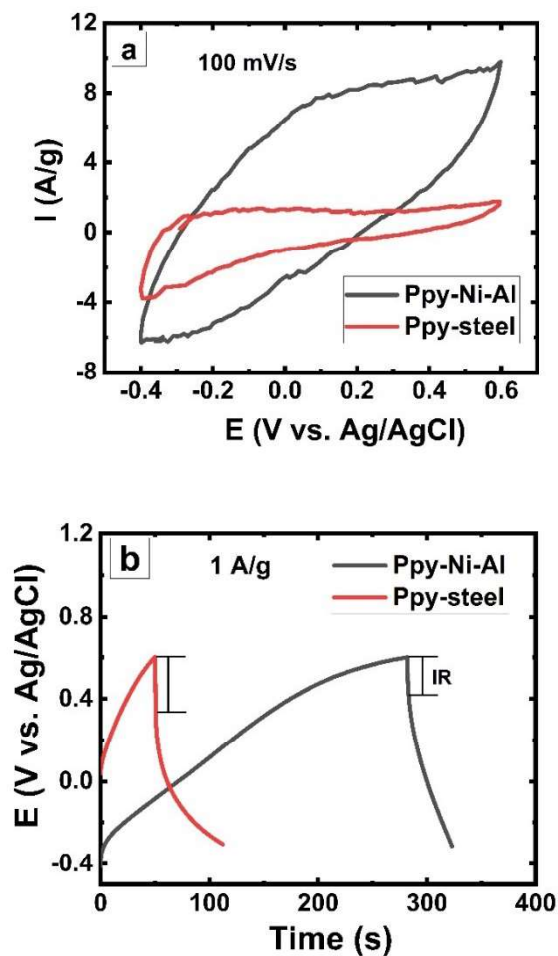


Figure 9.2. (a) Cyclic voltammetry curves at 100 mV/s, (b) Galvanostatic charge-discharge curves at 1 A/g of polypyrrole-coated nickel-modified aluminum mesh (Ppy-Ni-Al) and polypyrrole-coated steel (Ppy-steel) mesh electrodes respectively.

where C_s is the specific capacitance, I is the specific current, Δt is the discharge time, m is the mass of the electrode, and ΔV is the potential change during discharge. The specific capacitance value of the polypyrrole-coated nickel-modified aluminum mesh electrode is comparable to the previously reported value of polypyrrole-reduced graphene oxide composite thin film (132 F/g at 1 A/g) [7] and polypyrrole thin film (96 F/g at 1 A/g) [8] deposited on carbon bundle fiber and stainless steel substrates respectively. In addition, the

equivalent series resistance (ESR) which constitutes the inherent resistance of the electroactive material, electrolyte resistance, and the contact resistance at the electrode-electrolyte interface [7] has been calculated from the galvanostatic charge-discharge curves of the electrodes by taking the ratio of the potential drop (V_{IR}) between the charge and discharge curves to the discharge current. The obtained equivalent series resistance values are $0.18 \Omega \cdot \text{cm}^2$ and $0.26 \Omega \cdot \text{cm}^2$ for the polypyrrole-coated nickel-modified aluminum mesh and, polypyrrole-coated steel mesh electrodes, respectively. The superior performance of the polypyrrole-coated nickel-modified aluminum mesh electrode (Ppy-Ni-Al) is attributable to the enhanced electrical conductivity due to Ni coating which facilitates fast electron transport during the redox reactions. Additionally, its layered morphology provides a maximum surface area for enhanced charge storage.

9.5 Conclusions

A simple potentiostatic electrodeposition technique has been used to synthesize polypyrrole coatings on nickel-modified aluminum mesh and steel mesh. The polypyrrole-coated nickel-modified aluminum mesh electrode achieved a specific capacitance of 91 F/g while that of the polypyrrole-coated steel mesh electrode is found to be 40 F/g at a specific current of 1 A/g. Furthermore, the conductivity of the polypyrrole-coated nickel-modified aluminum mesh electrode which is evidenced by the equivalence series resistance ($0.18 \Omega \cdot \text{cm}^2$) is superior to that of the polypyrrole-coated steel mesh electrode ($0.26 \Omega \cdot \text{cm}^2$). The obtained results and observations show that the type of substrate influences the supercapacitor performance of polypyrrole-based electrodes.

9.6 References

- [1] J. Chen, Y. Wang, J. Cao, Y. Liu, Y. Zhou, J.H. Ouyang, D. Jia, Facile Co-Electrodeposition Method for High-Performance Supercapacitor Based on Reduced Graphene Oxide/Polypyrrole Composite Film, *ACS Appl. Mater. Interfaces*, 9 (2017) 19831-19842.
- [2] J. Zhao, J. Wu, B. Li, W. Du, Q. Huang, M. Zheng, H. Xue, H. Pang, Facile synthesis of polypyrrole nanowires for high-performance supercapacitor electrode materials, *Prog. Nat. Sci.: Mater. Int*, 26 (2016) 237-242.
- [3] M. Feng, W. Lu, Y. Zhou, R. Zhen, H. He, Y. Wang, C. Li, Synthesis of polypyrrole/nitrogen-doped porous carbon matrix composite as the electrode material for supercapacitors, *Sci Rep*, 10 (2020) 15370.
- [4] R.B. Choudhary, S. Ansari, B. Purty, Robust electrochemical performance of polypyrrole (PPy) and polyindole (PIn) based hybrid electrode materials for supercapacitor application: A review, *J. Energy Storage*, 29 (2020) 101302.
- [5] M.S. Javed, A.J. Khan, S. Asim, S.S.A. Shah, T. Najam, S.H. Siyalg, M.F. Tahir, Z. Zhao, W. Mai, Insights to pseudocapacitive charge storage of binary metal-oxide nanobelts decorated activated carbon cloth for highly-flexible hybrid-supercapacitors, *J. Energy Storage*, 31 (2020) 101602.
- [6] S.H. Lee, H. Lee, M.S. Cho, J.-D. Nam, Y. Lee, Morphology and composition control of manganese oxide by the pulse reverse electrodeposition technique for high performance supercapacitors, *J. Mater. Chem. A*, 1 (2013) 14606.
- [7] H.A. Abdul Bashid, H.N. Lim, S. Kamaruzaman, S. Abdul Rashid, R. Yunus, N.M. Huang, C.Y. Yin, M.M. Rahman, M. Altarawneh, Z.T. Jiang, P. Alagarsamy, Electrodeposition of Polypyrrole and Reduced Graphene Oxide onto Carbon Bundle Fibre as Electrode for Supercapacitor, *Nanoscale Res Lett*, 12 (2017) 246.
- [8] M.V.S. R. Ramya, Analysis of polypyrrole-coated stainless steel electrodes – Estimation of specific capacitances and construction of equivalent circuits, *J. Chem. Sci*, 120 (2008) 25–31.
- [9] M. Harilal, S.G. Krishnan, B.L. Vijayan, M. Venkatasamy Reddy, S. Adams, A.R. Barron, M.M. Yusoff, R. Jose, Continuous nanobelts of nickel oxide–cobalt oxide hybrid with improved capacitive charge storage properties, *Mater. Des.*, 122 (2017) 376-384.

9.7 Supporting information

The Nyquist plots in Figure S9.1 further explore the charge transfer kinetics of the Ppy-coated Ni-modified-aluminum (Ppy-Ni-Al) mesh, and Ppy-coated steel (Ppy-St) mesh

as potential electrodes. The charge transfer resistance (R_{ct}) values estimated from the diameter of the semicircle in the Nyquist plots are $11 \Omega \cdot \text{cm}^2$ and $45 \Omega \cdot \text{cm}^2$ for the Ppy-Ni-Al mesh, and Ppy-Steel mesh electrodes respectively. Also, the incline straight line in the lower frequency region of the Nyquist plots is shorter and steeper for the Ppy-Ni-Al mesh compared to that of the Ppy-Steel mesh. This indicates rapid ion diffusion from the electrolyte into the Ppy-Ni-Al mesh electrode, hence better capacitive characteristics complementing the obtained specific capacitance values [9]

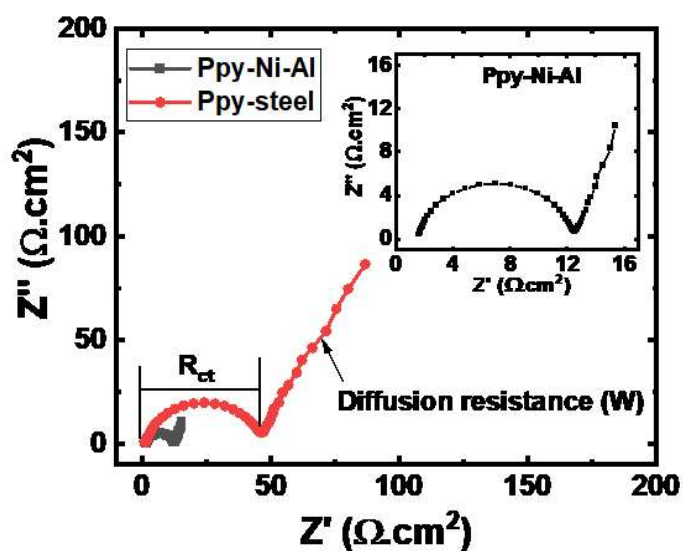


Figure S9.1. Nyquist plots of the Ppy- coated Ni- modified-aluminum (Ppy-Ni-Al) mesh, and Ppy-coated steel (Ppy-Steel) mesh electrodes.

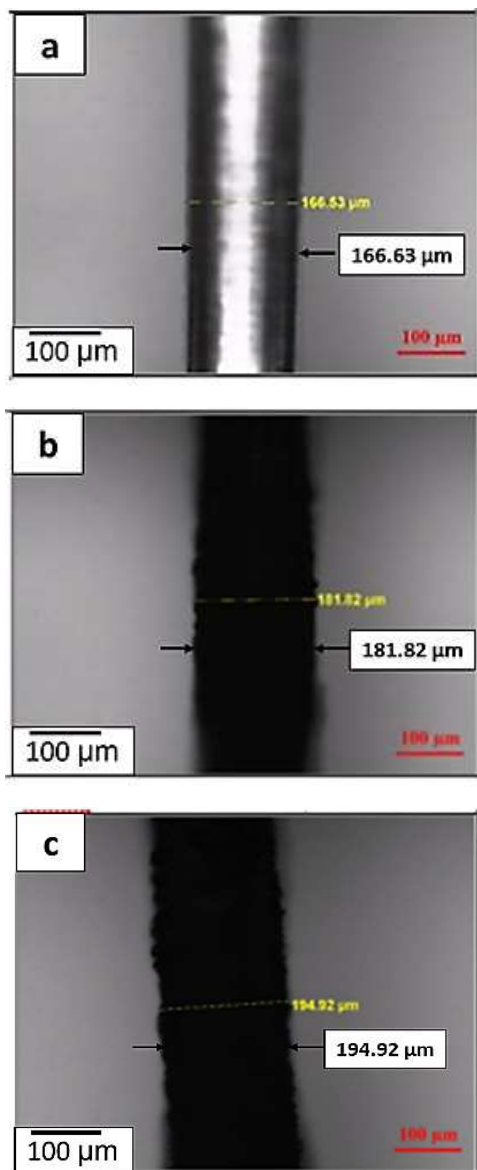


Figure S9.2. Optical microscope images of a micro-rod from (a) a cleaned aluminum (Al) mesh, (b) a Ni modified- aluminum (Ni-Al) mesh, (c) Ppy coated-Ni modified-aluminum (Ppy-Ni-Al) mesh.

The optical microscopy images of a micro rod of the aluminum mesh have been provided in Figure S9.2. The increase in diameter from the pristine rod from 166.53 μm to 181.82 μm after the surface medication with nickel coating confirms the presence of the nickel coating on the bare aluminum mesh. Similarly, the increase in diameter from 181.82 um to 194.92

μm after the polypyrrole electrodeposition confirms the presence of the polypyrrole coating. The optical microscope analysis complements the findings of the FTIR and EDX for the nickel-modified polypyrrole-coated aluminum mesh.

CHAPTER 10: GENERAL CONCLUSIONS AND FUTURE

RECOMMENDATIONS

10.1 Conclusions

Supercapacitor energy storage devices offer a practical solution to the problem of intermittent energy supply and a way of storing renewable energy sources for future use. To improve the efficiency of supercapacitor energy storage devices, the fabrication of nanostructured electrode materials having high capacitance, long cycle stability, and reproducibility is crucial. Thus, the objectives of this research were to engineer nanostructured electrode materials for supercapacitor energy applications via the chemical precipitation and electrodeposition synthesis routes and validate their electrochemical performance. Based on the research findings, the following conclusions have been established:

1. NiO and Co₃O₄ electrode materials were synthesized by a simple chemical precipitation route. The bonds of Ni-O and Co-O revealed by the AT-FTIR spectra confirmed the formation of the NiO and Co₃O₄ materials respectively. A complementary analysis by EDS showed the presence of elemental Ni, and O (for the NiO material), and O and Co (for the Co₃O₄ material). However, both electrodes performed poorly, with low specific capacitance values of 40 at 28 F/g and a specific current of 1 A/g. The poor performance was attributed

to the porous-free and agglomerated morphological features and the high mass loading of electrode materials.

2. A carbon-free Ni-NiO nanocomposite thin film electrode material (composed of nanospherical features of size ~ 50 nm) was prepared on titanium (Ti) substrate by a novel combined cyclic voltammetry and pulse reverse electrodeposition technique. XRD analysis confirmed the formation of Ni and NiO phases. While the presence of elemental Ni and O were revealed by EDX analysis. The carbon-free Ni-NiO nanocomposite thin film electrode material presents great potential for long-term supercapacitor electrode application, as it exhibited very high specific capacitance of 2000 F/g (at a current density of 1 A/g) and 97.4 % long cycle stability. The excellent performance of the carbon-free Ni-NiO nanocomposite thin film electrode materials could be attributed to the combined effects of highly porous nanospherical active surfaces and increased Faradaic redox reaction.

3. Co-Co₃O₄ nanocomposite thin film electrode materials were synthesized by optimizing the molar ratio of electrolyte precursor and the modes of the electrodeposition process. By optimizing the molar ratio of electrolyte solution (composed of cobalt acetate and cobalt chloride salt), Co-Co₃O₄ nanocomposite thin film electrode materials were fabricated on nickel foam substrates via a novel combined cyclic voltammetry and pulse reverse electrodeposition technique. The deposited films, showed variations in both surface morphology and microstructure of Co-Co₃O₄ materials, resulting in different electrochemical behaviors. The XRD spectra analysis revealed the formation of both Co and Co₃O₄ phases, as well as the variations in crystallinity. Furthermore, ATR-FTIR and EDX analyses confirmed the presence of Co₃O₄ absorption bands, and elemental O and Co, respectively. The specific capacitance values obtained were in the range of 460-2580 F/g at 1 A/g.

Furthermore, the capacitance retention values recorded were in the range of 60-90.5 % after 500 cycles under a high current load of 20 A/g. It was observed that An optimized ratio of cobalt acetate: cobalt chloride (20:80) exhibited the maximum specific capacitance of 2,580 F/g (at 1 A/g) and capacitance retention of 90.5 % after 500 cycles (under a high current load of 20 A/g).

4. Regarding optimization of electrodeposition mode, Co-Co₃O₄ nanocomposite electrode materials were deposited on nickel foam (NF) substrates in four different electrodeposition modes, namely, cyclic voltammetry (CV), a combination of cyclic voltammetry and potentiostatic (at -1.4 V (CV PS -1.4V)), combination cyclic voltammetry and potentiostatic at 1.0 V (CV PS +1.0V) and combination of cyclic voltammetry and pulse reverse potential (CV PRP). The presence of the phases of Co and Co₃O₄ for the four electrodeposition modes, as well as variations in crystallinity, were revealed by XRD studies. The capacitance values of Co-Co₃O₄ composite thin films obtained by CV, CV PS -1.4V, CV PS +1V, and CV PRP, respectively, were found to be 1661, 1400, 1866, 2580 F/g at an applied current load of 1 A/g, while the capacitance retentions after 500 cycles (under a high current load of 20 A/g) were 85.8, 77.8, 87.1, and 90.5 %, respectively. Comparative analysis showed that electrode material deposited by the CV PRP process had high specific capacitance and charging/discharging cycle stability.

6. To further enhance the electrochemical performance of the Co-Co₃O₄, Ag was incorporated in Co-Co₃O₄ (presenting superior capacitive behavior and cycle durability) to fabricate Ag/Co-Co₃O₄ nanocomposite thin film electrodes using the novel combined cyclic voltammetry and pulse reverse potential (CV PRP) modes of electrodeposition. The XRD studies revealed the phases of Co, Co₃O₄, and Ag. Furthermore, SEM analysis revealed a

porous nanoflakes network of the Ag/Co-Co₃O₄ features and increased specific surface area. The Ag/Co-Co₃O₄/NF electrode exhibited a high specific capacitance of 2800 F/g, outstanding specific energy of 140 Wh/kg, power of 294.9 W/kg, and capacitance retention of 82.6 %, after 1000 cycles. It was observed that the incorporated Ag particles improved the electrical conductivity, faster electron transport, as well as increased active sites for enhanced charge storage.

7. A simple potentiostatic electrodeposition technique was used to synthesize polypyrrole coatings on nickel-modified aluminum mesh and steel mesh. The polypyrrole-coated nickel-modified aluminum mesh electrode exhibited a specific capacitance of 91 F/g (at a specific current of 1 A/g), compared to 40 F/g, for the polypyrrole-coated steel mesh electrode. Furthermore, the conductivity of the polypyrrole-coated nickel-modified aluminum mesh electrode (with equivalence series resistance (ESR=0.18 $\Omega\cdot\text{cm}^2$)) was superior to that of the polypyrrole-coated steel mesh electrode (with ESR=0.26 $\Omega\cdot\text{cm}^2$). Again, it was observed that the presence of the nickel coating, enhanced electrical conductivity, thereby facilitating fast electron transport during the redox reactions, thus increasing electrochemical performance.

Overall, the electrode materials engineered via the novel combined CV and PRP electrodeposition modes technique, look promising as electrode materials for practical applications in a supercapacitor device.

10.2 Future recommendations

In this research, an attempt has been made to fabricate nanostructured supercapacitor electrode materials. While remarkable achievements have been made, there are still opportunities for advancement. It is therefore suggested that future works should be focused on the following:

1. As it has been proven that a large specific surface area and an optimum mass loading of electroactive material are critical for high specific capacitance and general electrochemical performance, future research can optimize the mass loading of active materials (NiO and Co₃O₄) produced by the chemical precipitation route. Furthermore, synthesis parameters such as temperature and time can be optimized to obtain morphological features that offer high specific surface areas for enhanced specific capacitance.
2. Further studies need to be conducted to gain more insight into the electrochemical reactions during the electrodeposition process for a deeper comprehension of the nucleation and growth process of the metal-metal oxide composite. Again further optimization process can be carried out by varying the CV deposition cycles to obtain nanoscale features to further enhance the electrochemical performance of the metal-metal oxide composites.
3. Fabrication and electrochemical assessment of a supercapacitor device with the high-performing nanostructured electrode materials (Ni-NiO, Co-Co₃O₄, and Ag/Co₃O₄) to explore their practical applications presents another direction for future study. Furthermore, future research can explore widening the potential window of the engineered metal-metal

oxide electrodes by fabricating composite metal/metal oxide-carbon materials to improve the energy density.

4. In-situ characterizing techniques can be explored to identify changes in morphology and structure to gain insight into factors that cause a reduction in capacitance during the extended cycling process.

5. With the polypyrrole electrodes, future work can be focused on increasing the specific capacitance and cycle stability by incorporating metal oxide and carbon materials.

6. Finally, future work can be directed at investigating further improvements on the engineered materials and their potential uses in the field of other energy storage applications such as electrochemical water splitting to produce hydrogen and oxygen gas for fuel cells.

LIST OF PUBLICATIONS

Journal articles

1. Rania Afia Nuamah, Saleema Noormohammed Dilip Kumar Sarkar, Pulsed Reverse Potential Electrodeposition of Carbon-Free Ni/NiO Nanocomposite Thin Film Electrode for Energy Storage Supercapacitor Electrodes, *Coatings*, 11, 7 (2021) 780.
2. Rania Afia Nuamah, Saleema Noormohammed Dilip Kumar Sarkar, Specific capacitance behavior of Co-Co₃O₄ nanocomposite thin films synthesized via different electrodeposition modes, *Int. J. Energy Res.*, 46 (2022) 4434-4444.
3. Rania Afia Nuamah, Saleema Noormohammed Dilip Kumar Sarkar, Supercapacitor performance evaluation of nanostructured Ag-decorated Co-Co₃O₄ composite thin film electrode material, *Int. J. Energy Res.*, 46 (2022) 13099-13110.
4. Rania Afia Nuamah, Saleema Noormohammed Dilip Kumar Sarkar, Effect of molar ratio modulation of cobalt precursors on supercapacitor behavior of engineered Co-Co₃O₄ nanocomposite electrodes, *ACS Appl. Eng. Mater.*, 1 (2023), 241-251

Conferences Attended (Oral and Poster presentations)

1. Rania Afia Nuamah, Saleema Noormohammed, Dilip Kumar Sarkar, (November 2021). Capacitive behavior evaluation of electrochemically synthesized polypyrrole-coated nickel-modified aluminum mesh electrode, oral presentation at International Conference on Material Characterization and Modelling (ICMCM 2021) virtual. (Best presentation award)
2. Rania Afia Nuamah, Saleema Noormohammed, Dilip Kumar Sarkar, (November 2021). Comparison of supercapacitor behavior of polypyrrole coated aluminum and nickel oxide coated titanium foil, poster presentation at at journée des étudiants du REGAL, Centre des congrès de Trois-Rivières Marriott Hotel.
3. Rania Afia Nuamah, Saleema Noormohammed, Dilip Kumar Sarkar, (October 2020). Electrodeposited polypyrrole -electroplated aluminum mesh electrode for supercapacitor applications, poster presentation at at journée des étudiants du REGAL, Quebec, QC.